A THIN FILM BLOOD FLOWMETER

by

WILLIAM M. MORRIS

Thesis presented for the Degree of Doctor of Philosophy at the University of Edinburgh,

JANUARY 1972

ACKNOWLEDGMENT

I would like to express my appreciation for the help received from many colleagues in the Department of Electrical Engineering and in the Poultry Research Centre. I would also like to thank Mr A. MacKenzie of the P.R.C., who carried out the X.R.F. analyses; Mr G.R. Angell of the Department of Geology, who carried out the X-ray diffraction analyses; Mr J. Telford, of the P.R.C., who carried out the A.A.S. analyses; and Messrs I. McGee and J. Moir who provided the evaporation facility.

Special thanks are due to my supervisors, Professor W.E.J. Farvis, Mr J. Murray and Dr. M.H. Draper, for their help and encouragement throughout the work; and to Dr. J.H. Filshie for many useful conversations. Finally, I would like to thank my wife and my parents for their support and encouragement.

SUMMARY

A pulsed thermal blood flowmeter is described. It was designed to satisfy the need for an implantable flowmeter which is capable of continuous operation over a period of weeks on small diameter (1 mm) blood vessels. The mean flow rate in the range 0 to 100 ml/minute is measured. Sampled measurements of flow rate are made by periodically monitoring the variation of the dissipation factor of a thin film thermistor with the flow velocity over it. Information on the blood temperature is also obtained from this system. The data is transmitted from the source and processed digitally.

No suitable commercial thermistor was available so that it had to be manufactured. A description of the D.C. diode sputtering system which was used to deposit the thermistor material is described. A limited study of the structure and composition of the sputtered thermistor material, a mixture of three transition metal oxides, is also included. The design of the thermistor involved an examination of the heat transfer problem in order to establish approximate equations relevant to the design. The process steps involved in thermistor production are outlined.

The test circuitry used to assess the flowmeter is described. The implant circuitry consists of a pulse generator, an oscillator and a transmission gate. The data processing equipment includes a counter and PDP8-L computer.

The flowmeter was found to operate successfully. Its power consumption is sufficiently low for it to be useful in many applications. Its calibration curve is non-linear and it is capable of detecting both forward and reverse flow; however, it does not sense flow direction.

C O N T E N T S

Chapter 1

INTRODUCTION

1.1 Introduction

The detection of blood flow is necessary in much of physiological research. The circulation system is responsible for the transportation of materials around the body and for the regulation of parameters such as temperature, water balance and acid-base equilibrium. Data on the variations in blood supply can furnish useful information in a study of the dynamic operation of a region or organ. There is, however, no generally applicable technique of flow measurement: instead there is a number of different techniques which are designed for specific applications. This thesis is concerned with the development and evaluation of a blood flowmeter which will satisfy the requirements of a particular research programme to be carried out by the Poultry Research Centre (P.R.C.), Edinburgh.

The programme is primarily concerned with the dynamic operation of the oviduct and the renal portal system in domestic hens. The oviduct is the tube in which the albumen, shell membrane and shell are built up around the ovum, or yolk, to produce the egg. A complex control mechanism operates to supply the necessary components to the appropriate section of the oviduct when they are required by the presence of an ovum in the section. The blood supply plays a significant role in transporting components. It is the operation of the control mechanism that is the subject of the research. The approach to the investigation is to study the relative blood flow rates to sections of the oviduct over a period of time during which

controllable parameters affecting the bird's condition are changed. By comparing the blood supply under different conditions both with and without an ovum present in the duct it is possible to establish which parameters affect the flow and hence to achieve an insight into the control mechanism. Another vascular problem of importance is the blood supply system to the avian kidney, which differs from the mammalian equivalent in that it has two blood supplies, a renal arterial supply and a renal portal system. The objective of this research programme is to establish both when and why flow occurs in each vessel of the renal portal system.

Accurate quantitative data on blood flow rates are not available for the regions concerned. However, it has been estimated by workers in the field that the values lie in the range 0 to 2 ml/s in the renal portal system[1] and 0 to 0.5 ml/s in an active oviduct segmental blood supply system.[2] The internal diameters of the blood vessels concerned are approximately 1 mm. In both cases it can be assumed[3] that the flow is essentially steady with only a small pulsatile component whose fundamental frequency is 5 Hz. Further, changes in flow rate can be assumed[3] to occur over a period of the order of seconds. Relatively large changes in mean flow rate in unrestrained birds are of interest, particularly the times at which the flow rates change, and their mean values when the steady flow component is constant. The time scale of the measurements[4] is of the order of 10 hours, repeatable over a period of days.

1.2 The flowmeter specifications

The continuous measurement of mean volumetric flow rate is

required in vessels whose internal diameters are approximately 1 mm and whose lengths[3] are of the order of 1 cm. The steady nature of the flow and its slow rate of change will permit sampled measurements to be made at a frequency of not less than 1 Hz without loss of significant data. If the pulsatile flow component is very small compared to the changes in the steady flow component then it may be neglected. If not, then the mean flow rate may be obtained by averaging the sampled measurements over the period in which the steady flow component is constant. Averaging cannot, however, be employed when the steady flow component is changing, so that the sampled flow measurements and hence the timing of the occurrence of a change in flow rate is subject to an error associated with the pulsatile flow component. Figure 1.1 illustrates this argument. The timing error is expected to be small or negligible compared to with the period over which the steady flow component has a constant value. The detection of the direction of flow is not important; however, the system must be capable of detecting zero flow and of measuring low flow rates. The instrument must be implanted in the bird in order to avoid the restraining effect of external leads. The experiments are to be carried out on caged birds after they have recovered from surgery.

Implantable circuitry which is required to operate for long periods imposes restrictions on the power consumption of the system. It is proposed to use Duracell type WH3 batteries as the power source. They have a capacity of 160 mA hours and a nominal voltage of 1.35V. The maximum practical battery volume that can be implanted restricts the voltage available to a maximum of 12V. A

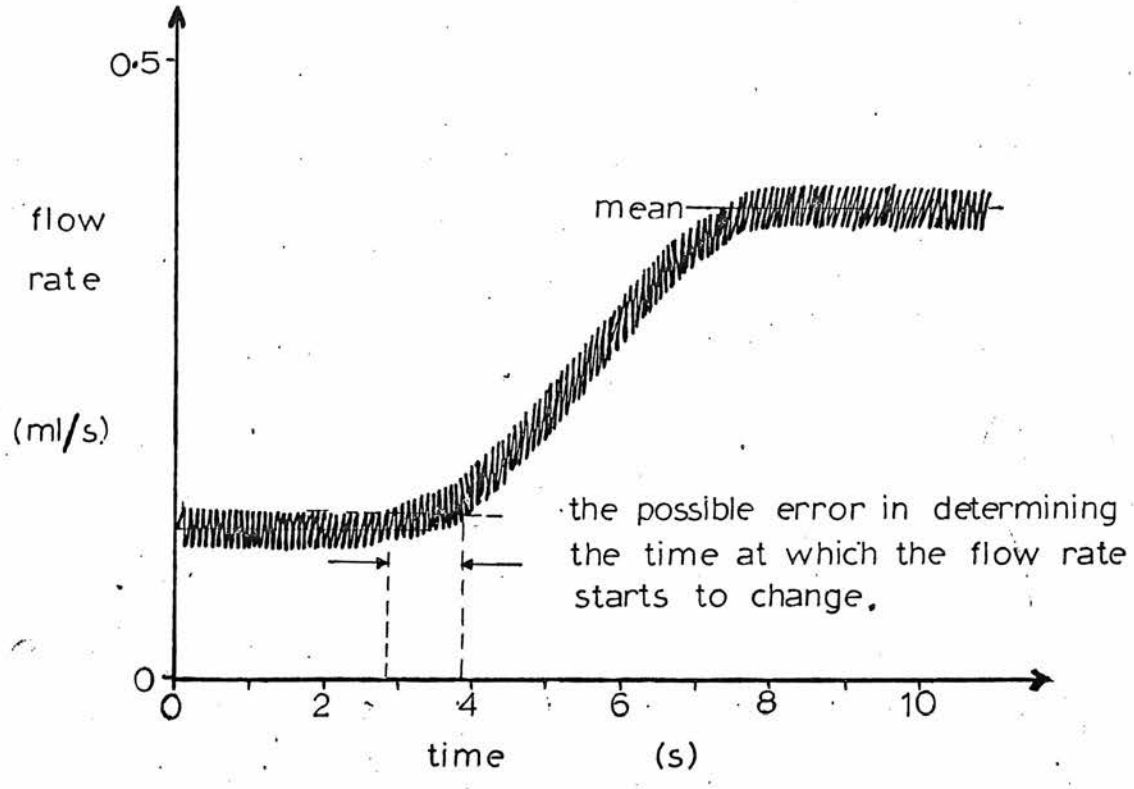

Figure 1.1. An illustration of a possible source of error which occurs when sampled measurements are made of flow rate with a significant pulsatile component.

6V system is preferable, however, because it is compatible with existing implantable instruments used by the P.R.C. to detect variations in the diameter of the oviduct. Further work is being carried out by the P.R.C. to develop a rechargeable battery system in which R.F. power is transmitted into the bird from a primary coil on the cage to an implanted secondary coil. Preliminary results indicate that the system, which includes rectification and smoothing, is capable of producing 6V d.c. with a current of 1 mA for an input power of 15W.

1.3 Principle of operation

A short survey of blood flowmeters is given in Appendix 1. A summary of the limitations of the different methods of flow measurement is contained in Tables 1.1 and 1.2. In these tables the frequency response of each method is considered generally under the heading 'Detection of pulsatile flow'. 'Cannulation' is defined here as severance of the blood vessel. 'Indirect measurement of volumetric flow rate' implies that flow velocity is measured. The other factors listed are self explanatory. Now, the requirements of continuous flow measurement or of sampled measurement at a frequency of greater than 1 Hz in an unrestrained bird restricts the choice of flowmeters to electromagnetic, ultrasonic, hydrodynamic and thermal types. The low power condition cannot be readily satisfied with electromagnetic systems, and ultrasonic transducers are difficult to manufacture with a lumen diameter of less than 3 mm, thereby restricting their use to larger vessels. Hydrodynamic flowmeters are, in general, not suitable as long-term implants. Of the four

Table 1.1. Flowmeter limitations

methods	duration and continuity	for detection of pulsatile flow	bidirectional	linear calibration	cannulation necessary	dependence on fluid properties	direct measurement of volumetric flow rate
outflow method	short time repeatable at intervals	no	no	yes	yes	no	yes
venous occlusion	short time repeatable at intervals	no	no	yes	no	no	yes
travelling markers	single determination repeatable at intervals	no	no	yes	in some cases	no	yes
marker dilution	single determination repeatable at intervals	no	no	—	no	in some cases	no
displacement methods	short time repeatable at intervals	no	no	yes	yes	no	yes
thermal	continuous	in some cases	in some cases	no	in some cases	yes	no
electromagnetic	continuous	yes	yes	yes	no	no	yes
ultrasonic	continuous	yes	in some cases	yes	no	no	no
hydrodynamic	see Table 1.2.						

Table 1.2. Hydrodynamic flowmeter limitations

methods	duration and continuity	for detection of pulsatile flow	bidirectional	linear calibration	cannulation necessary	dependence on fluid properties	direct measurement of volumetric flow rate
venturi	continuous	no	no	no	yes	no	no
orifice	continuous	poor	yes	no	yes	no	no
pitot	continuous	yes	yes	no	no	no	no
pressure gradient	continuous	yes	yes	no	no	no	no
rotameter	continuous	no	no	yes	yes	no	yes
electroturbinometer	continuous	no	no	no	yes	no	yes
bristle & pendulum	continuous	yes	yes	no	yes	yes	no

types, a thermal method appears best to satisfy the dimensions and conditions of this application. The isothermal flowmeter is the only thermal type suitable for use in very low flow conditions. However, this flowmeter requires complex control circuitry, which is difficult to implant. It was decided, therefore, to use a new variation of the type that exploits the dependence of the dissipation factor of a thermally-sensitive resistor on the velocity of the ambient medium.

First considering the transducer, both metal films and transition metal oxide thermistors have been used in steady state heat transfer flowmeters. Metal films such as platinum-silver alloys have a positive temperature coefficient of resistance[5] of the order of 0.1%/°C at 20°C, while thermistors of the transition metal oxide type have negative t.c.r.s[6] in the range 1 to 5%/°C at the same temperature. The t.c.r. of the transducer will, in part, determine the sensitivity of the flowmeter for a given heating power. Therefore it is proposed to employ the transition metal oxide type. The resistance of this type of thermistor, R, at temperature, T, is approximately given[7] by

$$R = R_o \exp\left(B\left(\frac{1}{T} - \frac{1}{T_o}\right)\right), \qquad 1.1$$

where Ro is the resistance at reference temperature To. The units of temperature are degrees Kelvin. B is a constant for a particular thermistor material and has units of temperature. Equation 1 may be linearised by introducing the approximation

$$R = R_o(1 - \alpha_o(T - T_o)) \qquad 1.2$$

which is valid when $T-To \ll To$. α_o is the temperature coefficient of resistance measured around To. It is defined[6] as

$$\alpha = \frac{1}{R}\left(\frac{dR}{dT}\right) . \qquad 1.3$$

Substituting equation 1.1 in 1.3 and differentiating gives

$$\alpha = -\frac{B}{T^2} . \qquad 1.4$$

Over the temperature range involved in the flowmeter application α_o can probably be assumed to be constant, providing To lies within this temperature range.

The basic principle of the flowmeter is illustrated in figure 1.2 for a negative temperature-coefficient thermistor. A train of identical constant-current pulses is supplied to the thermistor which is located in the blood stream. The magnitude of the current pulses is sufficient to cause significant Joule heating during the pulse. The pulse repetition rate is adjusted to permit the device to cool to ambient temperature between pulses. Considering a single pulse, the leading-edge height of the voltage pulse is determined by the resistance of the thermistor at ambient temperature. The trailing-edge height is determined by the resistance at some higher temperature which is a function of the Joule heating, the thermal capacity of the device and the rate of flow of heat from its boundaries. When the temperature of the thermistor surface rises above ambient temperature and forced convection operates, the rate of flow of heat into the blood is a function of its velocity over the heated surface. In this situation the trailing edge height is a function of several factors, including the flow velocity averaged over the period in which convection contributes to the transient heat transfer. Hence the resulting measurement of flow velocity is an average value and, if the period of averaging is comparable to the pulsatile flow period, then

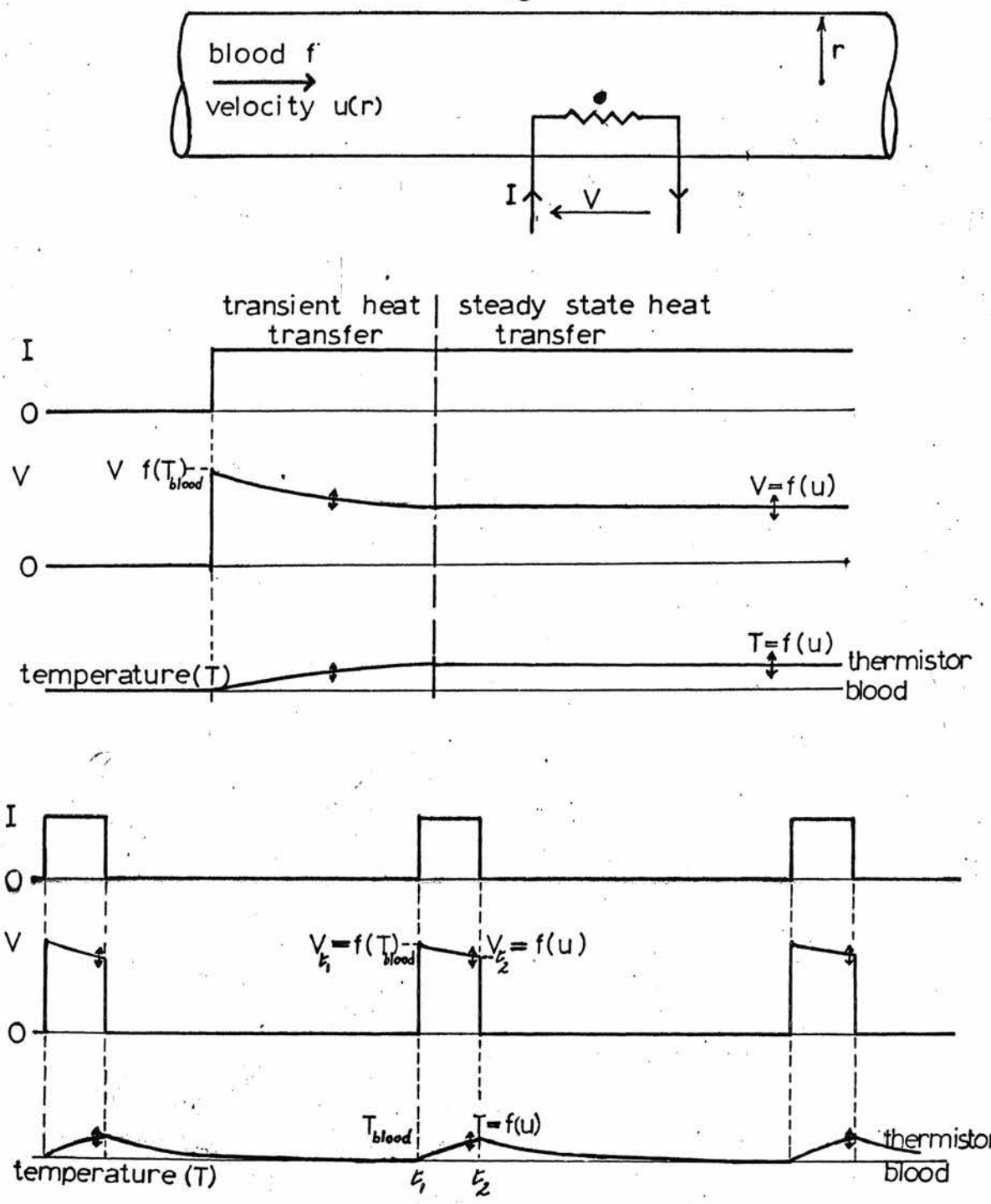

Figure 1.2. The voltage and temperature response of a N.T.C. thermistor to a step and pulsed heating current. The thermistor is located in the blood stream.

the accuracy of the flow measurement is improved, particularly when the steady flow component changes.

The relationship between the relevant factors can be evolved from the following approximate analysis. The instantaneous power equation applicable to the thermistor at time t_2 can be written thus:

$$P_{t_2} = C\frac{dT}{dt} + K^1(u)(T - T_b) \qquad 1.5$$

where P is the power dissipated in the thermistor. T and T_b are the temperatures of the thermistor and blood respectively. C is the heat capacity of the thermistor, that is, the energy required to raise its temperature by $1^{\circ}C$ without heat loss from its boundaries. K(u), the dissipation factor, is the power required to maintain the thermistor at $1^{\circ}C$ above the ambient temperature. Its value is a function of the geometry of the device and of both the thermal properties and velocity of the ambient medium. Rasmussen[8] established an empirical relationship between the dissipation factor of bead thermistors and the velocity of the medium, u, in the form

$$K(u) = K(o) + a(1 - e^{-bu}) \qquad 1.6$$

where K(o) is the dissipation factor at zero flow (i.e. the dissipation constant) and K(o) + a is the limiting value approached at high relative velocities. Both a and b are constants. K(u) is measured under steady state heat transfer conditions so that $K^1(u)$, a modified dissipation constant, must be used in equation 1.5 to take into account the limited development of the thermal field in the blood at time t_2. K(u) and $K^1(u)$ bear similar relationships to velocity. This is discussed in Chapter 4.

The power dissipated in the thermistor is given by

$$P = I^2R = I^2R_o\left(1 - \alpha_o(T - T_o)\right)$$
$$= I^2R_o\left(1 - \alpha_o\left((T - T_b) + (T_b - T_o)\right)\right) \qquad 1.7$$

providing $T-T_o \ll T_o$. Variations in blood temperature in the regions concerned in this application have been estimated[1] to be $\pm 2^oC$ about the mean value, 40^oC.

In addition, assume that the current pulse width is sufficiently small for the temperature rise to be regarded as linear, so that

$$\frac{dT}{dt} = \frac{T - T_b}{t_2 - t_1} \qquad 1.8$$

where the times t_1 and t_2 are defined in figure 1.2.

Substituting equations 1.7 and 1.8 in 1.5 gives

$$I^2R_o\left(1 - \alpha_o\left((T-T_b) + (T_b - T_o)\right)\right) = c\,\frac{T - T_b}{t_2 - t_1} + K'(u)(T - T_b)$$

$$T - T_b = \frac{I^2R_o\left(1 - \alpha_o(T_b - T_o)\right)}{K'(u) + \frac{c}{t_2 - t_1} + I^2R_o\alpha_o} \qquad 1.9$$

The temperature difference at t_2 is a function of two variables, the blood temperature and the dissipation factor, the other factors in the equation being constant in this application. Hence, by measuring both the leading-edge height and the difference in leading- and trailing-edge heights of the voltage pulses, it is possible to monitor periodically the blood temperature and the blood velocity over the transducer. The velocity measurement must be corrected for variations in blood temperature. The sampling frequency is inversely related to the thermal time constant of the thermistor at zero flow. The flowmeter can be calibrated in terms of volumetric flow rate providing the flow is laminar, the diameter of the vessel and the

fluid properties are constant and the location of the transducer is fixed with respect to the velocity profile of the flow. The instrument is, in fact, measuring mass flow rate. However, provided that the density of blood is constant, the flowmeter output can be regarded as representing volumetric flow rate. In turbulent flow, the blood velocity over the transducer is a function of local turbulence which cannot be readily related to the volumetric flow rate.

The flowmeter is potentially capable of measuring both forward and reverse flow, but it is unable to sense flow direction. The calibration curve is non-linear and has the shape, derived from equations 1.6 and 1.9, which is illustrated in figure 1.3. It can be seen that the flowmeter is more sensitive at low flow rates. This transient mode of operation, compared with the steady state heat transfer mode, has the advantages that only one thermistor and relatively simple implant circuitry is required. Further, there is no possibility of overheating the environment. The system may be operated using constant voltage pulses and monitoring the resulting current pulses. However, with negative temperature coefficient thermistors there is a possibility of thermal runaway occurring and for this reason the constant current mode is used.

1.4 The transducer

The complete transducer consists of a thermistor located in a fixed position in a short section of artificial blood vessel which replaces a section of the natural vessel. The minimum diameter of the natural vessel in which the system can be employed is imposed by the dimensions of the thermistor and by the surgical problems of

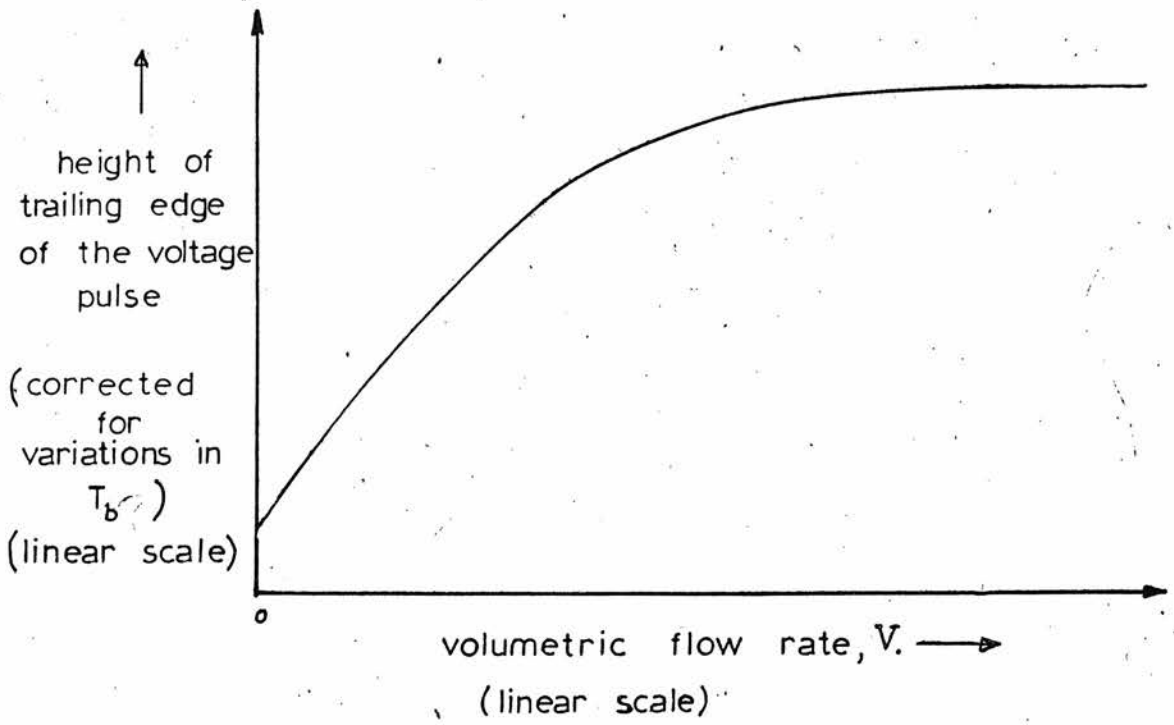

Figure 1.3. An illustration of the shape of the flowmeter calibration curve derived from equations 1.6 and 1.9.

implantation. The conditions restricting the thermistor dimensions are that it must not obstruct the flow and it must be of such a shape as to minimise hemolysis. The mode of operation of the transducer imposes further conditions. The thermal time constant of the thermistor and its support is inversely related to the sampling rate of the flow measurement. The thermal time constant, τ, is given[7] by the equation

$$\tau = \frac{C}{K(u)} \qquad 1.10$$

Hence, it is directly related to the volume of material involved, and is a decreasing function of the surface area of the device. Therefore, ideally, a device with a minimum volume and a maximum surface area is required. The geometry also defines, in part, the transit time of the thermal disturbance between the region in the device in which heat is generated and the device surface. The transit time is obviously required to be small compared to the duration of the heating pulse. This point is well illustrated by preliminary experiments which were carried out to test the basic principle of operation. An S.T.C. p-type bead thermistor with a diameter of 0.5 mm was supplied with a constant current pulse which was sufficiently large to cause significant self heating. This was carried out in both still air and still water environments which were at the same temperature. When identical current pulses were applied identical voltage pulses were produced even when steady state heat transfer conditions were approached. This implies that thermal equilibrium is approached without involving heat transfer from the surface of the bead. Hence, in order to satisfy the above conditions, the geometry most suited to this application is a thin film. A mechanical support

is necessary for the device, irrespective of its geometry, when used in potentially high velocity environments. The support will contribute to the effective volume which determines the thermal time constant of the device. The contribution is a function of the duration of the heating pulse and is minimised by the use of materials with suitable thermal properties.

The one commercial thin film thermistor available has too large a surface area (3 x 3 mm^2) to be of use in small diameter vessels. Further, the factors of high cost (£20), poor quality of manufacture and long delivery times do not recommend it for use in larger vessels. It was therefore considered necessary to manufacture suitable thin film thermistors as the first stage in the development of the flowmeter.

1.5 Associated circuitry

A block diagram of the proposed implant and receiver-data processing systems is shown in figure 1.4. The requirements of implantation, and hence the radio transmission of data, suggests a data extraction system based on frequency counting techniques applied to a carrier which is frequency modulated by the voltage pulses. The problem of identifying the information bearing section of the received signal is solved by transmitting only during the heating pulse. A wide bandwidth at the receiver input is permissible because the location of the receiver antenna can be close to the bird and so achieve a good signal-to-noise ratio. The logic circuitry controls the input of an UP/DOWN counter so that frequencies corresponding to voltages averaged over a short period at the leading and

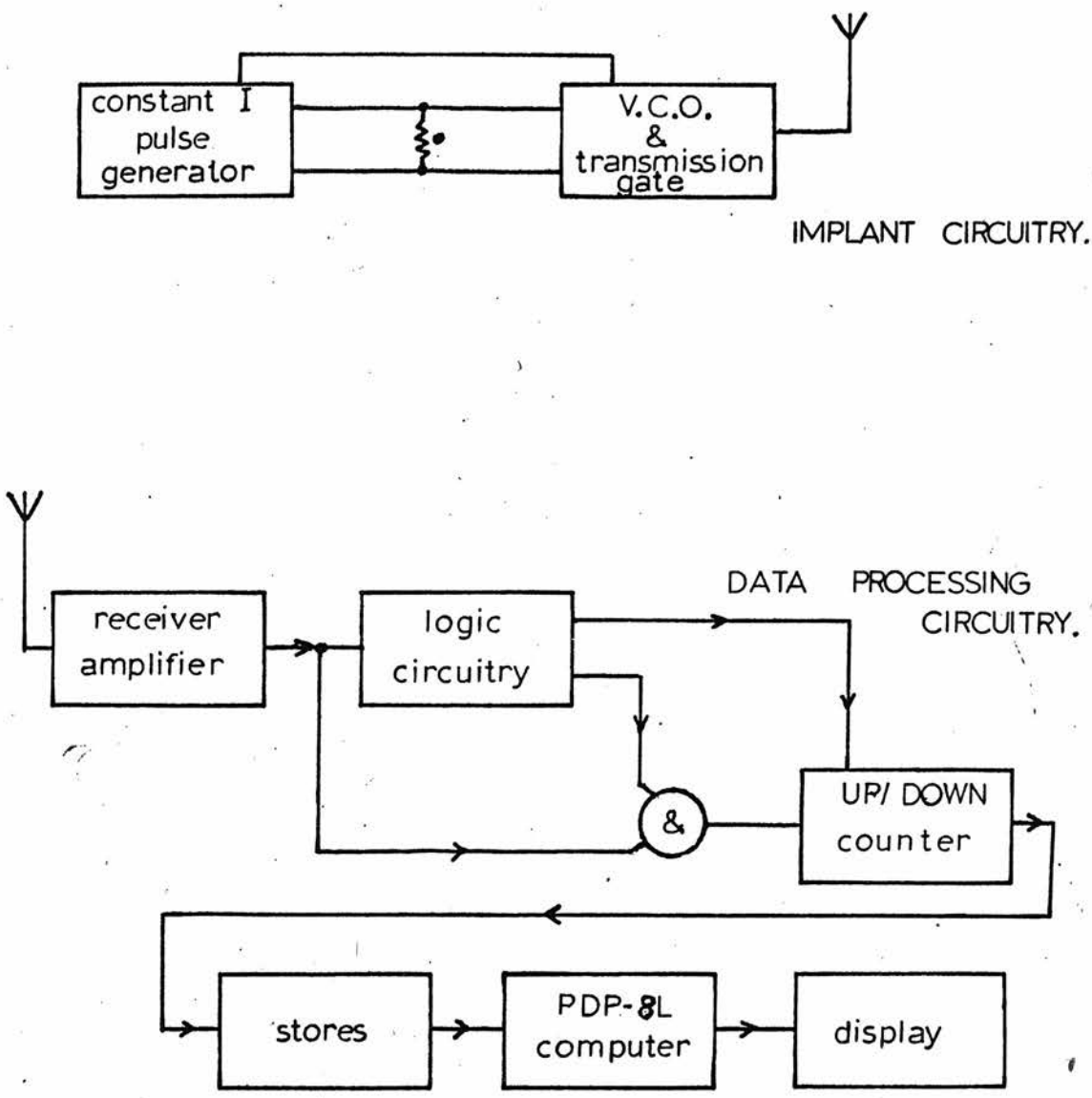

Figure 1.4. A block diagram of the flowmeter circuitry.

trailing edges of the voltage pulse are registered. A PDP-8L computer is used to correct the flow readings for variations in deep body temperature, to average the pulsatile flow component and also for data compression.

This thesis is concerned with the circuitry required to evaluate a thin film thermistor as the transducer in the pulsed thermal flowmeter described. It is intended to investigate the performance using a model flow system with circuitry designed to meet the test requirements. The telemetry link is being developed separately by the P.R.C.[9]

Chapter 2

SPUTTERING - THEORY AND EQUIPMENT

2.1 Introduction

A literature survey revealed one paper[10] concerned with the deposition of films of transition metal oxides. In it the authors describe the D.C. and R.F. triode equipment used to sputter a range of sintered oxides of manganese, nickel and cobalt; of manganese and cobalt; and of manganese and nickel. The D.C. target used was a 1" diameter disc 40 mil. thick; the R.F. target was a slab with dimensions 5" x 5" x 3/16". With a D.C. potential difference of -1.4 kV the deposition rates were 2 to 3 Å/minute. R.F. deposition rates as high as 1500 Å/minute were achieved, but the R.F. power input was not stated. The chemical composition and structure of the D.C. sputtered films, produced in an argon atmosphere, were found to be identical to the target material. The R.F. sputtered films required a 5% oxygen : 95% argon atmosphere to produce films with the same chemical composition and electrical properties as the target. The target was not apparently cooled.

Chapters 2 and 3 are concerned with a description of the sputtering equipment and the relevant theory together with the results obtained when the author attempted to repeat the work described in the above paper using a diode system.

2.2 Mechanisms

The mechanisms advanced to explain sputtering divide into two types, namely, chemical and physical. The mechanism of chemical sputtering is based on the formation of volatile transient compounds

created by the reaction of the atmosphere gas with the target material. These compounds partially decompose when deposited to form a film of the target material. This mechanism is therefore limited to cases where the chemical components of such compounds are present. The sputtering yield is almost constant and independent of the incident ion energy.

Two types of theory have been advanced to explain physical sputtering; evaporation theory and momentum transfer theories. In recent years, with the increased availability of experimental data, the latter has gained importance. However, the evaporation theory may still apply in special cases.[11] The first evaporation theory was advanced by von Hippel[12] (1926), and was later extended by Townes (1944).[13] It is based on the concept that the impinging ion gives up its energy to the surface, producing a rapid rise in temperature over a small region of atomic dimensions, causing local evaporation of the surface material. This theory fails to explain several important points:

1. It predicts a linear relationship between yield and incident ion energy which is, in general, not found experimentally. (Figure 2.1).
2. The energy range of the ejected particles is considerably higher than the value predicted by this theory.
3. The number of the ejected particles is found to be a function of the ratio of the mass of the incident ion to the atomic number of the target atoms. (Figures 2.2 and 2.3).
4. The angular distribution of the ejected particles is a function of the angle of incidence and energy of the bombarding ions. (Figures 2.4 and 2.5).

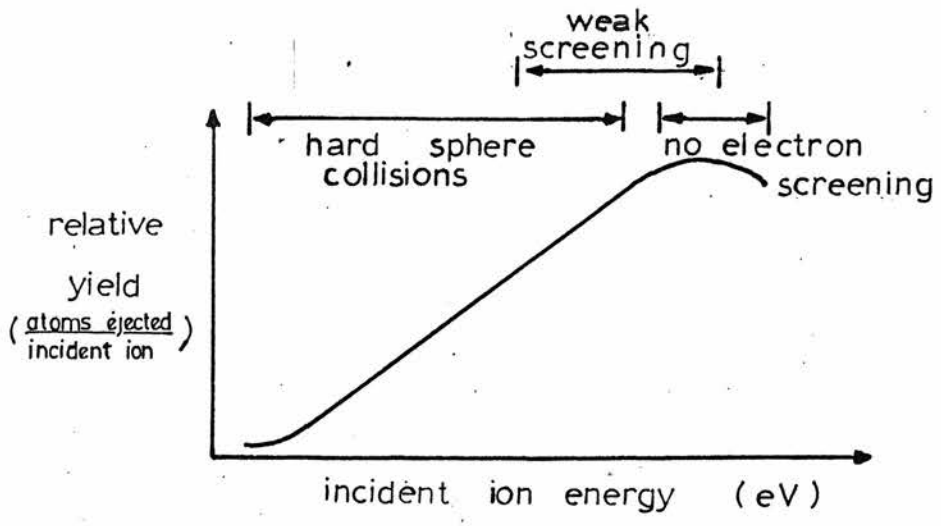

Figure 2.1. A typical sputtering yield graph.[14]

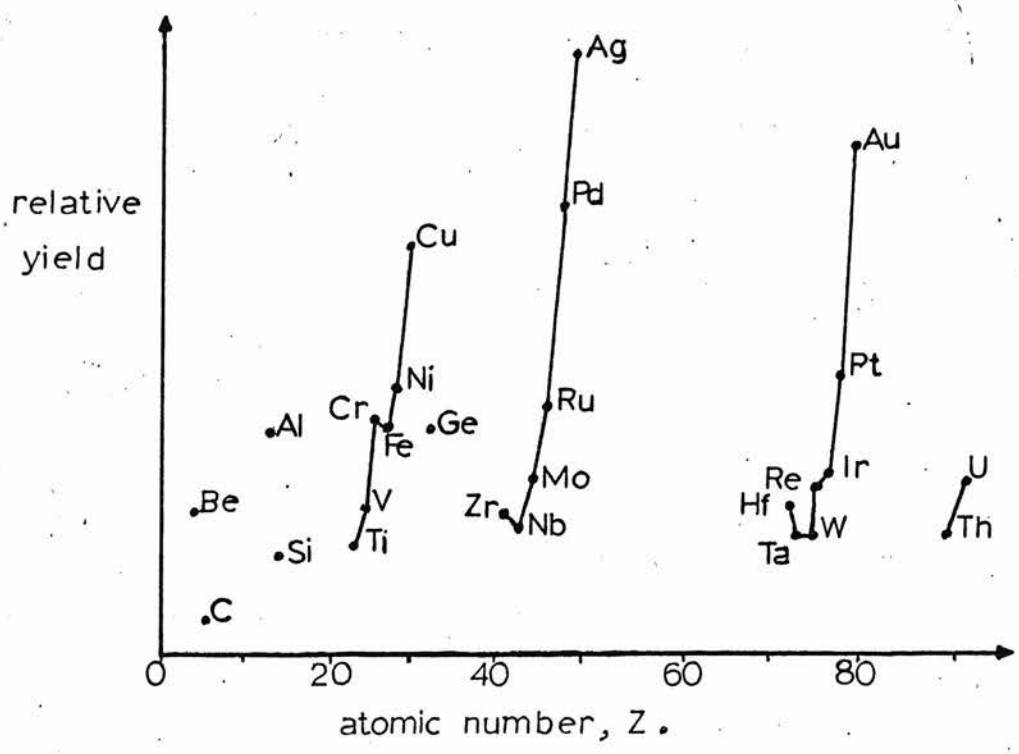

Figure 2.2. Sputtering yield versus atomic number using argon ions of energy 400eV.[15]

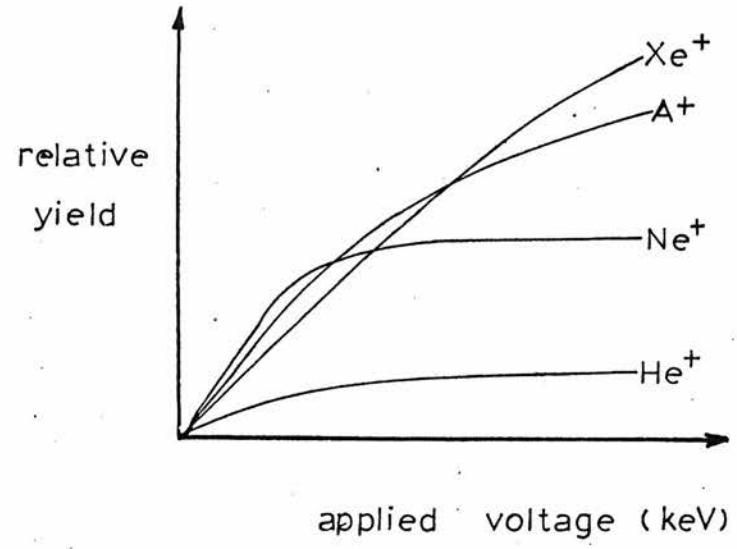

Figure 2.3. Sputtering yield versus ion energy for sodium bombarded with Xe^+ A^+ Ne^+ and He^+ ions.[16]

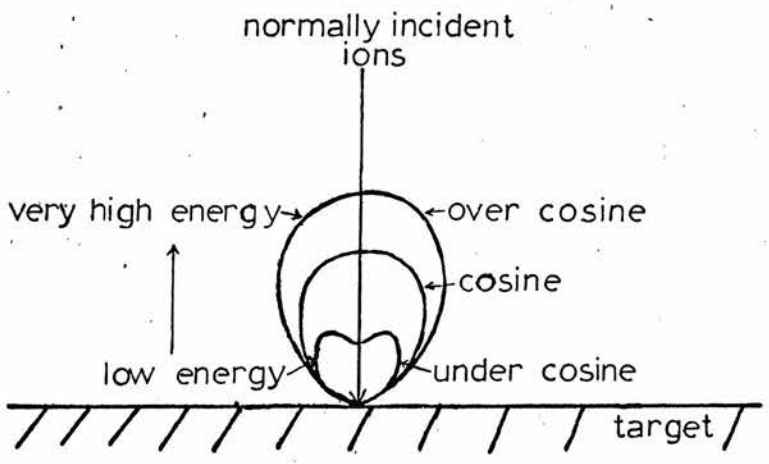

Figure 2.4. Angular distribution of sputtered atoms from a target bombarded by normally incident positive ions for different ion energies.[17]

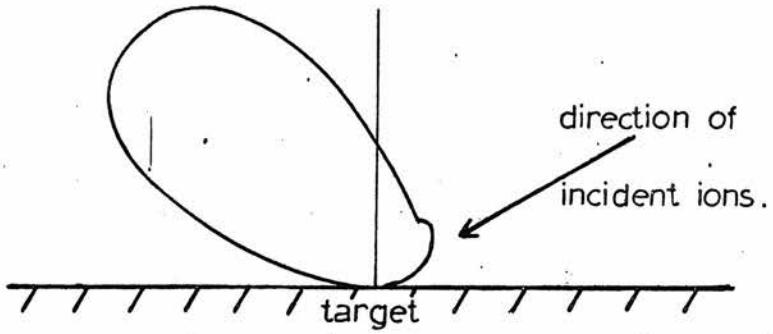

Figure 2.5. Angular distribution of material sputtered under oblique incidence.[17]

The inability of the evaporation theory to explain the above points has resulted in a decline in its acceptance. The points, however, are satisfactorily explained by momentum transfer theories which are based on the concept of elastic impacts occurring between the incident ions and the target atoms, with the transfer of momentum to the target. Particles may be ejected by the initial impact or by subsequent collisions between displaced atoms within the crystal lattice.

In 1908 Stark[18] proposed a mechanism based on the incident ions entering the target material and undergoing a series of collisions with the target atoms. In order for sputtering to occur by such a collision process, the momentum vector of the incident particle must be rotated through 180^{o} as a result of collisions, with transfer of momentum to the surface atoms. Kingdon and Langmuir[19] suggested a two-stage interaction where initially the bombarding ions drive the target atoms into the surface, forming microscopic depressions. Further ions may then be elastically scattered from the displaced atoms in the depression and may remove atoms from the edge of the depression. The experimental evidence in favour of this theory is, however, poor. Many workers have contributed to this field and several simplified treatments of this situation have been proposed in which it is assumed that the sputtering action is due to two-particle collisions. An interesting example, evolved by Pease,[20] produces theoretical results which are close to the experimental results. He derives an approximate expression to describe the sputtering ratio based on a collision model in which the impact phenomena are considered as a series of two-particle collisions between atoms, some of which are ejected from the surface. The incident ions may penetrate

the surface layers and displace atoms from lattice sites in the material. Sufficient energy may be imparted to the displaced atoms for them to produce further displaced atoms. Of the displaced atoms, 50% diffuse to the surface and escape. The sputtering ratio, χ, defined as the ratio of the number of atoms sputtered to the number of incident ions, is given by

$$\chi = (\sigma_p \bar{W} n^{2/3})\left(\frac{1}{4W_p}\right)(1 + N^{1/2}) \qquad 2.1$$

for normal incidence, and $2W_D < \bar{W} < W_{max}$, where W_D denotes the energy required to displace an atom from its site, $\bar{W}$ denotes the mean energy of the struck atoms and W_{max} denotes the maximum energy which can be imparted to a stationary atom. The first factor in the equation represents the mean energy deposited in each atomic layer in primary displacement collision; the second factor represents half the mean total number of displacements per unit energy deposited; the third represents the mean number of atomic layers which contribute to sputtering. Three types of collision interaction are recognised and classified according to the energy range of the incident ion. They are:

1. At high energies the incident ions penetrate the electron clouds of the target atoms and interact with the target atoms through Coulomb repulsion of their positive nuclear charges.
2. At intermediate energies the electron clouds partially screen the positive charges.
3. At low energies there is little penetration of the electron cloud and classical hard-sphere collisions occur between atoms.

When the variation in the collision cross-section term, $(\sigma_p n^{2/3})$, is

taken into account in equation 2.1, the shape of the theoretical yield/incident-ion-energy curve is similar to the experimentally derived curve shown in figure 2.1. In the hard-sphere collision range, the observed discrepancies between theory and experiment are that the theoretical values are approximately 1.5 times too low. (This is the energy range used in sputtering applied to film deposition.) This, Pease suggests, may arise from the approximations made in the treatment of secondary collisions. This aspect of the problem was considered by Silsbee.[21] He suggested that the transference of energy and momentum between atoms in a crystalline solid may be affected by the well-ordered nature of the lattice.

Energy and momentum from successive collisions may be focussed into those directions defined by the close-packed rows of atoms, and, on intersection with a free surface, give rise to preferential ejection in the same direction. Experimental work using single crystal targets has demonstrated that preferential ejection does occur in particular directions and with an energy distribution which are consistent with the focused collision concept.[22] In general both random and preferential ejection of particles take place in a polycrystalline target.[23]

It is now accepted that the ejection mechanism is one of momentum transfer in which the focusing mechanism plays an important role along with two-particle collisions on the surface. The theory shows good agreement with the experimental results of yield measurements. The fall-off in yield at very high energies can be explained by the decrease in collision cross-section and by the very deep penetration of the ions which, on recoil, fail to acquire sufficient

momentum for them to be transferred back to the surface. The tailing off of yield at low energies can be explained by a process in which several collisions are necessary to dislodge a surface atom. The ejection energies and angular distribution of the sputtered atoms of all energies are in a range and direction which are consistent with this theory.

2.3 D.C. Diode sputtering

In a D.C. diode sputtering system, a glow discharge is created between parallel plate electrodes in a low pressure gas. The target material is used as the negative electrode and hence is bombarded by positive ions. The sputtered atoms are deposited principally on the anode where the substrates are located. A short description of the glow discharge mechanism is given in Appendix 2 together with a description of the method of shielding those parts of the cathode from which no sputtering is required.

For sputtering to occur at a useful rate the discharge must be operated in the abnormal glow region of its V-I characteristic where the current density at the cathode is high and the glow covers this electrode. The condition for a stable discharge (equation A.2.4) is

$$\frac{1}{\gamma} = e^{\alpha d'}$$

where γ is the emission coefficient, α is the first Townsend coefficient and d' is approximately the length of the cathode glow. The parameters which control the discharge (that is, the parameters which determine the values of α and γ) in a particular gas with a specified target are pressure and applied voltage. The deposition rate typical of D.C. sputtering is 100 Å per minute. This is achieved when

operating with a gas pressure of between 10^{-2} and 10^{-1} torr with an earthed anode and a cathode potential of the order of -1 kV. The lower pressure limit is set by the pressure necessary to produce a self-sustaining abnormal glow discharge, and the upper pressure limit is the value above which an arc discharge occurs. The deposition rate is an increasing function of pressure and applied voltage in the above ranges. The electrode separation, d, is not a significant controlling factor in the discharge providing $d>d'$. However, it does assume importance when considering the uniformity of the deposited film. This is examined in a later section.

Argon is used as the atmosphere in the glow discharge because it is inert, readily available and has a low breakdown voltage. When electronegative gases, such as oxygen, are used in addition to the inert gas the deposition rate of the sputtered particles is found to decrease significantly. Electronegative gases[24] are defined here as those gases which have a pronounced tendency temporarily to attach electrons and form negative ions in the glow discharge environment. The decrease in deposition rate reflects the decrease in positive ions which are available to bombard the target. Recent work[25,26] using small partial pressures of oxygen (10^{-5} to 10^{-4} torr) has introduced some doubt as to the validity of the electron attachment hypothesis as the complete explanation. Jones et al.[27] suggest that the observed decrease in deposition rate is due to oxygen adsorption on the target surface creating a surface layer which sputters less readily than the original target components. In the pressure range used in the work in this thesis the relative importance of the two hypotheses is not yet clear.

A magnetic field acting parallel to the discharge field is often used in order to reduce the number of electrons lost to the chamber wall. It also causes an increase in the number of ionising collisions by increasing the mean free path of the electrons so that the energy they acquire between collisions increases. The net effect is an increase in the number of positive ions available to bombard the target and an increase in the deposition rate. This is considered in detail in Appendix 3.

2.4 R.F. diode sputtering

A D.C. glow discharge can be used as a source of ions to sputter conducting targets only, since a positive charge will build up on the surface of a non-conducting target and prevent further bombardment. This problem can be overcome by applying a radio frequency potential to a metal electrode behind the non-conducting target. Power is fed into the chamber via the displacement current through the dielectric material so that its exposed surface effectively has a time varying potential applied to it. By using this arrangement as one electrode in a diode system, the other being earthed, it is possible to create a self-sustaining glow discharge between the electrodes in a low pressure atmosphere.

During each cycle of the applied R.F. voltage, electron current and positive ion current alternatively flow from the plasma to the target. Since the electron mobility is considerably larger than the ion mobility, an excess of electrons can be expected to arrive at the target each cycle, leaving a net negative charge on the target surface and causing its effective potential with respect to the plasma potential to become more negative. This process will continue until

sufficient net charge has been deposited on the target surface to cause its effective potential to reach an equilibrium value about which the radio-frequency swing causes equal electron and ion currents to flow. Thus the ion current will flow for appreciably more than half the total cycle to compensate for the high mobility of the electrons. This was first explained by Butler and Kino [28] when they studied plasma sheath formation by radio-frequency fields. A pictorial representation of their explanation of the mechanism is shown in Figure 2.6.

The target surface can be considered to have an effective negative D.C. potential with an R.F. component superimposed. The magnitude of the D.C. potential is a function of the frequency and amplitude of the applied R.F. potential, the plasma density and the geometry of the target. For frequencies above 10 KHz, the effective D.C. potential closely approaches the peak R.F. potential. Butler and Kino's results of measurements of R.F. voltage applied versus D.C. wall potential obtained are shown in Figure 2.7.

The existence of a negative potential on the target surface results in the creation of an ion sheath over the target surface and ion bombardment of the surface. The thickness of the ion sheath is time varying and defined by the R.F. component. The average energy of the bombarding ions is equal to the effective surface D.C. potential and the spread of energies is a function of both the frequency of the applied potential and of the plasma density. As the frequency increases, the quantity of positive charge accumulated per cycle on the surface decreases, so that the extent of the variation in surface potential decreases. A frequency of 13.56 MHz,

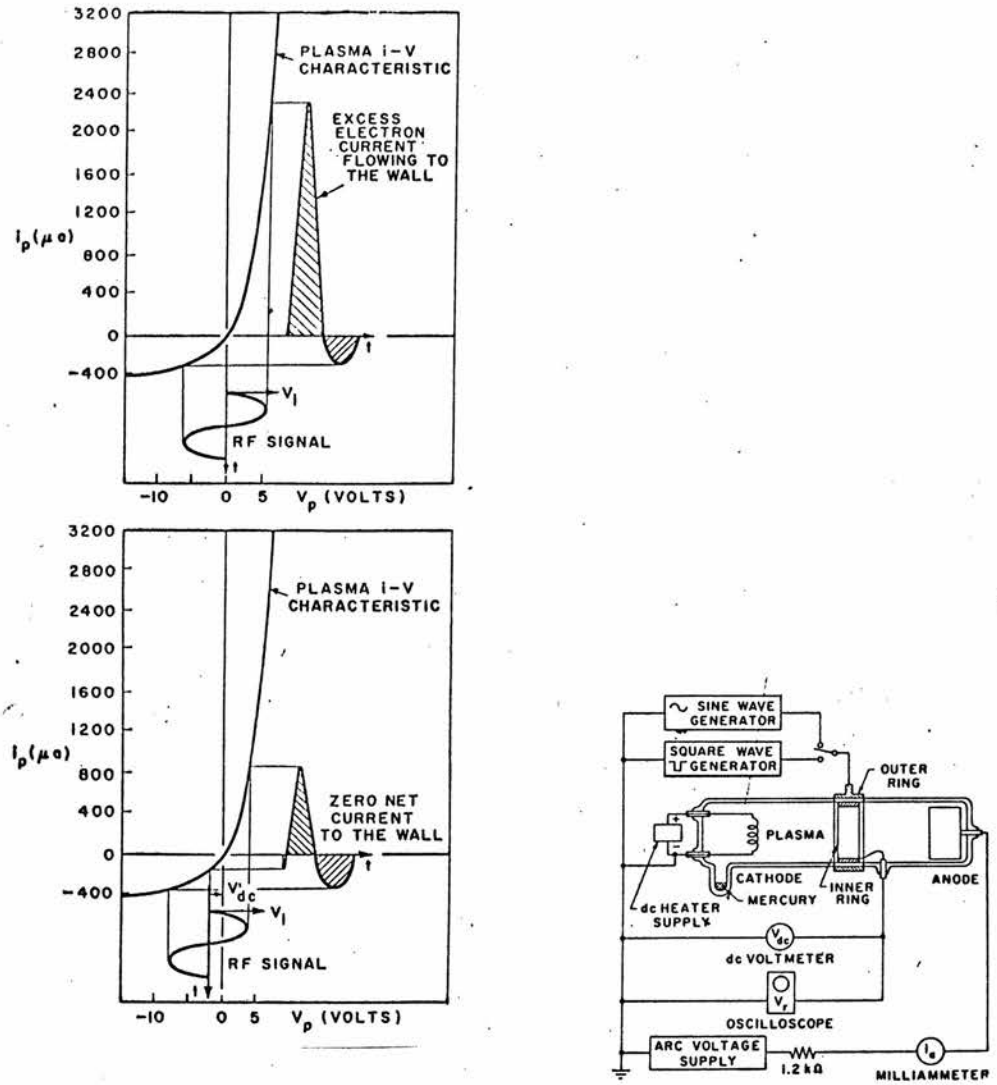

Figure 2.6. A pictorial representation of the mechanism by which a positive ion sheath is formed.[28]

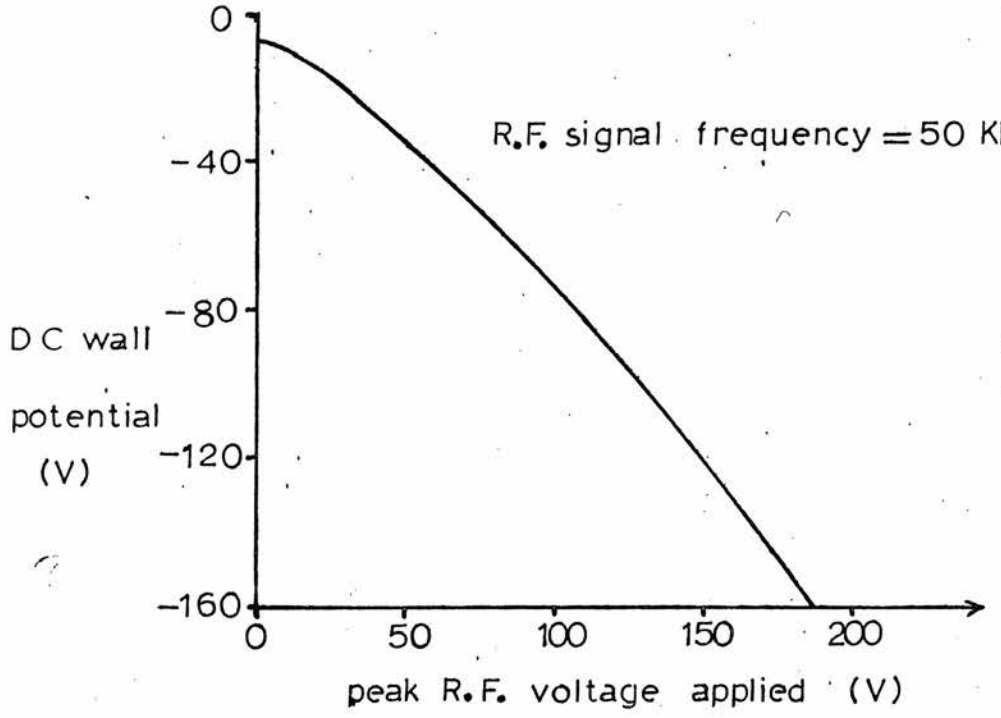

Figure 2.7. Peak R.F. applied voltage versus resulting D.C. wall potential.[28]

allotted by the G.P.O. for industrial use, is used in this work. In general, for a fixed frequency and a fixed system geometry, the deposition rate obtained when using R.F. power is an increasing function of the applied R.F. voltage or power, and is an increasing function of pressure within a limited pressure range. Pressure determines the plasma density.

The physical appearance of the discharge resembles that of the abnormal D.C. glow discharge. The controlling parameters of applied power at 13.56 MHz and pressure operate in a similar manner to the D.C. abnormal glow case. However, the pressure range for R.F. discharge work is considerably lower, namely, between 10^{-3} and 10^{-2} torr. Also the deposition rates are higher. Operating at 8×10^{-3} torr with a power input of 300 W the deposition rate is typically 450 Å per min. The high deposition rates make this system attractive for sputtering conductors as well as insulators. One way of achieving this is by placing an insulator between the conducting target and the electrode in order to satisfy the condition of no net D.C. current flow. The effects of an applied magnetic field and of electronegative gases in the atmosphere are similar to the D.C. case.

2.5 Multicomponent Targets

When the target material is an alloy or a compound and the film produced is required to have the same composition as the target it is necessary to consider further the interaction at the target surface and also at the substrate surface. The sputtering rate of a particular atom is a function of the mass of the atom, its binding energy and its surface concentration relative to other surface atoms.

Therefore, different elements in a compound target sputter at different rates. In the initial period of sputtering those elements whose sputtering rates are high are removed, thereby reducing the surface concentration of these components and exposing a larger surface area of the components which sputter more slowly. Hence, the components with an initially lower sputtering rate increase their surface concentrations at the expense of those with the initially higher rates, and the sputtering rates alter correspondingly. It is found that an equilibrium occurs in which the sputtering rates achieve values such as to eject particles in the same concentrations as they are present in the bulk target. In this situation the concentrations of the different sputtered atoms arriving at the surface of the growing film are the same as the bulk concentration.[29] This presupposes that the elevated temperature of the target due to the bombardment does not increase to the point where ions can diffuse from the bulk to the surface.

The rate at which a component is incorporated into the film depends on several factors, the two most significant being its resputtering rate and its sticking probability, that is, the ratio of the number of particles being absorbed on the surface to the number arriving at the surface. The influence of the resputtering rates of the components on film composition decreases with increasing deposition rate. The sticking coefficient for metals on a growing metal film has been found to be approximately one[29], and most molecular gases have sticking coefficients on metal substrates which are less than unity.[29] Therefore, it is probable that films will be deficient in those components which are normally found in the gaseous state.

To compensate for this loss it is possible to add traces of the gas to the sputtering chamber atmosphere. Chemical combination can take place in three possible sites, namely, on the target surface, in flight, and on the substrate surface. If the target surface is, for example, a non-stoichiometric oxide or a mixture of oxides, then chemisorption of the reactive gas is possible at suitable sites on the surface. The chemisorbed gas is then sputtered with the target material, thereby increasing the concentration of the gas atoms in the particles arriving at the substrate surface. In flight recombination is important when the mean free path of the sputtered atoms is small compared to the interelectrode spacing so that there is a high probability of collision with the reactive gas. Gas incorporation at the substrate can arise from highly energetic particles which penetrate into the growing film, and from chemisorption on the surface[30] of the film which may be followed by a second adsorption process[31] thus:

$$\text{site} + \tfrac{1}{2}\,O^2 \rightleftharpoons \text{O-chemisorbed}$$

$$\text{O-chemisorbed} + M \longrightarrow \underset{\text{(solid solution)}}{MO}$$

A description of the chemisorption process at the target and substrate is extremely complex. The gas is present in the discharge in ionic, atomic and molecular states, and the particles can have a wide range of kinetic energies,[32] so that several different chemisorption processes probably occur, each process possibly involving more than one stage. Also the gas particles may be physically trapped prior to a chemical reaction. It is possible, however, to examine the processes in a simplified way and indicate the controlling

parameters and their relationships. For chemisorption to occur the adsorbate must have the necessary activation energy, E, and must collide at or near a suitable vacant site on the adsorbent. The total number of sites available is defined by the nature of the adsorbent. For the particle to become permanently adsorbed it must lose, during its impact with the surface, any energy in excess of that required for the chemical reaction, otherwise it will desorb. This factor is important when physical adsorption is a precurser to chemisorption. Finally, not every particle is adsorbed. Even when all the above conditions are met, only those which satisfy all the stages of a particular process are chemisorbed. These conditions can be expressed in terms of the sticking probability, S, for the activated adsorption of a particle,[30] thus:

$$S = \sigma f(\theta)\, e^{-E/RT} \qquad 2.2$$

σ is the probability factor that the particle will pass through all stages of a particular adsorption process. $f(\theta)$ is a function of the surface concentration, θ, of adsorbed particles and represents the probability that collision will take place at an available site. T denotes temperature and R is a constant. Both σ and E may vary with θ. It is frequently found that the rate of adsorption decreases extremely rapidly with increasing surface coverage by the adsorbate and this can only be explained in terms of a variation in the activation energy and/or the probability factor. Now, the number of gas particles arriving in unit time is proportional to the gas pressure, hence, the number of sites occupied in unit time is a function of pressure, the exact relationship depending on the nature of the

adsorption. The effect of an increase in temperature is to increase the sticking probability. Therefore during the sputtering process, when adsorption sites are created at the target and substrate, the sticking probability of a gas particle is an increasing function of temperature and is a function of the reactive gas pressure.

Consider now the situation where the number of gas particles arriving at the surface is of the same order of magnitude as, or greater than, the number of chemisorbed sites being created. An equilibrium is achieved where the number of adsorbed particles equals the number of desorbed particles, and the fraction of available sites occupied, ϕ , is constant. The term ϕ is found to be a function of temperature and pressure and from Langmuir's adsorption theory[30] is given as

$$\frac{\phi}{1-\phi} = K p e^{E_D/RT} \qquad 2.3$$

where E_D denotes the activation energy for desorption and K is a constant. Therefore, although the number of available adsorption sites is defined by the nature of the adsorbent, the maximum number that may be occupied is directly related to pressure and is a decreasing function of temperature. The factor $f(\theta)$ in equation 2.2 will therefore decrease with increasing temperature in the equilibrium situation. Thus the sticking probability becomes a more complex function of temperature than suggested by equation 2.2.

The inclusion of the inert atmosphere gas, argon, in the film is also probable. However, the quantities involved are small, because only those argon particles with sufficient kinetic energy to penetrate into the growing film[32] will contribute significantly to adsorption at these surface temperatures.

2.6 Sputtering Equipment

A diode system with a grounded anode is used (Figure 2.8). The cathode block was made from designs supplied by the Plessey Company. It consists of a 4" diameter water cooled cathode with earthed shields spaced approximately 3 mm from it. The target material is clamped on the exposed surface of the cathode by part of this shield with the appropriate insulation. The power supply is connected to the copper water pipes on the cathode and these are insulated from the earth by 4' lengths of Teflon tubing. Feedthroughs to a tungsten filament are included in the cathode block so that the filament can be heated to assist in initiating an R.F. discharge. The anode is water cooled and its height is adjustable so that the interelectrode spacing can be varied between ½ and 6 cm. A roller blind shutter, which is made of Kapton, a Du Pont plastic (melting point - none: zero strength temperature 815°C), is fitted to the anode block. The chamber is a 6" bore Q.V.F. Pyrex glass cylinder. This rests on an aluminium collar which is designed to permit the introduction of various feedthroughs into the chamber. The feedthroughs are made from 1" diameter stainless steel bolts modified to serve as inlets for gas and cooling water, and as rotary and electrical feedthroughs. The gauge head of an Edwards Model 8/2 Pirani gauge used to monitor chamber pressure is connected into the chamber using a suitable modified stainless steel bolt. The cathode shield, anode, aluminium collar and base plate are carefully earthed.

The pumping unit consists of an Edwards E04 water cooled diffusion pump and an Edwards ED150 rotary pump with a water cooled chevron baffle and baffle valve on the diffusion pump, and an alumina

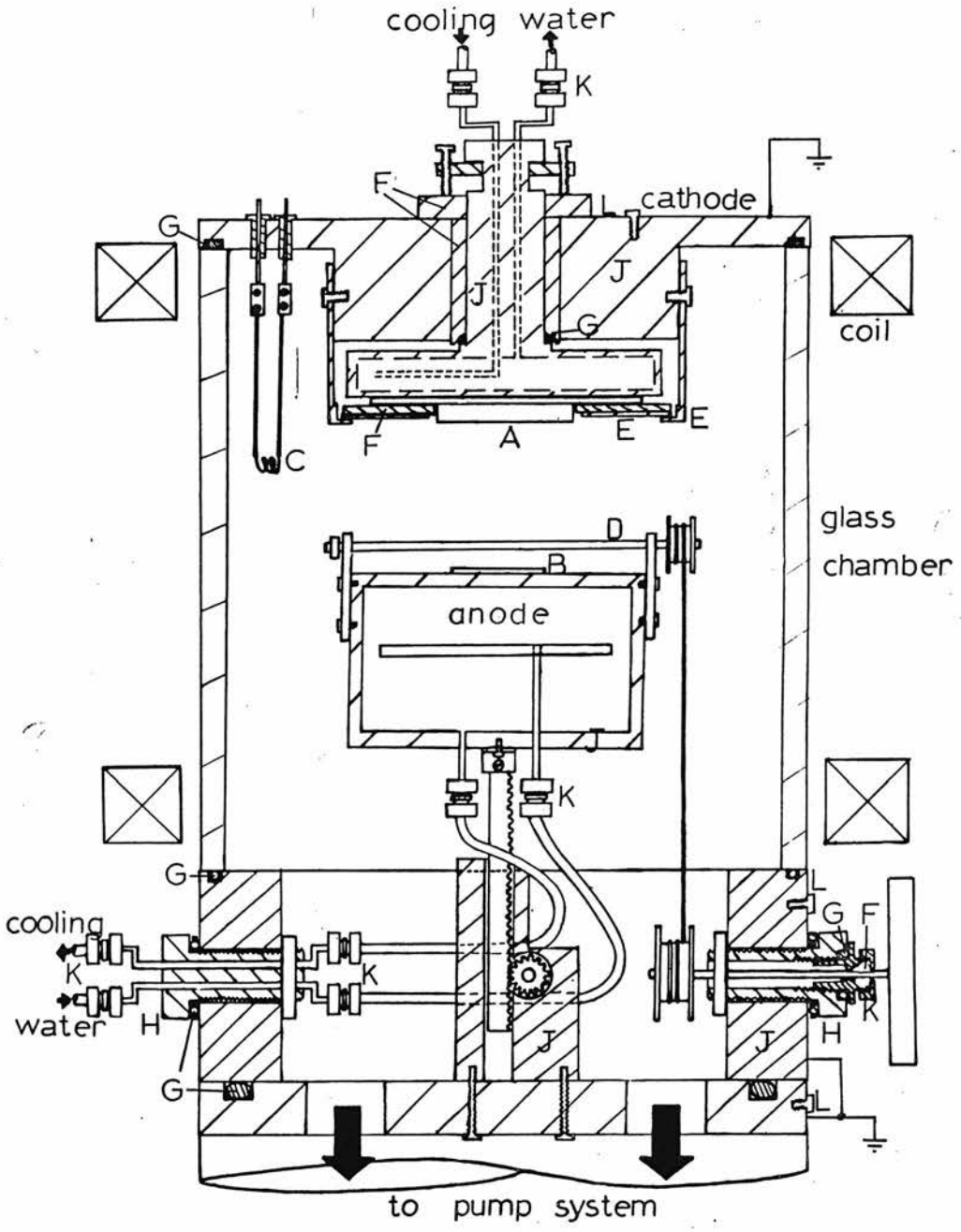

Figure 2.8. A diagram of the sputtering chamber.

(see key on page 40)

A - target

B - substrate

C - heater filiament

D - roller blind shutter

E - earthed shield and clamp

F - P.T.F.E.

G - oarings

H - stainless steel bolts

J - aluminium

K - Simplifix couplings

L - screws for earth connection

Key to Figure 2.8

oil trap in the roughing line. This system achieves an ultimate chamber pressure of 10^{-5} torr. Pressure is measured by an Edwards Model T101 Pirani gauge in the backing line and an Edwards Model T1001 Penning gauge in the roughing line (Figure 2.9). A photograph of the system is shown in figure 2.10.

The D.C. power supply[33] is variable between 0 and 4 kV and can deliver up to 1 A. The R.F. power supply consists of a National power amplifier Model NCL-2000 excited by a Heathkit DX-40V transmitter. This system provides a maximum continuous output power of 1 kW at 13.5 MHz. A Variac is connected across the primary of the transformer which provides the H.T. supply to the output valves of the power amplifier in order to allow adjustment of the output power to any value below 1 kW. Power is fed by a 52 Ω coaxial line, through a Bird model 43 R.F. power meter and a matching unit to the cathode block. The matching unit consists of a water cooled variable inductor earthed at one side and directly connected to the cathode cooling pipes at the other with a variable capacitor connected across it. The inductor resonates with the electrode-shield capacitance and the electrode-plasma capacitance near the operating frequency and the variable capacitance is used for final tuning (Figure 2.11). When this unit is adjusted for minimum reflected power in the line the value of V.S.W.R. lies between 1.1 and 1.2. All components are placed close together and the unit is situated at a small fraction of the operating wavelength from the sputtering chamber. Any length of cable can be used to connect the power generator to the matching unit, since this appears as a correct termination to the line. Two Helmholtz coils (Electroinductor Products, type EI0101, 500 turns

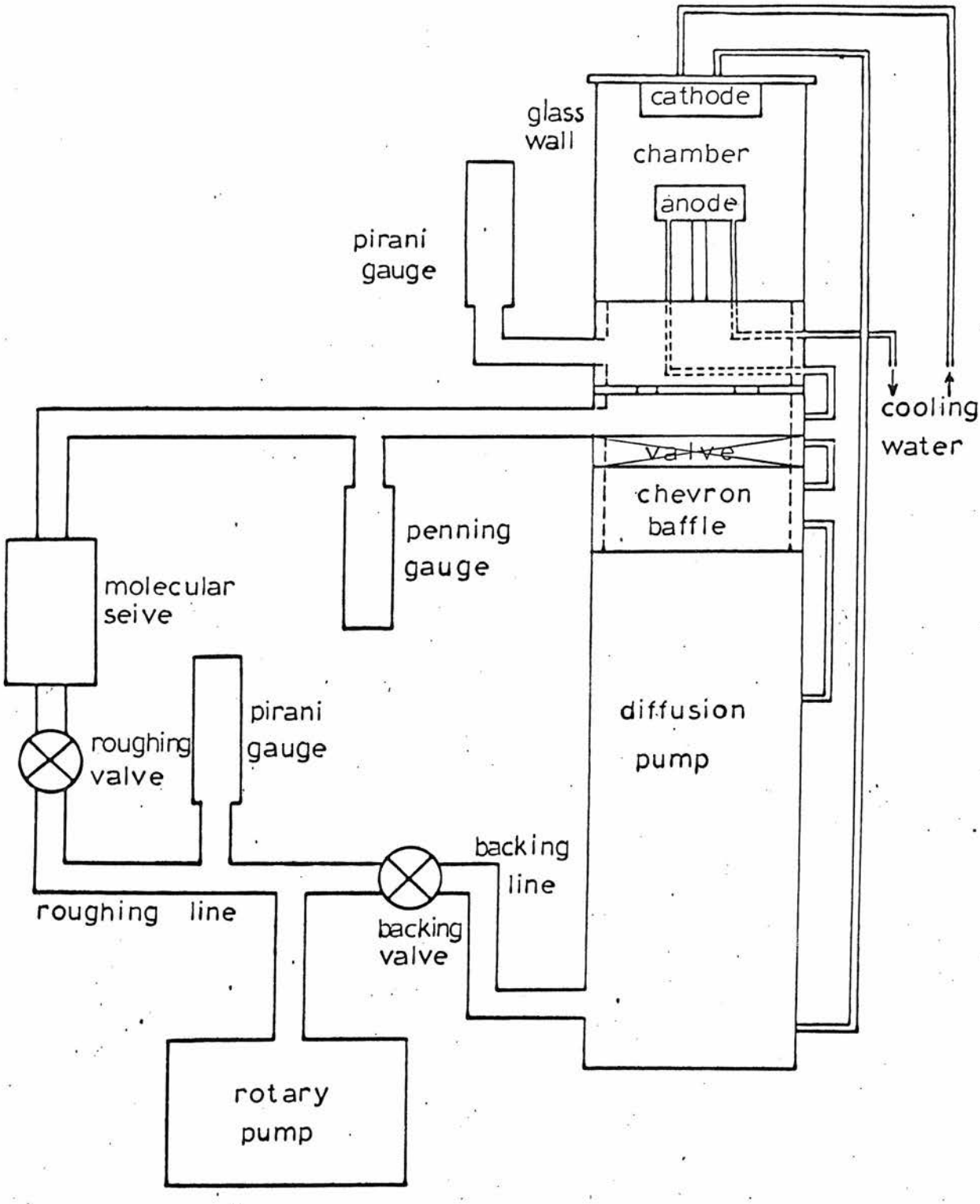

Figure 2.9. A schematic diagram of the vacuum system.

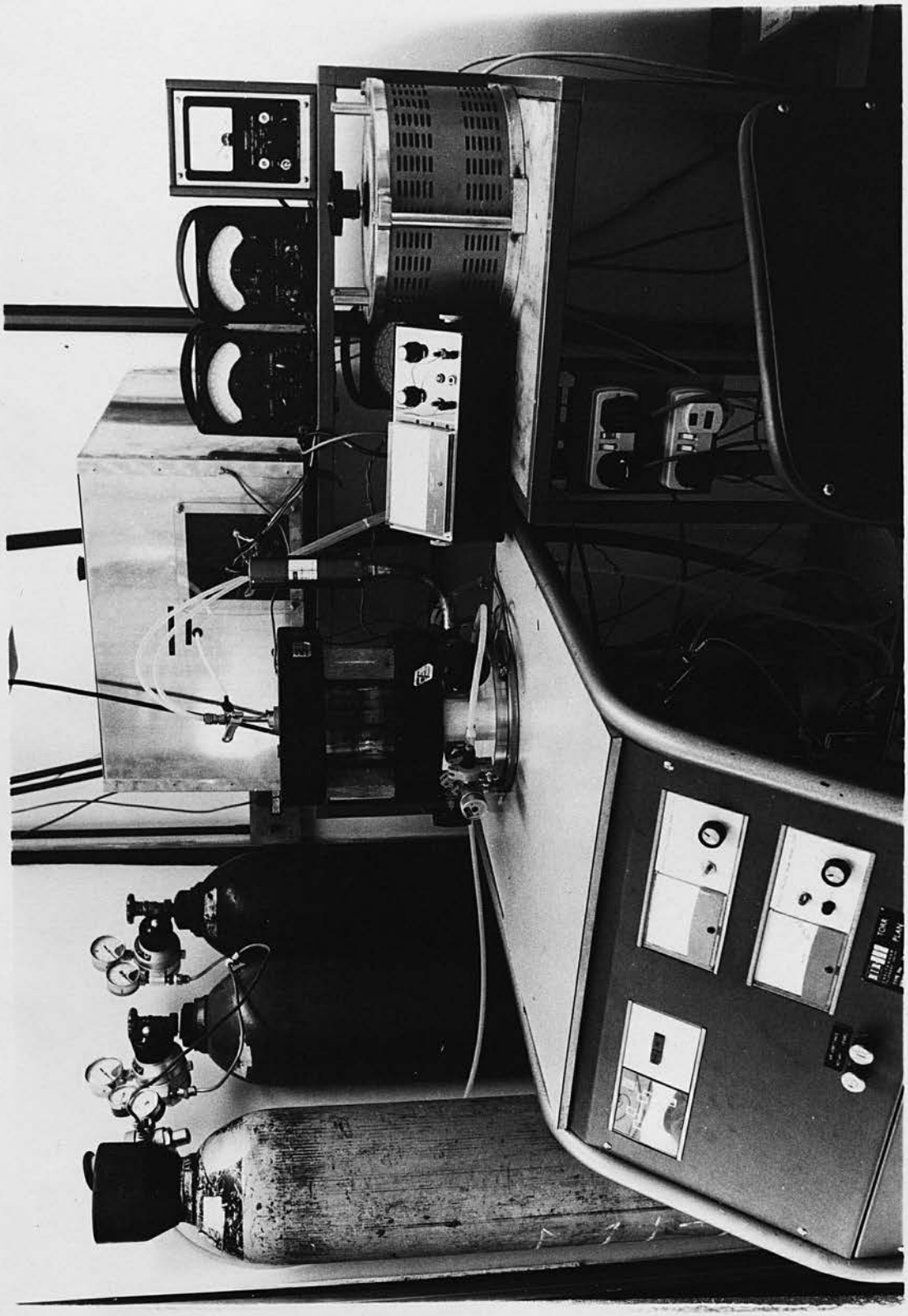

Figure 2.10. The sputtering system.

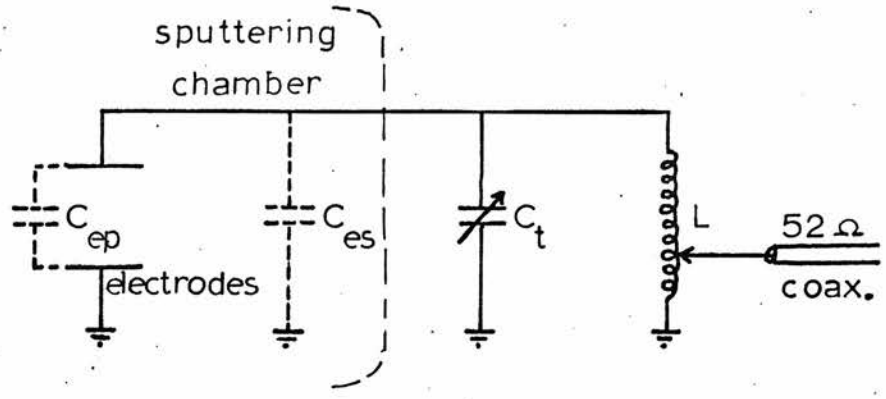

C_{ep} electrode-plasma capacitance
C_{es} electrode-shield capacitance
C_t variable tuning capacitor
L variable inductor (1/4" dia. copper tube, water cooled, 6 turns)

Figure 2.11. The matching unit.

each) are placed outside the chamber to provide a magnetic field normal to the target and substrate. The current in the coil is variable between 0 and 5 A.

The gas mixing system, shown in figure 2.12, is used to prepare the required gas mixtures for the chamber atmosphere. The gases are bled into the premix cylinder to form the required mixture and the component gas cylinders closed. The mixture is then bled into the chamber using a Leybold micrometer screw valve. 50% of the mixture is fed into the chamber during the initial pump down to insure that the chamber atmosphere has the required composition. This is done by pumping the chamber down to its ultimate pressure. The premixed gas is then flushed through the chamber using the rotary pump only and the chamber pumped down for a second time. The accuracy of this gas mixing method is a function of the ratios of the component gases. For the worst case when one component constitutes less than 10% of the mixture the possible error in this component is approximately ±25%.

The target material is supplied by Standard Telephone Laboratories, Harlow, and consists of a three oxide mixture of 50% manganese oxide (Fermac 74% Mn), 25% nickel oxide (Monde) and 25% copper oxide (Albright and Wilson) sintered into a solid solution structure. The process used is as follows: dry mix for two hours with 0.5% P.V.A. binder; compress into a 2" dia. ¼" thick dics; fire and sinter from room temperature at a rate of 125°C per hour to a maximum of 500°C, then 250°C per hour from 500°C to 1200°C; hold at 1200°C for four hours in a 5 litre per minute air flow; cool at 250°C per hour. The bulk resistivity of the disc produced is 13.3 Ω-cm at 25°C

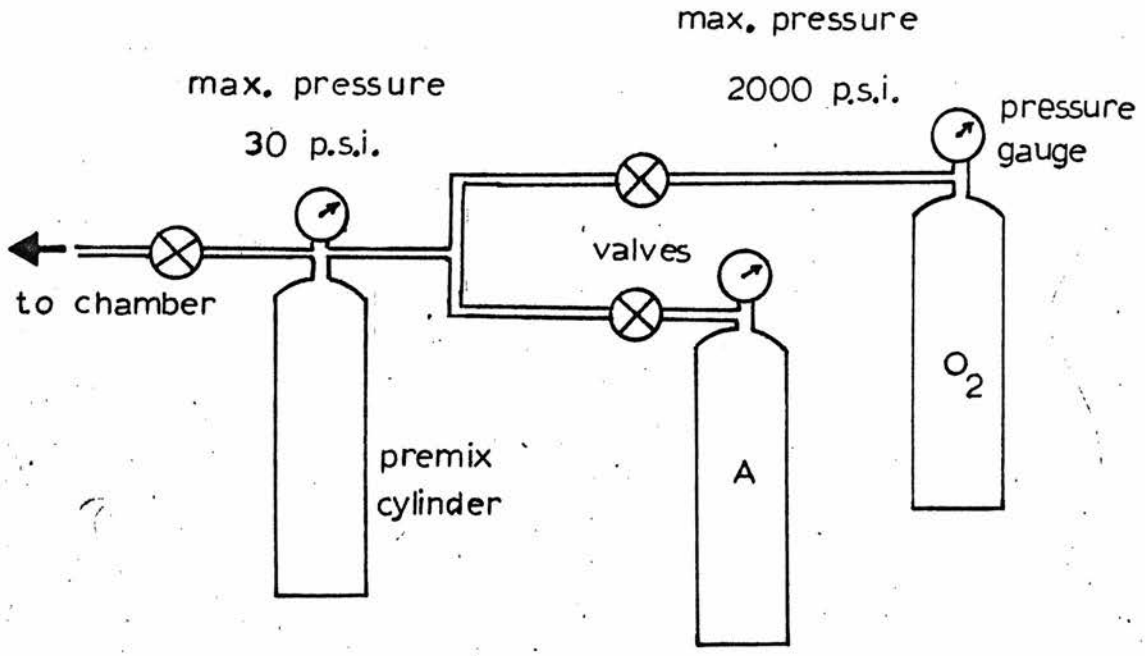

Figure 2.12. A diagramatic representation of the gas mixing system.

with a 12% spread over the surface and its B value is 2010, where

$$B = \frac{T_1 T_2}{T_1 - T_2} \ln \frac{R_{T_2}}{R_{T_1}} \qquad 2.4$$

where $T_1 = 343^{\circ}K$ and $T_2 = 298^{\circ}K$. The low resistivity material is chosen in order to produce thin film thermistors of around 1 KΩ with a practical geometry. This implies, however, that the sensitivity of the thermistor to temperature change is also low since the resistivity and B value are directly related. This point is discussed in a later section. The target is sputtered for four hours when first introduced into the chamber to facilitate outgassing. Also, before each film is deposited, the target is sputtered for 5 minutes with the shutter closed in order to allow the system to stabilise.

The substrates used in the basic sputtering work are 1" x ½" x 1/25" Corning 7059 microsheet glass, with a ¼" wide, 8,000 Å thick gold pad along two sides of the surface to produce a ½" square area of glass. The substrates were supplied by the Poultry Research Centre thin film group. The gold pads are partially shielded during sputtering and are used to establish electrical contact with the thermistor material. The substrates are carefully cleaned before sputtering using the following procedure:

1. Ultrasonic wash in R.B.S. 25 detergent.
2. Thorough wash in water.
3. Ultrasonic wash in analar acetone.
4. Repeat in a second beaker.
5. Ultrasonic wash in analar propane-2-ol.
6. Repeat in a second beaker.
7. Vapour bath in aristar propane 2-ol.

The substrates are placed on the anode block and the chamber pumped

down to its ultimate pressure before sputtering commences. When not in use the chamber is continuously pumped out to prevent gas adsorption on the chamber surfaces.

2.7 Operating characteristics

The uniformity of the deposited film varies with the inter-electrode spacing and with a magnetic field. It has been found, as an approximate rule, that the film is optimally flat when the dark space of the discharge occupies 2/3 of the inter-electrode spacing. Film uniformity is not a critical parameter in the production of small thermistors (> 2 mm^2) since the area covered by the thermistor material is very much smaller than the target area. In the experimental work an active area of $\frac{1}{2}$" square was deposited using a 2" diameter target. The inter-electrode spacing was adjusted to produce an optimally flat film for the average pressure and voltage used in the D.C. range and the anode fixed at that position. The uniformity of films, deposited with and without a magnetic field under conditions at the extremes of the pressure and voltage ranges used, was examined and found not to vary significantly from optimally flat. The same procedure was carried out with the R.F. discharge and the same result found.

The variation of deposition rate with applied D.C. voltage, pressure, and magnetic field is shown in figures 2.13, 2.14 and 2.15 respectively. These tests were carried out in an argon atmosphere using the 2" dia. S.T.L. thermistor disc as a target. Similar graphs for the R.F. discharge system are shown in figures 2.17, 2.18 and 2.19. As expected, the deposition rate is an increasing function

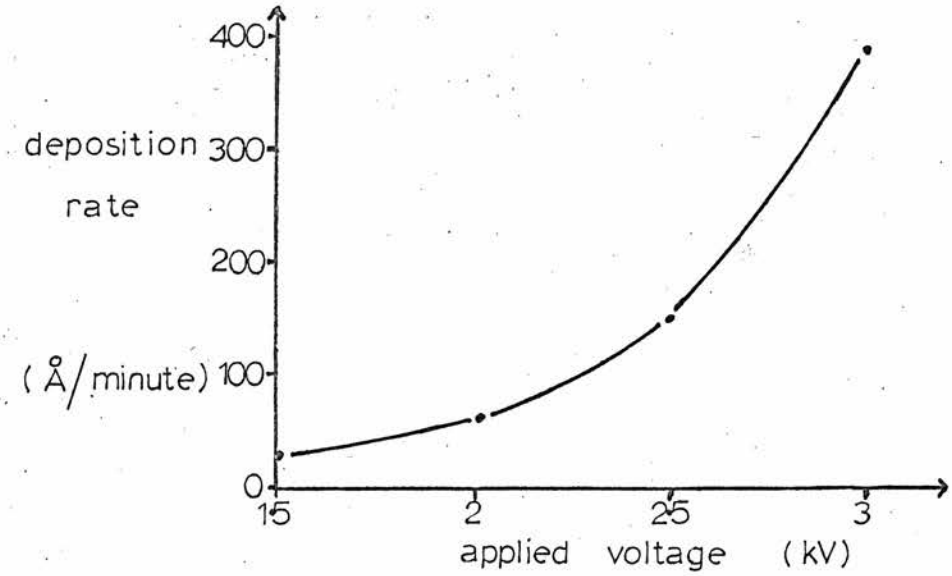

Figure 2.13. Deposition rate versus applied voltage for D.C. sputtering with pressure $= 3 \times 10^{-2}$ torr, time = 45 minutes, magnetic field current = 3·6 A and electrode spacing = 4 cm.

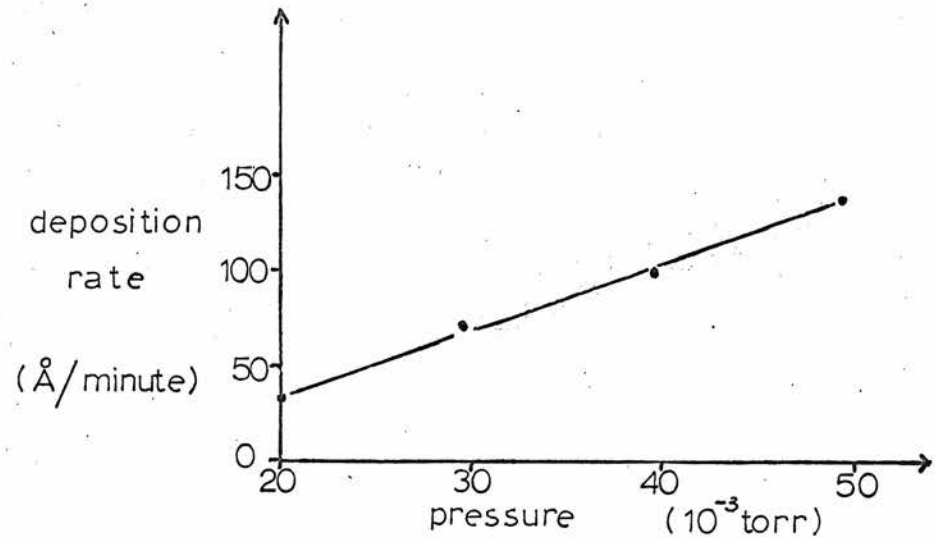

Figure 2.14. Deposition rate versus pressure for D.C. sputtering with applied voltage = −2kV, time = 40 min., magnetic field current = 3·6 A and electrode spacing = 4 cm.

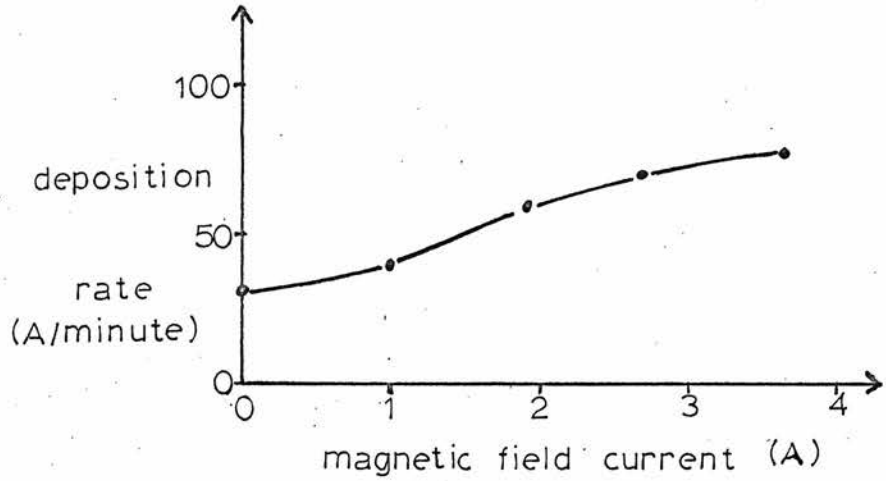

Figure 2.15. Deposition rate versus magnetic field current for D.C. sputtering with applied voltage = 2 kV, time = 40 min., pressure = 3×10^{-2} torr and electrode spacing = 4 cm.

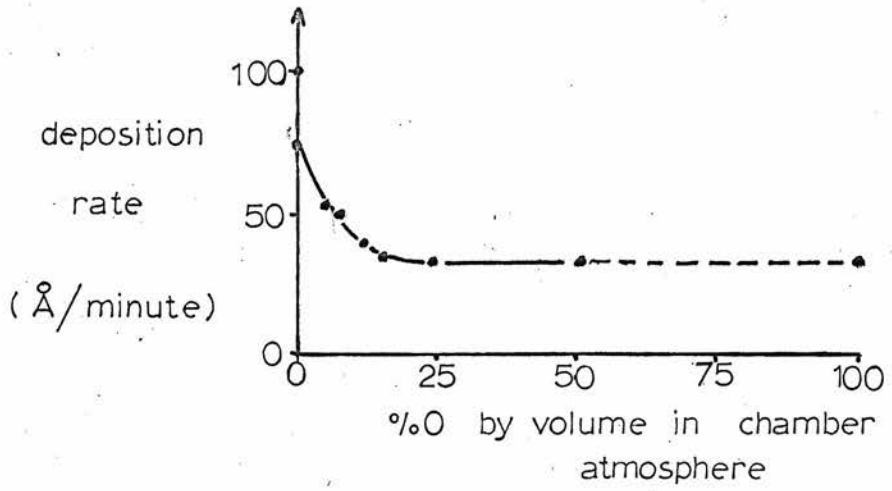

Figure 2.16. Deposition rate versus percentage of oxygen (by volume) in the chamber atmosphere for D.C. sputtering with pressure = 3×10^{-2} torr, time = 40 min, magnetic field current = 3·6 A and electrode spacing = 4 cm. The applied voltage = 2 kV.

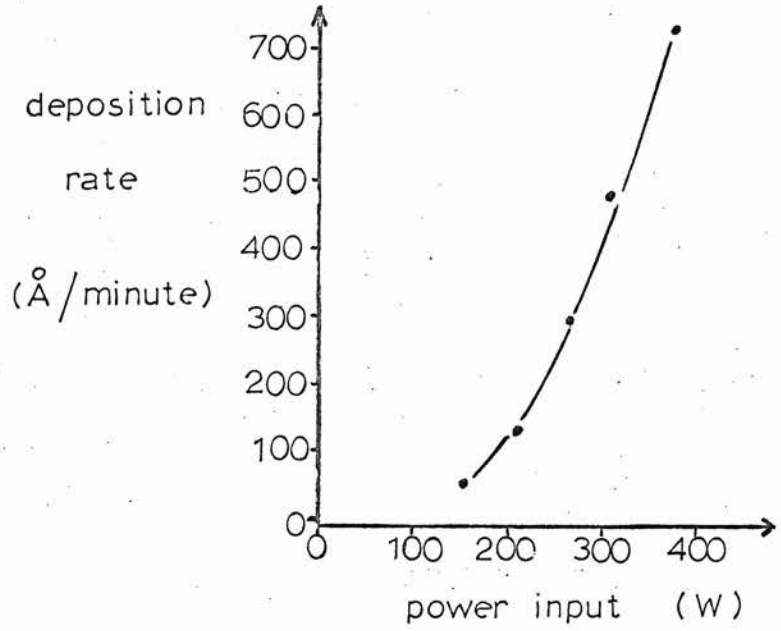

Figure 2.17. Deposition rate versus applied power for R.F. sputtering with pressure $=7\times10^{-3}$ torr, time $=10$ minutes, magnetic field current $=3{\cdot}6$ A and electrode spacing $=3{\cdot}5$ cm.

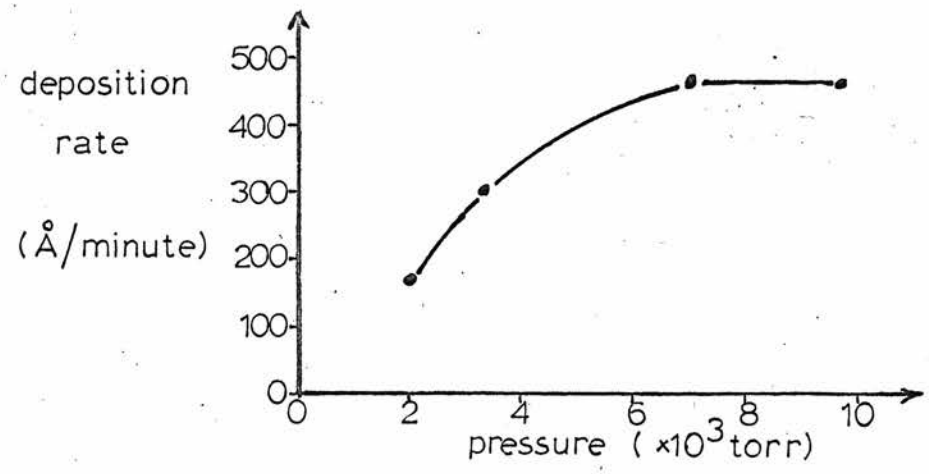

Figure 2.18. Deposition rate versus pressure for R.F. sputtering with applied power=300W, time $=10$ minutes, magnetic field current $3{\cdot}6$ A, and electrode spacing $=3{\cdot}5$cm.

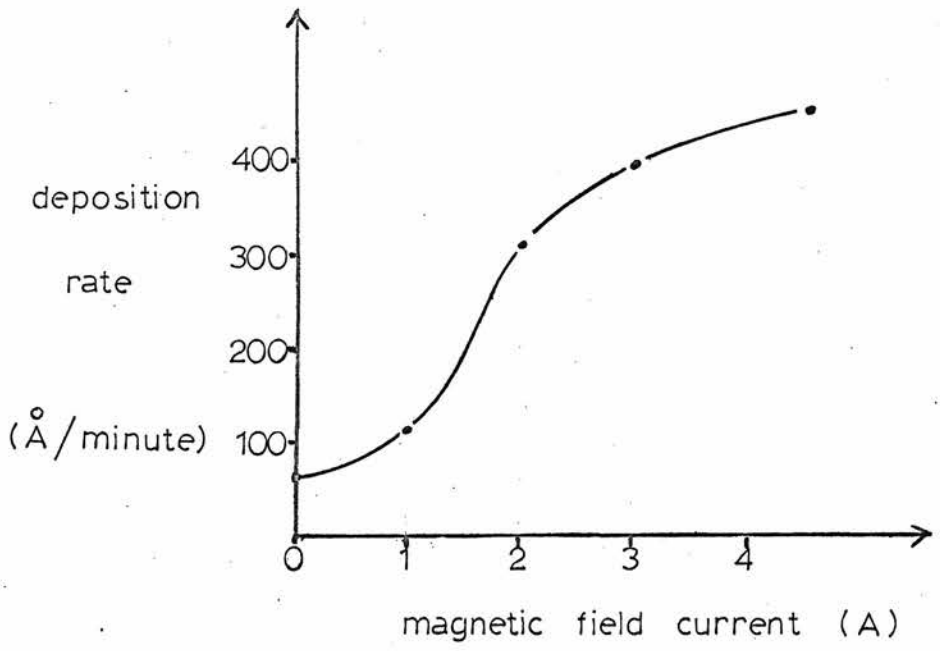

Figure 2.19. Deposition rate versus magnetic field current for R.F. sputtering with applied power = 300W, pressure = 7×10^{-3} torr, time = 10 minutes and electrode spacing = 3·5 cm.

of the energy of the bombarding ions and the number of bombarding ions which are determined by the power input and by the pressure respectively. The magnetic field acts to increase the deposition rate by increasing the amount of ionisation at constant pressure and voltage, and hence the number of ions bombarding the target. Figure 2.16 illustrates the variation in deposition rate with oxygen content in the atmosphere. The R.F. deposition rates are also a function of the type and thickness of insulator used between the target and the target electrode. Glass 5 mm thick is used in this work.

Chapter 3

AN EXAMINATION OF THE SPUTTERED FILMS

3.1 Equipment for Film Characterisation

This section is concerned with a description of the equipment and procedures used to determine the resistivity, composition and structure of the deposited films.

A four-point-probe resistivity jig is used to measure low resistivity films (< 50 Ω-cm) at room temperature. A current of 10 μA is arranged to flow between the two outer points, and the voltage developed across the two inner points is measured on a valve voltmeter. (Figure 3.1). The resistivity, ρ, is calculated by applying the formula

$$\rho = G \frac{V}{I} 2\pi s \qquad 3.1$$

where s = 0.0636 cm, the distance between the points, and G denotes the correction factor suggested in reference 34. The four-point-probe system is not designed to measure high resistivities and an alternative method is adopted in which resistivity is calculated from measurements made of the film dimensions and resistance. The resistance meter current varies between 200 μA on the low resistance range and 8.1 μA on the high range. In order to measure the thickness of the film each substrate is partially masked during sputtering so that a step is created between the substrate and the film surface. This step is measured by a Talysurf whose maximum resolution is ± 150 Å. The film resistivity is measured when all films have been produced in order to minimise the error introduced by variations in room temperature. The

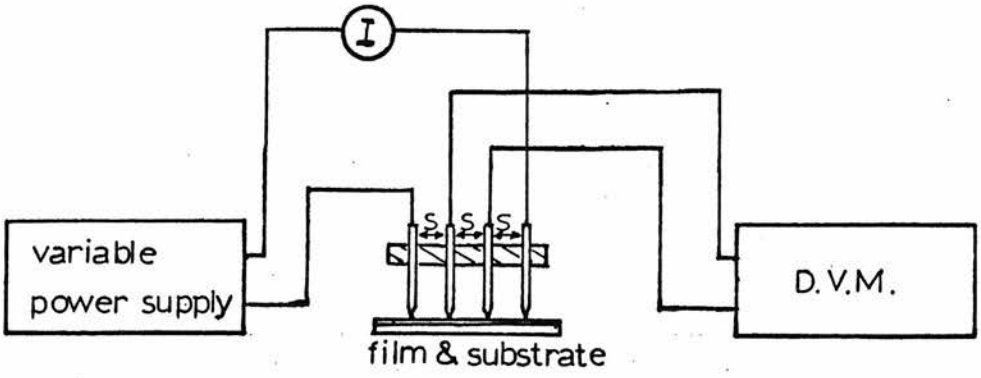

Figure 3.1. The 4-point probe system.

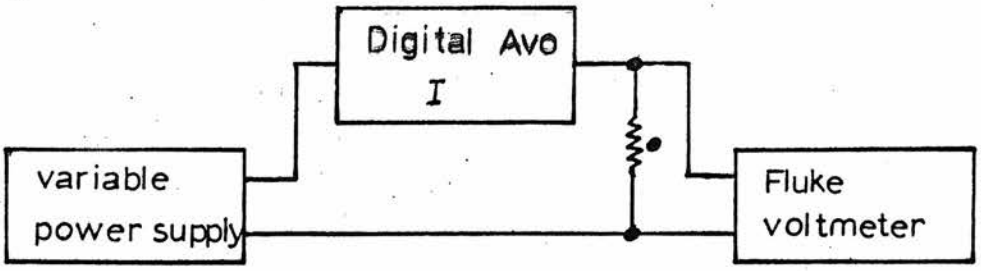

Figure 3.2. The self-heating test system.

possible error due to self heating is examined using the apparatus shown in figure 3.2. The Fluke voltmeter has an infinite input impedance when balanced. The resistance of a 100KΩ film is measured by applying a range of currents from 0.1μA to 250μA and measuring the voltage developed across the film. No significant change in resistance is detected, consequently no significant self heating occurs.

The variation of film resistance with temperature is measured using a liquid paraffin temperature bath which is constantly stirred. The accuracy of the temperature measured is $\pm$ 0.1°C. Resistance is measured using the resistance meter.

Structure is examined using a Philips PW1010 x-ray spectrometer. This instrument utilises the phenomenon of coherent diffraction from a crystal set at particular angles to an incident x-ray beam. The "reflection" of a particular wavelength, λ, of incident radiation occurs at an angle, θ, between the incident beam and the sample surface, when the Bragg condition

$$\sin\theta = \frac{n\lambda}{2d} \qquad 3.2$$

is satisfied. d denotes the interatomic spacing of the diffracting planes in the crystal and n denotes the order of the diffraction. If the angle of incidence of the x-rays varies, then "reflection" peaks are registered by a suitably placed detector/counter whenever the crystal structure is in the correct orientation to satisfy equation 3.2. The instrument, shown in diagramatic form in figure 3.3, operates by rotating the sample about one axis to vary θ and moving the detector/counter

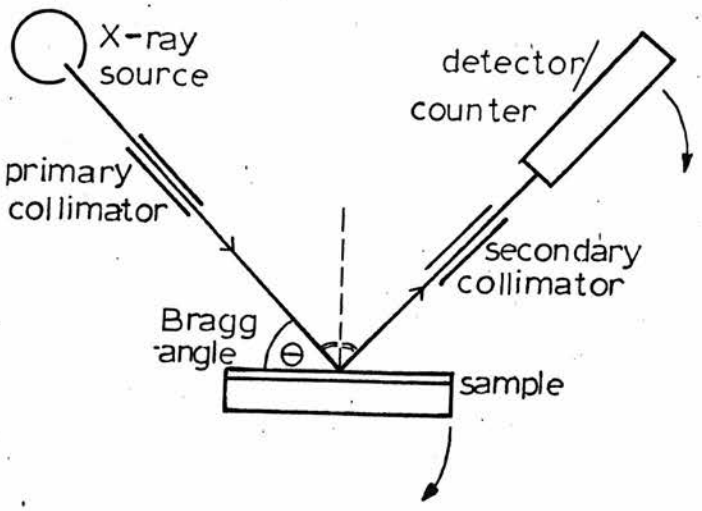

Figure 3.3. A diagram of the X-ray spectrometer.

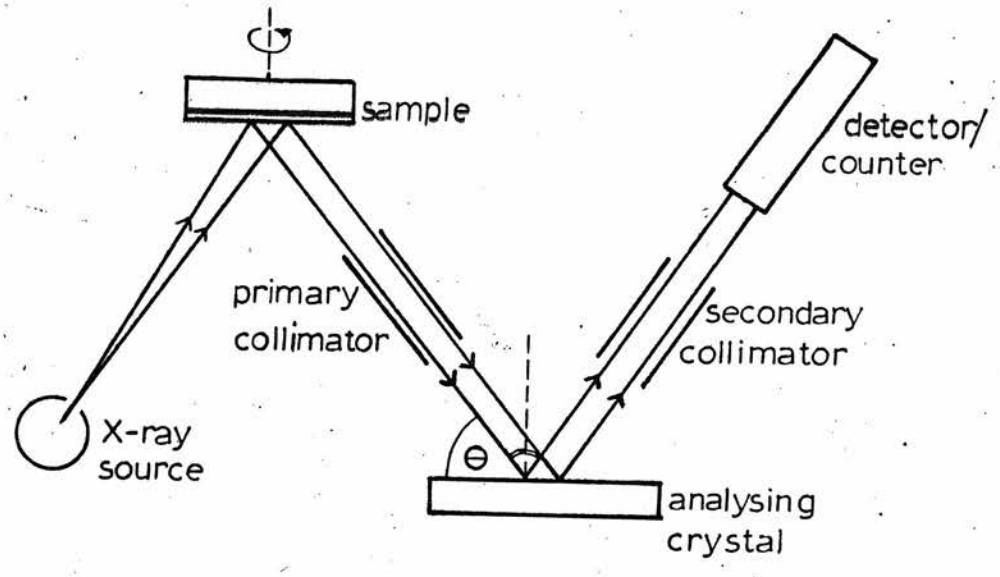

Figure 3.4. A diagram of the X.R.F. spectrometer.

simultaneously through 2 θ so that any reflected waves are registered by it. The reflected peaks are amplified and plotted on a chart recorder.

The structure of the sputtering target and films can be compared by examining the curves they produce. Polycrystalline samples, in which the crystallites are not aligned, produce broader peaks than single crystal samples and imperfections in the crystallites alter the intensity of the reflected wave. Thus the information that can be extracted from these curves divides into three parts;[35] crystal structure is indicated by the number of peaks and the Bragg angle at which they occur; the crystallite size is indicated by the peak width; and the imperfections in the lattice are indicated by the height of the peak. The analysis of the information contained in the curves is, in fact, considerably more complex than suggested. For example, the peak height is a function of film thickness, crystallite size and relative orientation of crystallites. However, only a limited analysis of the results is proposed in which the above statements are valid. The films examined are one micron thick in order that the reflected wave has a sufficiently large intensity to be easily detected above the background noise. The subtrates are amorphous and therefore cannot Bragg reflect the x-rays. However, they do scatter the x-rays and, along with air scatter, contribute to the background noise.

Chemical compositions are determined using a Philips PW1212 x-ray fluorescence (X.R.F.) spectrometer. The basic function of the spectrometer[36] is to provide a means of isolating selected

wavelengths of the characteristic radiation emitted by an element when excited by x-rays, in order that intensity measurements of this radiation may be made. The intensity of radiation of a particular wavelength above the background noise is a direct function of the concentration of the element present which produces it. The isolation of the selected wavelength is achieved by making use of the diffracting properties of a large single crystal. This analysing crystal is set at a particular angle to satisfy the Bragg condition for the selected wavelength which is then reflected into the detector. A diagram of the system is shown in figure 3.4. The sample is irradiated for ten seconds in this case and the integrated intensity measurement is given as a count. In practice there is a limit to the wavelength that can be isolated by a particular crystal in a particular spectrometer. This limit is determined by the value of d of the analysing crystal and by the maximum angle through which the detector system is free to rotate before being stopped by the presence of the sample chamber. For the system used the upper limit is approximately 20 Å so that elements with atomic numbers of less than 9 cannot be detected. The contribution to the background noise by air scatter is reduced by evacuating the system. Errors due to variation in composition over the sample are reduced by rotating the sample while it is being irradiated.

Each intensity measurement of copper, nickel, manganese and argon is carried out several times and the results averaged. The compositions of the films and target are represented as ratios of these elements in order to avoid the complexities and possible

errors involved in an absolute determination. The substrate is subjected to the same measurements and is found to contain insignificant quantities of these elements. Errors[36] due to long term instrument instabilities are minimised by measuring films approximately 1μm thick so that a sufficiently high intensity of radiation is measured during a short time period (10 seconds). The random error in the count can be taken as $\pm\sqrt{N}$ where N denotes the number of counts ($\sim 10^5$). Errors may also arise from effects due to the matrix and the chemical state of the elements. The electron distribution in the outer shells determines the wavelengths of the characteristic lines and also their relative intensities. The maximum wavelength shift arising from variations in electron distribution is small compared to the range examined using the collimation technique employed, so that a shift in wavelength does not introduce significant error. The error in the intensity measurement may be significant and is not readily calculable. However, with these samples the errors due to variations in the matrix are minimised since all the atoms in the film will be contributing to emitted radiation. The level of background noise in part reflects the influence of the matrix. The variation in background for the different samples was found to be negligible. Errors due to variations in chemical state are most significant in samples of low atomic number.

3.2 Results

In order to establish the quantity of oxygen required to be added to the chamber atmosphere to compensate for the oxygen loss

in the sputtering process, a range of thermistors was sputtered under identical operating conditions except for the percentage of oxygen in the atmosphere. This varied between 0% and 100%, one value being chosen per thermistor produced. Using the D.C. power supply, the operating conditions were: applied voltage = — 2.5 kV, chamber pressure = 3×10^{-2} torr, magnetic field current = 3.6 A, electrode spacing = 4 cm. In the R.F. case the conditions were: power input = 300 W, chamber pressure = 7×10^{-3} torr, magnetic field current = 3.6 A, electrode spacing = 3.5 cm. The minimum film thickness chosen was 1000 Å. The resistivity of the films was measured and compared with the target resistivity to indicate the quantity of oxygen required. However, neither the D.C. nor R.F. results, shown in figures 3.5 and 3.6 respectively as a graph of resistivity versus percentage of oxygen in the chamber atmosphere, indicated a plateau around 13.3 Ω-cm (the target resistivity) as expected. Figures 3.7 and 3.8 show the variation of individual film resistances with temperature for the R.F. and D.C. cases respectively. The B-values of the films are listed in Table 3.1. It is found that the B-value of the film decreases with increasing oxygen partial pressure in the sputtering atmosphere.

The structure of these films was examined using the diffractometer unit and further films were deposited on circular glass substrates of such a size that they could be fitted into the X.R.F. equipment to examine the film composition.

The composition of the target was examined before sputtering. The ratios of the elements on the surfaces of two identically

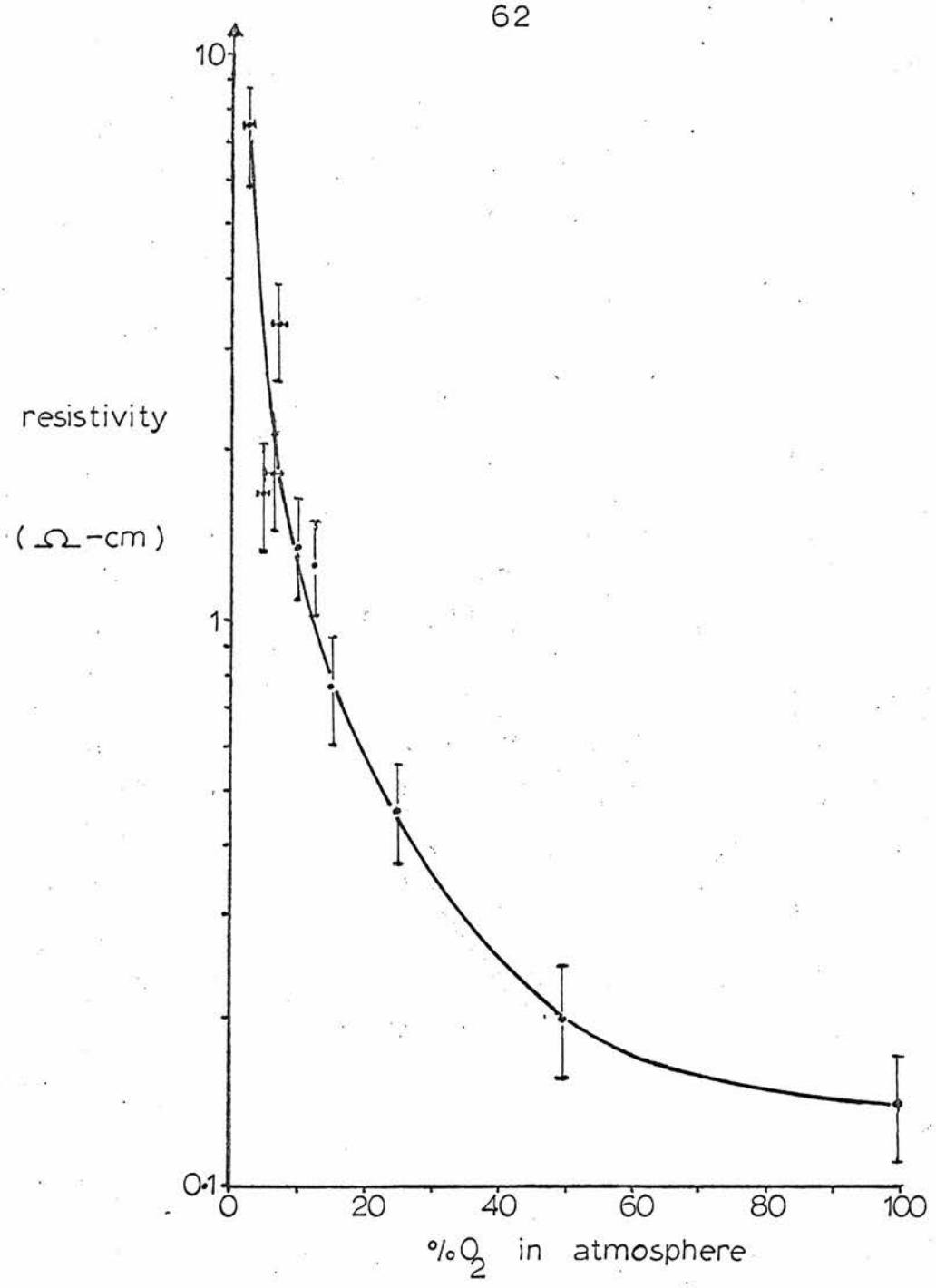

Figure 3.5. A graph of the resistivity of the material deposited by D.C. sputtering versus the percentage of O_2 by volume in the chamber atmosphere.

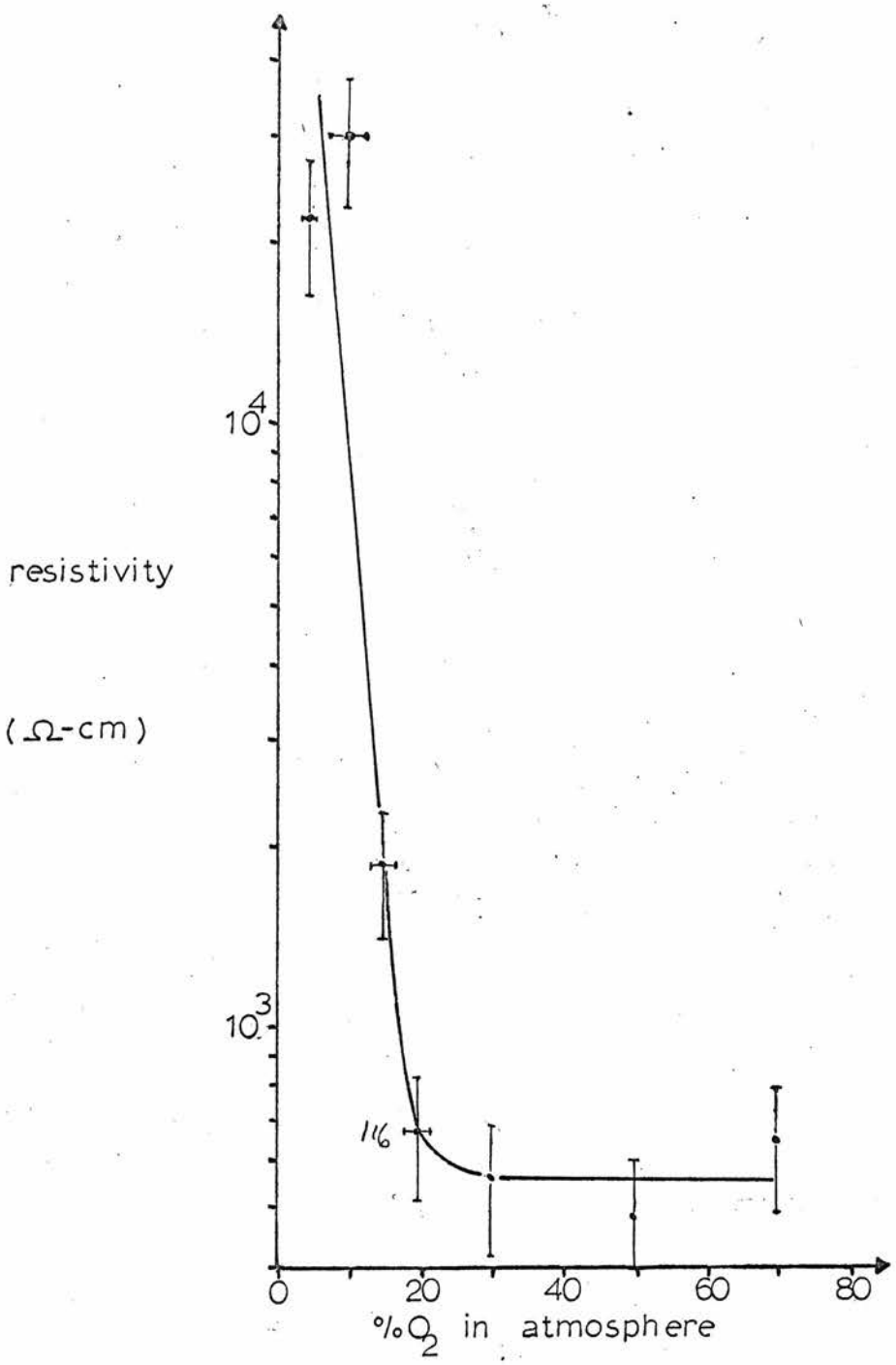

Figure 3.6. A graph of the resistivity of the material deposited by R.F. sputtering versus the percentage of O_2 by volume in the chamber atmosphere.

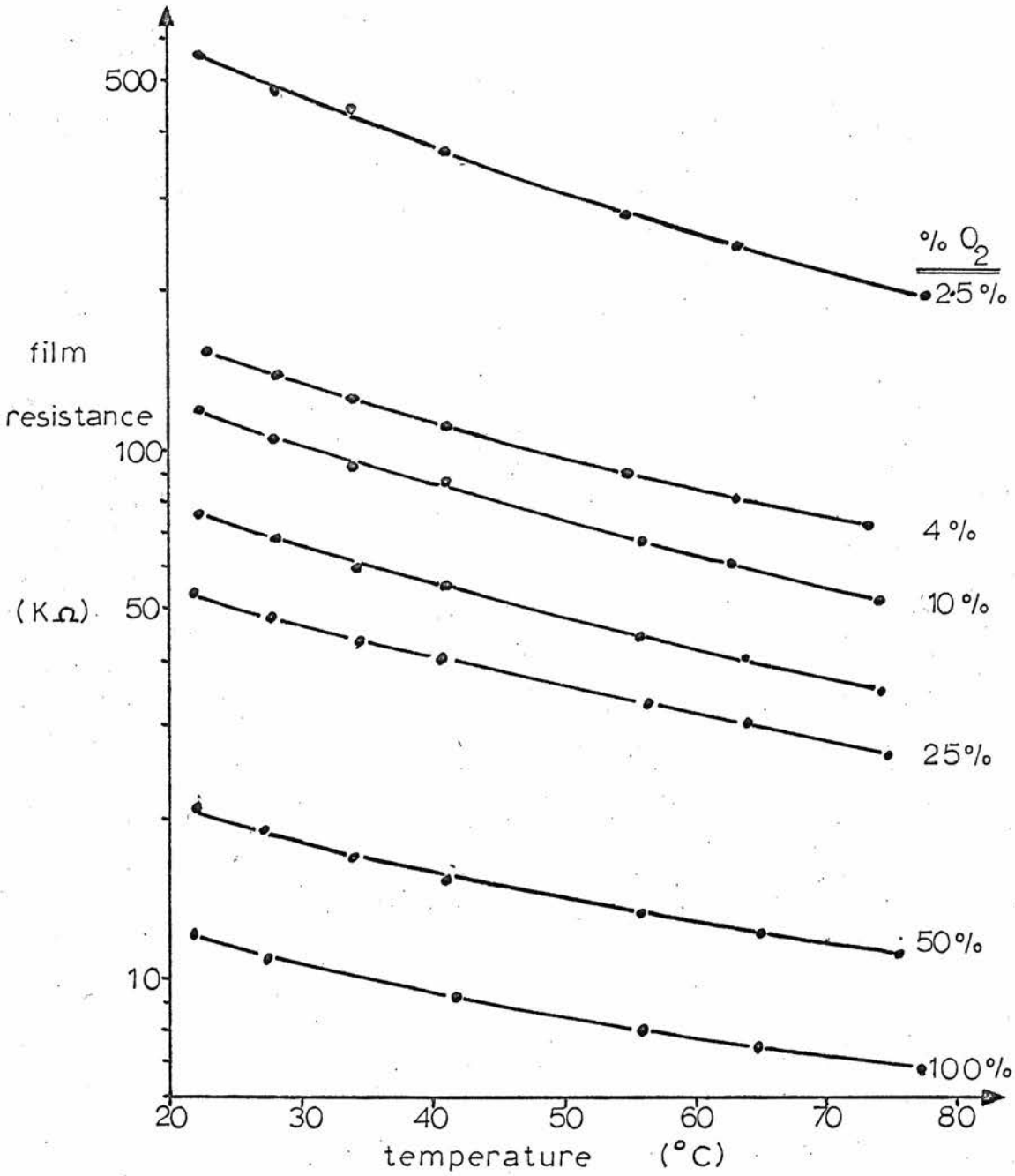

Figure 3.7. Graphs of the resistance of D.C. sputtered films versus temperature.

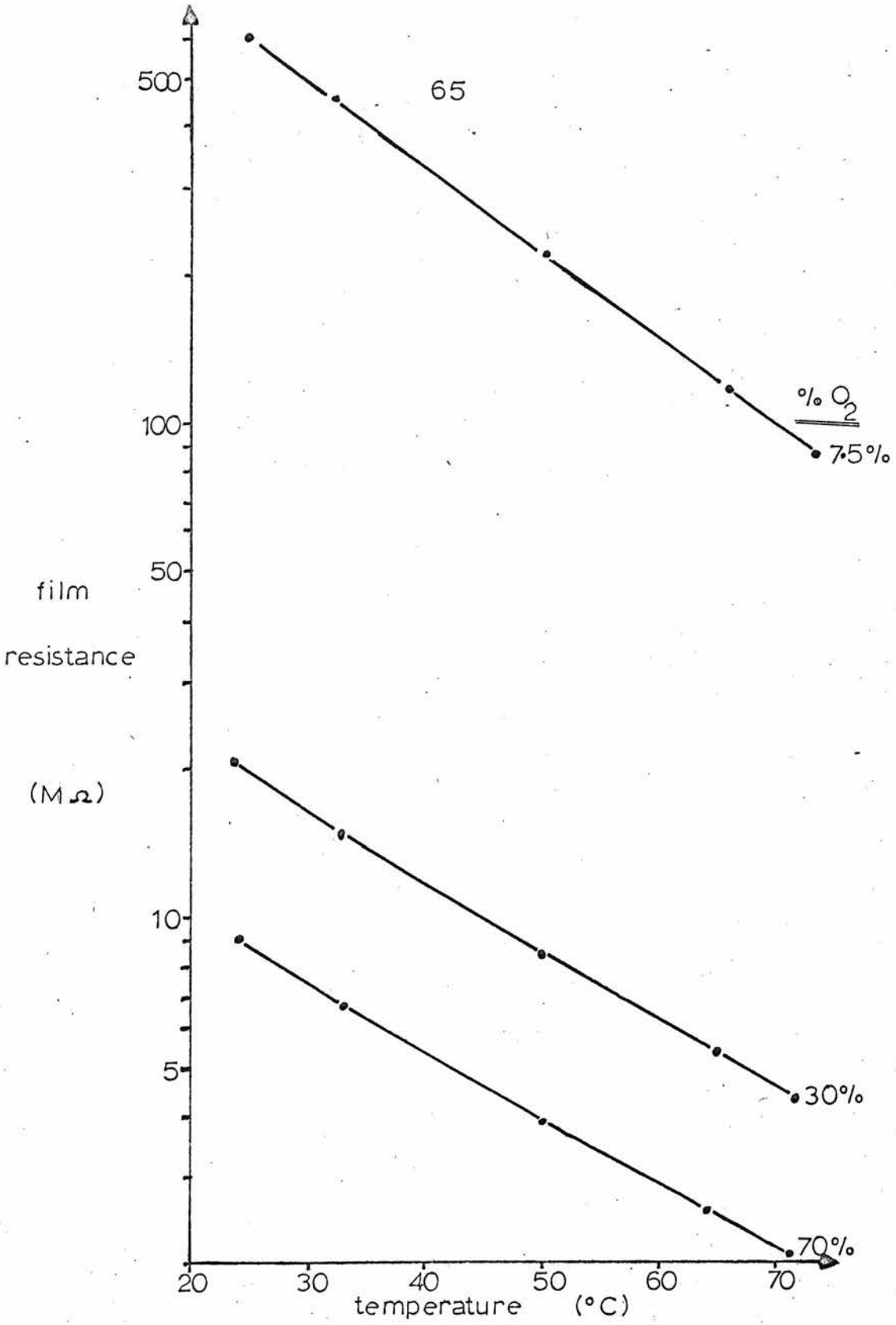

Figure 3.8. Graphs of the resistance of R.F. sputtered films versus temperature.

D.C. sputtered films

% O in atmosphere	2·5	5	10	15	25	50	100
resistivity (Ω-cm)	7·6	1·63	1·35	0·77	0·47	0·2	0·14
B-valve	2000	1540	1680	1520	1360	1230	1160

R.F. sputtered films

%O in atmosphere	5	30	70
resistivity (Ω-cm)	$2{\cdot}2\times10^{4}$	570	660
B-value	4060	3380	3140

$$\text{B-value} = \frac{T_1 \times T_2}{T_1 - T_2} \log_e \frac{R_{T_2}}{R_{T_1}} \quad \text{where } T_1 = 343^\circ K \text{ and } T_2 = 298^\circ K .$$

Table 3.1. The resistivity and B-value of films sputtered in atmospheres with different percentages of oxygen present.

produced targets were measured, then the surfaces were ground using fine emery paper to remove a 0.5 mm layer. After careful cleaning the measurements were repeated. The emery paper was examined for Cu, Mn and Ni content. This was found to be negligible. The results are shown in Table 3.2, and demonstrate that the material is not homogeneous. Therefore some variation in the composition of the sputtered films can be expected. The X.R.F. measurements of D.C. and R.F. films sputtered in atmosphere with different oxygen pressures are also shown in Table 3.2. A fourth section of this table shows the results obtained from D.C. films sputtered in different chamber pressures, the oxygen content being a constant 5% throughout. The X.R.F. ratios of the components in the sputtered films are considerably different from those in the target and suggest that apart from the target homogeneity other mechanisms operate to alter the composition. With the D.C. films the ratios vary consistently with the percentage of oxygen present and with pressure. The R.F. sputtered films produce ratios which change significantly when oxygen is added to the chamber atmosphere.

The random error in the X.R.F. ratios is $\pm$ 0.01. In order to check that the variations in the ratios are due to variations in the quantities of each metal present rather than to variations in their chemical states, four samples were dissolved in Aqua Regia and analysed by atomic absorption spectrophotometry. The maximum error involved in this technique is $\pm$ 5% so that large variations in composition are necessary to be successfully detected. The quantities of copper and manganese present in the films were compared to standard solutions and the results presented as the

sample	Cu/Ni	Cu/Mn	Ni/Mn	Ni/A
target 1—surface as supplied	1·325	2·17	1·64	—
—ground surface	1·36	2·11	1·56	—
target 2—surface as supplied	1·48	1·81	1·22	—
—ground surface	1·28	1·96	1·52	—
D.C. sputtered — 0 %O_2 (pressure = 30 μ)	1·24	3·3	2·75	—
— 5 %O_2	1·13	3·25	2·86	—
— 75%O_2	1·06	3·14	2·95	—
R F sputtered — 0 %O_2 (pressure = 7 u)	0·93	3·05	3·26	1·88
— 5 %O_2	0·92	3·2	3·5	2·13
— 50 %O_2	0·91	3·15	3·46	2·06
— 100 %O_2	0·93	3·14	3·4	2·12
DC sputtered — 25 μ (5%O : 95% A)	1·07	3·01	2·81	1·68
—30 μ	1·13	3·25	2·86	1·71
—40 μ	1·18	3·36	2·85	1·62
—50 μ	1·22	3·50	2·87	1·60

Table 3.2. The X.R.F. results.

ratio $\frac{Cu}{Mn}$. Each sample was tested three times. The results are shown in Table 3.3 and demonstrate that there is a difference in chemical composition between film 4 and films 1, 2 and 3. The differences between 1, 2 and 3 lie within the $\pm$ 5% possible maximum error.

The results of the investigation of the structure using the diffractometer unit are shown in Figure 3.9. Two targets, one with a 0.5 mm layer ground off the surface, were examined before sputtering and found to produce similar curves with several sharp peaks at a range of angles. Five films, which were sputtered using the R.F. system in atmospheres containing 5, 10,25,50 and 100% of oxygen, all produced a curve with one broad peak which occurred at the same angle. The curves produced by six samples, D.C. sputtered in atmospheres containing 0,10,15,25, 50 and 100% of oxygen each have one or more peaks which occur at different angles. The angles at which these peaks occur vary from sample to sample and there is no obvious relationship between the angle and the percentage of oxygen in the chamber. However, the angles do correspond to the angles at which peaks occur in the case of the target.

It can be concluded that the film structures are not identical to the target structure. However, in the D.C. case they may be similar. The crystallite size of the R.F. films is considerably smaller than that of the target and has approximately the same value for all R.F. films. The crystallite size of the D.C. films has a value which lies between the R.F. value and the target. This is, in fact, expected because the crystallite size in a growing

No.	sample	XRF ratio $\frac{Cu}{Mn}$	A.A.S. ratio $\frac{Cu}{Mn}$		
			(run 1)	(run3)	(run 3)
1	R.F. 5% O_2	3·2	0·850	0·851	0·852
2	R F 100% O_2	3·14	0·872	0·897	0·884
3	D.C. 25 μ	3·01	0·884	0·852	0·865
4	D.C. 50 μ	3·50	0·992	0·991	0·995

Table 3.3. The atomic absorption spectrophotometry (A.A.S.) results.

Figure 3.9. Diffractometer results (condensed)

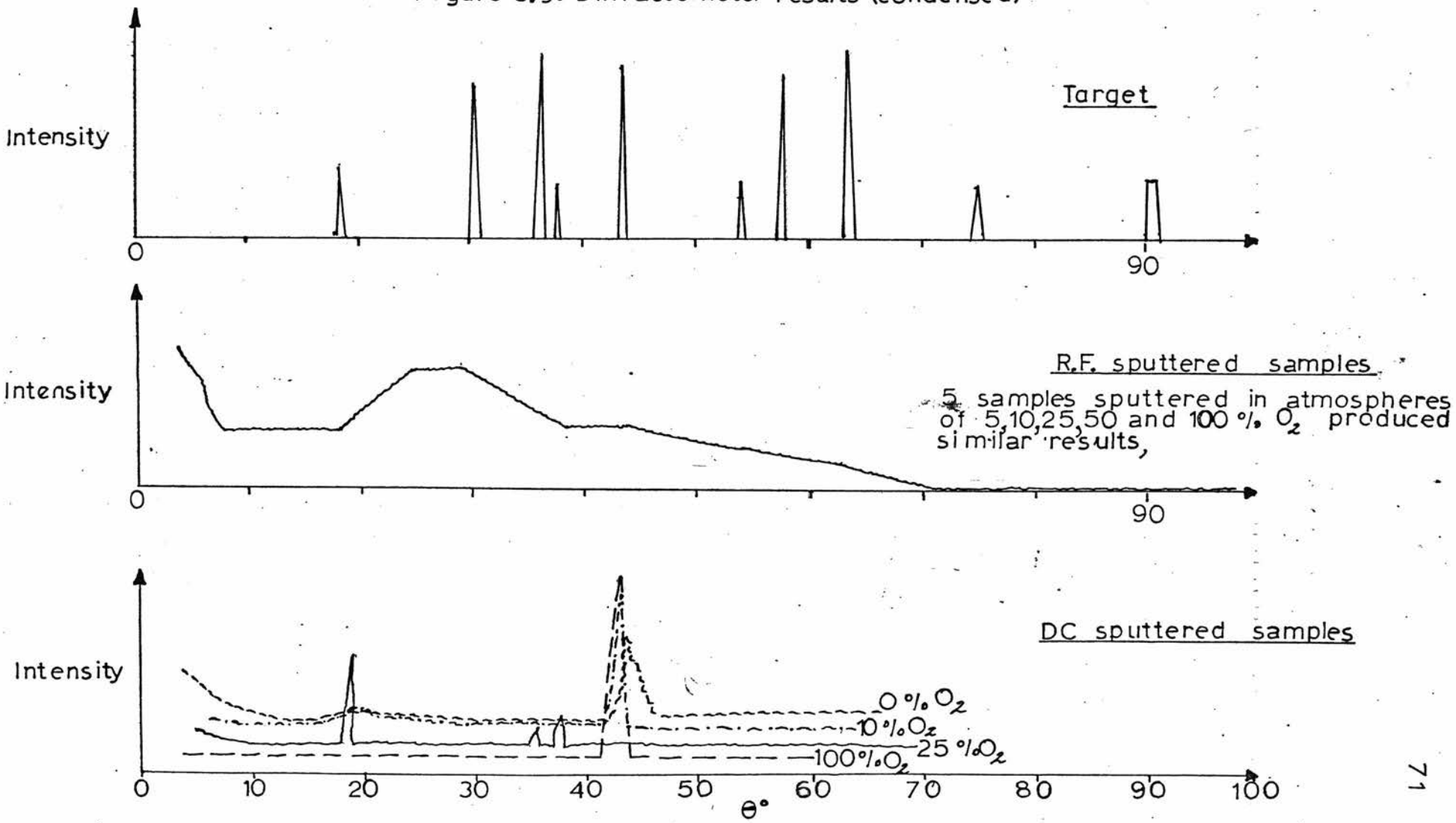

film is a decreasing function of the arrival energy of the components of the film. In the R.F. case the mean free path of the sputtered atoms is equivalent to the inter-electrode spacing so that the components have a high arrival energy at the substrate. In the D.C. case the arrival energy is much reduced by collisions with the atmosphere gas which is at a considerably higher pressure. Consequently the crystallite size in an R.F. sputtered film is expected to be smaller than in the D.C. sputtered film.

3.3 Discussion

In order to discuss the variations of the resistivity and B value of the films, produced under different deposition conditions, it is first necessary to consider the nature of the conduction mechanism in transition metal oxides. Single stoichiometric transition metal oxides are nearly all insulators, whereas non-stoichiometric oxides and solid solution mixtures of oxides, in which the different metal ions have different valency states, are semiconductors. For example, pure stoichiometric NiO is an insulator[37] with a resistivity $5 \times 10^{14}\ \Omega$-cm; on substituting small quantities of lithium into this lattice, the resistivity can decrease to $10^{-1}\ \Omega$-cm at room temperature. The cation-anion interaction in these single stoichiometric oxides produces sets of low-lying bonding energy levels which are completely filled and sets of high-lying anti-bonding energy levels that remain unoccupied. The presence of mixed valency cations in the semiconductors suggests that unoccupied sites are available due to the differences in valencies. The origin of the conduction mechanism must be sought in the process which permits an electron to jump from one cation to another. The

nature of this "hopping" process has not been fully explained. However, a general picture of the conduction process can be based on a simple model with localised electronic energy levels.[38] The charge carriers are essentially localised in the vicinity of the cationic lattice positions. The inter-cationic spacing is usually of such a size that, in the presence of lattice vibrations, the cations come close enough together for transfer of charge carriers with sufficient energy to occur with a high degree of probability. The charge carrier is then relocalised in its new site until it acquires sufficient activation energy to execute another jump. The localisation of the charge carrier may be increased by additional effects such as Landau trapping, which consists of polarisation of the crystal lattice around the charged particle. For such an effect to occur the charged carrier must reside on a given lattice site for a time that is comparable with, or greater than, the vibrational period of the lattice. Calculations of mobilities, which yield low values, and the absence of a measureable Hall effect, both indicate that such a trapping mechanism operates. If this model is valid, then the conduction mechanism can be considered as a thermally activated diffusion process[38] with a mobility

$$\mu = \frac{e d^2 \nu_0 \exp(-q/kT)}{kT}$$

q is the activation energy required to effect the transfer of charge from one site to the next. d is the jump length and ν_0 is the vibrational frequency. The conductivity of the material is given by

$$\sigma = ne\mu = \frac{ne^2 d^2 \nu_0}{kT} \exp(-q/kT)$$

where n is the number of sites per unit volume available for

conduction. The total number of sites is defined by the composition and structure of the material, as is the 'mobility' activation energy, q. The number of sites available is an exponential function of temperature.

Thus $$n \propto exp(-\frac{U}{2}/kT)$$

and $$\sigma \propto \frac{1}{kT} exp(-\frac{1}{kT}(q+\frac{U}{2})) \qquad 3.3$$

where U is the ionisation energy level of the sites which provide the current carriers. From this equation it can be seen that the variation of resistivity with temperature is primarily determined by the exponential term. The B-value term, used in thermistor technology, essentially describes the energy term, $(q + \frac{U}{2})$, in this exponential term. Consequently the B-value for the film is determined by its composition and structure. It has been found as a general empirical rule that resistivity and activation energy, and hence B-value, change in the same direction when composition changes. The sensitivity of the resistivity and B-value to variations in composition is shown in figures 3.10 and 3.11 for a MnO:NiO:CuO mix.[6] It can be seen that significant changes in these parameters occur for small variations in mix.

Figure 3.12 shows the variation of B-value with ρ found in the sputtering results and illustrates that there must be a significant change in composition and/or structure in the films compared with the target, and in the R.F. films compared with the D.C. films. The x-ray spectrometer results confirm that the R.F. film structure is considerably different from that of the D.C. films and the target. The small crystallite size will cause an increase in resistivity and, as the conduction mechanism across the crystal boundaries is also a

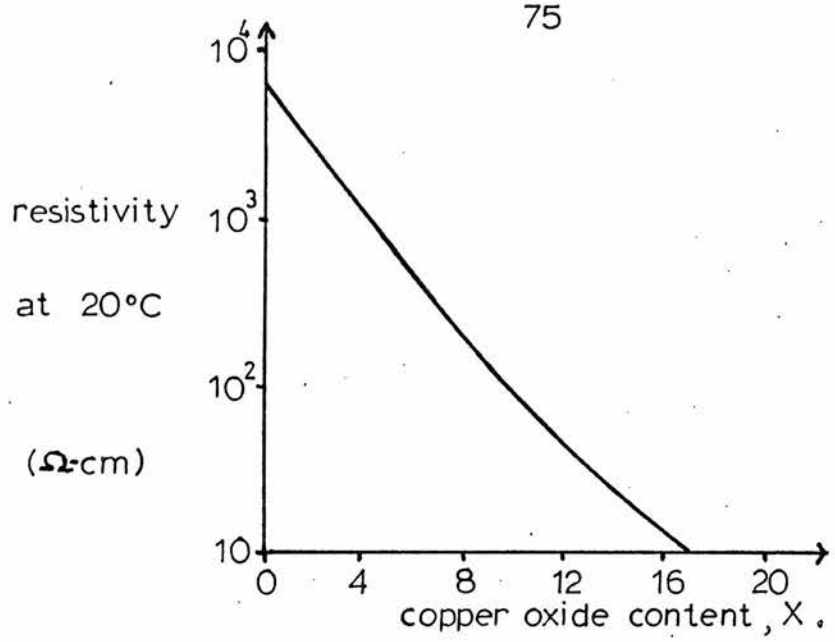

Figure 3.10. A graph of the variation of resistivity[6] at 20°C with copper oxide content for the mixture

Mn_2O_3	:	NiO	:	CuO
80	:	20	:	X

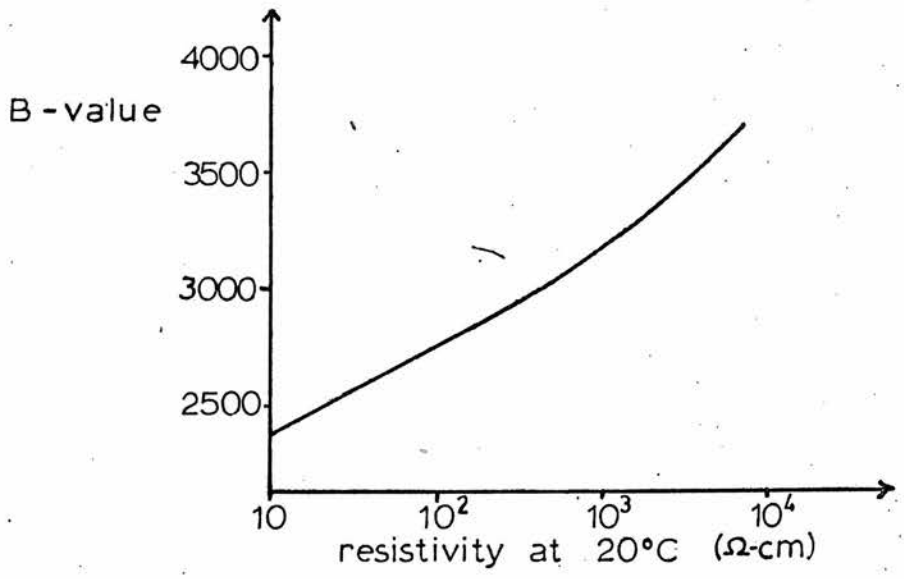

Figure 3.11. A graph of B-value versus resistivity[6] for the material shown in figure 3.10.

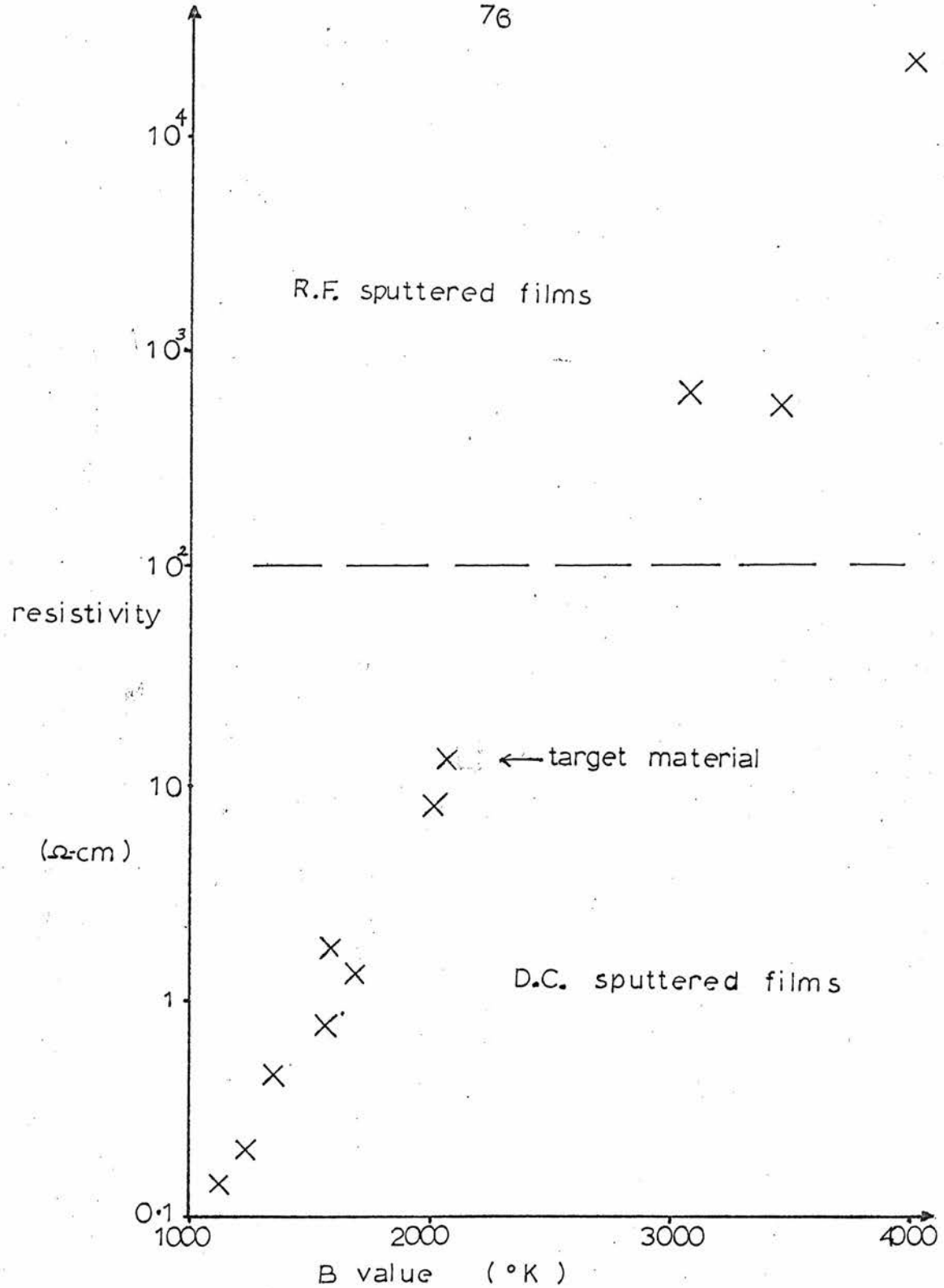

Figure 3.12. A graph of resistivity versus B-value of films sputtered under different conditions.

"hopping" process, the B-value will also increase. However, this is not a complete explanation of the R.F. results since ρ and B change with the oxygen content of the sputtering atmosphere even when the crystallite size of the films is approximately the same. Two possible explanations can be given for the ρ and B-value dependence on deposition conditions in both the D.C. and R.F. cases, namely, the ratios of the metal ions in the films may vary and also the valency states of these ions may vary. There is evidence to suggest that both may occur.

If the X.R.F. results are interpreted as indicating that the ratios of the metal ions vary with deposition conditions, as the atomic absorption spectrophotometry results partially confirm, then the resistivity and B-value will vary widely for small variations in the mix. Figures 3.10 and 3.11 illustrate the sensitivity of these parameters to variations in composition for a similar chemical system. The explanation of this variation in chemical composition probably lies in the interaction at the target surface. If the temperature of the target rises above the value where diffusion of ions from the bulk material to the target surface can occur, then the steady state conditions, where the concentrations of the different sputtered atoms arriving at the substrate in unit time is the same as the bulk concentration, is not achieved. The lattice structure of the surface layers of the target is considerably altered by the bombardment which causes the selective removal of different atoms due to their different sputtering rates. The mechanism of focused collisions results in severe deformation of the lattice several layers below the surface so that diffusion from this region is possible when

the bombarding ion energies are sufficiently high. The diffusion coefficient is exponentially related to temperature so that a significant increase in diffusion can occur for a small variation in target temperature. Now, considering the D.C. X.R.F. results (Table 3.2), variation of the chamber pressure and the oxygen partial pressure results in the ratios changing in opposite directions. That is, considering the ratio of $\frac{Cu}{Mn}$, its value decreases with increasing oxygen content and increases with increasing pressure. The deposition rate, and hence the target temperature, is an increasing function of the chamber pressure (Figure 2.17) and a decreasing function of the oxygen partial pressure (Figure 2.19) assuming that electron attachment to the electronegative gas plays an important role, so that these X.R.F. results are consistent with the above explanation. In the R.F. case, the X.R.F. ratios change on introducing oxygen into the chamber. The effect of increasing the oxygen content on the target temperature is complex because the negative ions may also bombard the target in the R.F. case. Attempts were made to reduce the target temperature by reducing the cooling water temperature using a refrigeration unit. However, thermal stresses across the target caused it to crack when the cooling water temperature was less than $10^{o}C$.

There is another possible explanation for the variation in chemical composition. This arises from the interaction at the substrate, when variations in the deposition conditions may cause a variation in the resputtering rates of the deposited atoms. However, the resputtering rates are small compared to the deposition rate of the film so that variations in their values are unlikely to cause

significant changes in the metal ion ratios. The sticking coefficients for metal atoms are generally accepted as having a value close to unity. However, there is a lack of information about the effects of variations in the deposition conditions on the sticking coefficients of the elements used in this work. Recent work[39] on the sputtering of silicon has shown that the sticking coefficient is strongly dependent on the deposition conditions.

Consider now the explanation that ρ and B vary due to changes in the valency states. The high resistivities of films deposited in low oxygen pressures, particularly in the R.F. case indicates that although there is a net oxygen loss in the system the deposited films are not even partly metallic. This suggests that the metal ions may adopt different valency states, resulting in the creation of oxide films whose structures are different from the target structure although the ratios of the metal ions in the films may be the same as in the target. Small variations in the X.R.F. ratios may then be interpreted as indicating variations in the chemical states of the metal ions. The author was unable to find a phase diagram applicable to this system, nor was the necessary diagnostic equipment available to test this hypothesis.

Since it has been confirmed that the metal ion ratio does change in at least one film it is probable that the metal ion ratio changes sufficiently in the other films to (largely) account for the variation in ρ and B-value. Variations in valency states and in structure also probably contribute to produce the range of resistivities and B-values obtained. The presence of argon in the films will also act to change the resistivity and B-value of the films by disrupting

the film structure.

It has not proven possible to repeat the work of Froemel and Sapoff[10] and obtain films which are identical to the target with respect to composition, resistivity and B-value. It has proven possible to produce negative temperature coefficient films whose resistivities vary from 0.1Ω-cm to 10^4Ω-cm and with B-values in the range 1000 to 4000°K, all from one target material (ρ = 13.3Ω-cm, B = 2010°K). Reproducible films of any value in this range (±10%) can be made by adjusting the deposition conditions to the required values.

Further work is necessary to establish the nature of the mechanism which alters the metal ion ratios and to determine the relative importance of composition, valency, and structural changes in determining the resistivity and B-values of the resulting films. The lack of information on the sputtering of these oxides make it desirable to carry out work to determine the behaviour of the single oxides and two oxide mixes when sputtered.

Chapter 4

AN EXAMINATION OF THE HEAT TRANSFER PROCESS

4.1 Introduction

The heat transfer problem involves conduction and forced convection at the boundary between a non-Newtonian fluid which is exhibiting unsteady flow and a film which is experiencing unsteady periodic heating. Unsteady conductive heat transfer also occurs from the film to its support and electrical leads. A diagram of the physical system is shown in figure 4.1. Considerable problems exist in obtaining analytical solutions of the mathematical equations describing the above system. Exact solutions are not possible. Much of the difficulty lies in establishing the boundary conditions. Further, a rigorous mathematical description of the motion of blood presents considerable difficulties. It is necessary to simplify the problems by applying a series of suitable approximations and assumptions in order to achieve a useful solution. It is proposed to present a general outline of the theory and to solve the relevant equations, using suitable approximations, so as to estimate the order of magnitude values of parameters relevant to the transducer design. Further penetration and accuracy are beyond the scope of this thesis.

The transfer of heat energy at a solid-fluid interface is governed by the laws of fluid dynamics and the laws of heat conduction and heat storage. The theory of fluid dynamics for an incompressible Newtonian fluid is considered first.

4.2 The fluid Dynamics Problem

The derivation of the equations of motion of an incompressible

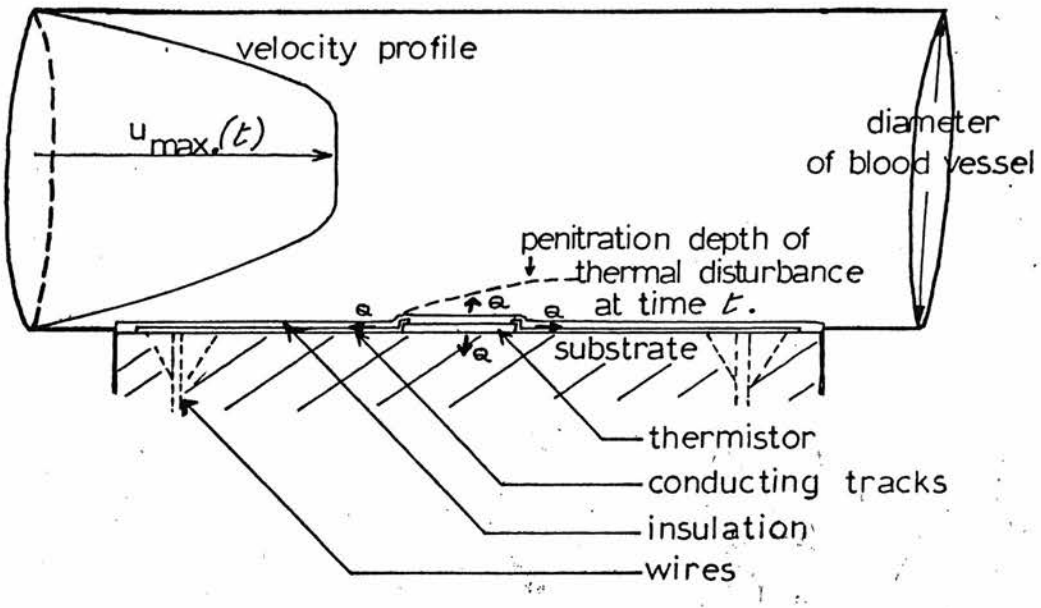

Figure 4.1. A diagram of the heat transfer problem at time

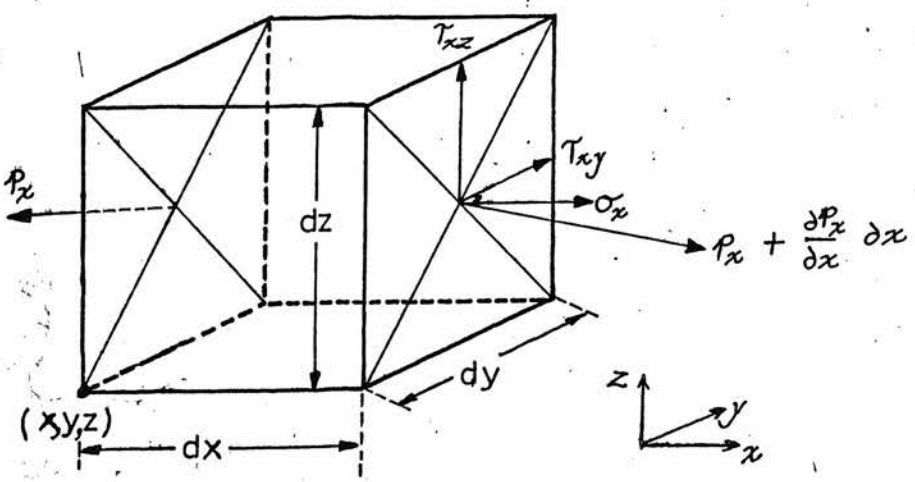

Figure 4.2. A diagram of a volume element of fluid.

viscous fluid[40] initially involves an analysis of the forces acting on a volume element of the fluid with a view to applying Newton's Second Law. For an element of fluid the Second Law can be written in the following vector form

$$\rho \frac{D\bar{w}}{Dt} = \bar{F} + \bar{P} \qquad 4.1$$

with $\bar{w} = iu + jv + kw$

$\bar{F} = ix + jy + kz$

and $\bar{P} = iP_x + jP_y + kP_z$

where ρ denotes density and $\bar{F}$ and $\bar{P}$ denote gravitational forces and forces acting on the boundary (i.e. pressure and friction) respectively. The symbol $\bar{W}$ denotes the flow velocity vector and $\frac{D\bar{W}}{Dt}$ represents the sum of two contributions, the local acceleration in non-steady flow and a convective contribution. Thus for the u-component

$$\frac{Du}{Dt} = \frac{\partial u}{\partial t} + u\frac{\partial u}{\partial x} + v\frac{\partial u}{\partial y} + w\frac{\partial u}{\partial z} \,. \qquad 4.2$$

Consider a rectangular element of fluid of volume dV = dx.dy.dz as shown in figure 4.2. The two faces of area dy.dz which are perpendicular to the x-axis experience two resultant stresses, i.e. resultant surface forces per unit area, $\bar{p}_x$ and $\bar{p}_x + \frac{\partial \bar{p}_x}{\partial x}.\partial x$ respectively. Hence the resultant surface force in the plane perpendicular to the x-direction is given by

$$\frac{\partial \bar{p}_x}{\partial x} . \partial x . \partial y . \partial z \,,$$

similarly for the components in the y- and z-directions. The resultant surface force per unit volume, $\bar{P}$, is therefore given by

$$\bar{P} = \frac{\partial \bar{p}_x}{\partial x} + \frac{\partial \bar{p}_y}{\partial y} + \frac{\partial \bar{p}_z}{\partial z} \,. \qquad 4.3$$

The vectors, $\bar{p}_x$, $\bar{p}_y$ and $\bar{p}_z$ can be resolved into components perpendicular

and parallel to each face. The normal stresses are denoted by σ with a subscript indicating direction. The shearing stresses, τ, have two subscripts, the first denoting the axis to which the face is perpendicular. The second indicates the direction to which the shearing stress is parallel. Hence $\bar{P}_x$ can be written

$$\bar{P}_x = i\sigma_x + j\tau_{xy} + k\tau_{xz} \qquad 4.4$$

and the x-component of $\bar{P}$ becomes

$$\bar{P}_x = i\left(\frac{\partial \sigma_x}{\partial x} + \frac{\partial \tau_{xy}}{\partial y} + \frac{\partial \tau_{xz}}{\partial z}\right), \qquad 4.5$$

similarly for the y- and z-components of $\bar{P}$. All the stress components can be conveniently represented in matrix form thus

$$\begin{vmatrix} \sigma_x & \tau_{xy} & \tau_{xz} \\ \tau_{yx} & \sigma_y & \tau_{yz} \\ \tau_{zx} & \tau_{zy} & \sigma_z \end{vmatrix} .$$

It is easily proven[40] that pairs of shearing stresses with subscripts which vary only in their order are equal, for example $\tau_{xy} = \tau_{yx}$.

Now, the system of surface forces determines the state of stress; however these surface forces depend on the state of strain of the fluid. It has been established empirically that for a fluid the stress is proportional to the rate of change of strain with time, called "rate of strain", $\frac{ds}{dt}$, which is identical to the flow velocity vector

$$\bar{w} = \frac{ds}{dt} = iu + jv + k\omega \quad .$$

Turning now to the stress-strain relationship for a compressible fluid, known as Stokes' Hypothesis. When written in matrix form in Cartesian coordinates it is given by

$$\begin{vmatrix} \sigma_x & \tau_{xy} & \tau_{xz} \\ \tau_{yx} & \sigma_y & \tau_{yz} \\ \tau_{zx} & \tau_{zy} & \sigma_z \end{vmatrix} = \begin{vmatrix} \sigma_m & 0 & 0 \\ 0 & \sigma_m & 0 \\ 0 & 0 & \sigma_m \end{vmatrix} + \mu \begin{vmatrix} \frac{\partial u}{\partial x} & \frac{\partial u}{\partial y} & \frac{\partial u}{\partial z} \\ \frac{\partial v}{\partial x} & \frac{\partial v}{\partial y} & \frac{\partial v}{\partial z} \\ \frac{\partial w}{\partial x} & \frac{\partial w}{\partial y} & \frac{\partial w}{\partial z} \end{vmatrix} + \mu \begin{vmatrix} \frac{\partial u}{\partial x} & \frac{\partial v}{\partial x} & \frac{\partial w}{\partial x} \\ \frac{\partial u}{\partial y} & \frac{\partial v}{\partial y} & \frac{\partial w}{\partial y} \\ \frac{\partial u}{\partial z} & \frac{\partial v}{\partial z} & \frac{\partial w}{\partial z} \end{vmatrix} - \frac{2}{3}\mu \begin{vmatrix} \operatorname{div}\bar{w} & 0 & 0 \\ 0 & \operatorname{div}\bar{w} & 0 \\ 0 & 0 & \operatorname{div}\bar{w} \end{vmatrix}$$

4.6

where μ denotes viscosity and σ_m represents the arithmetic mean of the normal stresses.

$$\sigma_m = \frac{1}{3}(\sigma_x + \sigma_y + \sigma_z) = -p \quad . \tag{4.7}$$

The negative of the mean stress is called the pressure in the fluid. In liquids the viscosity can be regarded as independent of pressure and a decreasing function of temperature. By assuming that the heat generated by friction is negligible the process can be considered isothermal. For an incompressible fluid the continuity equation, which states that for a unit volume there is a balance between the masses entering and leaving the unit volume per unit time, is

$$\operatorname{div} \bar{w} = 0 \quad . \tag{4.8}$$

Hence the last term in equation 4.6 is zero for an incompressible fluid.

By introducing the equation

$$\sigma_x = -p + \sigma_x' \tag{4.9}$$

it is possible to separate the non-viscous pressure terms from the frictional terms in the final equation. From equation 4.6 the frictional terms of the stress components can be written

$$\begin{aligned} \sigma_x' &= 2\mu \frac{\partial u}{\partial x} \quad ; \quad \tau_{xy} = \mu \left(\frac{\partial u}{\partial y} + \frac{\partial v}{\partial x} \right) \\ \sigma_y' &= 2\mu \frac{\partial v}{\partial y} \quad ; \quad \tau_{yz} = \mu \left(\frac{\partial v}{\partial z} + \frac{\partial w}{\partial y} \right) \\ \sigma_z' &= 2\mu \frac{\partial w}{\partial z} \quad ; \quad \tau_{xz} = \mu \left(\frac{\partial w}{\partial x} + \frac{\partial u}{\partial z} \right) \end{aligned} \tag{4.10}$$

Returning to equation 4.5, now

$$\bar{p}_x = \frac{\partial \sigma_x}{\partial x} + \frac{\partial \tau_{xy}}{\partial y} + \frac{\partial \tau_{xz}}{\partial z} \quad .$$

By substituting equation 4.9 in this, it becomes

$$\bar{p}_x = -\frac{\partial p}{\partial x} + \frac{\partial \sigma'_x}{\partial x} + \frac{\partial \tau_{xy}}{\partial y} + \frac{\partial \tau_{xz}}{\partial z}$$

and the substitution of equation 4.10 gives

$$\bar{p}_x = -\frac{\partial p}{\partial x} + \frac{\partial}{\partial x}\left(2\mu \frac{\partial u}{\partial x}\right) + \frac{\partial}{\partial y}\left(\mu\left(\frac{\partial u}{\partial y} + \frac{\partial v}{\partial x}\right)\right) + \frac{\partial}{\partial z}\left(\mu\left(\frac{\partial w}{\partial x} + \frac{\partial u}{\partial z}\right)\right)$$

$$= -\frac{\partial p}{\partial x} + \mu \frac{\partial^2 u}{\partial x^2} + \mu \frac{\partial}{\partial x}\left(\frac{\partial u}{\partial x}\right) + \mu \frac{\partial^2 u}{\partial y^2} + \mu \frac{\partial}{\partial x}\left(\frac{\partial v}{\partial y}\right) + \mu \frac{\partial^2 u}{\partial z^2} + \mu \frac{\partial}{\partial x}\left(\frac{\partial w}{\partial z}\right) .$$

By applying the continuity equation again this becomes

$$\bar{p}_x = -\frac{\partial p}{\partial x} + \mu \left(\frac{\partial^2 u}{\partial x^2} + \frac{\partial^2 u}{\partial y^2} + \frac{\partial^2 u}{\partial z^2}\right) . \qquad 4.11$$

Corresponding expressions are obtained for the y- and z-components.

If these expressions are substituted in the Second Law equation, that is equation 4.1, the fundamental equation of motion of incompressible Newtonian fluids, known as Navier-Stokes equations, are obtained

$$\rho \frac{Du}{Dt} = X - \frac{\partial p}{\partial x} + \mu\left(\frac{\partial^2 u}{\partial x^2} + \frac{\partial^2 u}{\partial y^2} + \frac{\partial^2 u}{\partial z^2}\right)$$

$$\rho \frac{Dv}{Dt} = Y - \frac{\partial p}{\partial y} + \mu \left(\frac{\partial^2 v}{\partial x^2} + \frac{\partial^2 v}{\partial y^2} + \frac{\partial^2 v}{\partial z^2}\right)$$

$$\rho \frac{Dw}{Dt} = Z - \frac{\partial p}{\partial z} + \mu \left(\frac{\partial^2 w}{\partial x^2} + \frac{\partial^2 w}{\partial y^2} + \frac{\partial^2 w}{\partial z^2}\right)$$

non-viscous pressure terms — frictional terms

4.12

The application of the Navier-Stokes equations to flow through straight tubes with circular cross sections conveniently permits

considerable simplifications. The Navier-Stokes equations in cylindrical coordinates (r, ϕ, x) are[40]

$$\rho \frac{Dv_r}{Dt} = F_r - \frac{\partial p}{\partial r} + \mu \left(\frac{\partial^2 v_r}{\partial r^2} + \frac{1}{r}\frac{\partial v_r}{\partial r} - \frac{v_r}{r^2} + \frac{1}{r^2}\frac{\partial^2 v_r}{\partial \phi^2} - \frac{2}{r^2}\frac{\partial v_\phi}{\partial \phi} + \frac{\partial^2 v_r}{\partial x^2} \right) \quad 4.13$$

$$\rho \frac{Dv_\phi}{Dt} = F_\phi - \frac{1}{r}\frac{\partial p}{\partial \phi} + \mu \left(\frac{\partial^2 v_\phi}{\partial r^2} + \frac{1}{r}\frac{\partial v_\phi}{\partial r} - \frac{v_\phi}{r^2} + \frac{1}{r^2}\frac{\partial^2 v_\phi}{\partial \phi^2} - \frac{2}{r^2}\frac{\partial v_r}{\partial \phi} + \frac{\partial^2 v_\phi}{\partial x^2} \right) \quad 4.14$$

$$\rho \frac{Dv_x}{Dt} = F_x - \frac{\partial p}{\partial x} + \mu \left(\frac{\partial^2 v_x}{\partial r^2} + \frac{1}{r}\frac{\partial v_x}{\partial r} + \frac{1}{r^2}\frac{\partial^2 v_x}{\partial \phi^2} + \frac{\partial^2 v_x}{\partial x^2} \right) . \quad 4.15$$

Let the x-axis be selected along the axis of the tube and let r denote the radial coordinate measured from the axis outward as shown in figure 4.3. Let there be only one velocity component present, acting parallel to the x-axis, denoted by u and a function of r only. These conditions represent steady laminar flow. By taking advantage of the rotational symmetry it is possible to evolve a two-dimensional equation describing the velocity profile. Equation 4.15 only is required and it simplifies to

$$\mu \left(\frac{\partial^2 u}{\partial r^2} + \frac{1}{r}\frac{\partial u}{\partial r} \right) = \frac{\partial p}{\partial x} , \quad 4.16$$

the boundary condition being $u = 0$ at $r = R$. The solution of this equation gives the velocity profile of the flow, thus

$$u_r = -\frac{1}{4\mu}\frac{dp}{dx}\left(R^2 - r^2\right) \quad 4.17$$

where $-\frac{dp}{dx} = \frac{p_1 - p_2}{L}$ = constant, is the pressure gradient. Hence, using the rotational symmetry, the velocity profile is in the form of a parabaloid. Equation 4.17 is known as the Hagen-Poiseuille equation. The maximum velocity, u_m, along the tube axis, is

$$u_m = \frac{R^2}{4\mu}\left(-\frac{dp}{dx}\right) . \quad 4.18$$

The mean velocity, $\bar{u}$, equals $\frac{u_m}{2}$ and the volume flow rate is $\pi R^2 \bar{u}$. It has been found empirically that laminar flow as described

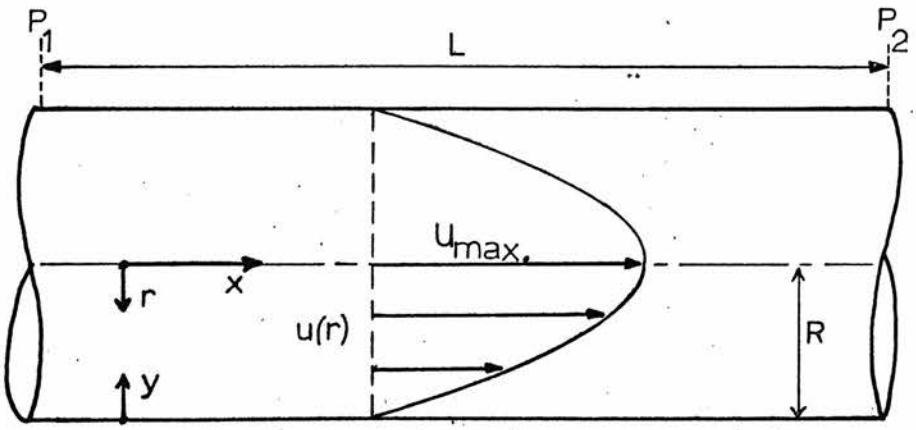

Figure 4.3. A two-dimensional representation of steady laminar flow through a pipe.

above occurs in practice only when the dimensionless number $2\bar{u}R\rho\mu^{-1}$, known as Reynolds' number, has a value[41] less than 2300. Above this critical Reynolds' number the flow becomes turbulent and the above equations do not apply. Further, the above equations apply to a situation in which the transient perturbation in the flow profile due to entry into the pipe has ceased, that is, where the steady state velocity profile is fully developed. For the worst case condition of a flat velocity profile at the tube entrance it has been established[42] empirically that, at a distance

$$x = 0.25\,\bar{u}\,R\rho\mu^{-1} \qquad 4.19$$

into the pipe, the transient perturbation disappears and the velocity profile is fully developed.

Now, if the flow rate is some periodic function of time, the Navier-Stokes equation, used in the Hagen-Poiseuille analysis, must be enlarged to include the acceleration term $\frac{\partial u}{\partial t}$. The other acceleration terms in equation 4.2 are zero since u is a function of r and t only. Therefore

$$\frac{\partial u}{\partial t} = -\frac{1}{\rho}\frac{\partial P}{\partial x} + \nu\left(\frac{\partial^2 u}{\partial r^2} + \frac{1}{r}\frac{\partial u}{\partial r}\right) \qquad 4.20$$

where $\nu = \frac{\mu}{\rho}$.

Assume a harmonically varying pressure gradient of the following form

$$-\frac{1}{\rho}\frac{\partial P}{\partial x} = K\cos(nt) \qquad 4.21$$

where K denotes a constant. Written in complex notation this becomes

$$-\frac{1}{\rho}\frac{\partial P}{\partial x} = K e^{int}. \qquad 4.22$$

Assuming the velocity function has the form $u(r,t) = f(r)e^{int}$ and

referring to equation 4.20, the following differential equation for the function $f(r)$ is obtained

$$f''(r) + \frac{1}{r}f'(r) - \frac{in}{\nu}f(r) = -\frac{K}{\nu} \quad .$$

The solution of this equation[43] is given by

$$u(r,t) = -i\frac{K}{n}e^{int}\left[1 - \frac{J_o\left(r\sqrt{\frac{-in}{\nu}}\right)}{J_o\left(R\sqrt{\frac{-in}{\nu}}\right)}\right] \quad . \qquad 4.23$$

Jo denotes the Bessel function of the first kind and of zero order, and is given by the expansion

$$J_o(x) = \sum_{k=0}^{\infty}\frac{(-1)^k}{(k!)^2}\left(\frac{x}{2}\right)^{2k} \quad .$$

In the blood flow problem, the fundamental frequency of the small pulsatile component of flow is 5 Hz. Hence the value of the dimensionless number R $(n\,\nu^{-1})^{\frac{1}{2}}$ is 1.44 when $\nu = 38 \times 10^{-3}$ $cm^2 sec^{-1}$ (from Table 5.1) and R = 0.05 cm. On expanding the Bessel function it is found that only the first two terms need be considered. Oscillations associated with variations in the steady flow component occur at a frequency of less than 1 Hz so that a similar approximation can be applied. Hence, considering these two components, equation 4.23 becomes

$$u(r,t) = -i\frac{K_1}{n_1}e^{in_1t}\left[1 - \frac{1 - \frac{in_1}{4\nu}r^2}{1 - \frac{in_1}{4\nu}R^2}\right] - i\frac{K_2}{n_2}e^{in_2t+\phi}\left[1 - \frac{1 - \frac{in_2}{4\nu}r^2}{1 - \frac{in_2}{4\nu}R^2}\right]$$

where ϕ is the phase difference between the two oscillations at time, t = 0. Returning to real notation, this becomes

$$u(r,t) = C_1 e^{jn_1t}(R^2 - r^2) + C_2 e^{jn_2t+\phi}(R^2 - r^2)$$

$$= (R^2 - r^2)(C_1\cos n_1t + C_2\cos(n_2t + \phi)) \qquad 4.24$$

where C_1 and C_2 are constants. It can be seen that the instantaneous

velocity profile of the flow is a simple parabaloid. Hence, the only effects of a harmonically varying pressure gradient in this case is to cause the amplitude of the velocity profile to be time dependent.

The foregoing analyses apply to Newtonian liquids. Blood, however, is non-Newtonian in behaviour, that is, its viscosity is a function of the rate of change of shear strain, which is called the 'rate of shear'. The relationships between shear stress and rate of shear for different types of fluid[45] are shown in figure 4.4. The non-Newtonian behaviour of blood is principally caused by the presence of the red cells,[45] which interact in different ways as the flow conditions change. The changes in the measured or apparent viscosity with flow conditions reflect these different interactions. The nature of the interactions is complicated[45] and not yet fully understood. The apparent viscosity is also a function[46] of the cell structure and haematocrit (i.e. cell concentration), and will therefore vary with different types of blood and also with different samples of one type where the haematocrit varies. Work is being done at present, principally on mammalian blood, to establish its rheological properties.[45] Mammalian blood is best described as a Bingham plastic with a small yield stress. For normal human blood the suggested[46] yield stress has a value of less than 0.1 dyne cm^{-2} and the experimental data on its flow properties are best fitted by the Casson equation. Figure 4.5 illustrates the variation of apparent viscosity of human blood with rate of shear.[46] This basic information is not yet available for avian blood, which differs from the mammalian type principally in that the red cell is nucleated. Both types of red cells are illustrated[3,4] in figure 4.6. In general

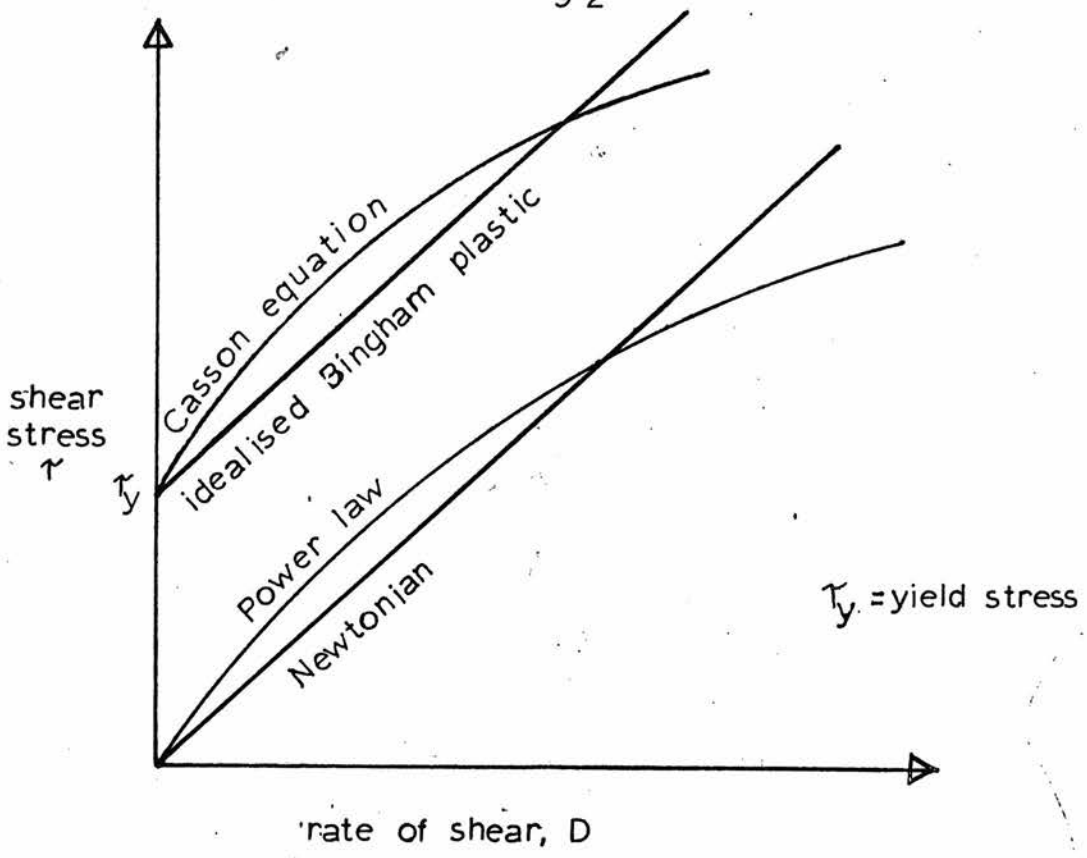

	type	apparent measured viscosity
	Newtonian	$\frac{\tau}{D}$
non Newtonian	Power Law	$\frac{\tau}{D^s}$, where s=constant
non Newtonian	Bingham	$\frac{\tau - \tau_y}{D}$
non Newtonian	Casson	$\frac{\sqrt{\tau} - \sqrt{\tau_y}}{D}$

figure 4.4. Flow curves of various types of material including the general equation for measured viscosity for each type.[45]

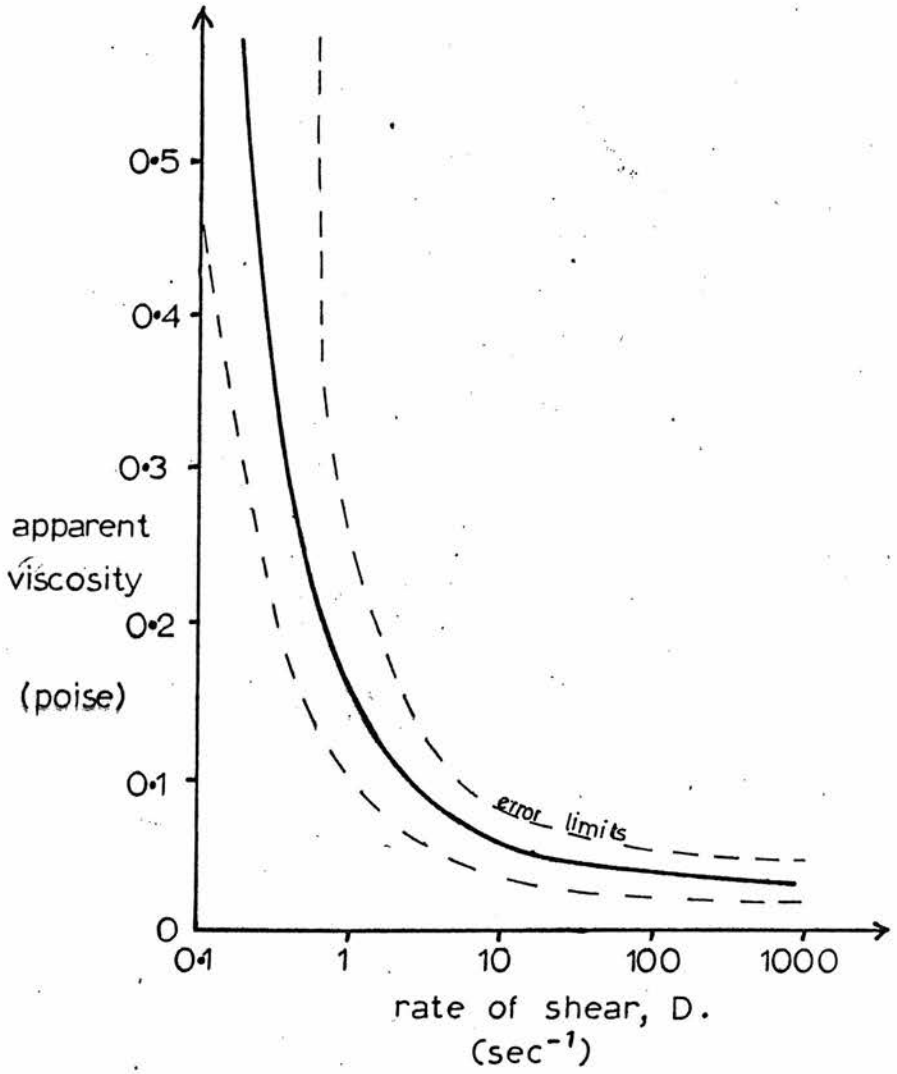

Figure 4.5. Variation of apparent viscosity of human blood[46] with rate of shear, plotted on the assumption that the viscosity of plasma is 0·012 poise.

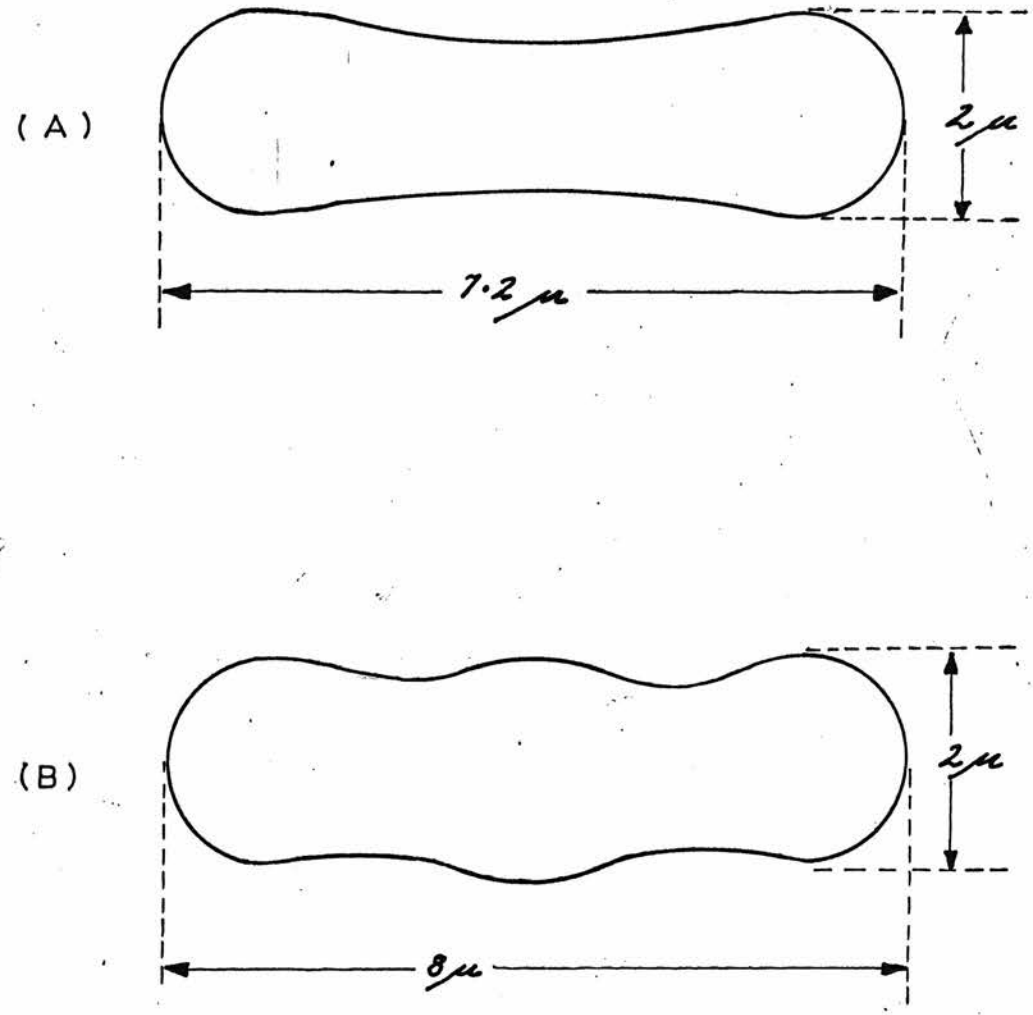

Figure 4.6. Diagrams of the average normal mammalian (A) and avian (B) red cells. (ref. 3&4)

because of the low level state of the theory, blood is considered as an approximately Newtonian fluid in convective heat transfer problems.

In the flowmeter application it is important that the flow pattern does not change to turbulent within the range of flow rates being measured. The transducer, located on the wall, is sensing the rate of deformation, $\frac{du}{dy}$, near the wall, which is reflected in the velocity profile. The measurements do not relate to volumetric flow unless the velocity profiles over the flow range are similar. The onset of turbulence and hence the critical Reynold's number, Re_c, must be reconsidered for a non-Newtonian suspension. Experiments reveal[50] that the onset of turbulence is a function of tube diameter and haematocrit. The value of Re_c is particularly sensitive to variations in tube diameter[51] in vessels with a diameter less than 0.6 mm. This results from the fact that the distribution of the red cells[52] over the tube cross-section is not uniform in laminar flow, rather there is a high concentration around the axis which decreases towards the wall until, at the wall, there is probably a cell-free zone of plasma. In small diameter tubes the cell-depleted zone occupies a greater percentage of the cross-sectional area of the tube with decreasing tube diameter, therefore the influence of this layer on Re_c increases with decreasing tube size and the value of Re_c increases.[50] The cell distribution[52] causes a deformation of the laminar flow velocity profile in the region of the tube axis. The profile is flattened[52] as shown in figure 4.1. The thickness of the cell-free layer was investigated by Vand,[53] who suggested a magnitude of $1.301 \times R_p$, where R_p denotes the radius of the suspended particle. Later workers[54] suggest that $0.7R_p$ is a more accurate figure and that

the "wall effect" is due to an inward radial displacement of particles caused by mechanical forces which are produced by the interaction of the fluid and the wall. For avian blood the cell-free layer is of the order of 1μm. The exact value of the critical Reynolds number in one millimeter diameter avian blood vessels is not known. However, providing that the pulsatile component of the flow is small, its minimum value can be assumed[48,50] to be 1000. The estimation of the value of the maximum flow rate, given in Chapter 1, is 2 ml/s. If this flow rate occurs in one vessel and if the values of viscosity and density are assumed[55] to be 0.03 poise and 1 g/ml respectively, then the corresponding maximum Reynolds number is 850. Hence, it is probable that the flow is laminar throughout the flow range involved.

Studies on inlet lengths after branches in canine blood vessels[49] reveal that for arterial vessels with a 0.6 mm diameter the distance required for streamline flow to re-establish itself is approximately 0.7 mm. It is reasonable to suppose that a disturbance in flow patterns due to the small discontinuity at a 1 mm diameter natural-artificial blood vessel join will disappear after a distance of several millimetres into the artificial tube. It is also probable that, in response to the discontinuity, proteins will be deposited in such a way as to minimise the discontinuity. If a 1 to 2 cm length of approximately straight artificial blood vessel is implanted, it is reasonable to expect that the flow pattern will be laminar in the region round the transducer when it is located in the middle of the length of tube. Considerable care must be taken in fitting the transducer into the wall in order to minimise the resulting discontinuity.

This point is considered in Chapter 5.

4.3 The heat transfer problem

In order to describe heat transfer at a solid-liquid interface, one further equation must be considered along with the Navier-Stokes equations (4.12) and the continuity equation (4.8). The required equation[44] for an incompressible fluid, known as the energy equation, is

$$\rho \frac{D(CT)}{Dt} = \frac{\partial}{\partial x}\left(k \frac{\partial T}{\partial x}\right) + \frac{\partial}{\partial y}\left(k \frac{\partial T}{\partial y}\right) + \frac{\partial}{\partial z}\left(k \frac{\partial T}{\partial z}\right) + \mu \Phi \qquad 4.25$$

where $$\frac{D}{Dt} = \frac{\partial}{\partial t} + u \frac{\partial}{\partial x} + v \frac{\partial}{\partial y} + \omega \frac{\partial}{\partial z}$$

and where T denotes temperature, k the thermal conductivity of the liquid and C its heat capacity. Φ denotes the dissipation function and is defined as the time rate of energy dissipated per unit volume due to the action of viscosity. For fluids of relatively low viscosity[44] experiencing velocities less than sonic velocity, the value of the dissipation function is negligible compared to the other terms in the equation. The problem of solving these equations while allowing for variation in the physical properties (ρ, C, k, μ) with temperature is so complex that it has so far defied analytical methods. The "isothermal solution" is therefore considered, in which the physical properties are assumed independent of temperature. With these approximations equation 4.25 becomes

$$\rho C \frac{DT}{Dt} = k\left(\frac{\partial^2 T}{\partial x^2} + \frac{\partial^2 T}{\partial y^2} + \frac{\partial^2 T}{\partial z^2}\right). \qquad 4.26$$

It is of interest to solve the equations for heat transfer at the blood-transducer interface in order to establish the parameters

which determine both the rate of flow of heat and the penetration depth of the thermal disturbance into the blood. However it is not possible to solve the transient heat transfer problem analytically, therefore the steady state case will be considered. The simplest case of laminar flow heat transfer in tubes was first solved analytically by Graetz.[56] As shown in figure 4.7, the velocity profile is fully developed and a length of the tube wall is maintained at a constant temperature, Tw, above the initial liquid temperature, T_L. The thermal boundary layer, δ_t, is the region in which an effective temperature gradient exists. Its limit is defined as the surface in the liquid at which the thermal disturbance has decreased to one precent of its maximum value. Assuming radial symmetry, the energy equation may be rewritten in cylindrical coordinates thus

$$u \frac{\partial T}{\partial x} = \frac{k}{\rho C}\left[\frac{1}{r}\frac{\partial}{\partial r}\left(r \frac{\partial T}{\partial r}\right)\right] \quad . \qquad 4.27$$

Since the flow is laminar and the velocity profile fully developed the Hagen-Poiseuille equation applies and equation 4.27 becomes

$$\frac{2\bar{u}}{R^2}\left[1-\left(\frac{r}{R}\right)^2\right]\frac{\partial T}{\partial x} = \frac{k}{\rho C}\left[\frac{1}{r}\frac{\partial}{\partial r}\left(r\frac{\partial T}{\partial r}\right)\right] \quad . \qquad 4.28$$

The solution[57] of this equation takes the form of an infinite series as follows

$$\frac{T(r)-T_L}{T_w-T_L} = \sum_{n=0}^{\infty} C_n \phi_n\left(\frac{r}{R}\right) \exp X' \qquad 4.29$$

where $$X' = -\beta_n^2\left(\frac{x}{R}\right) \Big/ \frac{\bar{u}L}{\alpha} \quad .$$

α is the thermal diffusivity of the medium and

$$= \frac{k}{\rho C} \quad . \qquad 4.30$$

C_n are coefficients, $\phi\left(\frac{r}{R}\right)$ are functions of $\left(\frac{r}{R}\right)$ determined by the boundary conditions and β_n are exponents determined by the boundary

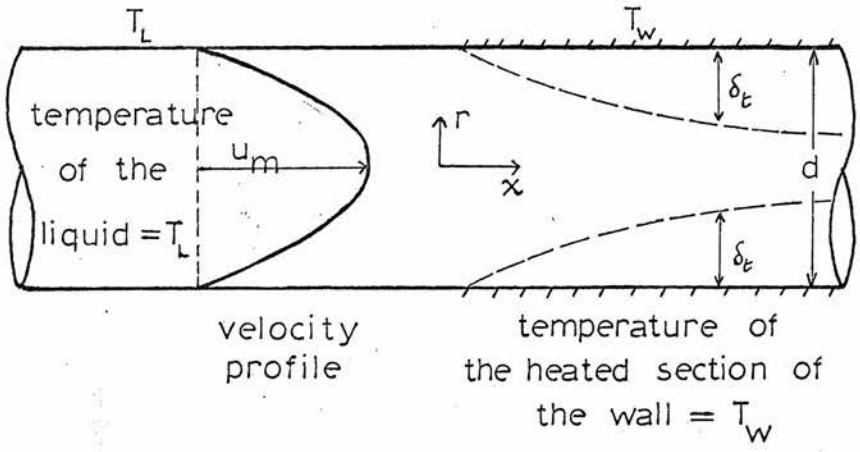

Figure 4.7. A diagram of the heat transfer problem solved by Graetz.[56]

conditions. Several workers[58,59] have contributed to this field by calculating some of the coefficients and functions. This equation illustrates that T(r) is a decreasing function of $\frac{x}{u}$ so that T(y) is an increasing function of $(\frac{x}{u})$.

The rate of flow of heat, q, at a solid boundary of surface area, A, is given by

$$q = hA(T_w - T_L)_{l.m.} \qquad 4.31$$

where h denotes the heat transfer coefficient and $(T_W - T_L)_{l.m.}$ denotes the logarithmic mean temperature difference. This equation is merely a definition of the heat transfer coefficient, so that the problem reduces to establishing a relationship for h. From the Graetz solution for the example discussed this is given[57] as

$$N_u = \frac{hd}{k} = \frac{\sum_{n=0}^{\infty} (C_n \phi_n'(1)/2) \exp X'}{2 \sum_{n=0}^{\infty} (C_n \phi_n'(1)/2\beta_n^2) \exp X'} \qquad 4.32$$

where $X' = -\beta_n^2 (\frac{x}{R}) / \frac{\bar{u}d}{\alpha}$.

N_u denotes the local Nusselt number. The first ten values of Cn, $\phi_n'(1)$ and β_n are given in reference 57 along with a graph of Nu versus $\frac{\bar{u}d^2}{\alpha x}$, which is reproduced in figure 4.8.

Sellars et al.[58] extended the analysis to consider the case of constant wall heat flux, and established the following relationship

$$Nu = \left[\frac{11}{48} + \frac{1}{2} \sum_{n=0}^{\infty} \frac{\exp X'}{\beta_n^4 \phi_n'(-\beta_n^2)} \right]^{-1} . \qquad 4.33$$

This is also shown on graph 4.8.

In more general situations, the heat transfer coefficient is evaluated from empirical formulae or formulae derived by approximate methods which apply to specific examples. A survey of the literature

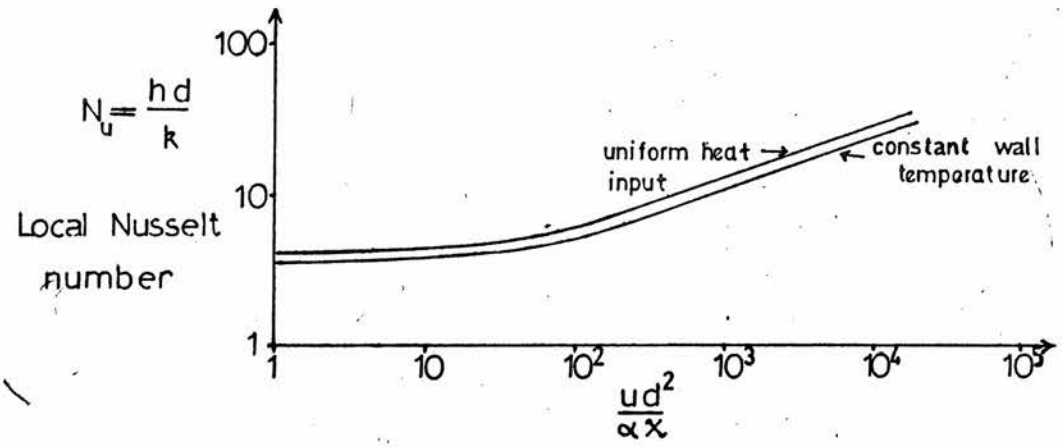

Figure 4.8. Graphs of the local Nusselt number for laminar flow in tubes.[57]

did not reveal any such formulae which could be applied to the conditions and dimensions of the blood-transducer problem. In this problem a small segment of the tube wall experiences an approximately linear increase in temperature with time from ambient temperature at time t_1, to some value, which is in part determined by the flow rate, at time t_2; whereupon the heat source is switched off and the segment cools to ambient. The heat energy dissipated at any time during this period is approximately inversely related to the segment temperature. Indirect measurements of the segment temperature are made at times t_1 and t_2. Initially, on the appearance of a temperature difference, the heat transfer mechanism into blood is conduction. When the penetration depth of the thermal disturbance is sufficiently large, the shape of the thermal boundary layer is determined by the velocity profile of the flow, that is, forced convection occurs. At time t_2 the relationship between x, $\bar{u}$ and h will have a similar form to the steady state examples above, that is, if $\frac{\bar{u}d^2}{\alpha x}$ is small, then conduction is the dominant heat transfer mechanism. Free convection may possibly contribute to a negligible extent. The value of h tends to a constant. As $\frac{\bar{u}d^2}{\alpha x}$ increases, so forced convection plays a more significant role, until at high values of $\frac{\bar{u}d^2}{\alpha x}$ forced convection is the dominant mechanism. Under these conditions h is an increasing function of $\frac{\bar{u}d^2}{\alpha x}$. For the steady state examples given, forced convection operates when the mean velocity is approximately given by

$$\bar{u} \doteq 6 \times 10^{-3} \frac{x}{d^2} \quad cm/s \quad , \qquad 4.34$$

where α blood = 1.44×10^{-3} cm^2/s. (from Table 5.1)

The penetration depth of the thermal disturbance into the blood

achieves a maximum value when conduction is the dominant heat transfer mechanism. The depth is a function of time and the fluid properties. When forced convection operates the penetration depth achieved in time t_1-t_2 is also an increasing function of $\frac{x}{u}$ as in the Graetz problem.

Now, from equation 4.31, the rate of flow of heat, q, from the surface is a function of both h and ΔT where, in this example, q and ΔT are dependent variables. In the practical case of heat transfer from the surface of a body whose central region is maintained at a constant temperature difference, $\Delta T'$, above ambient temperature, the relationship between q and u is contained in the empirically derived dissipation factor, K(u), of the body. That is,

$$K(u) = \frac{q}{\Delta T'} = \frac{h A \Delta T}{\Delta T'}$$

where K(u) is measured under steady state heat transfer conditions. The change in K caused by variations in u can be seen to be essentially dependent on the consequent change made in h. The variation of the heat transfer coefficient with velocity at time t_2 is similar to the equivalent steady state relationship, therefore $K^1(u)$, the dissipation factor at t_2 which is used in Chapter 1, is similar to the steady state relationship K(u). The dissipation factor tends to a constant value at high flow velocities because the temperature difference between the surface and the fluid tends to zero. Hence, variations in the value of the heat transfer coefficient with velocity do not significantly alter the value of the rate of flow of heat in the high velocity region. The upper limit of the mean velocity which affects the value of the dissipation factor is a function of the geometry and

dimensions of the device. In the thin film case, where

$$h = f\left(\frac{\bar{u}}{x}\right) \qquad 4.35$$

assuming d and α are constant, the upper limit of the velocity which affects the value of the dissipation factor is a function of the length of the device in the streamwise direction. Hence the length, x, of the device determines the range of velocities over which the device is sensitive in the flowmeter application.

In the case of blood flow the presence of the red cells must be considered. They will participate in the transient heat transfer process since the thickness of the cell-free layer at the transducer is only of the order of 1μm. Bellhouse[61] found that measurements of the heat transfer from identical constant temperature probes in plasma, packed red cells, and water produced identical results. Therefore,the possibility of varying concentrations of red cells in the region around the transducer does not appear to introduce significant error due to variation in the thermal diffusivity of the medium. This is further supported by the fact that a manufacturer[62] of a steady state heat transfer blood flowmeter recommends calibrating his instrument in water. This transducer consists of a metal film deposited round a 1 mm diameter bead which is placed on the tip of a catheter.

The effect of temperature variations on blood viscosity and yield stress is uncertain. A decrease in apparent viscosity of 1%/^{o}C rise has been reported.[47] However, it is not yet clear as to the relative importance of temperature effects on plasma and on the physical properties of the red cells. Merrill et al.[63] concluded that the yield stress is generally unaltered by temperature variations.

Temperature variation of the blood vessel wall within the range envisaged does not in itself appear to promote blood clotting. Studies of the effect of heat on human erythrocytes reveal that above a critical temperature the cell may be damaged irreversibly. The extent of the damage is proportional to the temperature rise and to the time of exposure. A temperature rise of $10^{\circ}C$ over a period of 12 s was found to produce hemolysis of between 0 and 0.3%. It is probable that the erythrocyte damage will be negligible as a result of heating blood by $10^{\circ}C$ over a period of the order of 10 ms. This temperature rise is adopted as the maximum permissible value.

4.4 Conductive heat transfer

So far the discussion has concerned heat transfer into the liquid. The basic theory of heat transfer to the substrate will now be considered. It is of interest to establish the relationship for rate of heat flow into a solid in terms of the physical constants and geometry of the solid, and also to establish the relationship for the penetration depth of the thermal disturbance in the same terms.

Using the principle of conservation of energy, the heat generated, Q_1, in a volume element of solid, dV, in the time interval, dt, equals the sum of the heat leaving the element across its boundaries, Q_2, and the heat stored within the element, Q_3, both in the time interval dt.

That is $$Q_1 = Q_2 + Q_3 \qquad 4.36$$

where $$Q_2 = -k \nabla^2 T \, dV \, dt, \qquad 4.37$$

$$Q_3 = \rho C \frac{\partial T}{\partial t} \, dV \, dt . \qquad 4.38$$

For the case of no internal heat generation, that is where $Q_1 = 0$, one

obtains the following expression on substituting equations 4.37 and 4.38 in 4.36.

$$\alpha \nabla^2 T = \frac{\partial T}{\partial t} \quad . \tag{4.39}$$

Consider the one dimensional heat transfer case of a rectangular solid shown in figure 4.9. Its thickness is semi-infinite and the sides are perfectly insulated. Let its exposed surface area, A, experience a step rise in temperature from an initial temperature, T_i, to a temperature T_W at time t = 0.

The integration of equation 4.38 with the above boundary conditions can be shown to have the form[65]

$$\Theta = \Theta_i f(H) \tag{4.40}$$

where $\Theta = T - T_w$ and $\Theta_i = T_i - T_w$

and $f(H) = \frac{2}{\sqrt{\pi}} \int_0^H e^{-H^2} dH$ where $H = \frac{x}{2(\alpha t)^{1/2}}$.

The function f(H) is known as Gauss's error integral, and its values are tabulated in reference 60.

The heat flow in the x-direction becomes

$$q = -kA \frac{\partial \Theta}{\partial x} = -kA \frac{\partial \Theta}{\partial H} \cdot \frac{\partial H}{\partial x}$$

$$= \frac{-kA\Theta_i \exp(-x^2/4\alpha t)}{(\pi \alpha t)^{1/2}} \quad . \tag{4.41}$$

For unit temperature rise and x = 0, the heat flow into the surface of the block at time instant t, when t > 0, is

$$q = -kA/\sqrt{\pi \alpha t} \quad . \tag{4.42}$$

The heat energy, Q, which has entered the block through the surface in time t is

$$Q = -kA\, 2\sqrt{\frac{t}{\pi \alpha}} \quad . \tag{4.43}$$

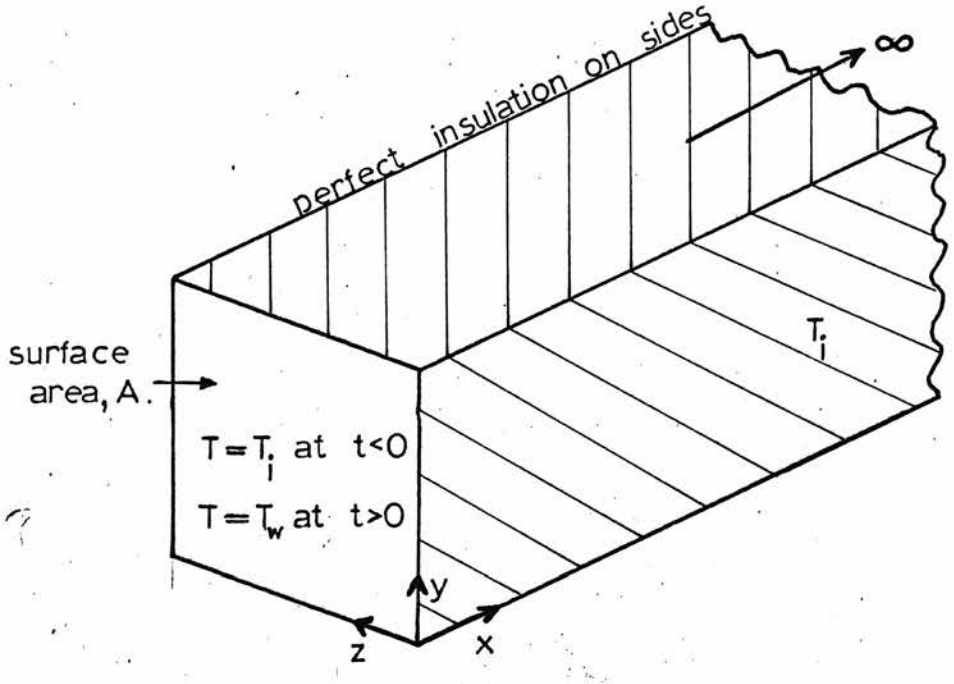

Figure 4.9. A diagram of the semi-infinite solid with an exposed surface and perfectly insulated sides.

For unit time and substituting equation 4.30 in 4.43, ~~it~~ 4.43 becomes

$$Q = -\frac{2}{\sqrt{\pi}} A \sqrt{\rho C k}. \qquad 4.44$$

Equation 4.44 describes the heat energy which flows into a solid with insulated sides and a semi-infinite dimension in one direction for unit temperature rise on its exposed surface in unit time measured from t = 0.

The criterion in selecting the substrate material and the material for the conductor tracks from the heat transfer viewpoint is to minimise their effectiveness as heat sinks and, thus, maximise the fraction of the heat generated which flows into the liquid. By applying equation 4.44 it is possible to assess the suitability of different materials as substrates and as conductor tracks. An indication of the relative magnitudes of heat flow into the substrate, liquid and conducting tracks can also be obtained by comparing their relative values calculated from equation 4.44. Thus

$$Q_{LIQUID} : Q_{SUBSTRATE} : Q_{\substack{ELECT. \\ TRACK}} = A_L\sqrt{\rho_L C_L k_L} : A_S\sqrt{\rho_S C_S k_S} : A_T\sqrt{\rho_T C_T k_T} \quad . \qquad 4.45$$

The application of this equation to the liquid case introduces the assumption that conduction is the only heat transfer mechanism in the liquid. This assumption will result in an underestimate of the heat flow into the liquid. Further errors arise in applying the one dimensional analysis when three dimensional heat transfer is, in fact, occurring. However, a useful estimate of the relative heat flows is obtained from a situation that is mathematically complex.

In the above analysis the media are considered semi-infinite in one direction. This assumption is valid provided their thicknesses are of such a value that they appear semi-infinite during the period

of the applied thermal disturbance.

Consider equation 4.40 which states

$$\frac{T - T_w}{T_i - T_w} = f\left(\frac{x}{2\sqrt{\alpha t}}\right) .$$

When the function $f\left(\frac{x}{2\sqrt{\alpha t}}\right)$ equals unity, then $T = T_i$

This occurs[60] when $\frac{x}{2\sqrt{\alpha t}} = 2$

Therefore the distance $x = 4\sqrt{\alpha t}$ 4.46

defines the limit of the effect of the thermal disturbance created by a step rise in temperature at x = 0 at time t = 0 assuming no heat loss in the y- and z-directions. Providing the thickness of the medium is greater than $4\sqrt{\alpha t}$, it can be considered semi-infinite for the purposes of this analysis.

Apart from the mathematical difficulties of attempting a more rigorous analysis of the heat transfer problem, there are also practical problems of establishing the exact physical system when blood is used. This results from the interaction of blood with the vessel walls. A protein layer[66,67] will probably be deposited from the blood on the surface of the walls and transducer and there may be some deposit of fibrin produced by the clotting reaction in response to any discontinuity in the blood vessel wall. Because of the uncertainty of the exact reaction to each individual implant, it is advisable to check the calibration of the instrument in vivo after measurements have been made.

Chapter 5

TRANSDUCER PRODUCTION

5.1 Thermistor location

The transducer is required to be in contact with the blood in a fixed orientation in the blood vessel. This may be achieved by mounting it on the wall of an artificial blood vessel which is then implanted in the bird, or by mounting it on a hypodermic needle which is inserted through the wall of the natural blood vessel. The principal advantage of the wall mounting method is that the position of the transducer with respect to the flow profile is fixed, so that there is no possibility of error in the volumetric flow measurement due to variations in position as in the case of the needle mounted transducer. Further, there is no possibility of the wall mounted device occluding the blood vessel. However, there is a greater possibility of a significant deposition of proteins from the blood onto the transducer when it is located on the wall, than when it is in the mid-stream position where deposits tend to be washed off by the flow. The wall mounting method is employed in this work so that the flowmeter can be used in small-diameter vessels. The lower limit on vessel diameter is now imposed by the surgical problems of implanting the artificial section.

In the proposed arrangement the thermistor, the conducting tracks and the bonding pads are deposited on a flat substrate as shown in figure 5.1. Figure 5.2 shows the thermistor implanted in the wall of the artificial blood vessel, which is made of silicone rubber. The thermistor is inserted in the wall at a distance of approximately 1 centimetre downstream from the join so that the

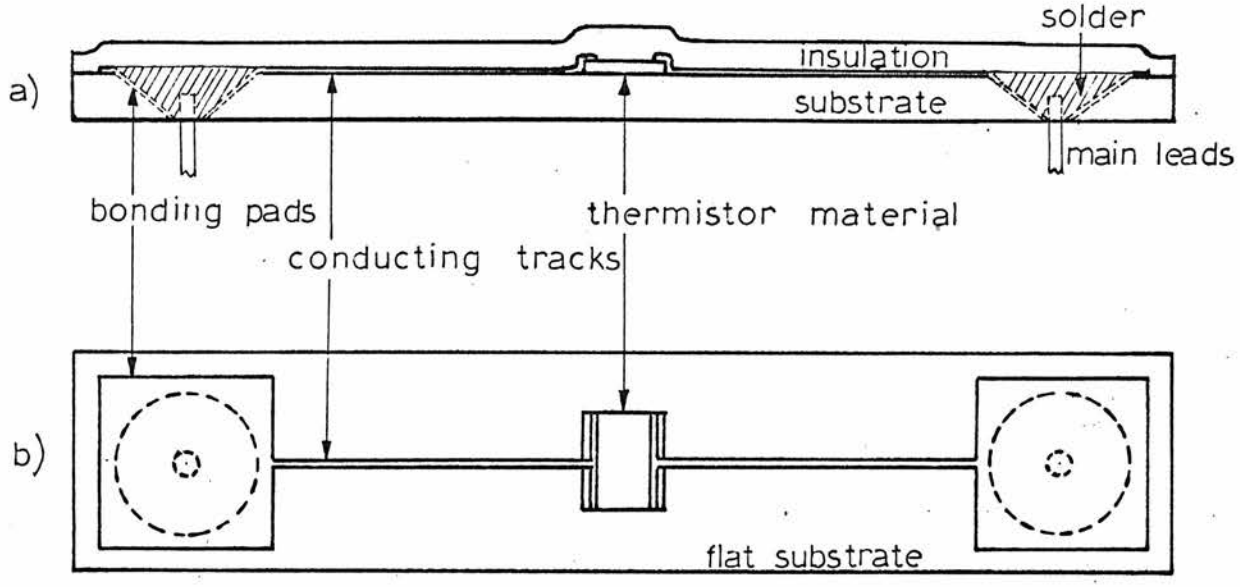

Figure 5.1. Diagram of the transducer (not to scale)
a) elevation b) plan.

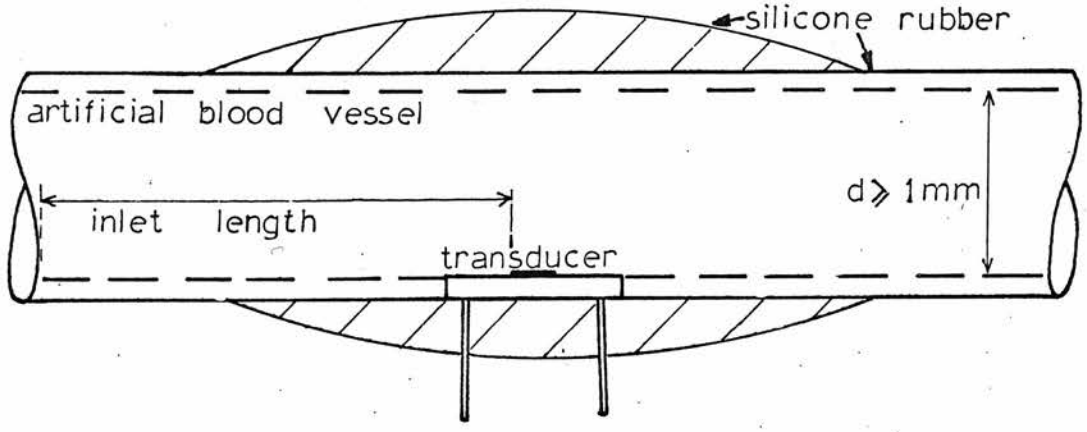

Figure 5.2. Diagram of the transducer located in an artificial blood vessel wall.

disturbances in the flow pattern created at its inlet decay before they reach the thermistor.

In this chapter the design decisions are outlined, the production steps detailed and the characteristics of the final device described. Table 5.1 summarises the values of the physical constants and equations which are referred to in this chapter. A value for the thermal conductivity of thermistor material was not found in the literature. The value quoted is an estimate based on the values of the thermal conductivities of the individual oxides. The units used are those most commonly found in the literature.

5.2 Substrate

The substrate is required to be biologically inert and to give mechanical support to the thermistor and leads without acting as a heat sink. Corning 7059 glass and mica were examined to establish their suitability from the fabrication viewpoint. The sputtered film on mica cracked severely on cooling after deposition. This suggests the presence of thermal stresses at the film-mica interface. Hence mica was rejected. An 1 mm thick Corning 7059 microsheet glass is used as the substrate. 1 mm diameter holes are drilled in the substrate in the area where bonding pads are to be deposited. The holes are then countersunk and polished. This operation is achieved by using a dental drill with a standard 1 mm diameter spherical burr and a conical shaped brass burr whose surface is covered with cloth impregnated with abrasive powder.

The surface areas of the film-substrate interface and the film-blood interface are approximately the same, so that the ratio of heat energy transferred to the substrate and to the blood is indicated by

material	density ρ ($g.cc^{-1}$) 37°	specific heat C ($cal.g^{-1}.°C^{-1}$)	thermal conductivity k ($cal.cm^{-1}.s^{-1}.°C^{-1}$)	thermal diffusivity $\alpha = \frac{k}{\rho C}$	kinematic viscosity ν ($cm^2.s^{-1}$)	relative heat flow $\sqrt{\rho C k}$ (equn. 4.4.4)	penetration depth $x = 4\sqrt{\alpha t}$ (cm) (equn. 4.4.6) t = 100 ms	t = 30 ms
water	0·993 (1)	0·998 (1)	$1·51\times10^{-3}$ (1)	$1·52\times10^{-3}$	7×10^{-3} (4)	$3·87\times10^{-2}$	$4·93\times10^{-2}$	$2·7\times10^{-2}$
plasma	1·026 (1)	0·94 (1)	$1·43\times10^{-3}$ (3)	$1·48\times10^{-3}$	146×10^{-3} (4)	$3·72\times10^{-2}$	$4·88\times10^{-2}$	$2·65\times10^{-2}$
blood	1·060 (2)	0·86 (2)	$1·31\times10^{-3}$ (3)	$1·44\times10^{-3}$	38×10^{-3} (4)	$3·46\times10^{-2}$	$4·8\times10^{-2}$	$2·6\times10^{-2}$
Corning 7059 glass	2·76 (5)	0·2 (5)	3×10^{-3} (5)	$5·44\times10^{-3}$	—	$4·06\times10^{-2}$	$9·34\times10^{-2}$	$5·1\times10^{-2}$
thermistor material	4·5 (6)	0·17 (6)	4×10^{-3} (1)	$5·3\times10^{-3}$	—	$5·5\times10^{-2}$	$9·2\times10^{-2}$	$5·05\times10^{-2}$
gold	19·282 (1)	0·031 (1)	0·705 (7)	1·18	—	$6·49\times10^{-1}$	1·375	0·75
P.T.F.E.	2·15 (8)	0·25 (8)	6×10^{-4} (8)	$1·12\times10^{-3}$	—	$1·8\times10^{-2}$	$4·23\times10^{-2}$	$2·3\times10^{-2}$

Table 5.1. The physical properties of the relevant materials with associated calculations. (references in brackets)

the ratio

$$\sqrt{\rho C k}_{glass} : \sqrt{\rho C k}_{blood} = 4{\cdot}06\times10^{-2} : 3{\cdot}46\times10^{-2},$$

which was developed in Chapter 4. Hence the substrate does not act as a heat sink. The application of this ratio assumes that the substrate is thick enough to be regarded as a semi-infinite medium. In order to calculate from equation 4.46 the penetration depth of the step thermal disturbance in the substrate, it is first necessary to estimate the duration of the heating pulse. This is achieved by assuming that the maximum permissible penetration depth into the blood is equal to the blood vessel radius, 0.5 mm. The time required for the thermal disturbance to travel this distance in blood is given by equation 4.46, using the values listed in Table 5.1, as 100 ms. Hence, the penetration depth into the substrate in 100 ms is 0.093 cm, which is comparable to the actual thickness, so that the substrate can be regarded as semi-infinite in the heat transfer context.

5.3 Geometry of the Thermistor Material

It is necessary to use a thermistor whose resistance is small in order to maximise the Joule heating it experiences. Both the resistivity and the geometry of the thermistor material are significant independent parameters controlling its accuracy as a flowmeter transducer. The resistivity is directly related to the B-value as shown in figure 3.12, so that a high temperature-coefficient of resistance implies a high resistivity. For example, the resistivity of the film whose temperature coefficient is -4%/^{o}C is 600Ω-cm. Considering the thermistor material dimensions, the length in the streamwise direction, x, determines the flow range over which the

transducer is sensitive. As discussed in section 4.3, a small value of x/d^2 is necessary to detect low flow rates, and the maximum velocity that can be detected is an increasing function of x. It is not possible to calculate the required length; however, an estimate can be made by considering the overall dimension of the flow system. A value of the same order of magnitude as the tube radius is selected. For a vessel with a radius of 500μm, the length chosen is 250μm. A total length of 350μm is in fact used in order to accommodate the conducting tracks. The thickness of thermistor has a practical upper limit imposed by the time taken for deposition. At deposition rates of the order of 100Å/minute, thicknesses of the order of 1μm are practical in the present non-automatic deposition system. A film thickness of 2.4μm, which is deposited in 4 hours, is used. The maximum width of the thermistor is defined by the diameter of the tube and by the discontinuity which can be tolerated at the substrate-tube join. A thermistor width equal to 1/6th of the circumference of the tube is arbitrarily adopted as the maximum value. This produces a step of 0.15r at the join, where r is the tube radius. Using this criterion for a 1 mm diameter tube, the maximum thermistor width is 500μm. The resistance of a thermistor at temperature T with these dimensions is $(21 \times 10^3 \times \rho_T)\Omega$, where ρ_T is the resistivity of the device at temperature T.

A compromise is necessary between resistance and B-value and is achieved by estimating the power required for a particular temperature rise in the thermistor at the trailing edge of the heating pulse. In estimating the power required in the transient mode of operation, the thermal capacity of the thermistor material, substrate and blood

must all be considered, so that the power required is greater than suggested by an assessment based on steady-state heat transfer examples. Hence, it is first necessary to estimate the volumes of the materials involved. For a heating pulse width of 30 ms the penetration depths of the thermal disturbance can be calculated from equation 4.46 as 0.026 cm and 0.051 cm in the blood and substrate respectively. 30 ms is chosen to produce a reasonable penetration depth into the blood, that is, a value equal to approximately half the tube radius. Now, assume that the volumes of blood and substrate which require to be raised in temperature equal 250 x 500 x 260 μm^3 and 250 x 500 x 510 μm^3 respectively. The power required to raise the temperature of the 3 volumes by $1^{o}C$ in 30 ms can be calculated using the data shown in table 5.1, and is approximately 4 mW. An insulating film covering the device will also require to be heated. However, in this approximate calculation it is assumed to be sufficiently thin to be neglected. Now, the variation of the B-value and temperature coefficient with resistance for a sputtered thermistor with the above geometry at $25^{o}C$ is shown in figure 5.3. The points plotted are calculated from the data shown in figure 3.12 (B-value versus resistivity of sputtered films at $25^{o}C$). The power dissipated in a resistor for a 6V supply is also shown. Hence, if 4 mW is required for a temperature rise of $1^{o}C$ and the temperature rise required lies in the range $1^{o}C$ to $10^{o}C$ then, from figure 5.3, the resistance must lie in the range 9KΩ to 0.9 KΩ. The temperature coefficients, from figure 5.3 range between $1.9\%/^{o}C$ and $1.5\%/^{o}C$. Now a large change in the thermistor voltage pulse is required so that a temperature rise of around $10^{o}C$ and hence a 15% change in the

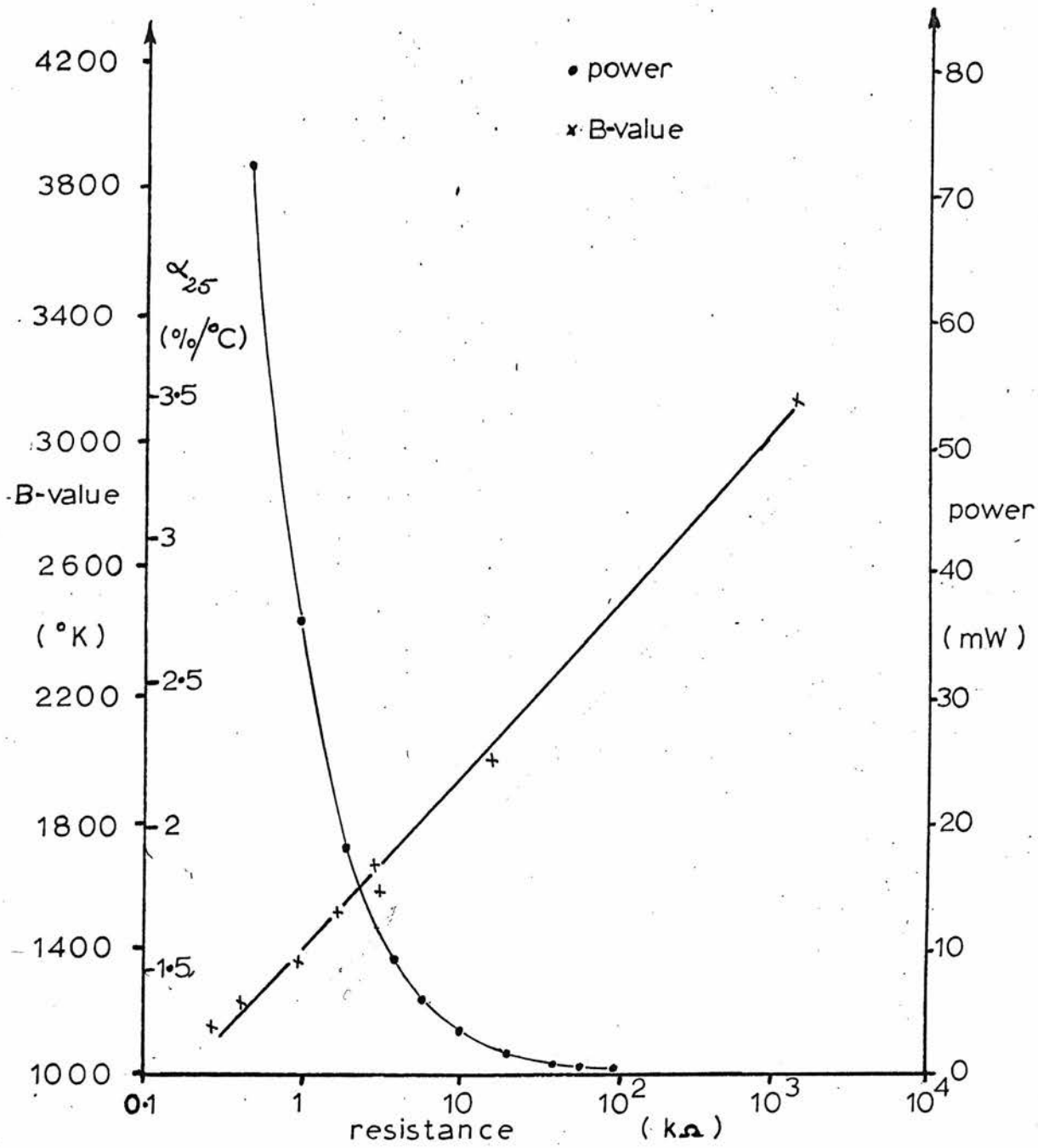

Figure 5.3. A graph of resistance versus B-value for sputtered thermistors with the dimensions 250μ × 500μ × 2·4μ at 25°C, and a graph of power dissipated in a resistor versus resistance for a 6V supply.

voltage is desirable. The optimum thermistor resistance and B-value is therefore around 1 KΩ at 25°C and 1350°K respectively. At the deep body temperature of the bird the B-value can be increased to approximately 1500°K. These values are, of course, only rough estimates because of the approximate nature of the calculations. They suggest that a resistivity of around 0.5Ω-cm is required and, from figure 3.5, is produced by D.C. sputtering in an argon/oxygen atmosphere in the ratio 3:1. This value of temperature coefficient is low for transition metal oxide thermistors. It is, however, still an order of magnitude higher than the values for metal films and is therefore worth pursuing.

The thermistor material is deposited over the substrate surface and the required shape is obtained using standard photo-etching techniques.[75] Two etches were found to dissolve the three oxide mixture. A 1N solution of ferric chloride at a temperature of around 60°C etches at the rate of approximately 100Å/minute and concentrated hydrochloric acid (10N) etches at the rate of 100Å/s. However the photoresist, which protects the required area, is also attached by the acid. Extra process steps must be added to overcome this problem with the result that the time required for etching is approximately the same in both cases. Both etching techniques have been used in different thermistor production runs.

Out of contact masks made of copper plated with nickel were considered for use during the film deposition as an alternative to the photo-etching process. However the resistivity of the thermistor material altered, which suggests that the masks are a source of contamination.

5.4 Leads

An evaporated nichrome-gold film is used for the conducting tracks. These materials were selected because an evaporation plant specifically for them was available.

Considering the relative abilities of the device materials to conduct heat, shown in table 5.1, it can be seen that the cross-sectional area of the tracks must be very much less than the surface area of the thermistor material in order that the tracks do not constitute a heat sink. They must also be sufficiently long to ~~effectively~~ (thermally) isolate the thermistor material from the bonding pads. From equation 4.46, which applies to a semi-infinite medium experiencing a step temperature rise on its surface, the penetration depth of the thermal disturbance can be evaluated as 0.75cm after 30ms. This represents the length of track between the thermistor and pad for thermal isolation for the worst case condition of no heat loss from the sides of the track. In the practical case, with heat loss and an approximately linear temperature rise a track length of 0.2cm is found to be sufficient. The bonding pad dimensions are chosen to facilitate the bonding operation. A square with 2mm sides is used.

Under ideal production conditions a track width of 1μm can be achieved. However, in the practical situation where relatively long tracks are required, the failure rate due to pinholes in the film is high. Therefore a track width of 25μm is chosen to ensure a good yield. The thickness of the track must be relatively large to ensure that the film is continuous over the step at the edge of the thermistor material. A value of 5000Å has been found to be

suitable. The sheet resistivity of such a film was measured as 0.04 Ω/square so that the tracks contribute a series resistance of 6.4Ω, which is insignificant.

A diagram of the dimensioned thermistor is shown in figure 5.4. The relative flow of heat along the conducting tracks and into the blood and substrate can be assessed by using equation 4.44. The evaluated expressions shown in figure 5.4 demonstrate that approximately 0.4% of the heat to the fluid flows to the tracks.

The tracks are produced by evaporating a 1000Å nichrome film, then 4000Å of gold, over the etched thermistor material and substrate surface. This operation is carried out with the substrate heated to 300 ^{o}C. (The thermal profile of the heating cycle is shown in figure 5.5). The nichrome film and the high temperature are necessary for good film adhesion. In an argon atmosphere at a pressure of 10^{-6} torr an electron beam gun is used to heat the crucible containing the evaporant. The nichrome film growth rate is typically 2 to 3 Å s^{-1} and the gold growth rate 20Å s^{-1} when the beam gun power supply delivers 50mA at 4kV.

The high substrate temperature necessary for good adhesion may cause the resistivity of the thermistor material to alter. The results of tests carried out to evaluate the change show that the resistivity of films whose original value is 0.5Ω-cm can increase by up to 50% of the original value. The change is not predictable within this limit. In an attempt to overcome the problem, the thermistor material was sputtered on to the gold tracks. However, this proved unsuccessful because the relatively high arrival energy of the sputtered atoms caused them to penetrate

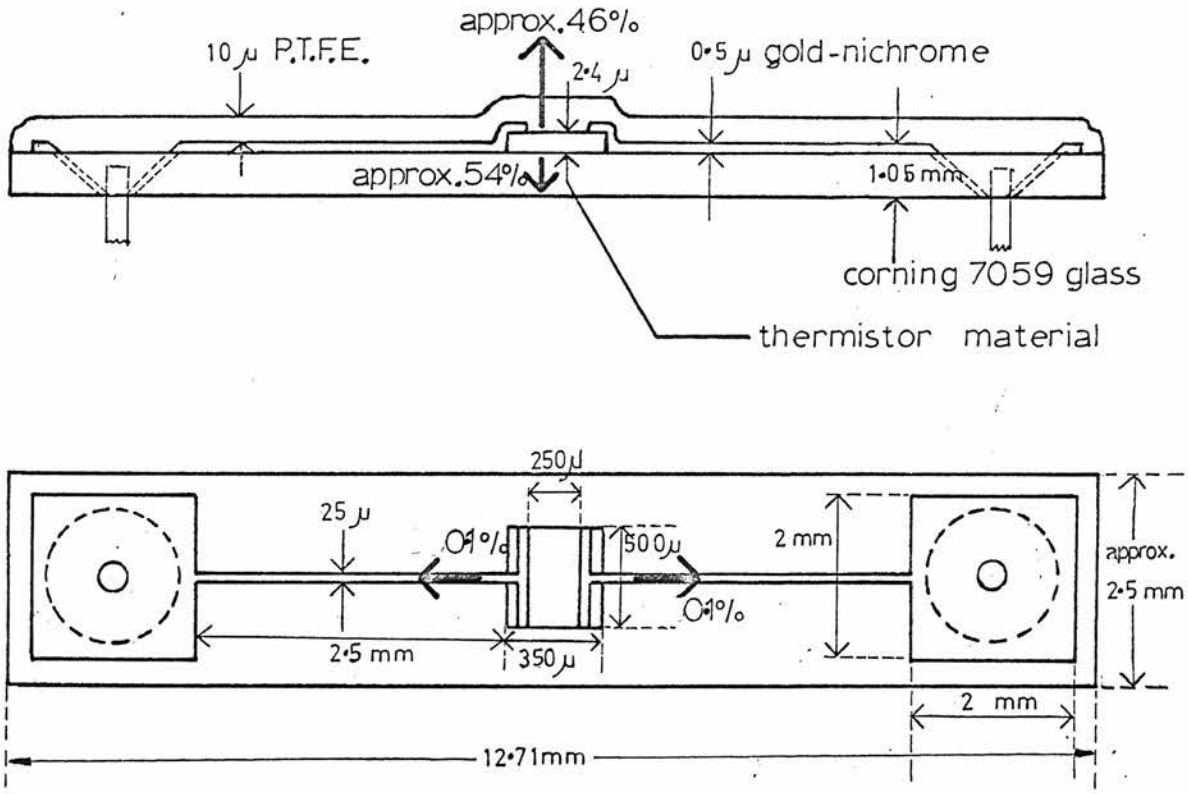

Figure 5.4. A diagram of the thin-film thermistor.

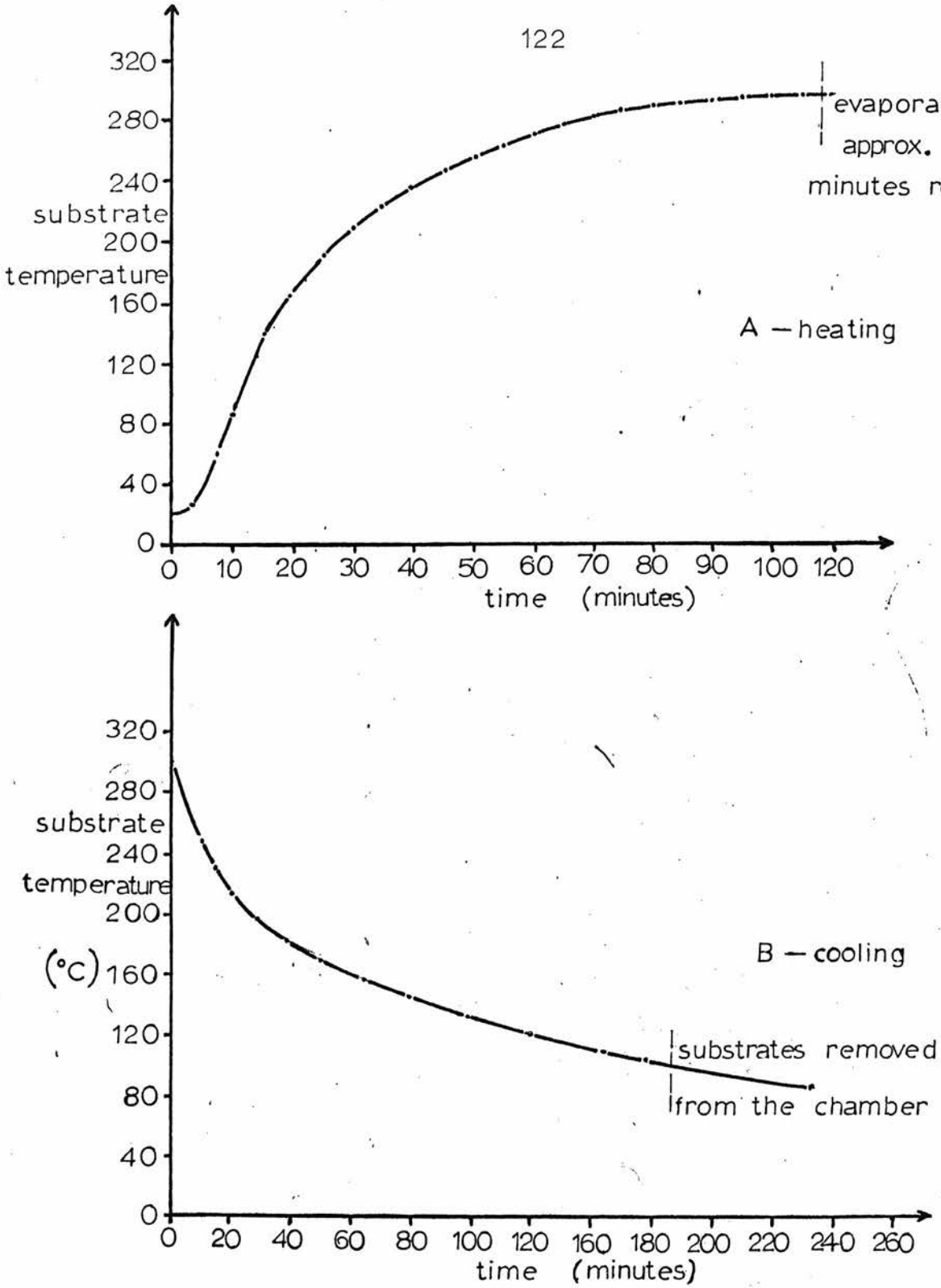

Figure 5.5. A profile of the substrate temperature while in the evaporation chamber.

the gold film, thereby creating pinholes through which the thermistor etch attacked the nichrome.

The gold is etched to the required shape using standard photo-etching techniques. A solution of 1 g of iodine crystals and 3 g of potassium iodide in 20 ml of distilled water is used at room temperature. The nichrome etch is composed of 1 g of ceric sulphate dissolved in 5 ml of concentrated nitric acid. This solution is diluted by a factor of 10 and used in the temperature range 50° to 60°C. Neither of these etches significantly attacks the thermistor material.

Eight thermistors are produced on a 1" by ½" substrate which is sliced up using a diamond saw with a 0.05 cm blade. 16 s.w.g. enamelled copper wire is inserted into the bonding pad holes through the back of the substrate and soldered to them in such a way as to produce a flat front surface. High temperature solder (melting point 301°C) is used to reduce the possibility of the solder re-melting when the insulation is deposited. Surface protusions at the pads, which would disturb the flow pattern, are removed with a fine needle file and fine emery paper. The mechanical strength of this arrangement is enhanced by glueing the wire to the back of the substrate with Araldite. A diagram of the production stages, figure 5.7, is included in the appropriate section.

5.5 Insulation

An electrically insulating film is required over the device surface. Several criteria must be considered in the selection of the film material. A high dielectric strength is necessary to

minimise the film thickness in order to maintain a fast thermal response time. The material must be impermeable to the ions present in the blood; further, it must be durable, non-toxic and anti-thrombogenic. Considerable research has been carried out to find a material which satisfies the final criterion, however a clear solution is not yet available. Two materials, quartz and P.T.F.E., both of which have been used previously in biological environments, were examined for use in this application.

Films of quartz and P.T.F.E. of various thicknesses were deposited by R.F. sputtering on substrates which were partially coated with a 0.5 μm film of nichrome-gold. By examining the film breakdown voltage in a IN saline solution it is possible to assess their dielectric strength and/or permeability to sodium ions. A diagram of the substrates and apparatus used is shown in figure 5.6 together with the results. The films are deposited in an argon atmosphere with a sputtering power of 80W, a chamber pressure of 5×10^{-3} torr and a magnetic field current of 3.5A. The deposition rates of quartz and P.T.F.E. are 0.3 $\text{Å}s^{-1}$ and 20$\text{Å}s^{-1}$ respectively. The adhesion of P.T.F.E. is good, and of quartz excellent. The results indicate that sputtered quartz is permeable to sodium ions when the applied voltage is approximately -2V. Sputtered P.T.F.E., on the other hand, is impermeable to sodium ions and exhibits a dielectric strength which is approximately similar to that of the bulk material. Calculations of the dielectric strength of the films are approximate because breakdown occurs at the step, where the film thickness is less than the measured value. P.T.F.E. is therefore selected for use as the device insulation. It satisfies[76]

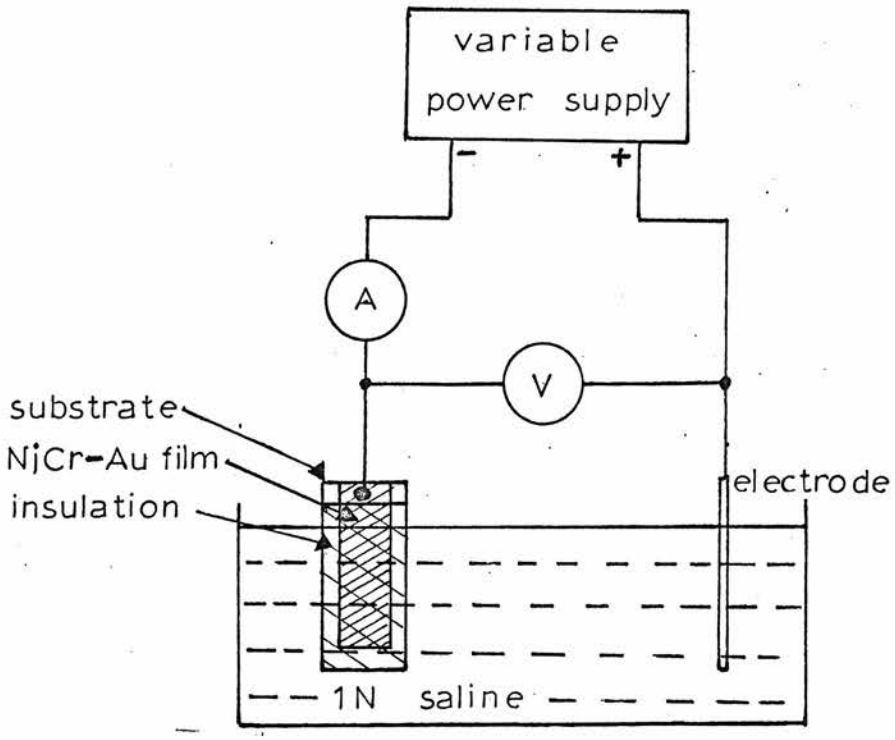

P.T.F.E.		SiO_2	
thickness (μ)	approx. breakdown voltage (V)	thickness (μ)	approx. breakdown voltage (V)
2·5	7	0·2	2
5	10	1	2
10	17	3	2

dielectric strength of bulk P.T.F.E. ≑ 2×10^6 V/m (ref. 74)
" " " P.T.F.E. film ≑ $1{\cdot}7 \times 10^6$ V/m
(10 μ sample)

Figure 5.6. The apparatus used to examine materials as insulation for the device, together with the results.

the toxicity and durability conditions and it is also anti-thrombogenic in this type of application.

The sputtering power employed in depositing the insulation is limited by the melting point of the solder. The limit is partly determined by the quality of the thermal contact between the substrate and the water cooled anode. A silicone paste with a high thermal conductivity is used at the substrate-anode interface to ensure effective thermal contact. The paste, Eccotherm TC-4, exerts a negligible effect on the vacuum down to the system's ultimate pressure, and does not decompose even when the relatively high power levels of around 300W are used. With this arrangement the maximum input power is found to be 80W with a chamber pressure of 5×10^{-3} torr and a magnetic field current of 3.5A in an argon atmosphere.

The maximum voltage to be applied across the thermistor in the flowmeter application is 12V, hence the insulating film must be capable of withstanding 6V. Further, the step of 2.4μm on the device surface causes a thinning of the insulation over the step, therefore a thicker film than suggested by the above results is required. A film thickness of 10μm was found to be sufficient. The dielectric breakdown of the insulation on the device was measured in blood and found to be around 10^{6} Vm^{-1}. The transit time of a step rise in surface temperature through such an insulating film can be calculated from equation 4.46 and is 12μs. Surface discontinuities in the region of the bonding pads may be of such a size as to require a thicker layer of insulation. This can be readily achieved by shielding the central area and depositing

more P.T.F.E. over the pads. A visual examination of the pads was found to be sufficient to establish if this is necessary.

A useful estimate of the minimum power required in the flowmeter application can be evaluated by considering the thermal capacity of the thermistor block, the gold on it and the insulation covering it. This total volume must experience the temperature rise before heat is transmitted into the blood. The thermal capacity of the total volume is

$$(\rho CV)_{thermistor} + (\rho CV)_{gold} + (\rho CV)_{insulation} = 3.6 \times 10^{-6} \text{ joules}/^{\circ}C .$$

It represents the heat required to raise the temperature of these components by $1^{\circ}C$. If the duration of the heating pulse is 100ms the power required is 36 mW. Using a 1 KΩ thermistor this defines the current as 0.19 mA/$^{\circ}$C rise, that is 1.9 mA for a $10^{\circ}C$ rise. If the heating pulse width is reduced to 10ms the current required increases to 6 mA for a $10^{\circ}C$ rise.

5.6 Process Steps

Figure 5.7 illustrates the process steps.

1. Substrate preparation

   a) Adhesive tape is placed over the surface to prevent scratching when the abrasive powders are used.

   b) The substrate is aligned over a photographic plate of the gold track pattern. Holes are drilled in the centre of the proposed bonding pad areas with a 1 mm diameter spherical tungsten carbide burr.

   c) The holes are counter sunk using a conical burr whose surface is covered with cloth impregnated with No. 225 Aloxite powder and water.

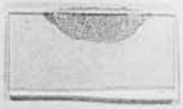

1" x ½" Corning 7059 microsheet substrate

Holes are drilled, countersunk and polished, to accommodate solder joints

The thermistor material is deposited by D.C. sputtering

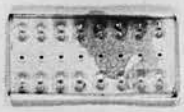

Photolithographic techniques are used to produce the required geometry

Gold and Nichrome films are evaporated onto the substrate

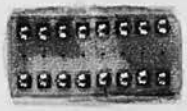

Conducting tracks and pads are produced using the photolithographic process

The substrate is then cut to produce individual thermistors. Leads are attached and an insulating film of P.T.F.E. is deposited by R.F. sputtering over the fromt surface

The thin film thermistor

Figure 5.7. The stages of the thermistor production process

d) The holes are polished using a similar burrimpregnated with jeweler's rouge and water. The surface finish must be polished to better than 1000 Å for good gold adhesion and to obtain continuous films.

e) The adhesive tape is removed by immersing the substrate in an ultrasonic bath of acetone.

f) The substrate is cleaned using the following procedure:

(1) by immersion in an ultrasonic bath of analar acetone

(2) repeated in a second bath

(3) by immersion in an ultrasonic bath of analar iso-propyl alcohol

(4) repeated in a second bath

(5) by placing in a vapour bath of aristar iso-propyl alcohol

2. Deposition of thermistor material

a) The clean dry substrate is placed in the sputtering chamber and the chamber pumped down to its ultimate pressure (10^{-5} torr, in this case)

b) The chamber is let up to atmospheric pressure by introducing a 3:1 argon-oxygen mixture.

c) The chamber is pumped down and the pressure adjusted to 3×10^{-2} torr with a constant through-put of the gas mixture. Sputtering is carried out with the shutter closed for five minutes with a magnetic field current of 3.6 A and a cathode voltage of -2.5 kV.

d) The shutter is opened and sputtering is continued for 4 hours to produce a film 2.4 μm thick.

3. Etching the thermistor material

a) The substrate is removed from the sputtering chamber and placed immediately on the spinner chuck, then spun at 6000 r.p.m. in order to remove any particles acquired in transportation to the spinner bench.

b) The film surface is coated with AZ 1350 photoresist applied through a hypodermic syringe with a 1μm Millipore filter attached.

c) The substrate is spun at 1500 r.p.m. for 30s.

d) It is then placed on a laminar flow bench for 15 minutes followed by 20 minutes on a hot plate at 80°C.

e) The photographic mask of the required tracks is aligned over the substrate on an exposure jig and exposed to U.V. light. A 40s exposure is necessary with the particular U.V. source used.

f) The photoresist is developed in AZ 1350 developer which is diluted to a 1:1 ratio with deionised water (D.I.W.). The development time is approximately 30s.

g) (i) Ferric chloride etch. The substrate is placed in a heated solution (60°C) of 1N ferric chloride and agitated occasionally until the thermistor material has been etched. It is washed thoroughly in D.I.W. The remaining photoresist is removed in an ultrasonic bath of AZ photoresist remover and the wash repeated.

(ii) Hydrochloric acid etch. The substrate is baked for 30 minutes at 150°C. It is then placed in

concentrated hydrochloric acid and agitated until etched, whereupon it is washed thoroughly in D.I.W. The remaining resist is exposed to UV light for 5 minutes and developed as in step 3.e. The substrate is washed thoroughly in D.I.W., rinsed in acetone and allowed to dry.

4. Gold evaporation

a) The cleaning procedure outlined in step 1.f is repeated.

b) The substrate is placed in the evaporation plant and the chamber pumped down to its ultimate pressure (10^{-7}torr). The substrate heater controller is set to 300°C.

c) When heated, glow discharge cleaning is carried out in an argon atmosphere at a pressure of 5×10^{-2}torr using a -1 kV D.C. supply for a period of 5 minutes.

d) A 1000 Å nichrome film is evaporated onto the substrate in argon at a pressure of 10^{-6}torr with the power supply set approximately to 4 kV, 50mA.

e) A 4000 Å gold film is evaporated under similar conditions. Film thickness is monitored by an Edwards film thickness monotor during the evaporations.

f) The system is allowed to cool to below 100°C before argon is admitted to the chamber.

5. Gold etch

a) On removal from the evaporation chamber the substrate is immediately placed on the spinner chuck and steps 3. a, b, c, and d are repeated. Second and third coats are applied in the same way. This is done to ensure that the

photoresist is continuous over the step. Exposure and development are carried out as in steps 3.e and f. A 55s exposure time is used.

b) After development the substrate is baked at 100°C for 20 minutes.

c) The gold is etched in the appropriate solution. After washing in D.I.W. the nichrome is etched in its etchant and the wash is repeated.

d) The remaining photoresist is removed in an ultrasonic bath of AZ photoresist remover, the substrate is then washed in D.I.W. and spun dry.

6. Lead attachment

a) The substrate is sliced up using a diamond saw with oil cooling.

b) The devices are cleaned by washing in acetone.

c) Leads are inserted through the back of the substrate and soldered to the pads using Multicore high melting point solder (melting point 301°C). Surface protrusions are removed using a needle file and fine emery paper.

7. Insulation

a) The cleaning procedure outlined in step 1.f is repeated.

b) The sputtering procedures outlined in steps 2.a and b are repeated using argon only with a P.T.F.E. target. Eccotherm TC-4 is used to ensure effective cooling of the substrates.

c) Sputtering is carried out for 84 minutes at 80 W R.F. power, a chamber pressure of 5×10^{-3} torr and a magnetic field current of 3.5A.

d) The devices are removed from the chamber and the pads inspected. In the case of imperfections, the central area of the device is shielded and more P.T.F.E. is sputtered over the pads.

e) When the insulation is complete Araldite is applied to the back of the substrate and the leads.

8. Insertion in the artificial blood vessel.

a) A section of the artificial blood vessel wall of a similar size to the device is removed with a scalpel.

b) The device is placed in position and secured with P.T.F.E. tape (there is no adhesive on this tape).

c) Cold cure Silastomer 9161 and its catalyst M9162 are mixed thoroughly and applied to the whole area, then allowed to harden completely.

Considerable care is taken throughout the process to ensure that the environment is clean. The cleaning procedures are rigorously performed and each stage is followed by a careful visual inspection. The surface area of the device was originally scaled up in order to facilitate the examination of production problems and of the resulting device so that large variations in clean room conditions could be tolerated. The dimensions of this large thermistor are shown in figure 5.8. Such a thermistor can be used in a 4 mm diameter tube in the flowmeter application.

A particularly critical production stage is the application and drying of the photoresist coating preceding development for the gold etch. The problem arises because of the step at the edge of the thermistor material where thick photoresist is required

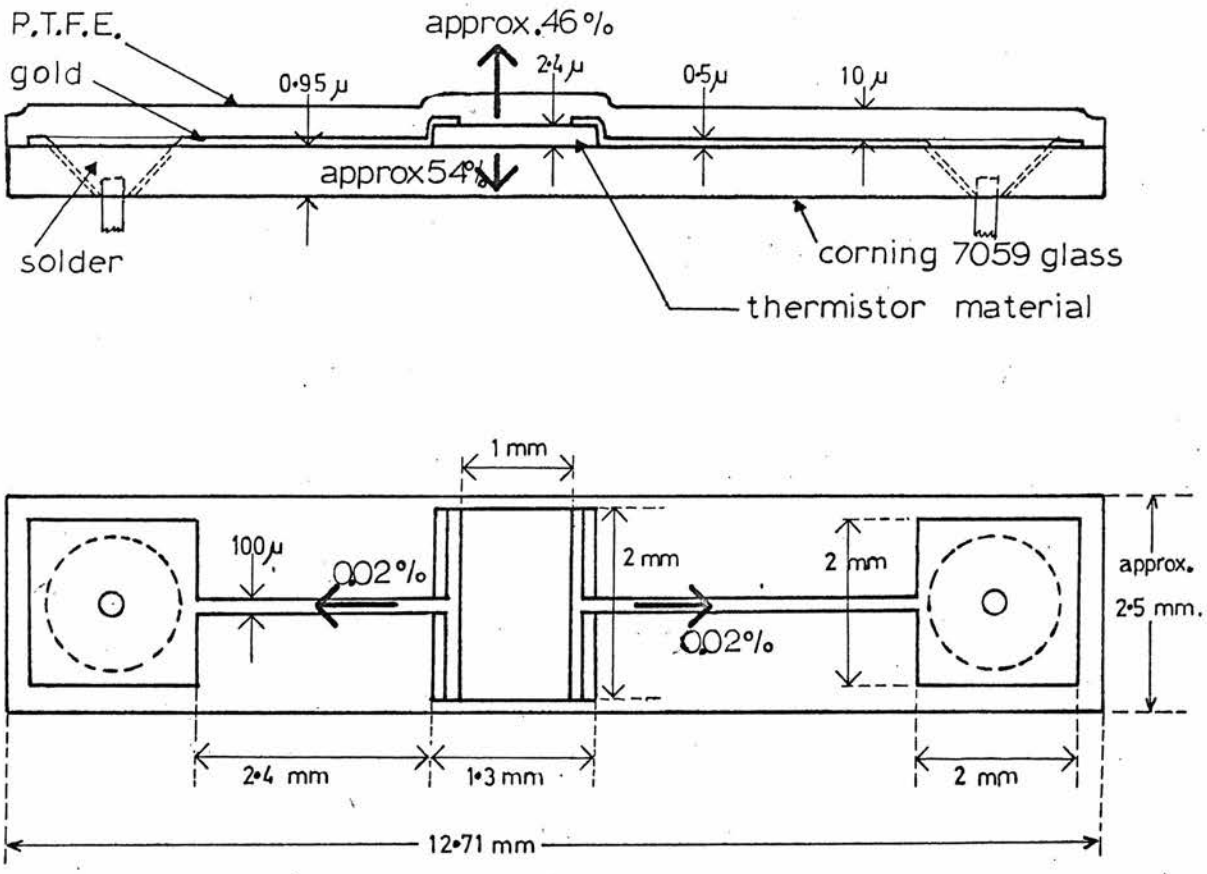

Figure 5.8. A diagram of the 'large' thin-film thermistor.

in order to produce a continuous coating over the step. This is achieved by applying three coats at 1500 r.p.m. for 30s using the standard photoresist drying technique between each coating. The thickness of each coating lies between 0.45μm and 0.5μm. Any further reduction in speed or spinning time causes an uneven distribution of photoresist. (This coating procedure has been simplified recently by the availability of a thicker photoresist material, AZ 1350H. One coat applied at 3000 r.p.m. for 30s has been found to be sufficient). The photoresist must be dried by the application of heat to the back surface of the substrate. The result of drying under an infra-red lamp, as suggested by the manufacturer, is illustrated by the photograph of the thermistor step shown in figure 5.9. It appears that a surface skin forms which prevents further evaporation of the solvent and leaves fluid photoresist under the thicker areas, in this case at the step. The fluid photoresist and its immediate covering is removed in the development process to expose a section of the required track to the etches.

5.7 Thin Film Thermistor Characteristics.

The B-values of the thermistors were calculated from measurements made using the apparatus described in section 3.1. The resistance at 25°C and the B-values are found to vary from the design values by -10% to +60% and -8% to +20% respectively. The factors contributing to these ranges are the temperature cycling during the metalisation and insulation production stages together with the spread of values obtained in sputtering the thermistor material. A typical resistance-temperature characteristic is shown in figure 5.10.

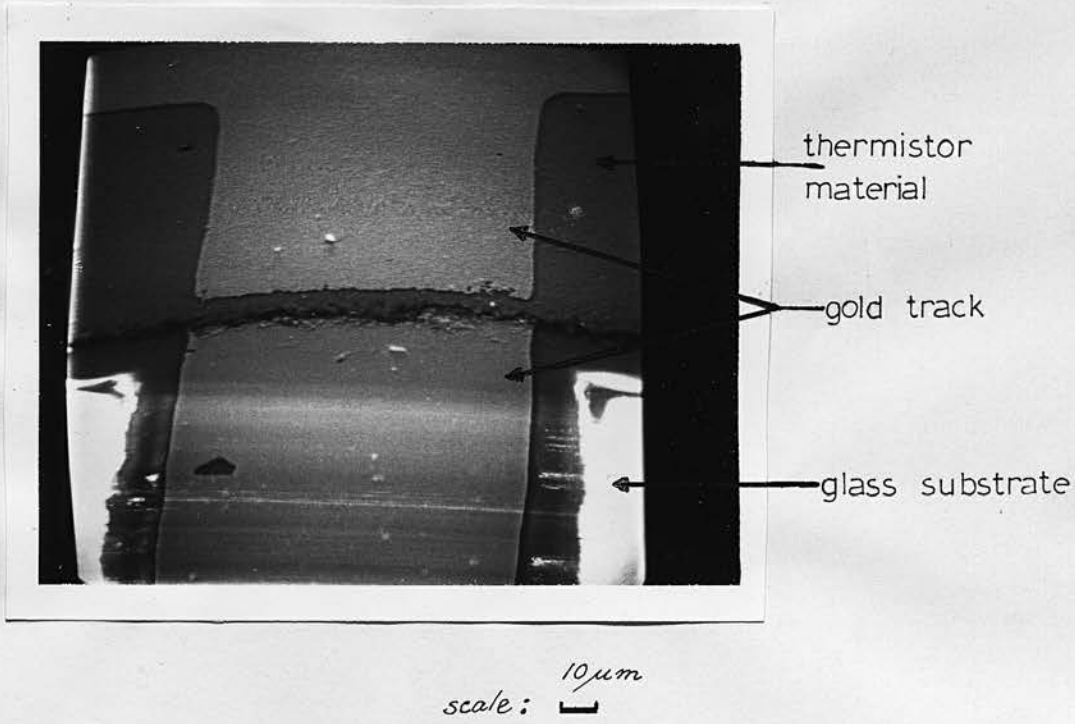

Figure 5.9. The step fault.

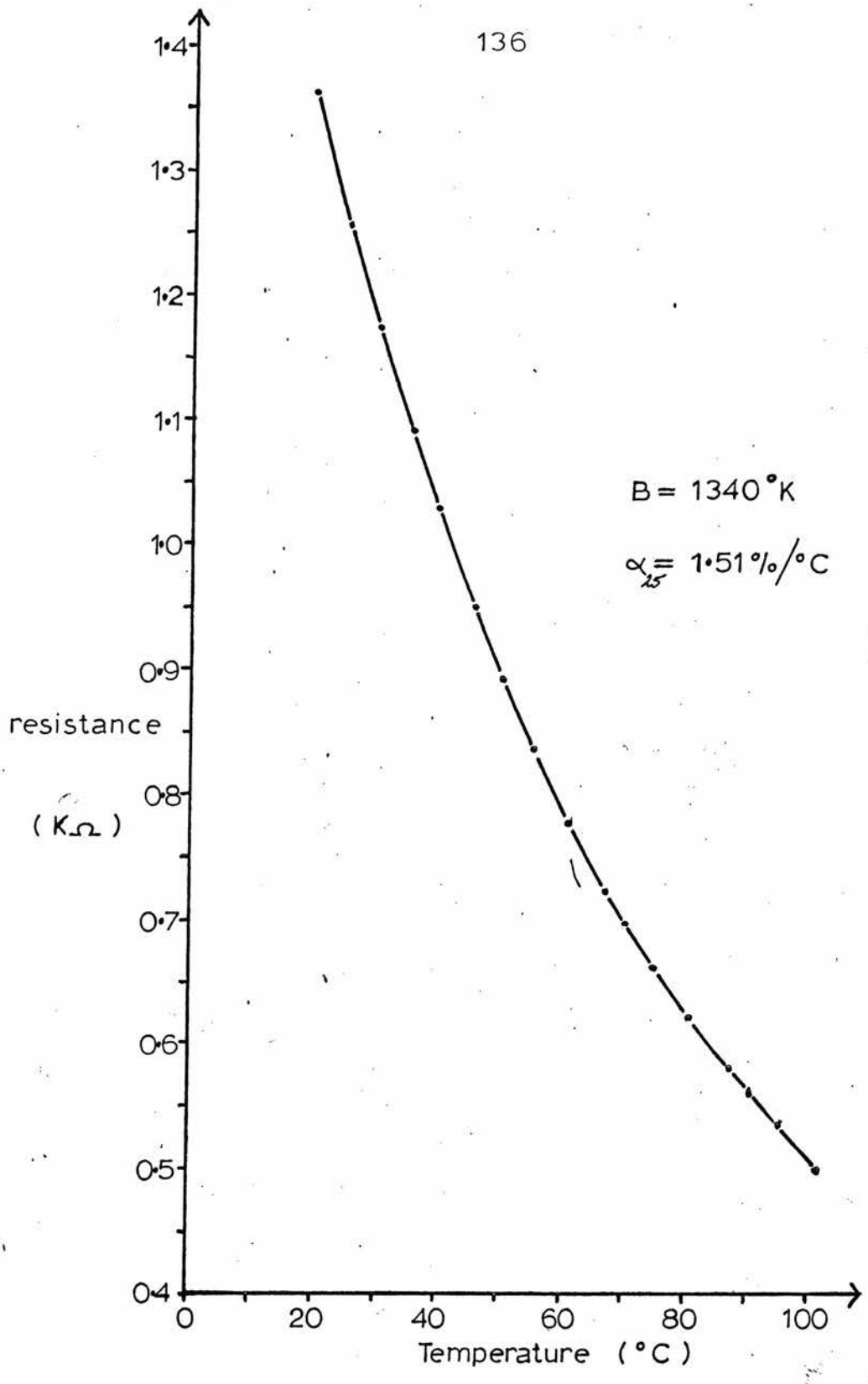

Figure 5.10. The resistance—temperature characteristic of a thin film thermistor.

The voltage-current characteristics of small and large thermistors in still air and still water were measured. The results for small and large thermistors are shown in figures 5.11 and 5.12 respectively. These tests were carried out to destruction, which occured at current densities of the order of 10^3 A cm^{-2}. A photograph of a small thermistor after this treatment is shown in figure 5.13a. The dissipation constants of the two devices can be calculated from the above data by applying the standard thermistor equation

$$R = R_0 e^{\beta\left(\frac{1}{T} - \frac{1}{T_0}\right)}$$

at selected points on the V-I characteristics to obtain the temperature rise, $T - T_0$, produced by the Joule heating at these points. Hence the power required to maintain the device temperature at $1^{\circ}C$ above ambient temperature can be calculated at each selected point. These values are included in the graphs of the V-I characteristics. As expected, the dissipation constant is an increasing function of the surface area of the device and is higher in water than air. The dissipation constants for a bead thermistor[8] in air and in water differ by a factor of times 5. The relatively small change in the case of thin film thermistors is attributable to the presence of the glass substrate. Despite careful measuring techniques, the influence of free convection can be seen to be significant at higher values of Joule heating. The dissipation constants quoted must therefore be regarded as approximate values since it is not possible to ensure that the environment is still.

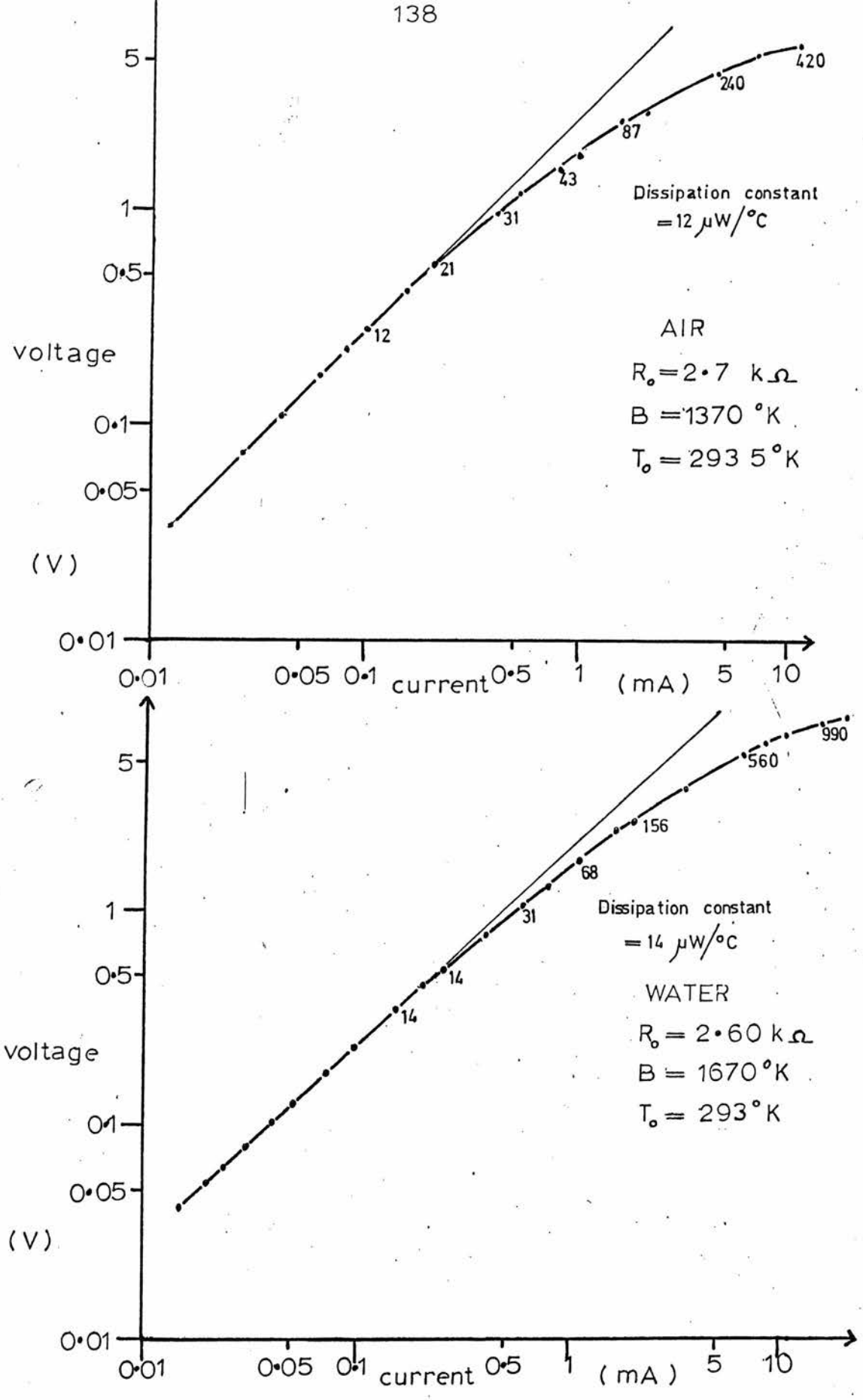

Figure 5.11. The voltage-current characteristics of a small thermistor in still air and still water.

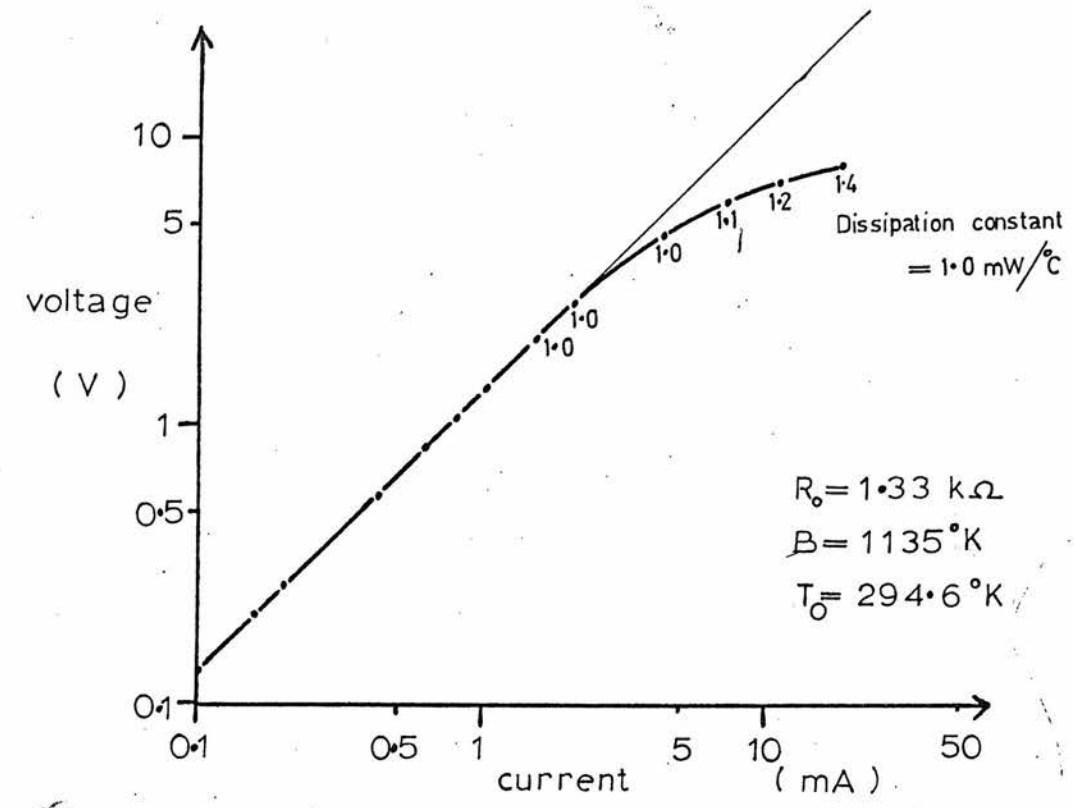

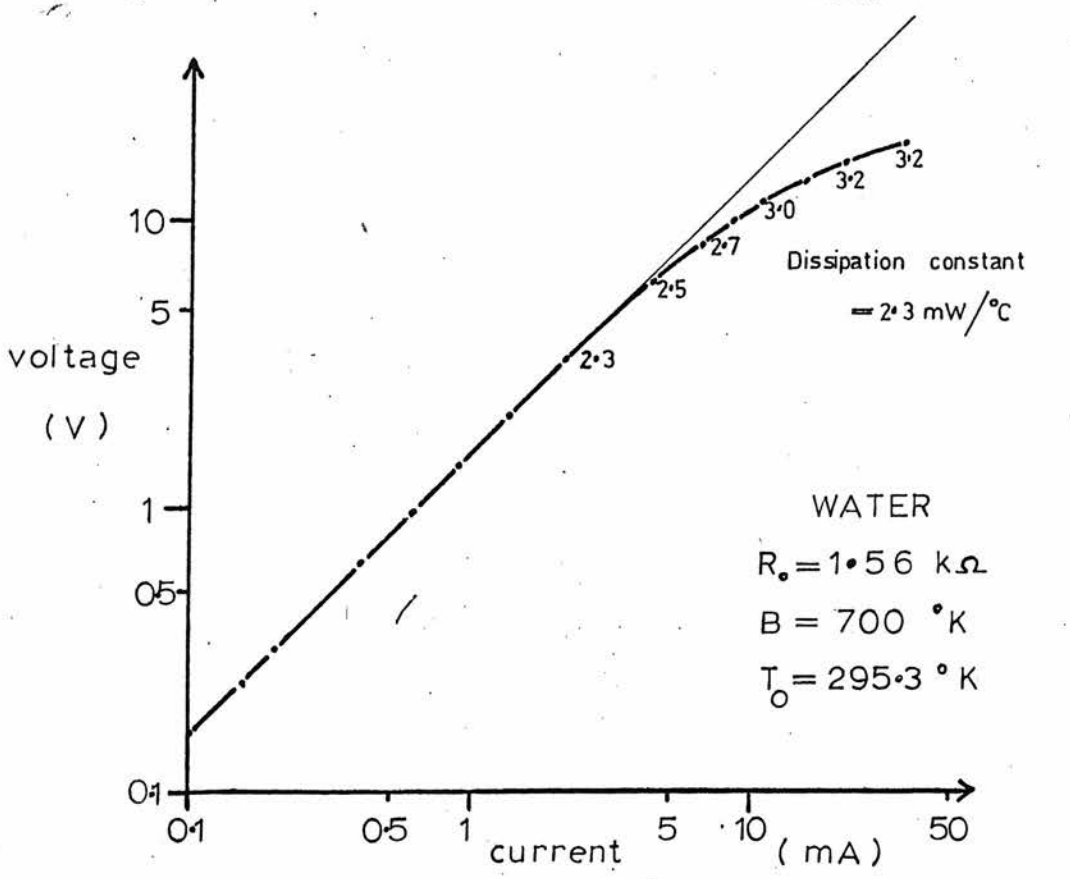

Figure 5.12. The voltage-current characteristics of a large thermistor in still air and still water.

magnification : x 200

Figure 5.13a. The result of the test to destruction.

The heating and cooling time constants of the devices are essentially determined by the volume and thermal properties of the substrate. These time constants were measured in air and liquid paraffin using the apparatus shown in figure 5.13. In the case of air the device was rapidly inserted into, and after a suitable interval, removed from, an oven. For liquid paraffin two baths at different temperatures were employed and the device was rapidly transferred between them. The results from the exponential graphs obtained are included in figure 5.13.

When the thermistors are used in the pulsed mode as for flow measurement, there are three time constants which are of interest. The first is associated with the time taken for a thermal pulse to travel through the thermistor material and insulation to the device-fluid interface. This can be calculated from equation 4.46 and equals 12 μs, assuming that the distance travelled equals half the thickness of the thermistor plus the thickness of the insulation. It is this fast time constant which makes the thin film thermistor attractive in the flowmeter application. An experiment was set up to measure this time constant, in which a thermistor was supplied with a current pulse in air and in water. The pulse had a rise time of 2 μs and an amplitude which was sufficiently large to cause significant self heating. A C.R.T. trace of the resulting voltage pulse across the thermistor did not display a significant discontinuity to isolate positively this fast time constant for measurement. This result occurs because the values of the thermal properties of the surrounding materials are not sufficiently different to reflect the presence of their boundaries.

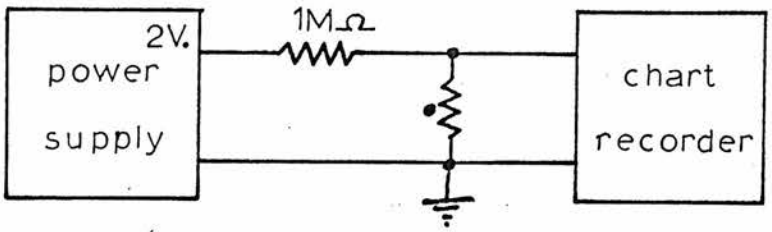

Table 5.2

The thermal time constants of the devices

	large thermistor	small thermistor
heating (in air)	6·9 S	8·7 S
cooling (in air)	22 S	26 S
heating (in liquid paraffin)	1·8 S	2·7 S
cooling (in liquid paraffin)	3 S	6 S
dimensions of glass substrate	12·71 X 2·13 X 0·95 =25·72 mm^3	12·71 X 2·5 X 1·05 =33·36 mm^3

Figure 5.13. The apparatus used to measure the heating and cooling time constants of the devices in air and liquid paraffin, together with a table of the results.

The second time constant is associated with the transient response of the device in self heating. A step rise in current to a level sufficient to cause self heating is applied to the device, which is located in air. It is repeated in water. The pulse generator used is that described in section 6.2, modified for one-shot operation. The resulting voltages were measured from a C.R.T. trace obtained from a differential input oscilloscope. The relevant results are shown in figure 5.14. These reflect the complex interaction of conductive heat transfer from the thermistor material to the surrounding media, conduction in the substrate and between the media, and possibly free convection in the fluid. Comparing the small and large thermistor responses, it can be seen that point A on figure 5.14 is largely determined by the surface area of the device and hence the volume of the surrounding media, which initially acts as a heat sink. The thermal properties of the environment largely determines the "tail" of the response.

The third time constant is associated with the cooling time of the device after it experiences a constant current heating pulse of a particular duration. The apparatus which had been used in the previous test was modified by the addition of a 100 kΩ resistor across the switch. A 10 mA pulse amplitude was employed. The results, which were approximately exponential, are included in figure 5.15.

The ageing characteristics of the thermistors were examined by measuring the resistances of several devices at 25°C before and after immersion for 100 hours in a liquid paraffin bath at 100°C. The temperature stability of the bath was $\pm$ 5°C.

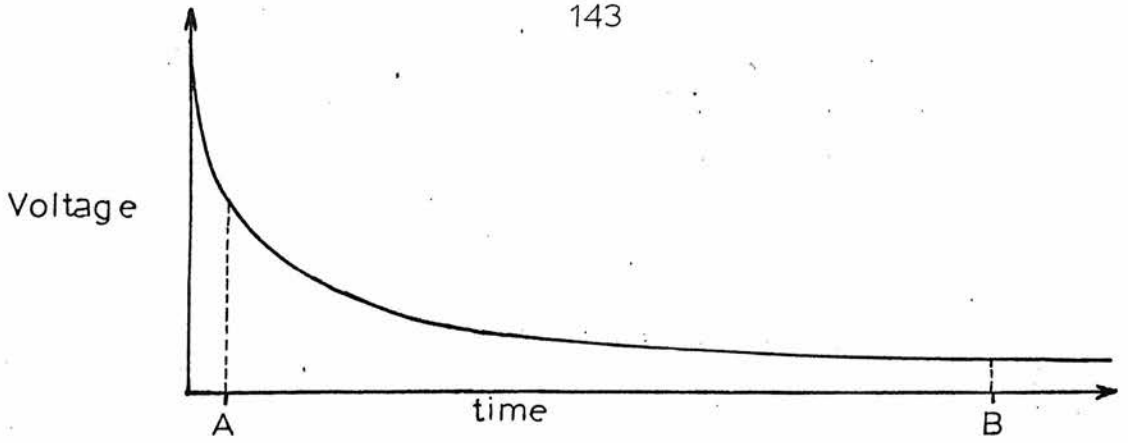

Figure 5.14. A graph of a typical voltage response to a step rise in current. The values of A & B obtained in air and water for small and large thermistors are shown immediately below.

thermistor	in air		in water	
	A	B	A	B
small	100 mS	9 S	100 mS	4 S
large	1 S	15 S	250 mS	5 S

thermistor	heating pulse width	in air	in water
large	100 mS	140mS	85mS
large	50 mS	104mS	57mS
small	100 mS	35 mS	30mS
small	50 mS	30mS	19mS

Figure 5.15. A table of the cooling time constants obtained for small and large thermistors in air and water.

The accuracy of the temperature measurement was $\pm 0.1^{\circ}C$ hence, for a 1KΩ thermistor, the resistance measurement accuracy required is $\pm$ 1Ω. No change in resistance outside this limit was detected. This excellent ageing characteristic may result from the nature of the deposition process and/or the temperature cycling of the thermistor material during the metalisation and insulation production stages.

Chapter 6

FLOWMETER TEST EQUIPMENT

6.1 General Outlines

The test apparatus differs from the proposed in vivo flowmeter principally in that a variable pulse generator is used and the telemetry link is omitted. The output of the transmission gate is directly connected to the counting circuitry. The telemetry link is being developed separately by the P.R.C. Thin Film Group. Block diagrams of the two systems are shown in figures 6.1 and 6.2. This chapter describes the test pulse generator, transmission gate, gating and counting circuitry and the flow system. The required computer programs have been developed by the P.R.C. Computer Group.

The pulse generator must be capable of supplying a train of identical constant current pulses into a load of 2 KΩ. The load consists of the thermistor in series with a 1 KΩ resistor which is included to facilitate the measurement of the current pulse amplitude and to check its shape. The pulse amplitude, width and repetition rate must be adjustable in the approximate ranges 1mA to 12mA, 10ms to 150ms and 2pps to 0.2pps respectively in order to test both the small and large thermistors. This specification is derived from the thermistor data shown in section 5.7 and preliminary flow tests.

The oscillator is the standard P.R.C. circuit for telemetry work. The gating and counting circuitry, which is also intended for use with the in-vivo system, is constructed from positive logic modules produced by Digital Equipment Corporation (D.E.C.). Their

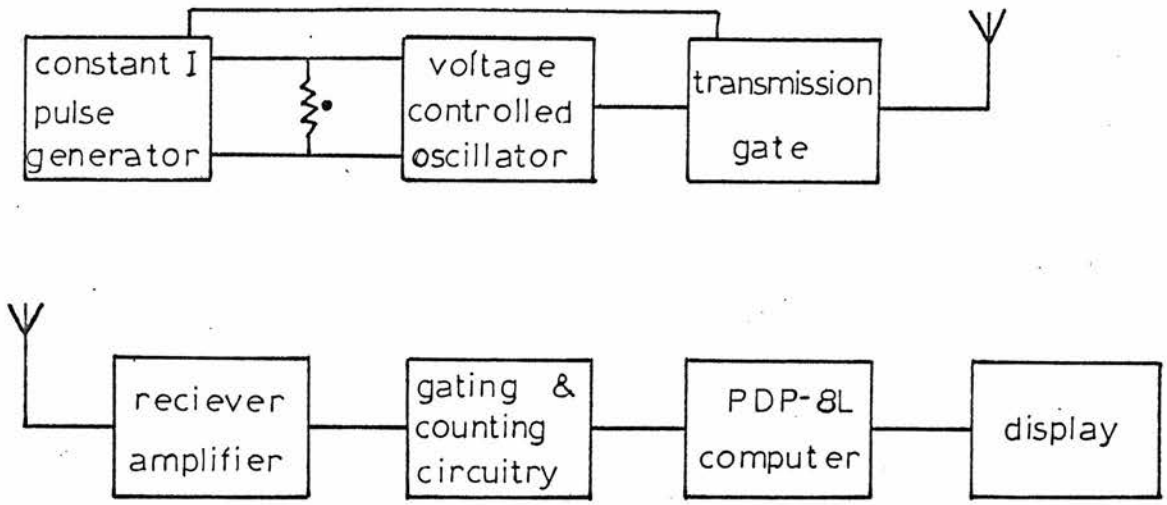

Figure 6.1. A block diagram of the proposed in vivo flowmeter circuitry.

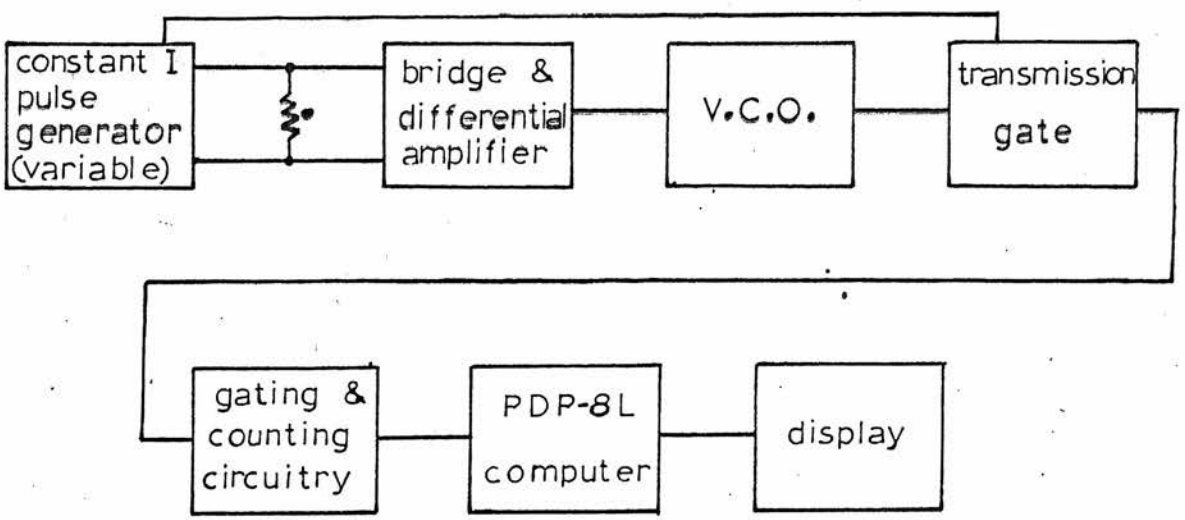

Figure 6.2. A block diagram of the test circuitry.

maximum operating frequency is around 10MHz.

6.2 Pulse Generator

No commercial pulse generator meeting the above specification was available, therefore the circuit shown as a block diagram in figure 6.3 and in detail in figure 6.4 was developed. The current pulses are generated by switching a transistor into saturation from the off state. The thermistor and resistor are connected in series to its collector together with a current regulator which controls the amplitude of the current pulse. The pulses which switch the transistor are generated by a monostable which is triggered by a unijunction transistor circuit. This arrangement introduces the problem that, in the off state, the reference level at the thermistor is the supply voltage rather than ground. The adjustment of the reference level is achieved by incorporating the thermistor and resistor in a bridge circuit. The voltage appearing across a tap of the bridge output load is amplified by a differential amplifier to produce a positive pulse from a zero volt reference.

The pulse repetition rate is defined by the R_1C_1 time constant in the trigger circuit and is variable between 50pps and 0.2pps. The output of this circuit is differentiated to ensure an unambiguous trigger pulse for the monostable. The monostable is constructed from a single integrated circuit (consisting of four 2-input nand gates) together with capacitor C_2 and variable resistor R_2. The charging time of C_2 through R_2 defines the pulse width which can vary from 18 to 160ms. Three of the gates are employed as inverters to adjust logical states and to produce a positive output pulse. The voltage levels of the pulse are 0 and 3 volts with

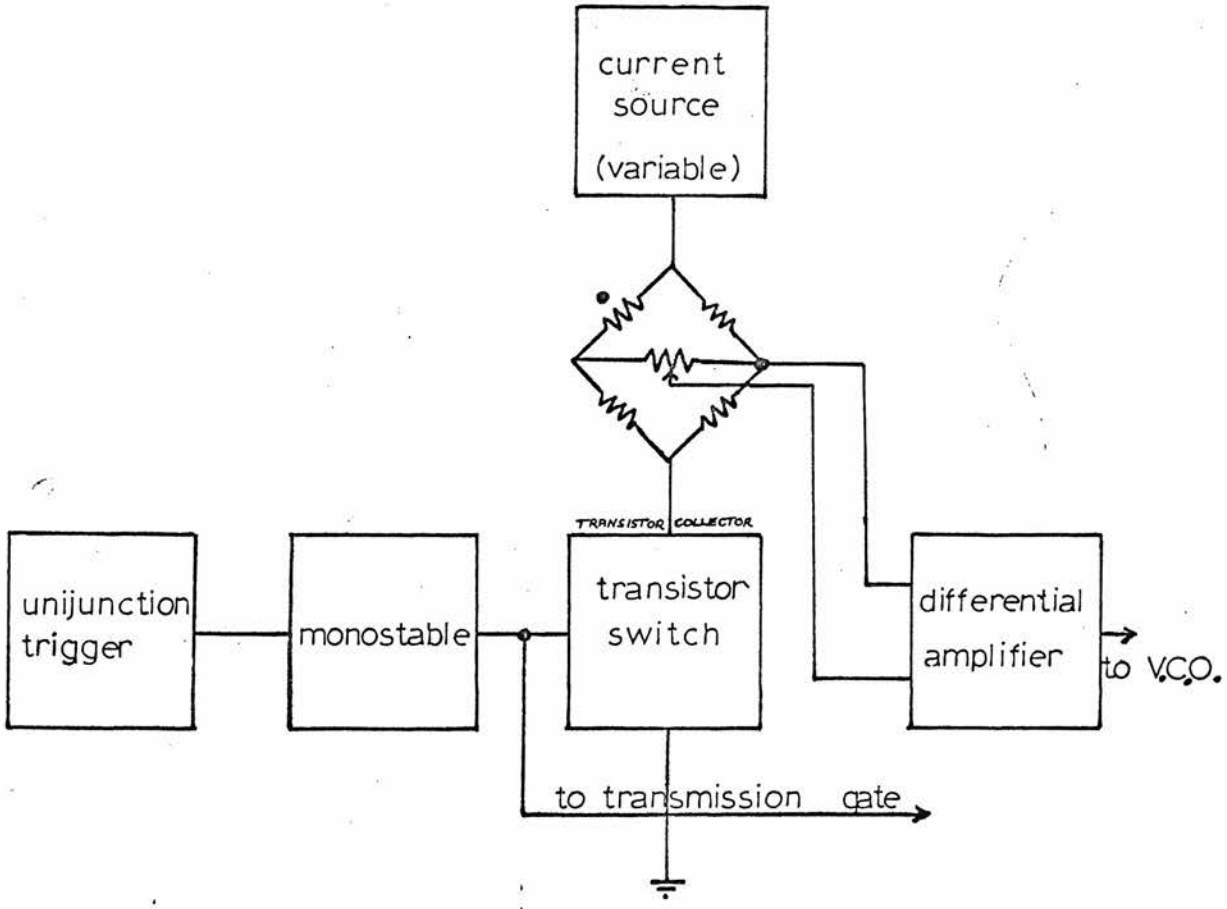

Figure 6.3. A block diagram of the pulse generator and level changer.

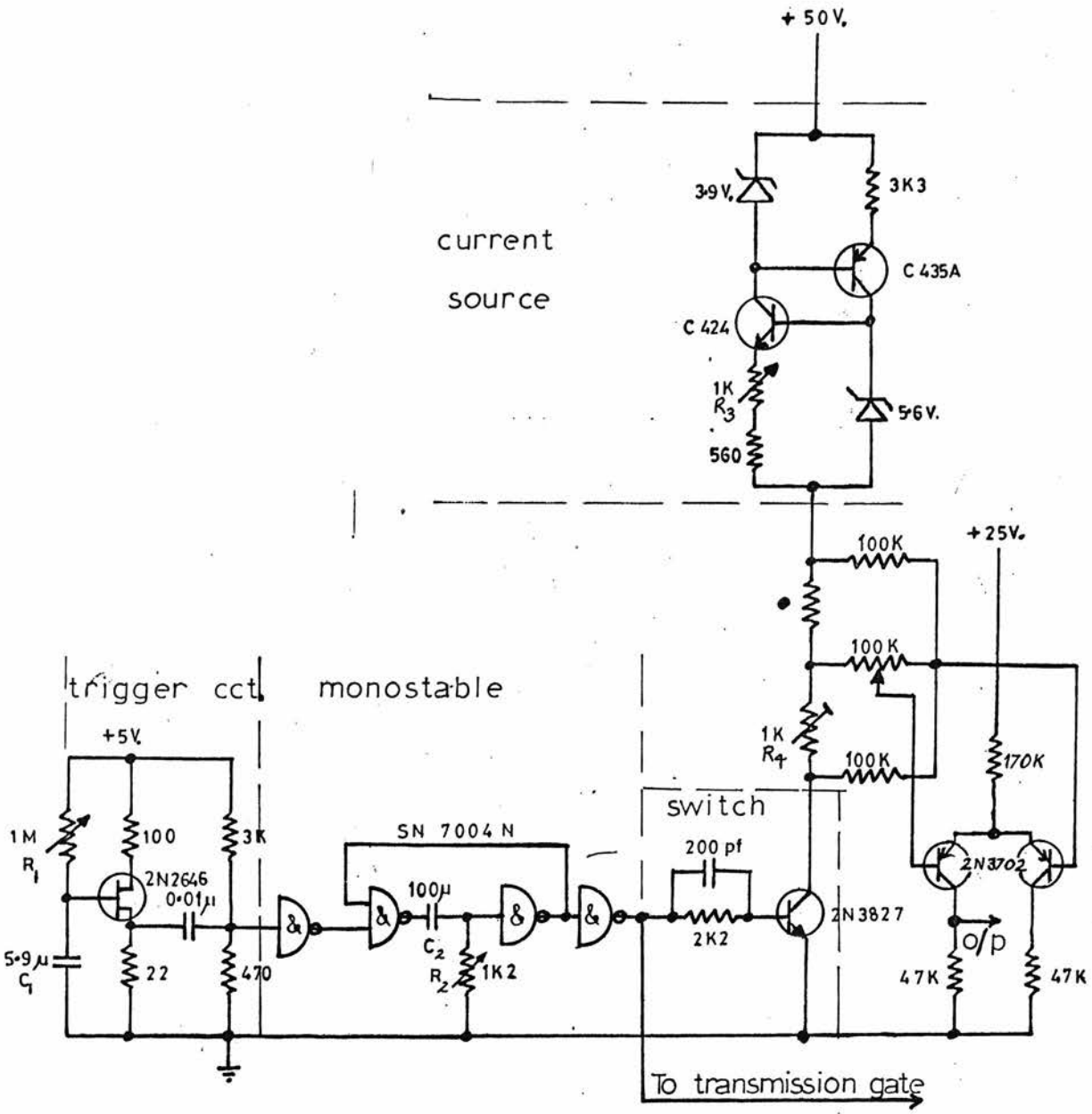

Figure 6.4. The circuit diagram of the pulse generator and level changer.

a rise time of better than 20ns. This signal is applied to the base of the switching transistor via a resistor(which is designed to limit the base current)and "speed-up" capacitor. The rise time of the current pulse through the thermistor is typically 300ns.

The V-I characteristic of the current source which is described in reference 77 is drawn in figure 6.5. The zener diodes define the voltage levels at the bases of the transistors while the emitter resistors define the currents through each arm. A potentiometer is used in one arm to permit adjustment of the current pulse amplitude. The component values used allow a variation in the range 1.2mA to 20mA. The slope resistance in the operating range is approximately 1 MΩ. The current pulse amplitude is measured by using a differential input oscilliscope to monitor the voltage appearing across the known resistor in series with the thermistor. The accuracy of this measurement is $\pm$ 5% and includes the error contributed by the bridge load current.

The differential amplifier is designed with a collector resistance of 47KΩ. A smaller value of resistance shorts the oscillator tank circuit to ground to an unacceptable extent. The mean of the excursions of the output pulse heights may be preset to a level suitable for modulating the V.C.O. This is achieved by selecting a suitable value for the series resistor, R_4, in the bridge. The maximum modulating voltage which is defined by the line voltage of the V.C.O. is, in this case, 4 volts. The system must be capable of reproducing the shape of the information bearing slope of the voltage pulse across the thermistor. To achieve this the gain is preset at unity by suitable attenuation of the bridge

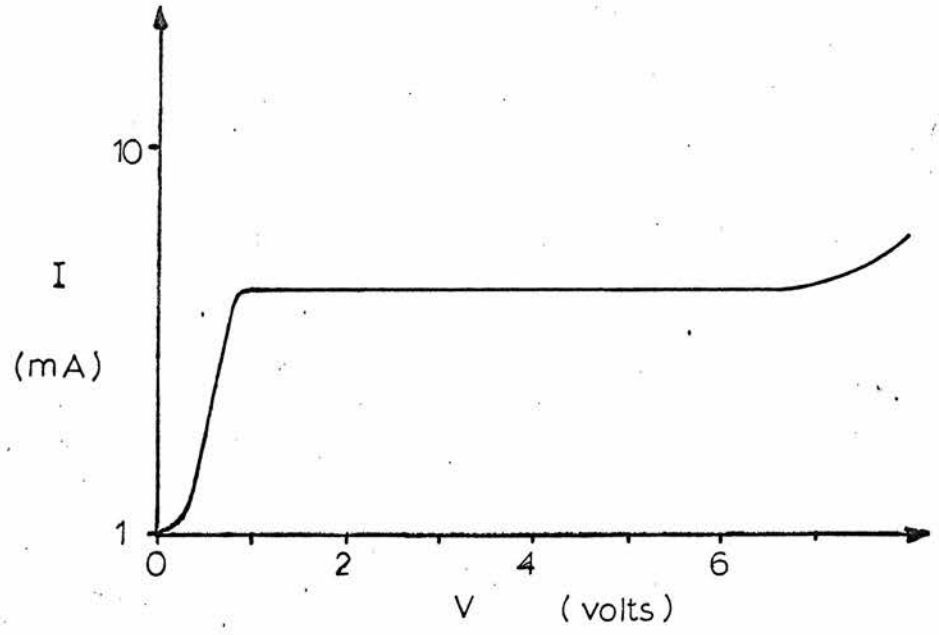

Figure 6.5. The V-I characteristic of the current source, for a particular value of R_3.

output voltage.

6.3 The Oscillator and Transmission Gate

The circuit diagram is shown in figure 6.6. The sensitivity of the overall system to flow rates is directly related to the value of the frequency and deviation of the voltage-controlled oscillator. The maximum possible frequency is defined by the maximum operating frequency of the counter which is approximately 10MHz. The frequency deviation of the oscillator is determined by the varactor diode and its series capacitor. For a large deviation the series capacitor must be large. The impedance at the input to the tuned circuit is capacitive. This impedance, together with the output impedance of the differential amplifier, introduces an integrating time constant which degrades the rise time of the modulating pulse. A 1000 pf capacitor is found to introduce a time constant of 20μs so that approximately 80μs must lapse before the pulse attains its maximum value.

Now, the measurement of the leading-edge height may be made at any time at the beginning of the heating pulse provided that the heat transfer mechanism is conduction only and that the measurements are carried out at identical times on each pulse. Therefore, assuming these conditions are met, a delay of 80μs between the leading edge and the start of counting will not introduce significant error in the measurement of the leading edge. By adjusting the transmission gate to introduce such a delay the counter will commence operation when the deformation of the modulating pulse due to this time constant is negligible.

The voltage-frequency characteristic of the V.C.O. was

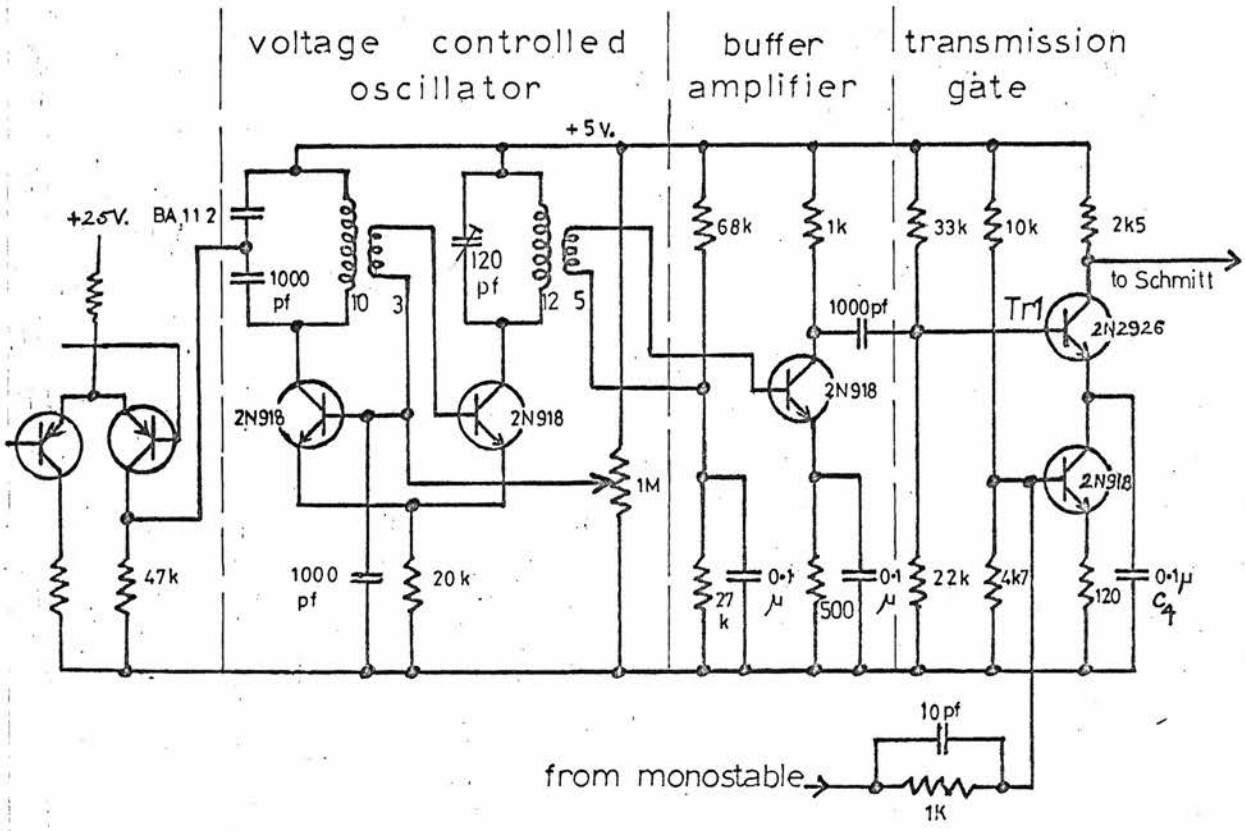

Figure 6.6. A circuit diagram of the oscillator and transmission gate.

measured using an Advance TC-8 timer/counter with an f.e.t. probe as shown, with the results, in figure 6.7. The frequency of the oscillator is temperature dependent (primarily because the capacitance of the varactor is temperature dependent). If room temperature is maintained approximately constant at $21^{\circ}C \pm 1.5^{\circ}C$, the stability of the oscillator is 10 MHz $\pm$ 1KHz (i.e. $\pm 0.01\%$). The variation of deviation with modulating voltage has been derived from figure 6.7 and the results are included in this figure.

A buffer stage is included between the V.C.O. and the transmission gate in order to improve the isolation of the V.C.O. The transmission gate is switched on by the monostable output via a resistor which is designed to limit the base current and a "speed-up" capacitor. The leading-edge shape of the envelope of the F.M. burst at the gate output is substantially determined by the action of capacitor C_4 which is connected in parallel with the switching transistor and its emitter resistor. The capacitor charges towards line voltage during the off period via leakage current through Tr1, so that it must discharge through the switching transistor and emitter resistor before the biasing conditions of the second transistor are such as to transmit the F.M. burst. Its value is adjusted to introduce the required delay. The timing of the delays at the leading edges of the differential amplifier output, the transmission gate output (and the Schmitt trigger which is associated with the counting circuitry) is shown in figure 6.8. A photograph of the circuit assembly is shown in figure 6.9.

By estimating a value for the period over which the frequency is to be counted it is possible to assess the sensitivity of such a

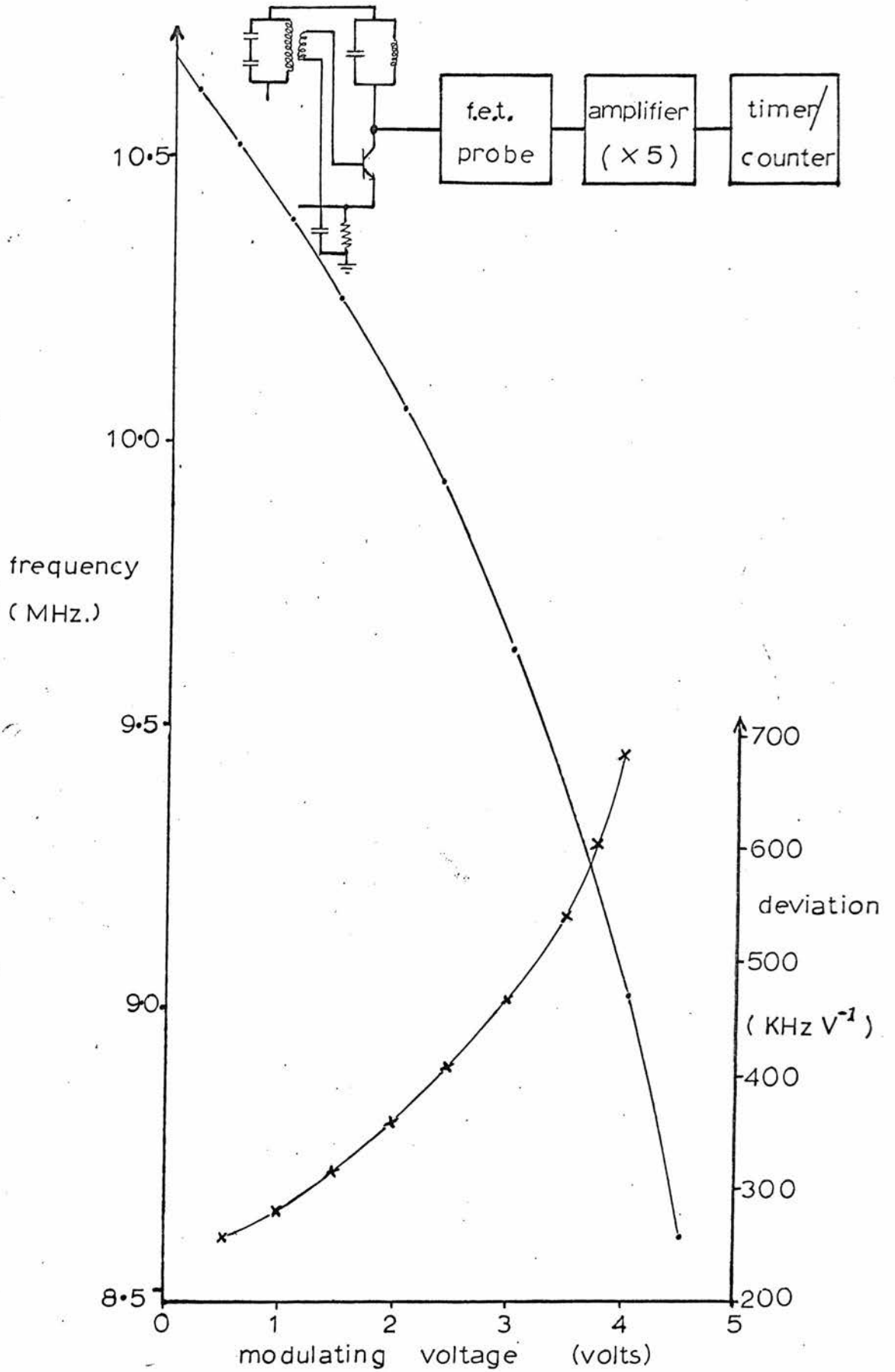

Figure 6.7. The voltage-frequency characteristic of the voltage controlled oscillator together with the equipment used to measure it.

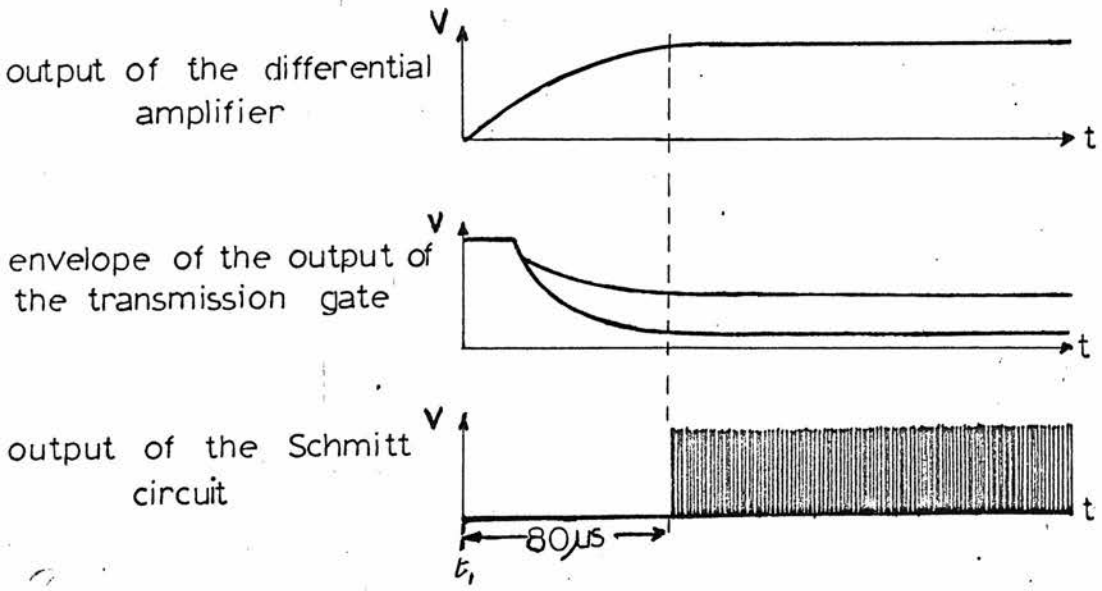

Figure 6.8. The timing of the leading edges of the above signals.

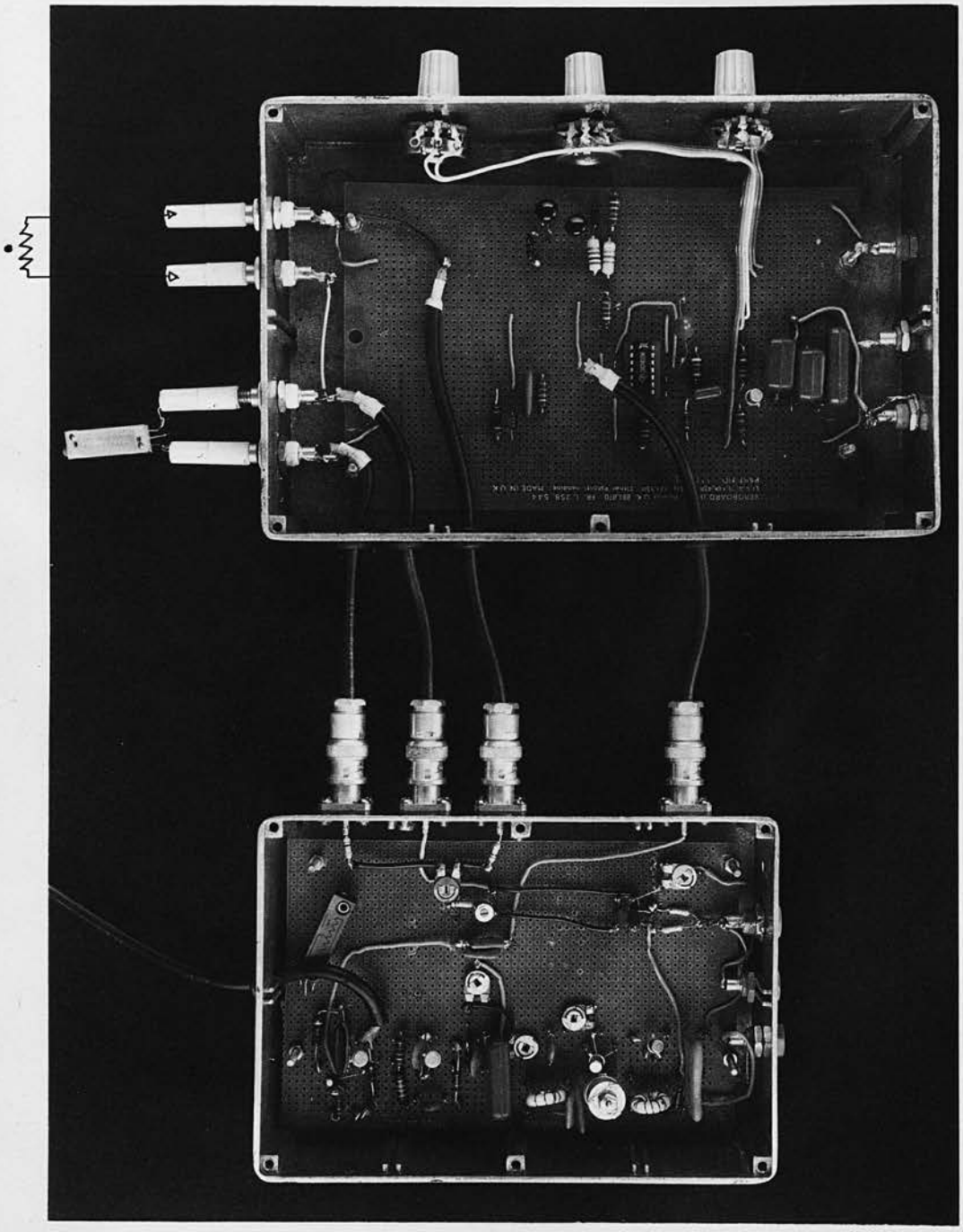

Figure 6.9. The circuit assembly.

system. The value of the current pulse width was estimated from preliminary experiments in which a pulse train with a 6mA pulse height was supplied to the thermistor, It was located on the wall of a 1mm diameter tube through which water was flowing. The voltage response to flow changes was examined using an oscilloscope. A current pulse width of around 50ms was necessary to detect flow variations. Now, the count period will in part determine the instrument's sensitivity and it is required to be as large as possible. A value equal to 10% of the pulse width is adopted. Hence, for a counting period of 5ms the total count registered at a frequency of 10 MHz is 5×10^4 counts, and, with a V.C.O. deviation of 400 KHz V^{-1}, one count represents 500 μV. The instability of the oscillator will introduce an error of $\pm$5 counts, which is equivalent to a voltage change of $\pm$2.5mV.

6.4 Gating and Counting Circuitry

The gating and counting circuitry was constructed using D.E.C. M-series modules in order to minimise the time required to assemble the system. A block diagram of the circuitry is shown in figure 6.10. The central part of the system is a 12 bit binary UP/DOWN counter which is capable of switching counting mode without disturbing the contents of the counter. Its input and operating conditions are controlled by the logic circuitry, as is the transfer of counter contents to the stores. The system is designed to count in the UP mode for a fixed period at the beginning of the F.M. burst and to count in the DOWN mode for an identical period towards the end of the burst. Both the UP and DIFFERENCE counts are transferred to separate stores to await processing by the computer.

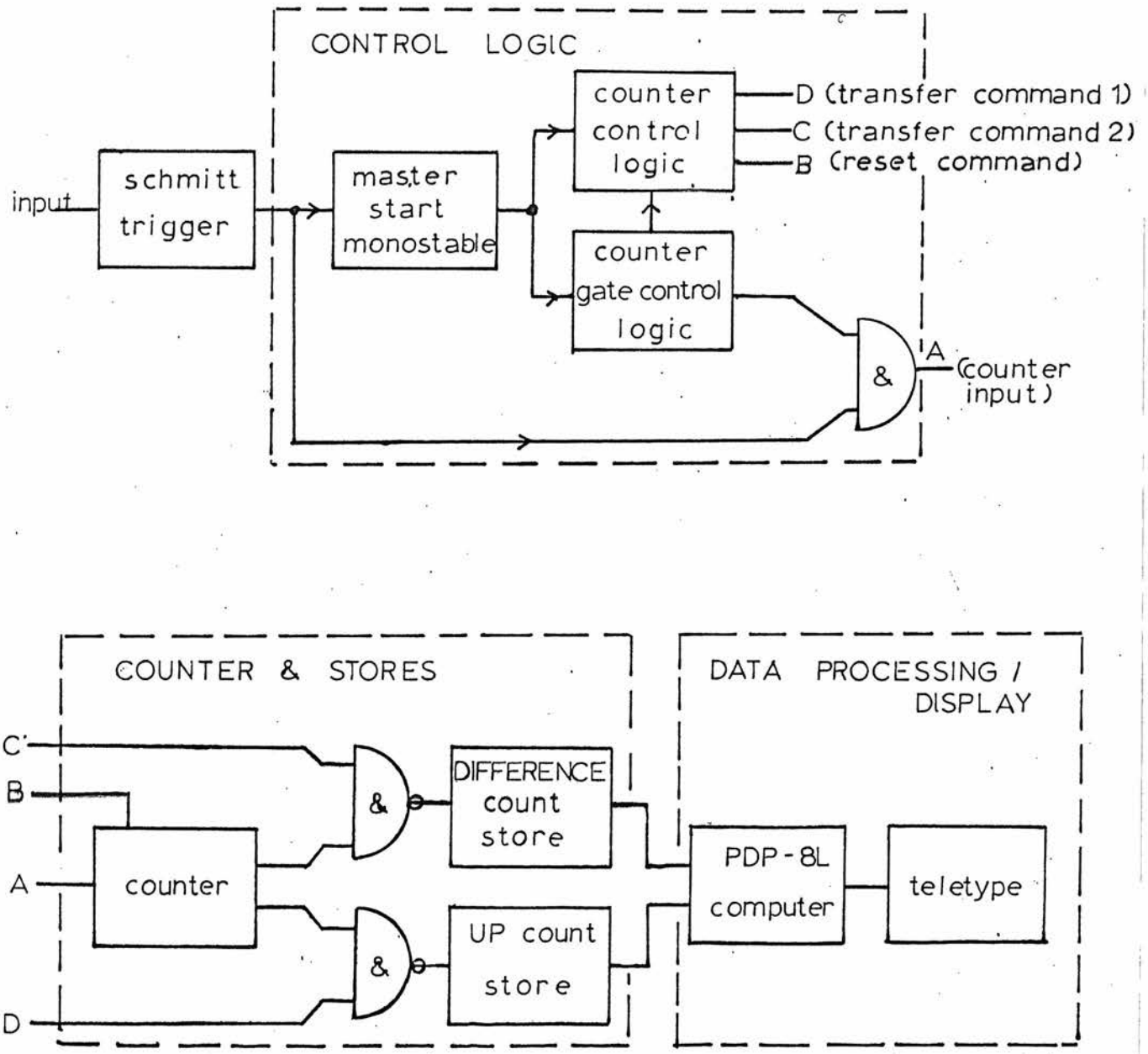

Figure 6.10. A block diagram of the gating and counting circuitry.

The timing of the control logic is referred to the first pulse of the F.M. burst which has been converted to a square wave pulse train by a Schmitt trigger. This initial pulse triggers the master start monostable which controls subsequent circuits.

6.4.1 Gating Pulse Logic

The control logic design was approached by first considering the system necessary to generate the counter gate control pulses. From this the counter control logic was developed. Since identical counter gate pulses are required, one monostable is used to generate both pulses, with a second monostable determining the interval between them. The logic and timing diagram of this section is shown in figures 6.11 and 6.12 respectively. The monostables are triggered by a negative transition and the counter responds to a positive transition. Considering figures 6.11 and 6.12, the leading edge of the first pulse of the F.M. burst triggers M1 causing the output to change from the logical 0 state to the logical 1 state. Its complementary output is transmitted by gate 1, and triggers M2 to produce the first counter gate pulse at its normal output. The complementary output signal is transmitted and inverted by gate 2 to trigger M3 on the trailing edge. The output of monostable 3 performs two functions: its trailing edge causes a negative transition at the output of gate 1, retriggering M2 and hence generating the second counter gate pulse. Simultaneously it triggers M4 which inhibits gate 2 and thereby prevents M2 from retriggering M3. The counter gate pulses open gate 3 to feed the output of the Schmitt trigger to the counter for the required periods.

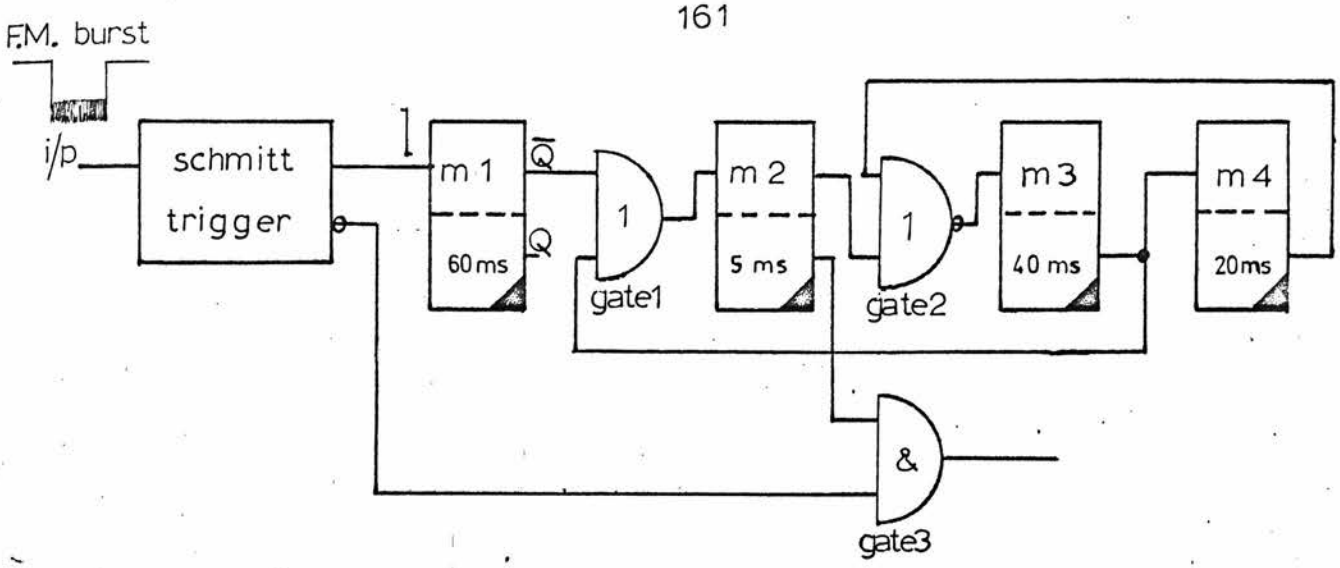

Figure 6.11. Logic diagram of the gating pulse circuitry.

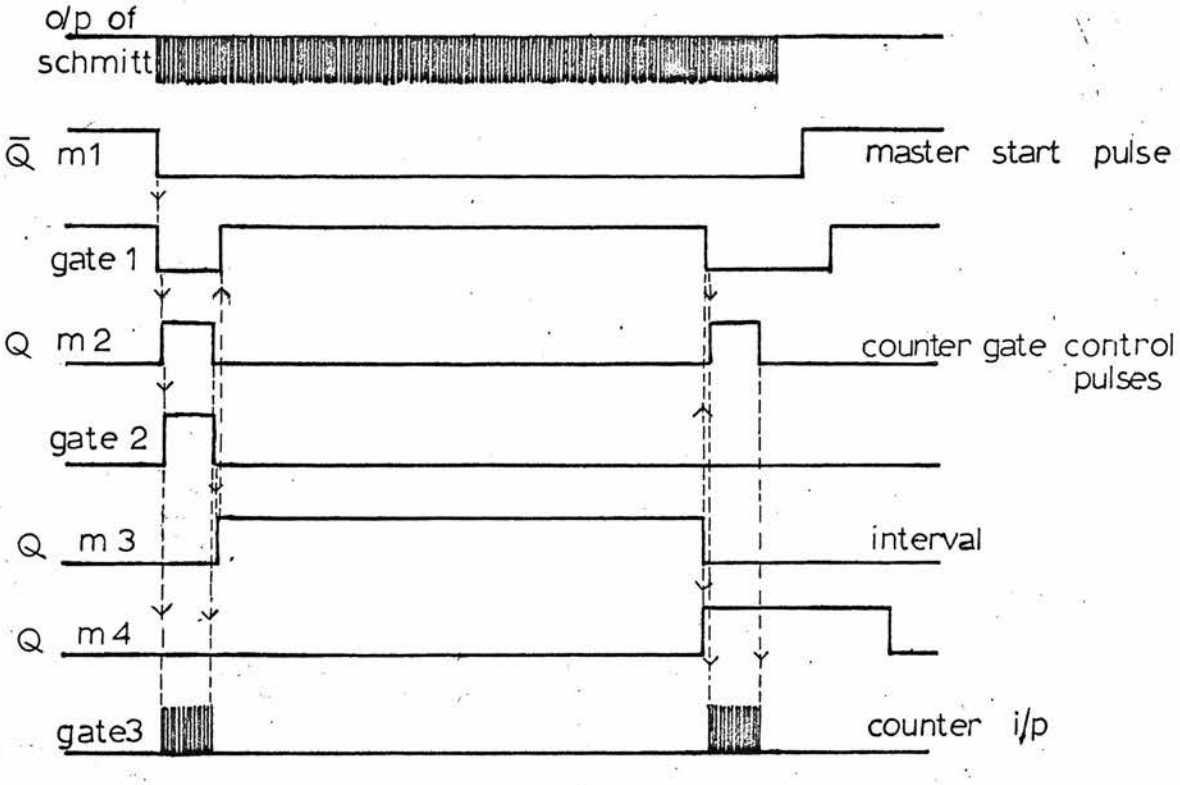

Figure 6.12. The timing diagram of the gating pulse logic.

6.4.2.The Counter Control Logic

The counter control logic is designed to meet the counter operating conditions and timing requirements shown in figure 6.13 and also to generate the necessary reset and transfer commands. A logic diagram of the complete system is shown in figure 6.14. The associated timing diagram is illustrated in figure 6.15. Referring to these diagrams, the output of gate 4, which provides the enable signal, is switched to the logical 1 state by the leading edge of the master start pulse. M5 and M6 are associated with the disable command which must occur prior to a change in the counting mode. M5 defines the time when the command occurs with respect to the leading edge of the master start pulse. M6, which is triggered by the trailing edge of M5, defines its duration. Further, the output of M6 is used as 'transfer command 1' since it occurs after the completion of the UP count. M7 ensures that a time greater than 500ns lapses before the counting mode is changed by triggering M8 with its trailing edge, and M8 returns to the stable logical 1 state at some time after the second counter gate pulse. 'Transfer command 2' is generated by gate 5 in response to the M1 and M4 logic levels. It produces a positive pulse which occurs at the trailing edge of the master start pulse. Finally the counter is reset to the logical 0 state by a pulse appearing at the output of M9 when triggered by the trailing edge of 'transfer command 2'. The complete cycle is repeated on the arrival of the next F.M. burst.

This system is realised using five M302 dual delay multivibrator modules, a M111 inverter module and a M121 AND/NOR gate module. The M302 module contains two individual monostables which,

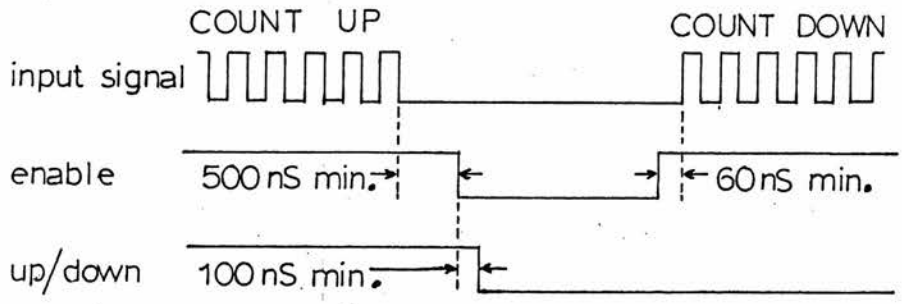

Figure 6.13. The counter operating conditions and timing requirements.

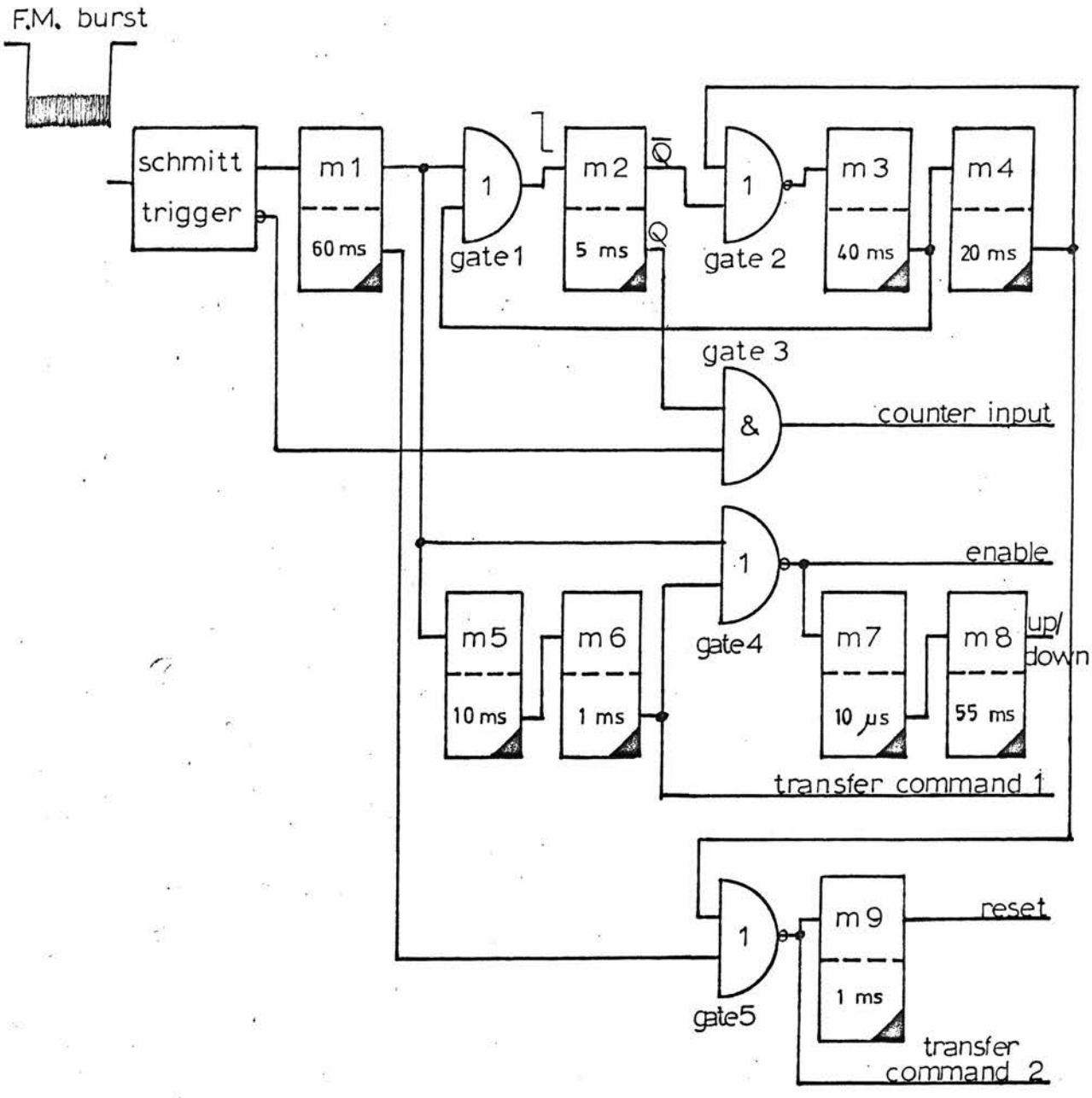

Figure 6.14. Logic diagram of the control logic circuitry.

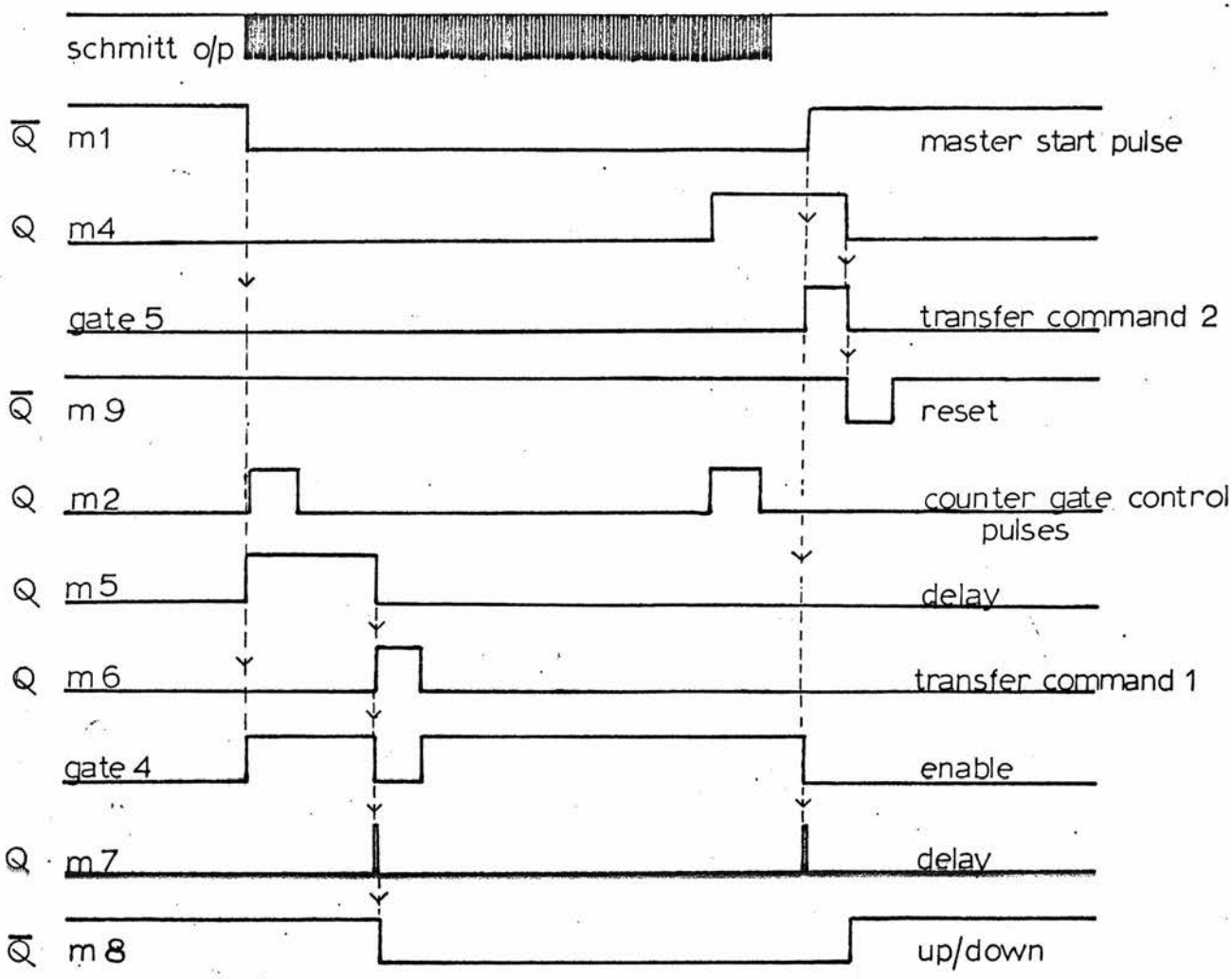

Figure 6.15. The timing diagram of the control logic.

when triggered by a negative edge, respond with a change from logical 0 state to the logical 1 state for a duration which is adjustable between 50ns and 7.5ms. By connecting the appropriate internal capacitor the approximate value required within this range can be selected. Fine adjustments can then be made using the potentiometer provided. The pulse width can be extended by the addition of external capacitors. 10μF and 100μF produce pulse widths adjustable in the ranges 5ms to 75ms and 50ms to 750ms respectively. The recovery time can be calculated from the equation[78]

$$t = 3 \times 10^{-4} C \qquad 6.1$$

where t is time in seconds and C is capacitance in microfarads. The input load and output drive capability are specified in terms of a number of unit loads. For the M302 the values are 2.5 and 25 unit loads respectively. The M111 module contains sixteen individual inverters. The input load is 1 unit and the fan out 10 unit loads. The M121 module, which contains six individual AND/NOR gates was selected, employing economic considerations, from the range of gate modules available. A diagram of an AND/NOR gate is shown in figure 6.16. The simple NOR gate module contains ten gates and is more expensive than the M121. The input load and fan out values of the M121 gates are 1 and 10 unit loads respectively. Loading problems arise in applying the reset command to each counter bit and in applying 'transfer command 2'. These are overcome by utilising the high fan out inverters (30 unit loads) which are supplied with the counter modules. A diagram of the control logic in D.E.C. symbols is shown in figure 6.17. Code

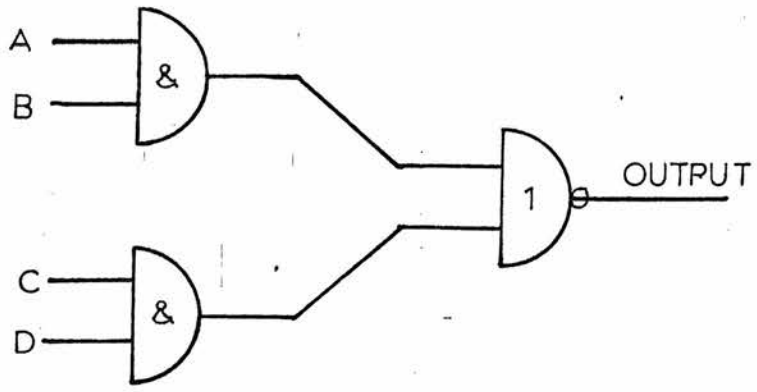

INPUTS				O/P
A	B	C	D	
0	0	0	0	1
0	0	0	1	1
0	0	1	0	1
0	0	1	1	0
0	1	0	0	1
0	1	0	1	1
0	1	1	0	1
0	1	1	1	0
1	0	0	0	1
1	0	0	1	1
1	0	1	0	1
1	0	1	1	0
1	1	0	0	0
1	1	0	1	0
1	1	1	0	0
1	1	1	1	0

Figure 6.16. The AND/NOR gate with its truth table.

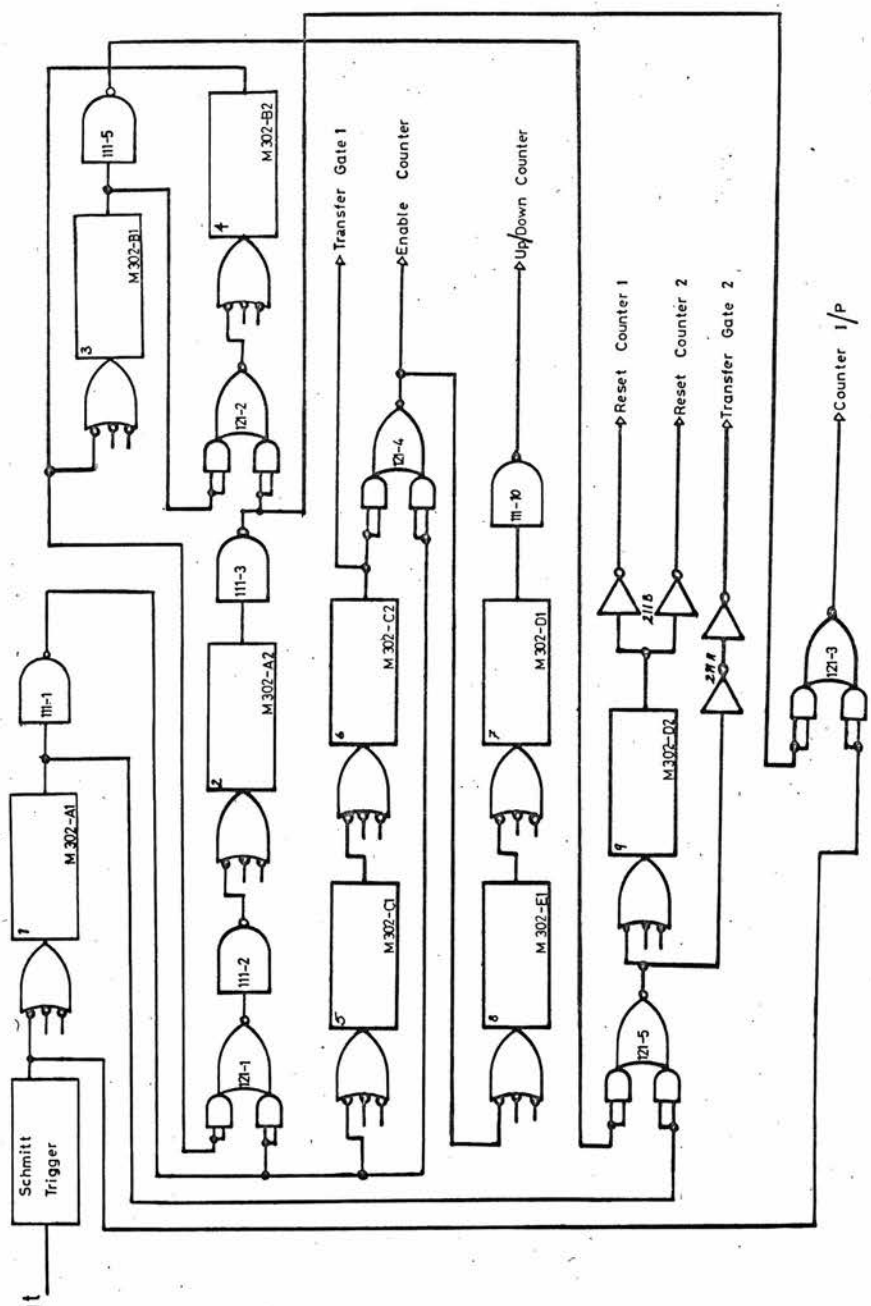

Figure 6.17. The control logic in DEC symbols.

numbers are attached to each card in the physical system and these are included in this diagram.

Module M501 is basically a Schmitt trigger with variable threshold and hysteresis. It has an upper threshold level variable between 1.7 and 2V and a lower threshold variable between 1.1 and 0.8V. The threshold levels are adjusted to produce a pulse train with a mark/space ratio of 1:1. Both an inverted and a non-inverted output are provided with fan outs of 8 and 10 unit loads respectively. The output voltage levels of 0 and 3 volts are compatible with the M-series modules.

The propagation delays of the modules which generate the counter gate control pulses require investigation in order to insure that gate 3 opens sufficiently quickly to transmit all the pulses from the Schmitt output. Typical delays introduced by an inverter and a gate are 15ns each. The delay introduced by the monostable between the trailing edge trigger and the leading edge of the output is typically 50 ns. From figure 6.17, it can be seen that the total propogation delay is 160 ns. Now, the pulse width of the Schmitt trigger output is approximately 500 ns, hence the initial pulse will be transmitted. Further, considering figure 6.17 the enable command will occur 95 ns prior to the arrival of the pulse train at the counter input, thereby satisfying the counter timing requirements.

Unused monostable inputs are connected to a +3V line in order to ensure maximum noise immunity. The principal error in the system is concerned with the stability of the monostable M2. Stability values are not quoted by the manufacturer so that these

measurements were carried out using the Advance TC-8 counter with a P6 plug-in unit. The accuracy of its internal oscillator is $\pm$ 1 in 10^7 Hz in the temperature range 10 to 40°C. M2 produces two pulses, one at the leading edge and one at the trailing edge of the voltage pulse. The accuracy of the width of the first pulse was found to be temperature dependent and was measured as 5 ms $\pm$ 2μs (i.e. $\pm$ 0.04%) in the temperature range 21 $\pm$ 1.5°C. The second pulse was compared to the first on two separate channels of an oscilloscope. The pulses were separated by using two 2-input nand gates. In one case the inputs of the nand gate were connected to the outputs of M2 and M5, in the other the output of M2 and the complementary output of M8 were used. The two pulses differed in width by 6μs $\pm$ 0.5μs in the above temperature range, the first pulse being longer. The accuracy of the system may be improved during flow measurement by monitoring the width of the first pulse and adjusting the values of the counts obtained for variations in pulse width. An offset will be present in the DIFFERENCE count due to the 6μs difference in pulse widths. This offset is an increasing function of the counter gate pulse width.

An examination of the output of the Schmitt circuit revealed two possible sources of error. The leading edge of the envelope of the Schmitt output varies by approximately $\pm$ 3μs with respect to the leading edge of the heating pulse, and, the Schmitt circuit does not respond to some of the input cycles during the first 5μs after the first Schmitt transition. A variable error with the maximum value of 20 counts was attributed to these sources. This value was obtained by monitoring the first pulse width of the output of

M2 and correcting the UP and DIFFERENCE counts while employing a 10 MHz signal and maintaining ambient temperature constant. It was found that 80 measurements had to be taken to eliminate the variance in the error due to the Schmitt. The distribution of the values of these measurements is not normal. It tends to be bimodal, as it was noted that during 20 consecutive measurements the maximum value of the counts with an error of $\pm$ 2 counts and the minimum counts with a similar error were recorded. Therefore, an alternative method of treating this error, when using a p.r.f. of around 1pps, is to take the mean of the maximum and minimum values obtained from 20 consecutive counts. These errors then reduce to $\pm$ 4 in the UP count and $\pm$ 4 plus a constant offset count in the DIFFERENCE count. These errors, which are the limits of the error magnitude, will be referred to as the Schmitt error.

6.4.3 Counter and Store

The counter and store are shown in block diagram form in figure 6.18. Figure 6.19 illustrates the basic unit from which the system is constructed. The basic counter module, type M211, is a 6 bit binary counter. Set and reset inputs are available for each bit together with both the output and its complement. Its operating conditions have already been described and are illustrated in figure 6.13.

It is intended to minimise the counter hardware required by registering only those bits which are determined by the blood temperature and flow rate. The counter will operate with a constant overflow. The total number of counts corresponding to

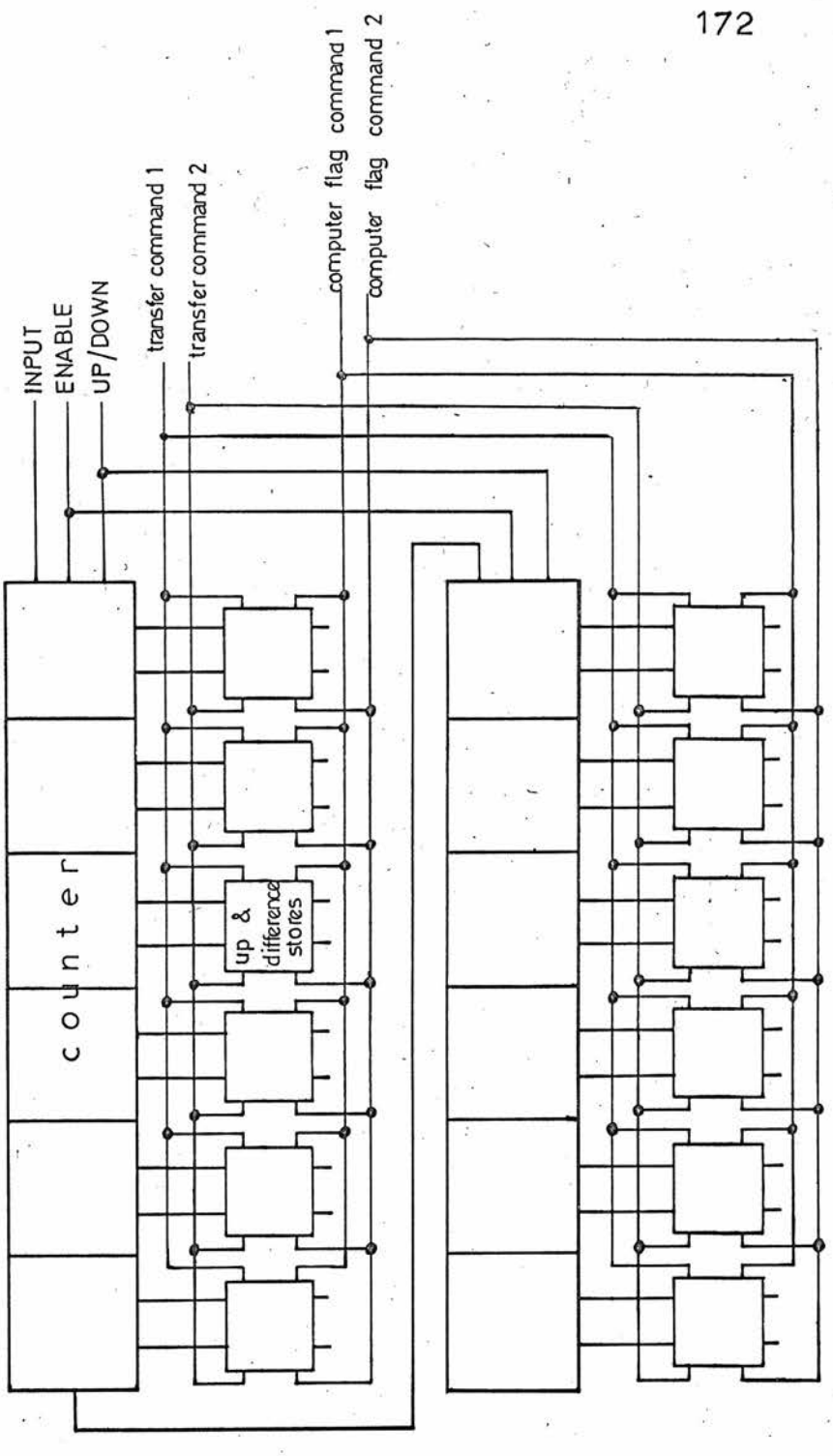

Figure 6.18.A block diagram of the counter and store.

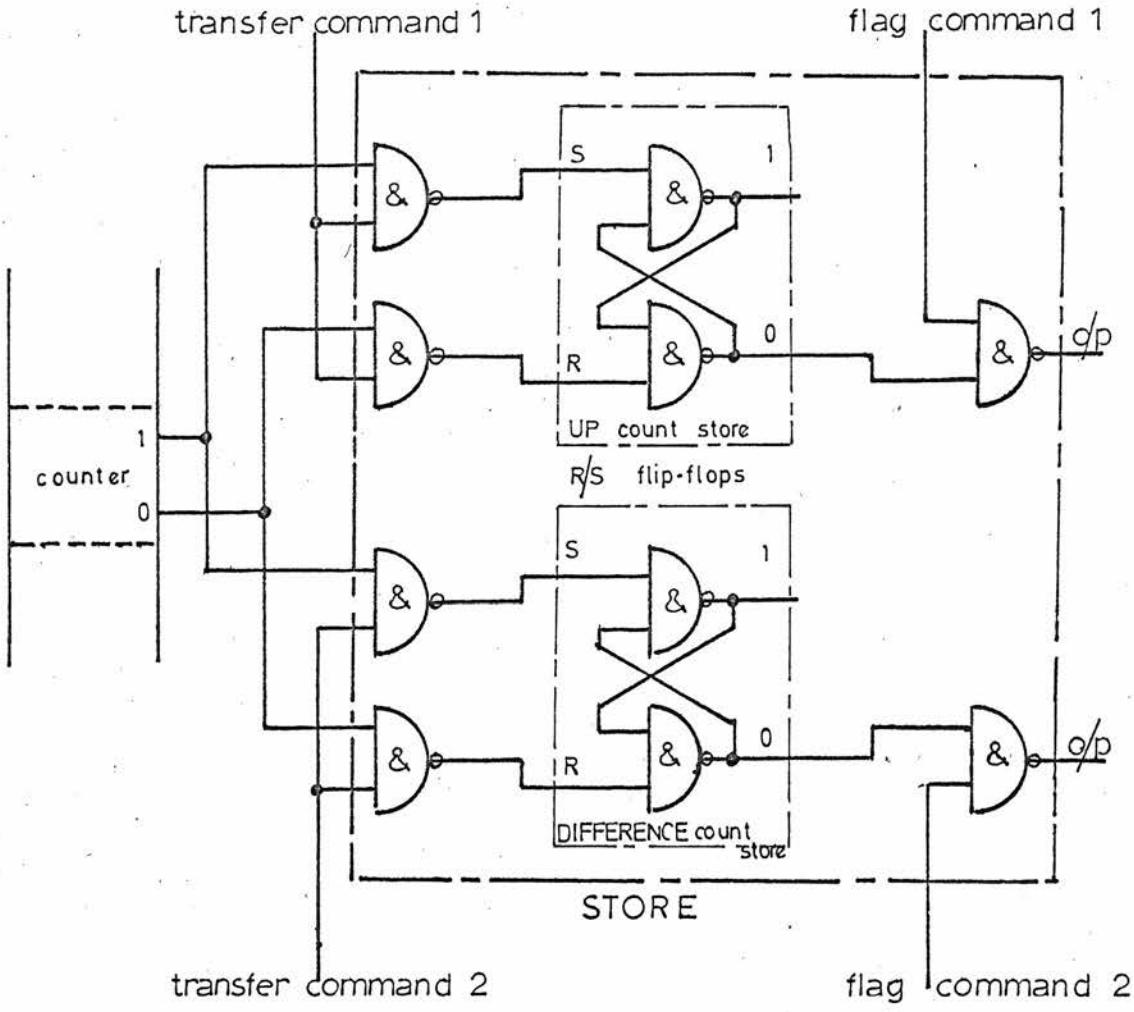

Figure 6.19. A diagram of the basic unit of the counter and store system.

the leading edge height of the voltage pulse must be calculated if it is required. This is achieved easily by calculating the total number of counts obtained at the known frequency with the known counter gate pulse width. Division by the counter capacity yields the number of times the counter overflows. The size of the counter required can be calculated by estimating the count change produced by the maximum temperature change and the maximum flow change. For the case of the 12 volt supply using a 1 KΩ thermistor with a temperature coefficient of -1.6%/°C., the voltage change is 0.196 mV/°C. The maximum change in deep body temperature in the bird is 4°C. Therefore, the voltage change is 784 mV, producing a count change of 1568 when a 5 ms counter gate pulse is used with a deviation of 400KHz/V. If the heating pulse in the zero flow case generates a 10°C temperature rise, this corresponds to a count difference between leading and trailing edges of the heating pulse of 3920. An increase in the flow rate will cause the count difference to diminish. Therefore, the estimated maximum count which is required to be measured is 3920 so that a 12 bit counter is required.

The counter is constructed by connecting two M211 modules in series. Two stores with the gates, shown in figure 6.20, are connected in parallel to each counter bit, so that by applying the appropriate transfer command to the appropriate gate, one store will contain the UP count and the other the DIFFERENCE count. The store unit employs Reset-Set type flip flops, eight of which are supplied as the M203 module. Each flip flop is made up of two 2-input nand gates with the outputs cross-coupled. Its input gating is

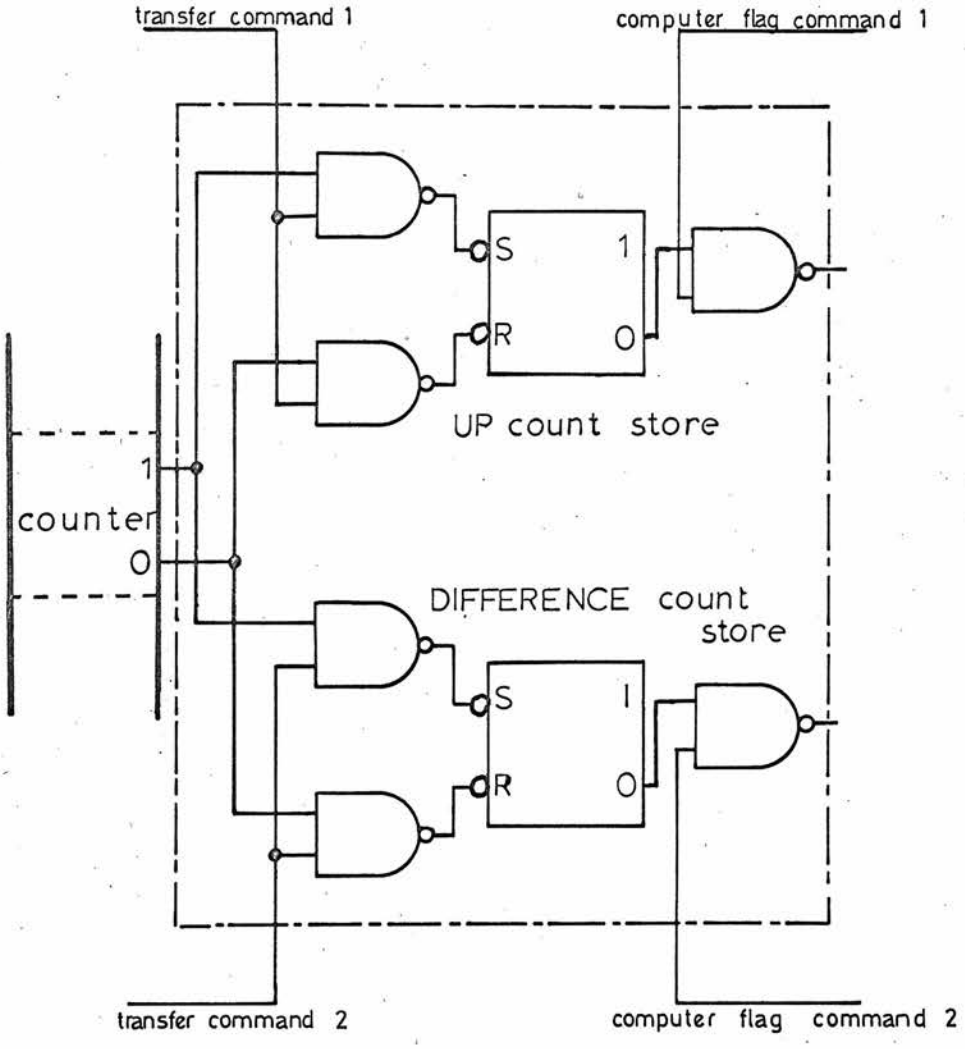

Figure 6.20. The basic unit of the counter and store in D.E.C. symbols.

constructed by connecting a 2-input nand gate to both the set and reset inputs. A further 2-input nand gate is connected to the complementary output of the flip flop to control the transmission of the store contents to the PDP-8L computer. The computer supplies the flag command.

The information contained in both stores is transferred to the computer at some convenient time between heating pulses. It is converted from binary to decimal form and printed out on a teletype as two columns of figures. One column contains the UP counts and the other the DIFFERENCE counts, while each line contains the information relating to one heating pulse. The computer is programmed to display twenty consecutive lines following a manual start command. The temperature corrected flow measurement is calculated from this data. With the in vivo flowmeter it is intended to use the PDP-8L computer to correct the flow measurement for changes in blood temperature, to obtain the mean values and to display the results in graphical form.

The counter system, a photograph of which is shown in figure 6.21, was tested using the apparatus shown in figure 6.22. The oscillator was modulated by a d.c. voltage adjustable in the range 0 to 4 volts, while its frequency was monitored by the TC8 Advance timer/counter. A pulse generator operating at a frequency of 1 pps opened the transmission gate for 100 ms. The width of the counter gate pulses was 8 ms in this case. Data from 20 consecutive pulses were recorded for each value of modulated voltage and the mean of the maximum and minimum values calculated for both the UP and DIFFERENCE counts. Figure 6.23 shows the results plotted as a graph of frequency

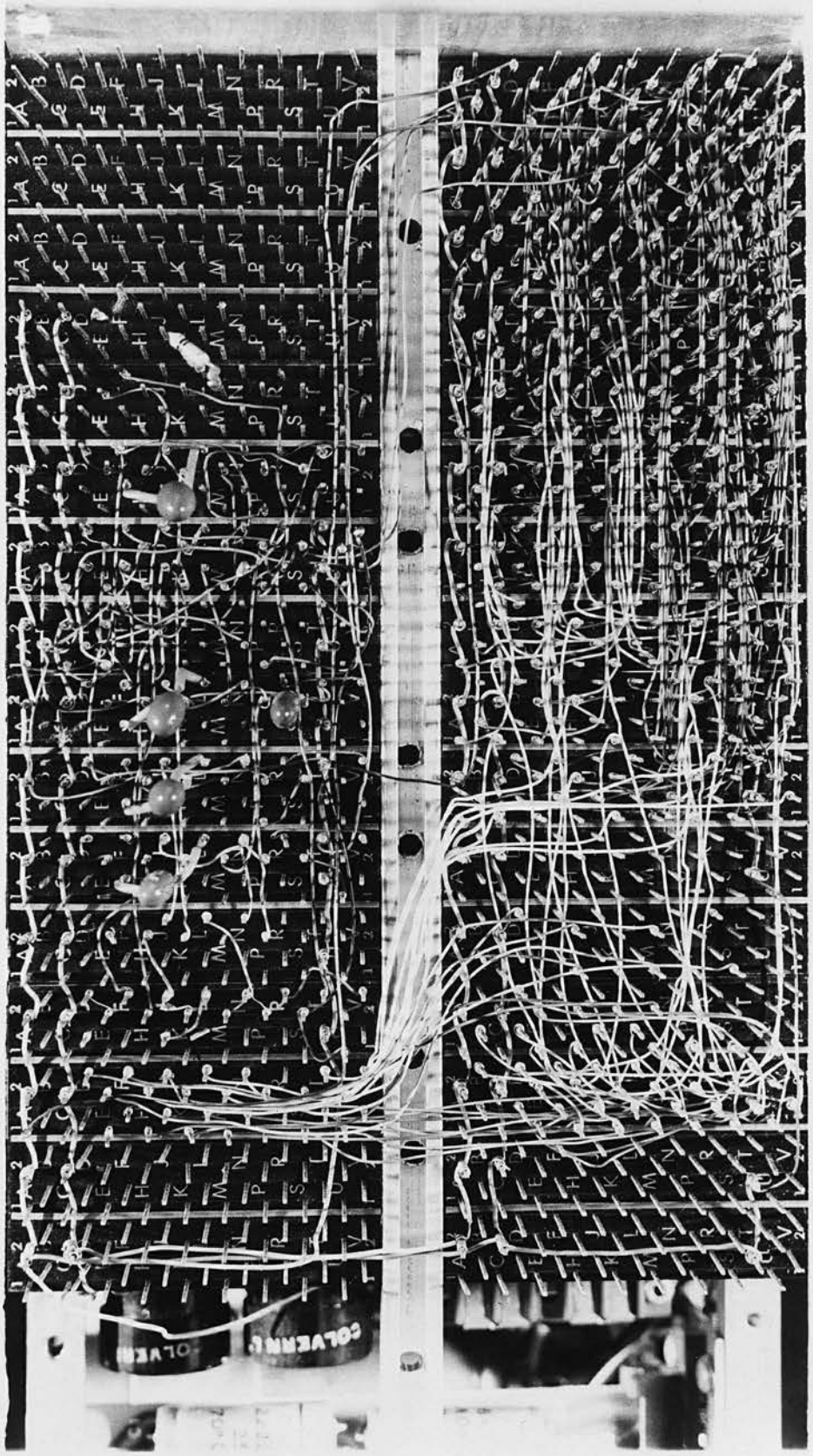

Figure 6.21. The DEC. circuit assembly.

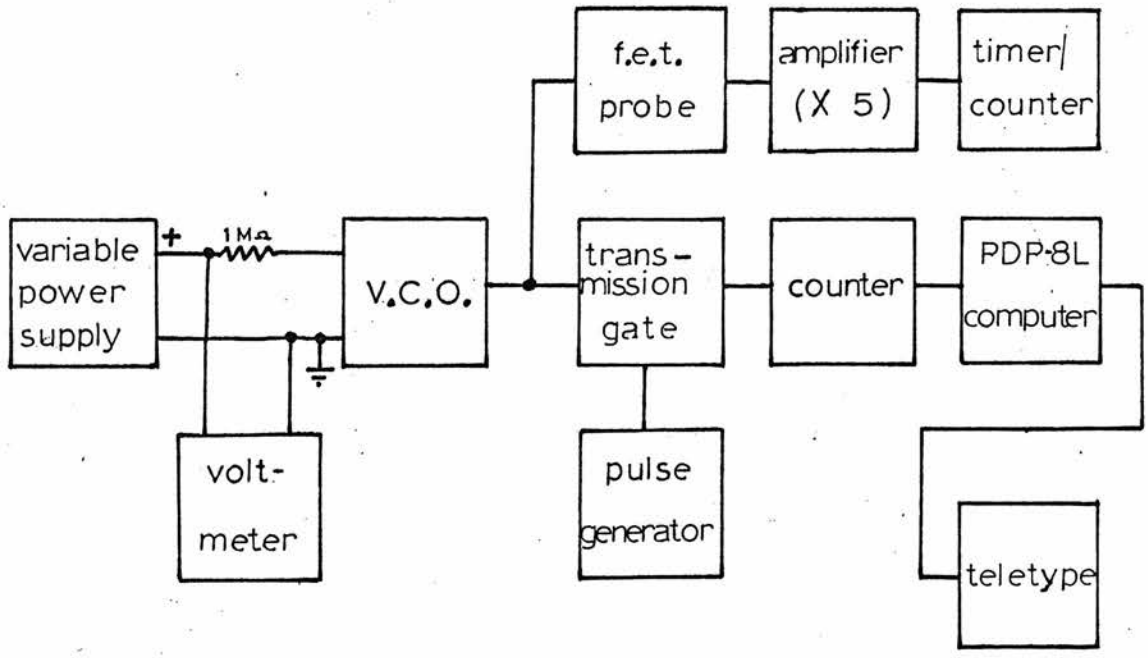

Figure 6.2.2.A block diagram of the equipment used in testing the counter.

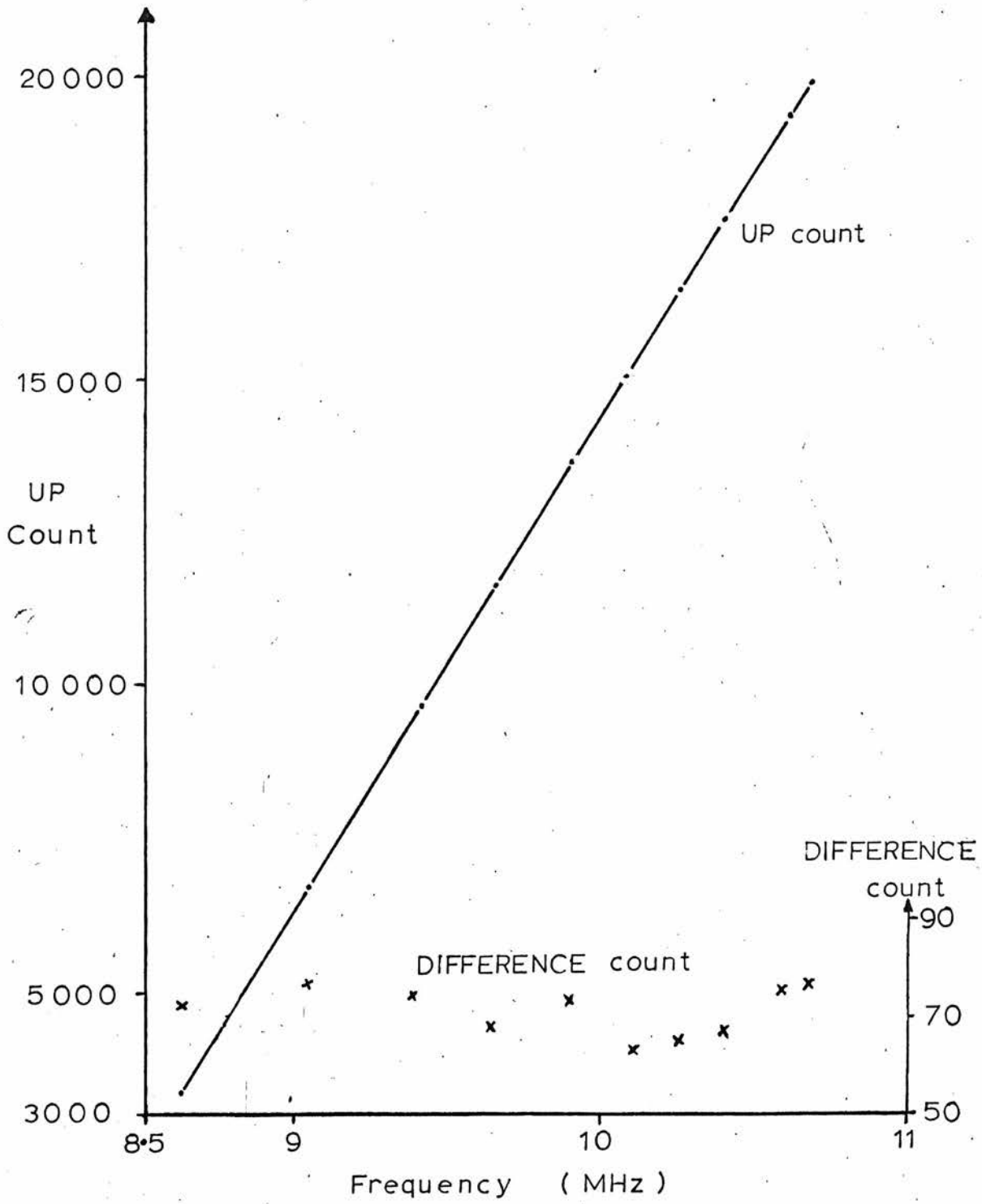

Figure 6.23. A graph of frequency versus UP and DOWN counts (pulse width = 100 mS : counter gate pulse width = 8mS)

versus UP and DIFFERENCE counts. Room temperature for these measurements lay within 21 ± 1.5°C. The sources of error already described, namely the oscillator stability, the counter gate pulse width and the Schmitt error, can be shown to account for the measured errors. For a 10 MHz signal the maximum error caused by the oscillator stability in both the UP and DIFFERENCE count is ±8 counts. This assumes that, in the short term (100 ms), the stability is such as to contribute no additional error to the DIFFERENCE count. The counter gate pulse width contributes a maximum error ±32 counts (0.04%) in the UP count and ±5 counts in the DIFFERENCE count. The offset caused by the difference in the widths of the two pulses has a value of approximately 80 counts with an 8 ms pulse. The Schmitt error is ±4 counts in the UP and DIFFERENCE counts with a constant offset of-10 counts. Hence the total error limits in the UP count are ±44 counts and in the DIFFERENCE count ±17 for a 10 MHz signal. The results lie within these limits.

6.5 The Model Flow System

The flow system which is used with water and blood is shown in figure 6.24. A glass reservoir is mounted approximately 3 metres above the level of the thermistor. (The height is limited by the height of the laboratory.) The liquid flow rate in the outlet tube is controlled by a tap at its base, the output of which is deflected either into a second reservoir or into a measuring cylinder. The maximum flow rate of water and blood through a 1 mm diameter tube was found to be 1.56 ml s^{-1} and 0.72 ml s^{-1} respectively. Different maximum flow rates for a given pressure head are, of course, expected from the data on kinematic viscosity shown in table 5.1. The pressure

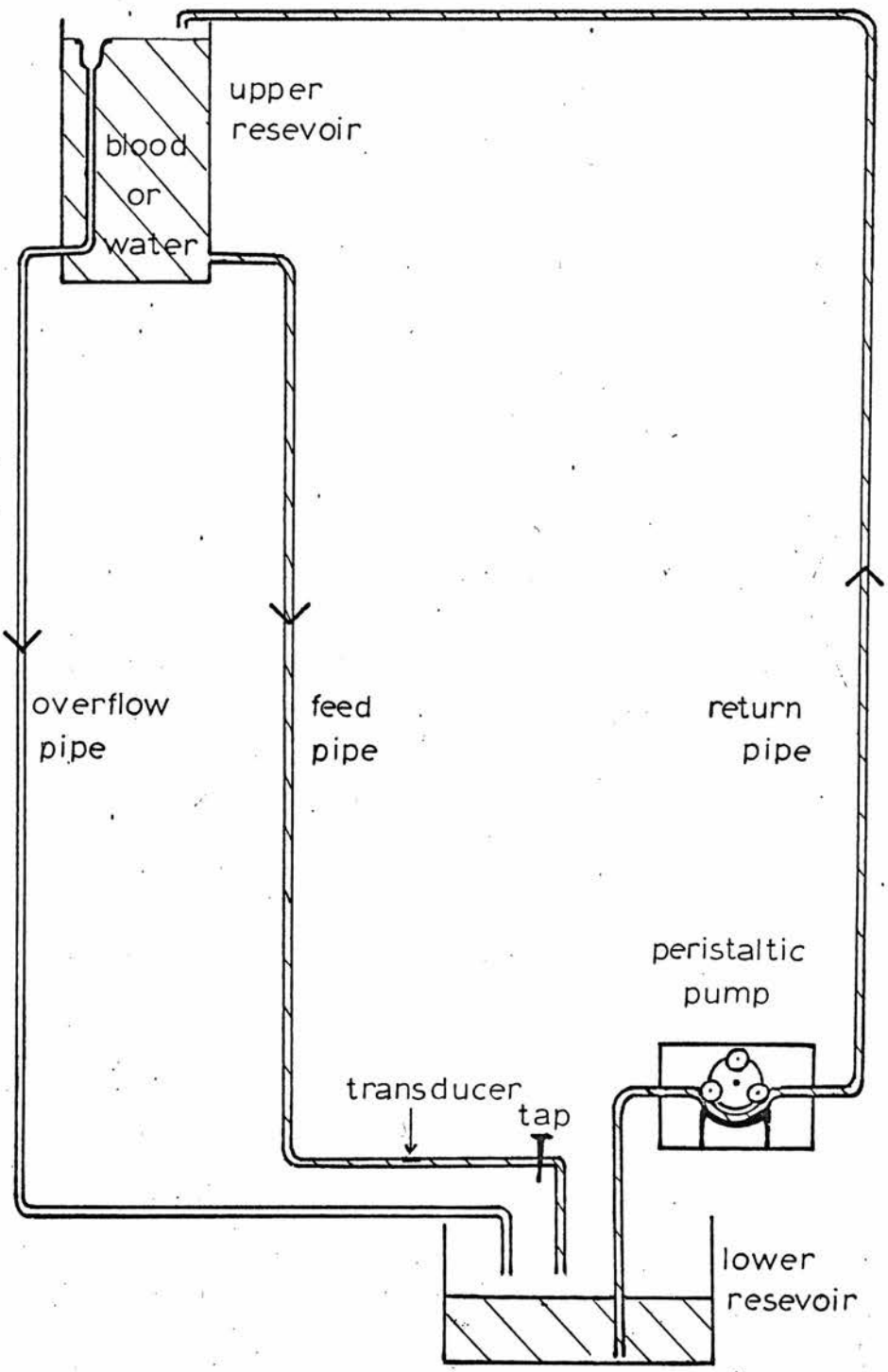

Figure 6.24. A diagram of the flow system.

head constancy is achieved by pumping the liquid from the lower to the upper reservoir and draining the excess back to the lower reservoir via the overflow tube. P.V.C. tubes are used, with the exception of the section containing the thermistor which is silicone rubber. No reaction was observed between the system materials and the blood, which was citrated human blood. However, a clotting reaction occurred at the overflow inlet when there was a very low flow rate at that point. The problem was solved by a suitable adjustment of the pump to increase return flow. The volumetric flow rate, controlled by the tap, was measured by directing the flow into the measuring cylinder for a known time. The maximum error in the flow rate measurement was assessed as ±5% by carrying out several measurements at one of a range of flow rates and examining the spread of the results.

Chapter 7

FLOWMETER ASSESSMENT

7.1 Test conditions and errors

In the tests to assess flowmeter performance a thermistor with a resistance of 1.24 KΩ at 25°C and a B-value of 1330 (α_{25} = 1.5%/°C) was used. All flow measurements were carried out at room temperature (21°C ± 1.5°C) in order to avoid the problem of maintaining the flow system at the deep body temperature of the bird (40°C ± 2°C). The variation in ambient temperature was kept to the practical minimum of ±1.5°C in order to minimise the temperature dependent equipment errors. The thermistor resistance and temperature coefficient at 21°C are 1.32 KΩ and 1.54%/°C respectively. The fluids used in the tests were tap water and citrated human blood. The blood was obtained from a blood bank as outdated stock and was stored at 0°C before use. Avian blood was not used because of the difficulty of obtaining sufficient to fill the flow system.

Circuit adjustments are made in the following order. The heating current is measured by monitoring the voltage pulse train appearing across the known resistor in series with the thermistor, and is adjusted to the required value. The absolute accuracy of the pulse amplitude measurement is ±5%. The amplitude of the voltage pulses appearing at the output of the differential amplifier is adjusted to a suitable value to modulate the oscillator. A leading edge voltage of around 2.5 V was chosen. The counter gate control pulse is then measured on an oscilloscope and is adjusted to the required width. The number of times that the counter overflows during the UP count can now be calculated. In general, however, the total

number of UP counts is not required.

The width of the first counter gate pulse of each heating pulse was monitored during the flow measurement using the Advance TC-8 timer/counter. The error in the UP count introduced by the variation in pulse width (±0.04% or ±2μs for a 5 ms pulse) was reduced by applying a suitable correction to the count. For a 10 MHz signal, the UP count is corrected by the addition or subtraction of a number of counts equal to the variation from the required value. This variation is derived from the TC-8 reading. The accuracy of the timer/counter measurement is ±0.1μs, so that this contribution to UP count error is reduced to ±1 count. When the same correction is applied in the case of a 5 ms pulse with a signal frequency of 10.4 MHz or 9.5 MHz the error is reduced to ±2 counts. At all frequencies the variation in pulse width is used as the value of the UP count correction. The magnitude of the error in the DIFFERENCE count caused by the variation in the two counter gate pulses is more complicated to establish. The second pulse width is equal to the first minus 6μs ±0.5μs. At constant signal frequency the DIFFERENCE count error is simply that contributed by 6μs ± 0.5μs. However, different signal frequencies, f_1 and f_2, during the UP and DOWN counts respectively, will cause an error in the DIFFERENCE count equal to

$$\pm((f_1 - f_2) \times 0.04\% \text{ of the first pulse width})$$

in addition to the contribution made by the 6μs ±0.5μs. Further, the frequency, f_2, corresponding to a particular flow rate is also a function of temperature, so that there is the possibility of producing further error, which arises during the 6μs ± 0.5μs period as f_2

changes with temperature. For a 5 ms pulse and a frequency difference, $f_1 - f_2$, of 500 KHz the DIFFERENCE count error is ±1 plus the contribution during the 6μs ± 0.5μs period. At a frequency, f_2, of 10.3 MHz ± 100 KHz the error produced by the 6μs ± 0.5μs difference in pulse widths is 62 ± 6. Thus, the total error in the DIFFERENCE count is a constant offset count of 62 and a variable error of ± 7 counts. The values used in this example have been chosen from the results in this chapter to produce the maximum error applicable to the flow measurements made.

Twenty consecutive readings were made for each measurement. The mean of the maximum and minimum values of both the UP and DIFFERENCE counts were calculated after adjusting the UP counts to account for variations in the counter gate pulses. As discussed in Chapter 6, the error in both the UP and DIFFERENCE counts due to variations in the initial response of the Schmitt circuit is a maximum of ±4 counts. It also contributes a constant offset of -10 counts. The oscillator stability contributes an error of ±5 in both the UP and DIFFERENCE counts (assuming that the carrier frequency does not drift in the interval between them). Hence, for a 5 ms counter gate pulse the total maximum equipment error is ±10 in the UP count and 52 ± 16 in the DIFFERENCE count for each measurement.

7.2 The correction factors

It is now necessary to evaluate the correction factor which is required to account for the variations in the deviation of the V.C.O. with modulating voltage. It is also necessary to establish the validity of the correction for variations in liquid temperature, $(1 - \alpha_o(T_b - T_o))$, which was developed in Chapter 1. Here the

temperature coefficient of resistance, α_o, is assumed to be constant.

The approach adopted for both cases is to examine the DIFFERENCE count measurements obtained when the thermistor is supplied with current pulses in a bath of still water at different temperatures. Calculated and experimentally derived results can then be compared. The heating and counter gate pulse widths were adjusted to 50 ms and 5 ms respectively. The reference value of the counter gate pulse, measured by the timer/counter, was 4.91 ms. The amplitude of the heating pulses was adjusted to produce a peak voltage of 6V across the thermistor at room temperature (21°C in this case). The difference in voltage between the leading and trailing edges of the pulses was measured as 0.9V. A pulse repetition rate of 0.2 pps was used to ensure that the device cooled to ambient temperature between pulses. The output of the differential amplifier was adjusted to a leading edge height of 2.5 V. The temperature of the water bath was measured with a mercury thermometer to an accuracy of $\pm$ 0.1°C. All measurements were made when the water appeared still. The temperature range used was restricted in order to satisfy the condition of maintaining the bath at a constant temperature over twenty readings without significant free convection. The results are shown in figure 7.1. It can be seen that, in the temperature range 21°C $\pm$ 1.5°C the DIFFERENCE count must be corrected by $\mp$ 4 counts for a change in ambient temperature corresponding to $\pm$ 9 counts. This is the value of the sum of the correction factors and it is used to correct subsequent results. However, before continuing, it is necessary to examine the components which make up this correction factor. It will be referred to as the "combined correction factor".

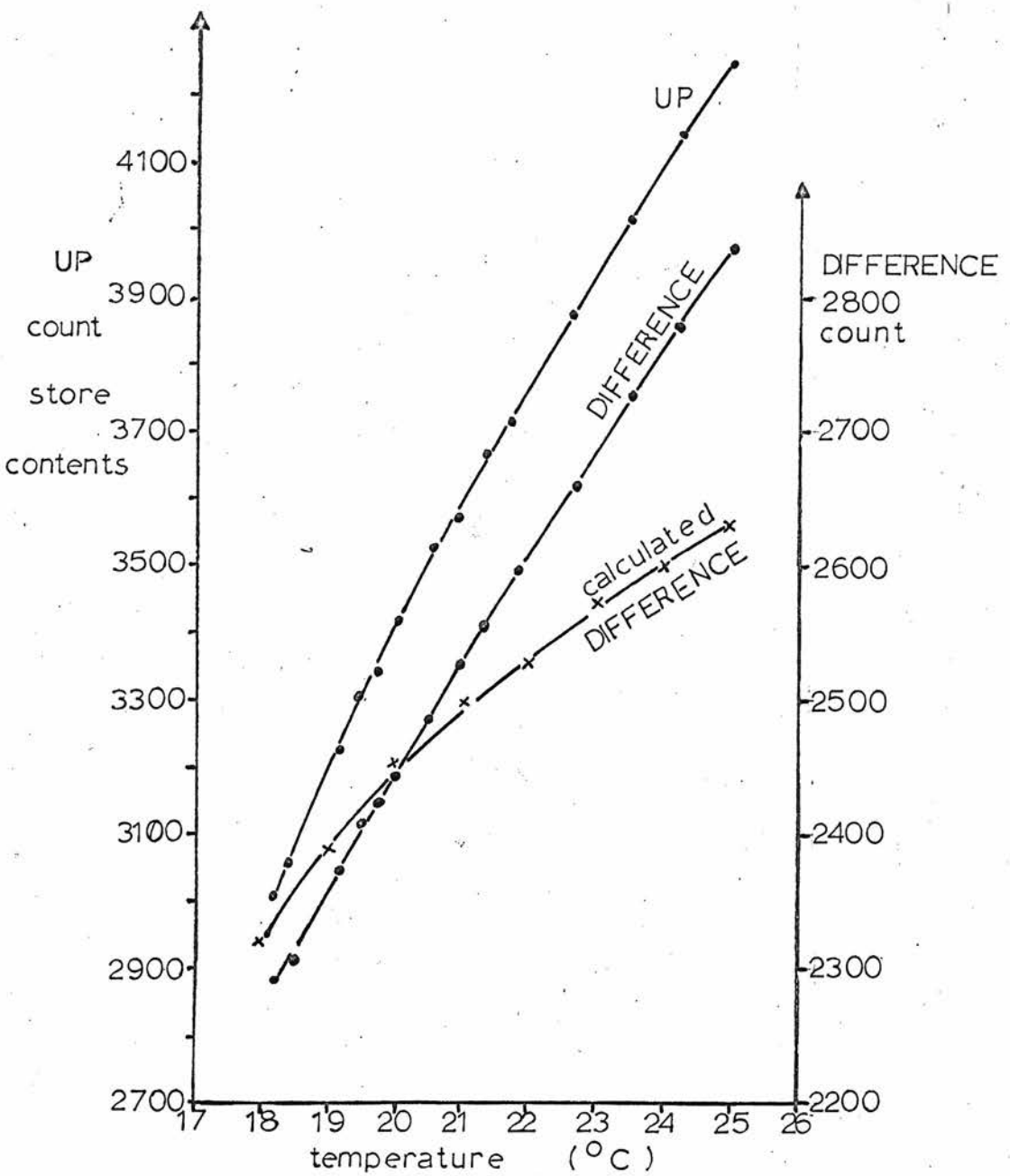

Figure 7.1. The graphs of UP and DIFFERENCE counts versus temperature for a thermistor in still water (P.A.=4·55mA: P.W.=50ms). The calculated values of DIFFERENCE count versus temperature are also included.

The amplitudes of the leading and trailing edges of the modulating voltages are known at 21°C so that it is possible to estimate the DIFFERENCE count at that temperature by estimating the resulting frequencies from figure 6.7 (the graph of oscillator frequency versus modulating voltage). Further, the DIFFERENCE counts over the temperature range can be estimated in a similar way by assuming a constant value of temperature coefficient, α_o, and a constant voltage difference of 0.9 V. (The DIFFERENCE voltage corresponding to the DIFFERENCE counts is smaller than this value because the frequency was counted over a period equal to 10% of the heating pulse width. However, this value of 0.9 V is sufficiently accurate for the purposes of this analysis). The leading and trailing edge voltages at 21 $\pm$ X°C are then ($V_{21°C} \mp V_{21°C} \times \alpha_o$) and ($V_{21°C} \mp V_{21°C} \times \alpha_o - 0.9$) volts. This presupposes that the value of the temperature correction factor, $(1-\alpha_o(T_b - To))$, is zero. The results of these calculations are plotted in figure 7.1. The change in DIFFERENCE count with temperature obtained in this way is attributable to the variation in deviation of the V.C.O. with modulating voltage.

An approximate value for the temperature correction factor which is applicable about 21°C can be calculated from the available data together with equation 1.9,

$$\frac{T-T_b}{1-\alpha_o(T_b-T_o)} = \frac{I^2R_o}{K'(\omega) + \frac{C}{t_2-t_1} + I^2R_o\alpha_o}$$

The DIFFERENCE voltage of 0.9 V measured at 21°C corresponds to a temperature difference, $T-T_b$, of 9.74°C, assuming α_o to be constant. If the temperature correction factor, $(1 - \alpha_o(T_b - T_o))$, is applied to this value for T_o = 20°C, then the corrected value is 9.89°C.

That is, the approximate value of the temperature correction factor is + 0.15°C per °C rise from the reference temperature. 0.15°C/°C rise corresponds to an increase in the DIFFERENCE voltage of 13.8 mV/°C rise. Now, if the value of the oscillator deviation is 330 KHz/V at a modulating voltage of 1.61 V, (i.e. 4.91 x 330 counts/V in this case) then the DOWN count is increased by 22 counts per °C rise and the DIFFERENCE count decreased by the same amount. (The DIFFERENCE count will, of course, decrease with increasing DOWN count because of the mode of operation of the counter and of the V.C.O. The DOWN count is larger than the UP count, hence the DIFFERENCE count is counted down from zero). Hence, the temperature correction factor in terms of counts corresponds to a decrease in DIFFERENCE counts of 22 counts per °C rise.

Combining the estimates for the "deviation and temperature correction factors" for the temperature range 21°C $\pm$ 1°C yields the approximate value $\mp$ 60 counts per $\pm$ 1°C. This does not correspond to the experimentally derived value of $\mp$ 80 counts per $\pm$ 1°C. The source of the discrepancy lies in the assumption that the temperature coefficient of resistance, α_o, is constant. α_o is by definition a function of temperature. Refering to section 1.3,

$$\alpha_o = \frac{1}{R} \frac{dR}{dT}$$

where $R = Ro \exp B(\frac{1}{T} \frac{-1}{To})$ 7.1

Therefore, $\alpha = -\frac{B}{T^2}$; or more commonly, $\alpha = \frac{-B}{T^2} \times 100$ %/°C. The change in α between 21°C and 22°C can be shown to be 0.011%/°C.

An approximate calculation of the temperature correction factor applicable about 21°C can be carried out using equation

7.1. The value of the DIFFERENCE resistance for a 10°C temperature rise from 21°C can be shown to be 182.5Ω. Repetition of this calculation for a 10°C rise from 22°C yields 178.6Ω. Thus there is a change in the DIFFERENCE resistance of -3.9Ω/°C, which is not accounted for when the approximate equation, $R = Ro\ (1-\alpha_o(T-T_o))$ is used. However, these calculations do not take into account the change in power dissipation with variations in ambient temperature. If the average temperature coefficient is assumed to be-1.46%/°C, then a 1°C increase in ambient temperature will reduce the power dissipation and the temperature rise at the trailing edge of the pulse by a similar percentage. This temperature rise achieved from an ambient temperature of 22°C is approximately 9.854°C. The DIFFERENCE resistance at 22°C for this temperature rise becomes 176Ω so that the change in the DIFFERENCE resistance now becomes -6.5Ω/°C rise. By an argument similar to that used previously to determine the temperature correction factor in terms of counts, this decrease in DIFFERENCE resistance corresponds to a decrease in the DIFFERENCE voltage of 29.5mV and an increase in the DIFFERENCE count of 47 counts/°C rise. The correction required is therefore -47 counts/°C rise. This is a more accurate value for the temperature correction factor which is, of course, already contained in the experimentally derived "combined correction factor". The sum of the calculated correction factors does not equal the experimentally derived value because of the approximate nature of the calculations.

One very important point has still to be considered: namely, the effect of variations of the temperature coefficient with ambient

temperature on the spread of DIFFERENCE counts obtained over the flow range. That is, if the temperature coefficient varies significantly over the temperature range experienced at the trailing edge of the heating pulse ($21^{\circ}C + 10^{\circ}C$) $\pm$ $2^{\circ}C$, then the variation of the trailing edge resistance with flow will also be a function of ambient temperature. The temperature coefficients calculated at $31^{\circ}C$ and $33^{\circ}C$ are 1.4391 and 1.4204 $\%/^{\circ}C$ respectively. Therefore, the temperature coefficient varies by $\pm$ $0.019\%/2^{\circ}C$ variation about mean ambient temperature. If the change in DIFFERENCE count between zero flow and maximum flow is 150 counts at $31^{\circ}C$ then a variation in ambient temperature of $\pm$ $2^{\circ}C$ alters this value by $\mp$ 2 counts. An error of $\pm$ $0.67\%/^{\circ}C$ is introduced in the flow measurement. This error cannot be corrected without considerable additional computations.

The above values, of course, apply to this particular thermistor and oscillator. It is envisaged that the combined correction factor for any flowmeter will be experimentally established about *mean* blood temperature using the technique described in this section. The computations then necessary to obtain the corrected DIFFERENCE count are considerably simplified by using the empirically derived relationship between UP and DIFFERENCE counts in the required temperature range.

It is possible to comment on the accuracy of the system for temperature measurement from figure 7.1. The UP count increases by 180 counts per $^{\circ}C$ rise, so that 1 count corresponds to $0.0056^{\circ}C$. However, an UP count error of $\pm$ 10 counts limits the accuracy to $\pm$ $0.056^{\circ}C$. This is more than sufficient to meet the normal requirements of deep body temperature measurement.

7.3 Results

The thermistor was fitted into the artificial blood vessel and included in the flow system. A photograph of the transducer is shown in figure 7.2. Initially water was used.

The change in DIFFERENCE counts between zero flow and maximum flow (95 ml/minute), ΔC_d, was measured for various current pulse widths. A current pulse amplitude of 4.55 mA, which produces a peak voltage of 6V at 21°C, was used. The counter gate pulse width was constant at 5 ms. The results are shown in figure 7.3. The maximum pulse repetition rate which permits the device to cool to ambient temperature between pulses was also determined for various current pulse widths. This repetition rate was taken as the maximum value for no significant change in 100 consecutive readings of the UP count under zero flow conditions. The results are also shown in figure 7.3. In these flowmeter tests the repetition rate used was slower than the suggested maximum values.

The change in DIFFERENCE counts between zero flow and maximum flow for various current pulse amplitudes was also determined. The current pulse width and gating pulse width were 50 ms and 5 ms respectively. The DIFFERENCE votage appearing across the thermistor at zero flow was also measured and the equivalent temperature rise calculated using equation 7.1. These results are presented in figure 7.4.

The error in the measurements of change of DIFFERENCE count contributed by the equipment is considerably less than shown in the graphs because the time between the zero flow and maximum flow readings was not sufficient to permit relatively large changes in

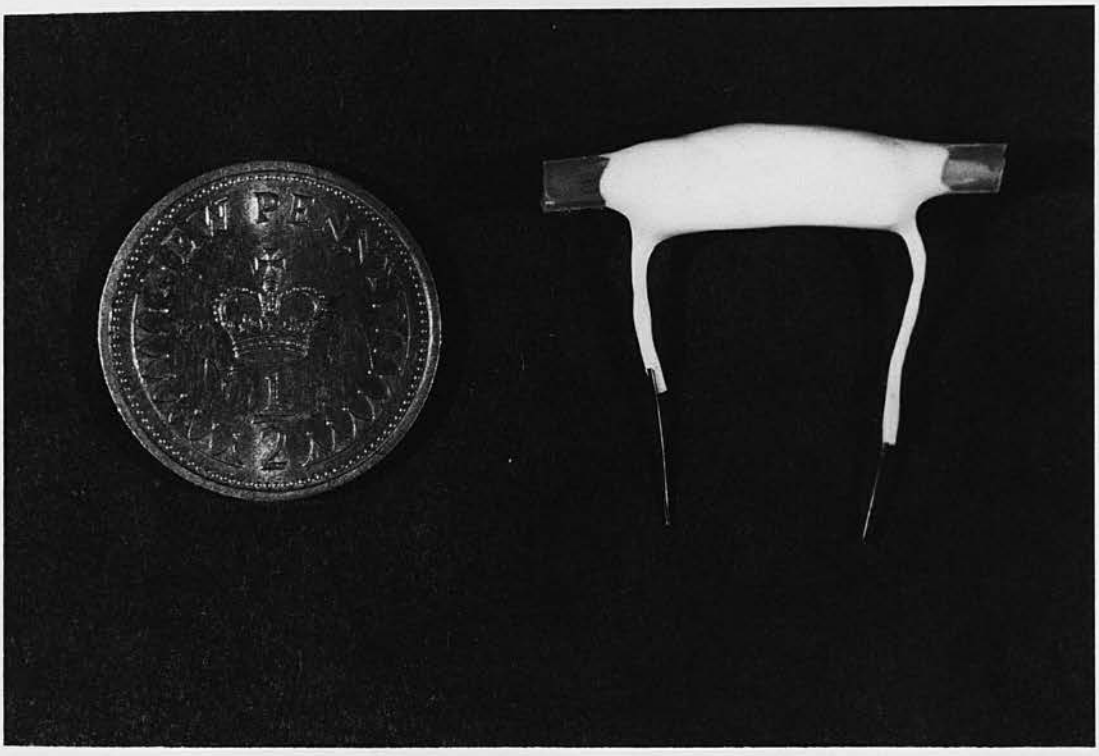

Figure 7.2. The transducer.

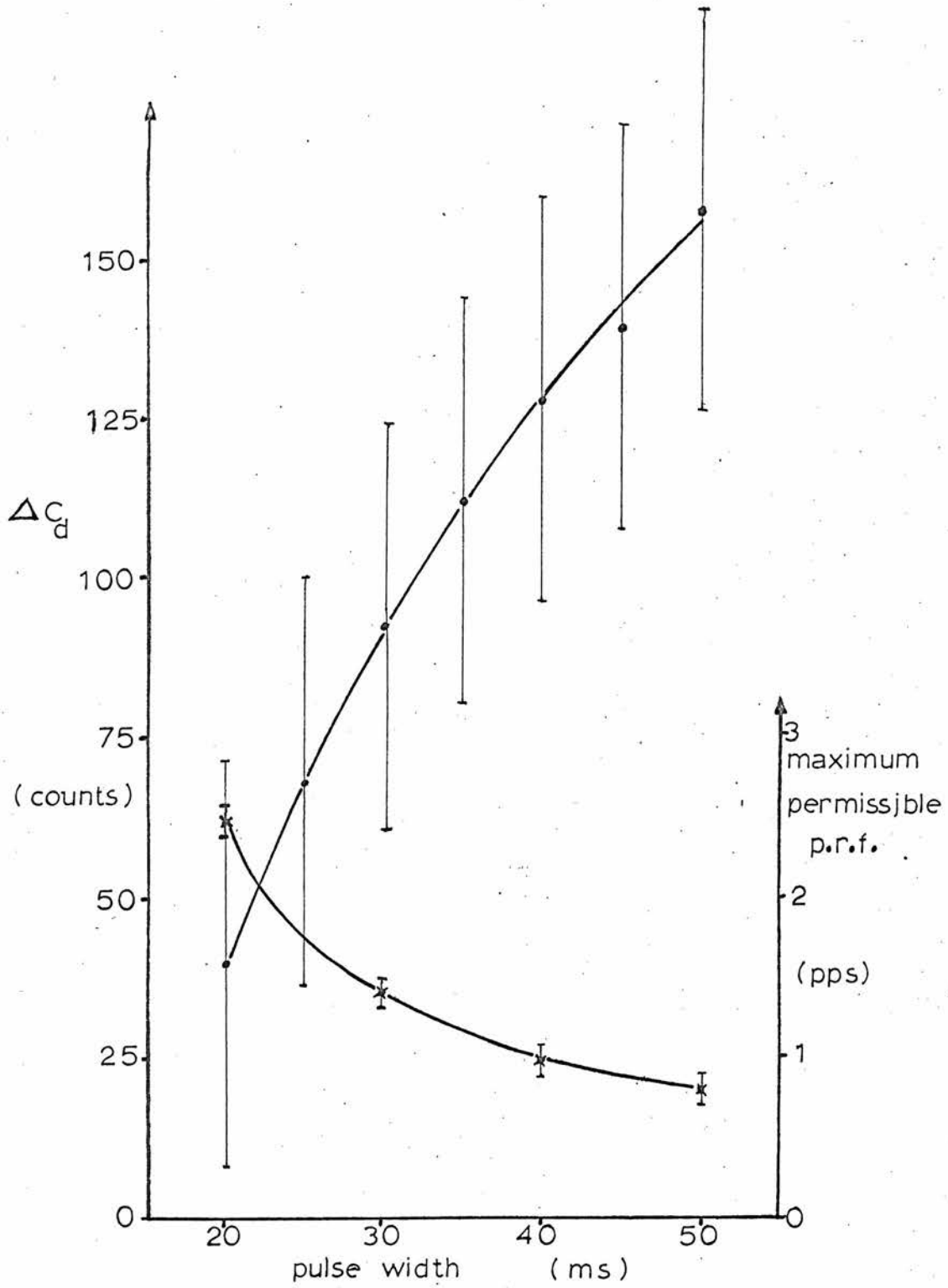

Figure 7.3. The graphs of current pulse width versus the change in DIFFERENCE count between zero flow and maximum flow, ΔC_d, and the maximum permissible p.r.f. (P.A. = 4·55 mA)

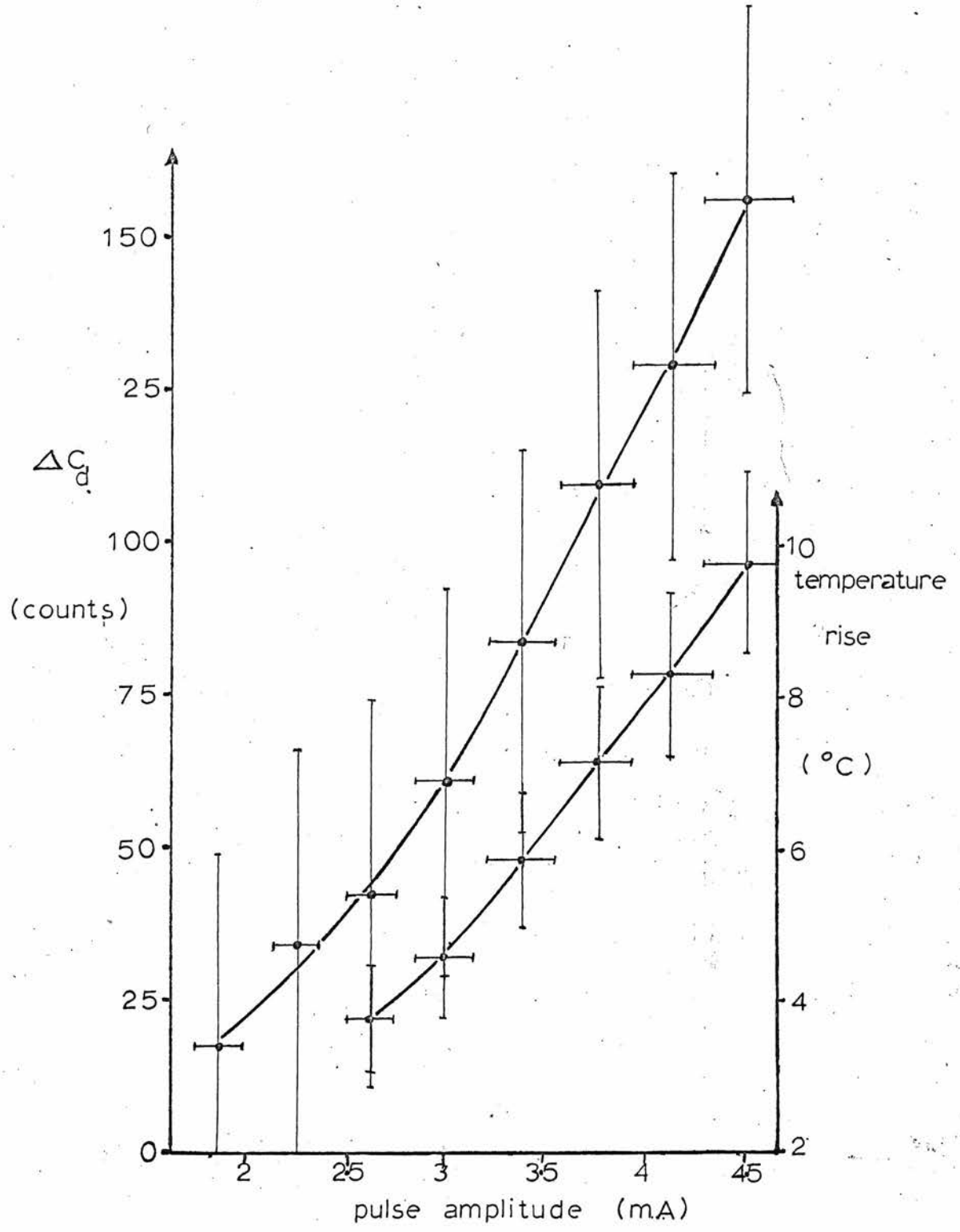

Figure 7.4. The graphs of current pulse amplitude versus the change in DIFFERENCE count between maximum flow and zero flow, ΔC_d, and the temperature rise achieved at zero flow. (P.W.=50 ms)

ambient temperature. The shapes of the graphs obtained conform to expectations. The change in DIFFERENCE count increases at a decreasing rate with the heating pulse amplitude. The maximum pulse repetition rate is a decreasing function of heating pulse width.

With this basic information on the performance of the flowmeter it is possible to indicate the required operating conditions in the bird. The minimum pulse repetition rate permitted is 1 pps and the maximum desirable temperature rise is 10°C. It is obviously desirable to maximise the change in DIFFERENCE counts with flow given these limitations together with the maximum voltage restriction. Therefore, for a thermistor at 40°C whose characteristics are similar to the thermistor used at 21°C the maximum value of ΔC_d is approximately 150 counts with a heating and gating pulse width of 40 ms and 5 ms respectively and a 6V supply. If the thermistor used in the above tests is used at 40°C, its resistance and temperature coefficient decrease to 1.03 KΩ and 1.38%/°C. Further, if the amplitude of the current pulse is increased to produce identical temperature rises then the values of ΔC_d are reduced by approximately 10%. It is, of course, possible to increase the current to obtain the same sensitivity without increasing the supply voltage; however, the temperature rise obtained may exceed the 10°C limit.

The relationship between flow rate and DIFFERENCE count over the temperature range 21°C $\pm$ 1.5°C was examined using a current pulse width and amplitude of 50 ms and 4.55 mA respectively and a gating pulse width of 5 ms. These values are chosen to produce a relatively large change in DIFFERENCE count over the flow range in

order to reduce the significance of the errors already discussed. The results for both water and blood, which are obtained under identical conditions, are shown in figure 7.5. It can be seen that the results are similar, which suggests that calibration tests may be carried out using water, and the results applied to blood flow measurement. This assumes that citrated human blood and avian blood have identical thermal properties and, in certain respects, similar flow properties. The flow range used with blood is restricted by the pressure head available. The shapes of the graphs are similar to that shown in figure 1.3 in Chapter 1. (As the flow rate increases and cools the device, the trailing edge voltage increases. The corresponding frequency decreases so that the counter contents at the end of the DOWN count increase.)

This flowmeter is most sensitive over the range 0 to 1 ml/s. The error in the flow reading is approximately $\pm$ 0.1 ml/s.

Measurements were made of the DIFFERENCE count at zero flow and at maximum flow immediately after filling the flow system with blood and at various times over a period of 2 hours. These results were reproducible within the stated error limits, which suggests that there was no significant deposit of material from the blood on to the transducer. This was confirmed by a visual inspection of the thermistor at the end of the experiment.

7.4 Discussion

It can be seen that equation 1.6

$$K'(u) = K'(0) + a'(1 - e^{-b'u})$$

fits the results obtained for flow rate versus DIFFERENCE counts when $a' = 170$ and $b' = 1{\cdot}8$. The value of a' in terms of counts

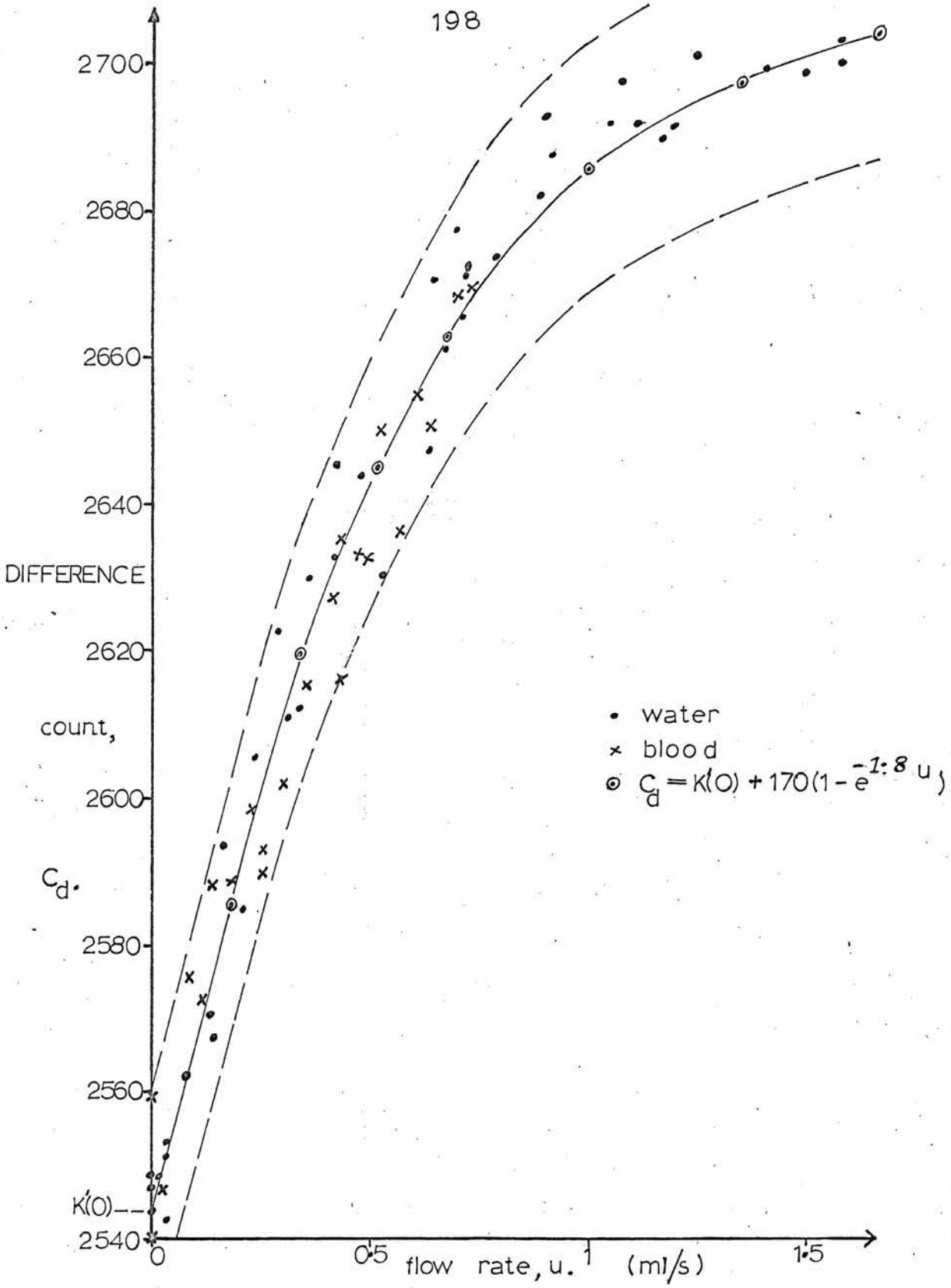

Figure 7.5. The graph of DIFFERENCE count versus flow rate for blood and water. (P.W.=50ms : P.A.=4·55mA) The graph of $C_d = K'(0) + 170(1 - e^{-1.8u})$ is also included.

is a function of several factors which include the B-value and resistance of the thermistor, the amplitude and width of the heating pulse, the counter gate pulse width, the frequency and deviation of the oscillator and the thermal properties of the materials involved in the heat transfer process. The value of b' is determined by the geometry and dimensions of the flow transducer. Its value is independent of the current pulse amplitude and width. The value of a' may be increased by increasing the frequency and deviation of the oscillator. Variation of the dimensions of the heating pulse in order to increase a' is limited by the restrictions on supply voltage (6 V), the temperature rise (10°C max.) and the pulse repetition rate (1 pps minimum), which were discussed in previous sections. It may be possible to increase a' by selecting another type of thermistor material with a more favourable relationship between B-value and resistivity.

It is possible to calibrate the output of the flowmeter described for different heating pulse dimensions from the available data together with the results of the experiment which must be carried out to determine the combined deviation and temperature correction factors applicable to a particular system. This experiment also yields the calibration curve for blood temperature versus counts and the value of $K'(0)$ at the pre-selected reference temperature, T_o. The value of b' does not change providing the flow transducer geometry is identical. The value of a' can be calculated. The change in DIFFERENCE counts from zero flow to 1.56 ml/s, ΔC_d, is known so that

$$a' = \Delta C_d \left(1 - e^{-1.8 \times 1.56}\right)^{-1}$$

Hence, the calibration curve for flow rate versus DIFFERENCE counts can be determined.

A computer can easily be programmed to apply the 'combined correction factor' to each reading and to compute the temperature and flow rate of blood from the calibration curves.

The accuracy of the flowmeter is primarily limited by the equipment error. This error can be considerably reduced by using phase lock loop (P.L.L.) integrated circuits in the input section of the data processing circuitry. This I.C., which is shown as a block diagram in figure 7.6, is only recently available. A block diagram of the proposed modifications [79] is shown in figure 7.7. A continuous F.M. signal is transmitted from the bird in this new arrangement. One P.L.L. I.C. is employed as a demodulator whose purpose is to locate the information bearing part of the received signal. The leading edge of the demodulated signal sets a bistable which is used to form the sampling pulses. The leading edge is also used to trigger a monostable whose output defines when the second sampling pulse occurs. A second P.L.L. I.C. is employed to track the carrier frequency. The narrow band filter included in its feedback loop is designed to smooth out the F.M. signal. The bistable is reset by the overflow output of the counter so that the counter gate pulse width is directly related to the carrier frequency. The original counter is controlled by pulses which are derived from the counter gate pulses. With this system the transmission gate of the implant circuitry is not required and the oscillator drift is compensated for by varying the counter gate pulse width. The use of a bistable to form the counter gate pulses

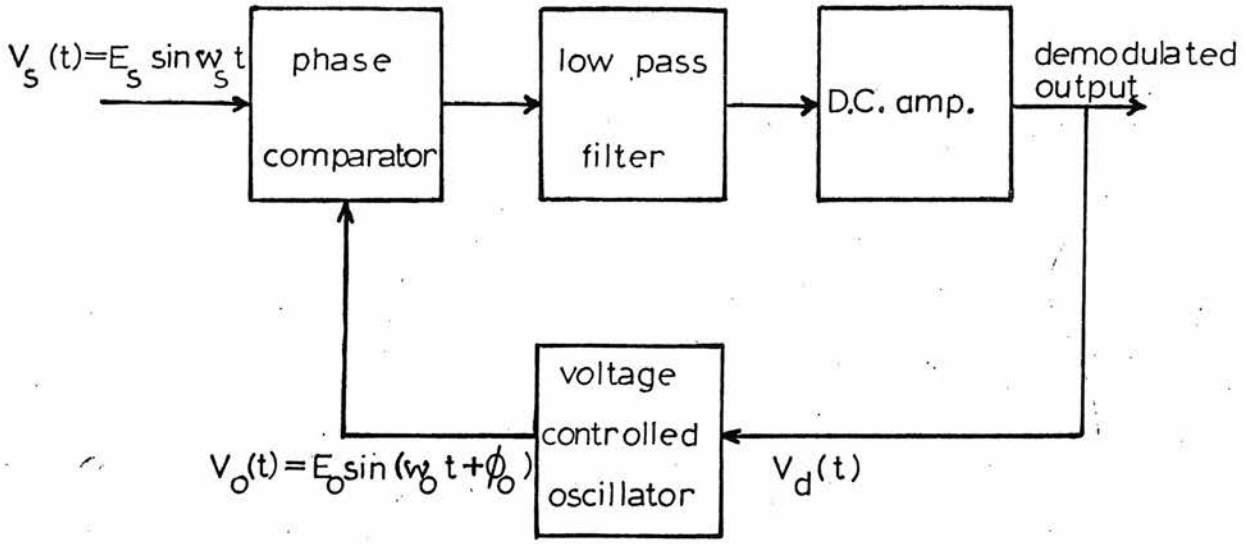

Figure 7.6. A block diagram of a phase-lock loop I.C.

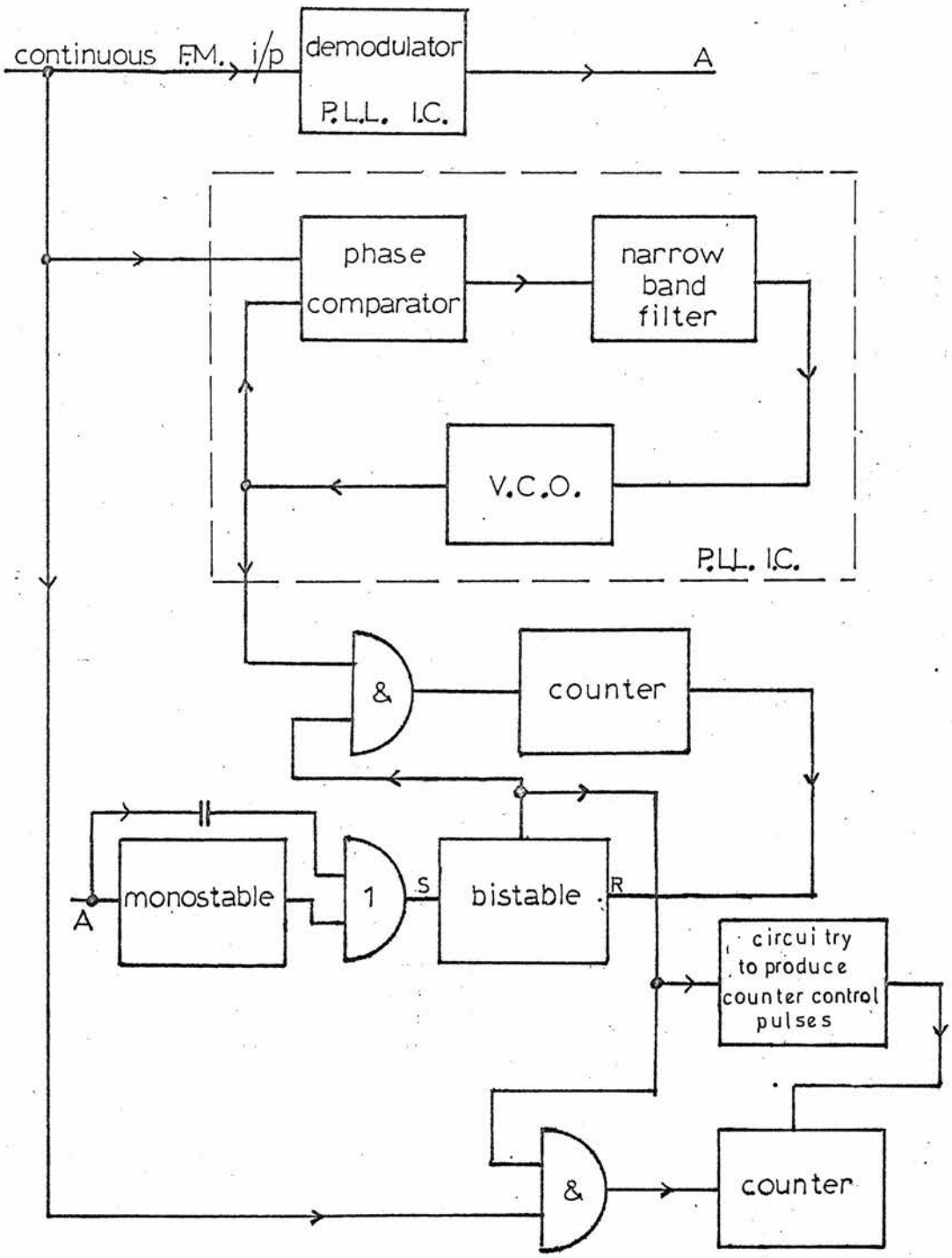

Figure 7.7. A block diagram of the proposed modifications to the receiver circuitry.[79]

removes the errors caused by the monostable M2 in the original system. Hence, the equipment error can be considerably reduced and possibly eliminated by using this modification. The error in the digital system is capable of being reduced to 1 count in the final place of the UP count and 2 counts in the final place of the DIFFERENCE count. The accuracy of the temperature measurement then becomes $\pm$ 0.0056°C and the error in the flow measurement $\pm$ 2% for a $\pm$ 2°C variation in ambient temperature.

The error in flow measurement in the bird is also a function of the amplitude of the pulsatile component of the flow. The period of the fundamental of this component is 200 ms so that it will not be averaged when the heating pulse width is 40 ms. However, the amplitude of this component is expected to be small compared with the amplitude of the range of flow rates. Further, it is relatively large changes in flow rate that are of interest to the physiologists. Two approaches may be taken to deal with the pulsatile component. The computer may be programmed to average it over the period in which the steady flow component is constant. These periods are expected to be of the order of or greater than 10s. Alternatively, the magnitude of the pulsatile component can be taken as the maximum sensitivity required of the flowmeter. The second approach is obviously dependent on the relative magnitudes of the flow components.

The power consumption of the flowmeter described can now be calculated. It is equivalent to a continuous consumption of 1.09mW, when the current pulse width and amplitude are 40 ms and 4.55 mA respectively and the thermistor resistance equals 1.32 KΩ. If half the battery capacity of 160 mA hours is available to drive the

transducer, then it will be capable of continuous operation for a period of 445 hours (i.e. approximately 18.5 days). This is sufficient to meet the requirements of the physiological experiments outlined in Chapter 1. The operating time may be increased at the expense of the sensitivity of the instrument if required.

The two flow ranges of interest in the physiological research are 0 to 0.5 ml/s in the oviduct blood supply system and 0 to 2 ml/s in the renal portal system. The kidney is supplied by several vessels so that the maximum flow rate in any one vessel can be taken as approximately 1 ml/s. The existing flow transducer will operate satisfactorily in both cases. The operating range of the flowmeter can be extended by increasing the diameter of the artificial blood vessel in order to reduce the velocity of the blood flowing over the thermistor. For a flow rate of 1 ml/s the velocity of the blood averaged over the cross sectional area of the vessel in the existing flowmeter is 128 cm/s. For an identical average velocity at a flow rate of 2 ml/s, the vessel diameter must be increased to approximately 1.4 mm. Now, if the current pulse width is maintained at 40 ms, the penetration depth of the thermal disturbance at the trailing edge of the heating pulse will not occupy the same proportion of the tube radius as with the 1 mm diameter vessel, and the sensitivity of the flowmeter will be reduced.

This flowmeter, then, is capable of meeting the requirements outlined in Chapter 1. It will measure the steady flow rate in small diameter blood vessels. The power consumption is sufficiently low for the transducer and its associated circuitry to be implanted in the bird. The associated circuitry consists of a pulse

generator and a voltage controlled oscillator, both of which can be fabricated in thin film form. Work is continuing in the development of this circuitry and of the receiver circuitry.

APPENDIX 1

A Short Survey of Techniques for Blood Flow Measurement

A.1.1 Introduction

There is no flowmeter exploiting a single physical principle which can meet all the requirements of blood flow measurement. Instead there is a large number of flowmeters exploiting different principles with different inherent restrictions which can measure specific cases of blood flow. The variety of methods used include mechanical, electrical, acoustical, thermal and optical techniques. Many types have largely been made obsolete by the latest work in the field. This survey concentrates on the more modern methods, while describing briefly some of the old ones. A fuller description of the older methods, along with the bibliography, is to be found in reference 80. A summary of the limitations of the methods described in this Appendix is contained in Tables 1.1 and 1.2.

A.1.2 Outflow methods

The simplest and most reliable method of measuring the mean volumetric flow rate consists of collecting blood from an opened vessel in a graduated cylinder over a measured period of time. This method is most frequently employed to calibrate other types of flowmeter. The system may be made more sophisticated by arranging that the cylinder contents are returned automatically to the circulation system after a known period of time. Short time measurements are obtained which are repeatable at intervals. The intervals are a function of the rapidity of emptying the cylinder.

For very low flow rates an alternative method has been developed[81] in which the time interval between drops leaving the

vessel is measured. The mean flow rate can be calculated by assuming each drop contains an identical known volume of blood. A photoelectric transducer may be used to detect each drop and control the timing device. These systems are obviously independent of the properties and velocity profile of the blood.

A.1.3 Venous occlusion method

This method[80] consists of temporarily occluding the venous flow from an organ or limb and measuring the resulting rate of change of volume by immersing the part in a container of water and noting the rate of displacement of the water. It is a rapid method of estimating the relative volumetric flow rate to a region.

A.1.4 Travelling markers

The earliest flowmeters designed to work in arteries[82] employed a U-tube containing saline solution inserted in the vessel with a tap system such that the blood could be diverted through the U-tube. Figure A.1.1 illustrates the arrangement. The flow measurement was made by diverting the blood into the tube and timing the blood-saline interface over a known length. The mean flow rate was then calculated assuming a known tube diameter. The principal disadvantage was that the tube had to be refilled with saline before the measurement was repeated.

More sophisticated systems have been developed[80] in which a transparent tube of known dimensions is implanted in the blood vessel. An air bubble of sufficient size to fill a short section of the tube is injected into one end and timed as it travels a known distance along the tube before being removed at the other end.

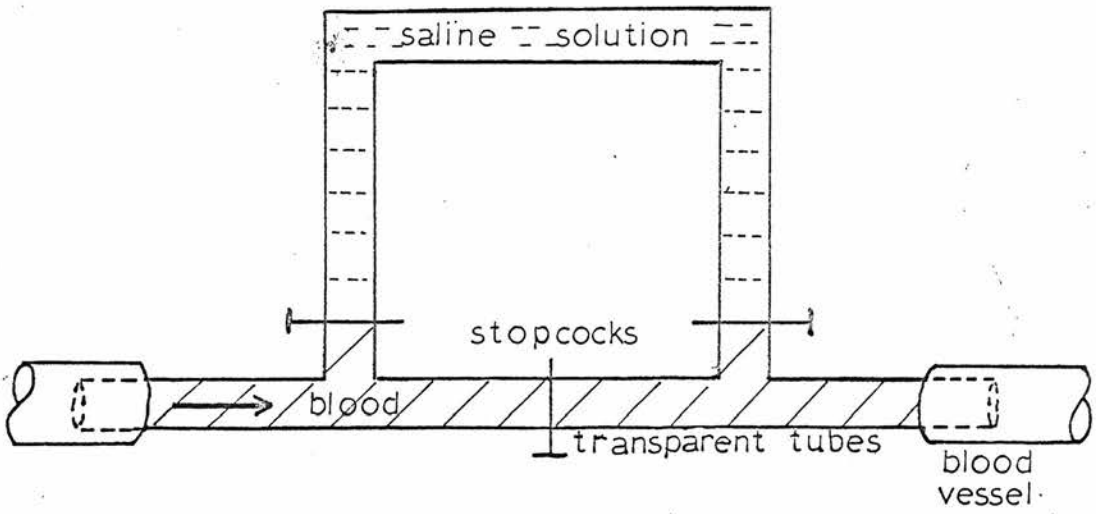

Figure A.1.1. A diagram of an early U-tube flowmeter

Automatic injection-timing-removal systems have been developed[83]. This method assumes that the bubble and blood velocity are identical. However, at high flow rates the bubble moves faster than the flow because it appears to lose contact with the wall and to travel in the axial stream. This produces an error[84] of less than 5% at a flow rate of 200 ml/minute in a 4 mm diameter tube.

A thermal marker technique has been described by Stow[85] in which a heated section of blood is timed between two temperature sensors a known distance apart in a tube of known dimensions. This has the advantage that no marker removal system is necessary. Dyes and radiopaque materials have also been used[80] as markers in systems using the appropriate detectors. In general these methods will only permit single short time recordings of mean volumetric flow rate which can be repeated at intervals. They depend on the marker remaining clearly defined in the blood stream over the measured distance. In general the calibration is independent of the velocity profile and physical properties of the blood.

A.1.5 Marker dilution methods

Several useful methods for estimating flow rate in capillary beds and through organs have been developed[80] using markers which mix with the blood. The volumetric flow rates are estimated by plotting a time-concentration curve of the marker at the injection site, as in the case of the capillary beds, or at the exit of an organ when the injection site is at its entrance. The method, in the case of capillary beds, assumes that the diffusion equilibrium of the marker in the blood and tissue is achieved extremely rapidly compared to the flow rate of the blood. The outflow from the

region contains a constant fraction of the total marker in the region. The fraction is dependent on the partition coefficient of the marker in the blood and the particular tissue. This coefficient is a constant so that the rate of clearance of the marker is proportional to the blood flow rate. Knowing the partition coefficient, the volume and density of tissue involved, and the quantity of marker injected, the amount of marker taken up by unit weight of tissue can be calculated. Thus the mean flow rate is calculated per unit weight of tissue. The markers include radioactive xenon or krypton dissolved in saline and nitrous oxide which is absorbed by the lungs.

Similar thermal methods[85,86] have been described in which a region of tissue experiences a short heating pulse. The effective thermal conductivity of the region is a function of the blood flow rate through it. Therefore a temperature-time graph describing the region immediately after the pulse reflects the flow rate.

The mixing method may also be used in blood vessels and organs with cavities, such as the heart, providing it can be assumed that the blood and marker are thoroughly mixed before being detected. A thermal[87] dilution method used in vessels involves injecting a stream of saline at a constant mass flow rate and at a known temperature into the blood whose temperature is also known. The mass flow rate is calculated from the temperature of the saline-blood mixture at some point downstream from the injection site. Dye substances with suitable detectors have also been used in this work. The description of the calculations required to evaluate the flow rate from marker concentration curves is contained in reference 90.

In a study[88] to evaluate the error in the dilution method, the dye dilution technique and an electromagnetic flowmeter were employed simultaneously to measure small peripheral artery flow in dogs. They consistently failed to yield results within ± 25% of each other. However, when cardiac output measurements were compared, the results were within ± 5% of each other. A maximum error of 6% is claimed in the electromagnetic flowmeter measurements. Lewis et al.[89] compared renal blood flow measurements in dogs using radioactive xenon and collection of the venous outflow. In the range 10 to 100 ml/minute they claim "almost identical results". Above a flow rate of 100 ml/minute the measurements varied by a maximum of ± 25%.

A.1.6 Displacement methods

A simple flowmeter registering the mean volumetric flow over a fixed time has been described by Dawes et al.[91] In principle the system consists of a chamber with two compartments separated by a flexible bag as shown in figure A.1.2. Blood is diverted into the lower compartment, and the saline within the bag is displaced into the upper compartment to make contact with two electrodes. The time taken for the saline to travel between the two electrodes indicates the volumetric flow rate of the blood. This system has an accuracy of ± 4% in the flow range 1 to 50 ml/minute and provides short time measurements repeatable at intervals.

A.1.7 Hydrodynamic methods

Hydrodynamic methods of flow measurement[80,92] subdivide into two types, those based on the registration of pressure differences

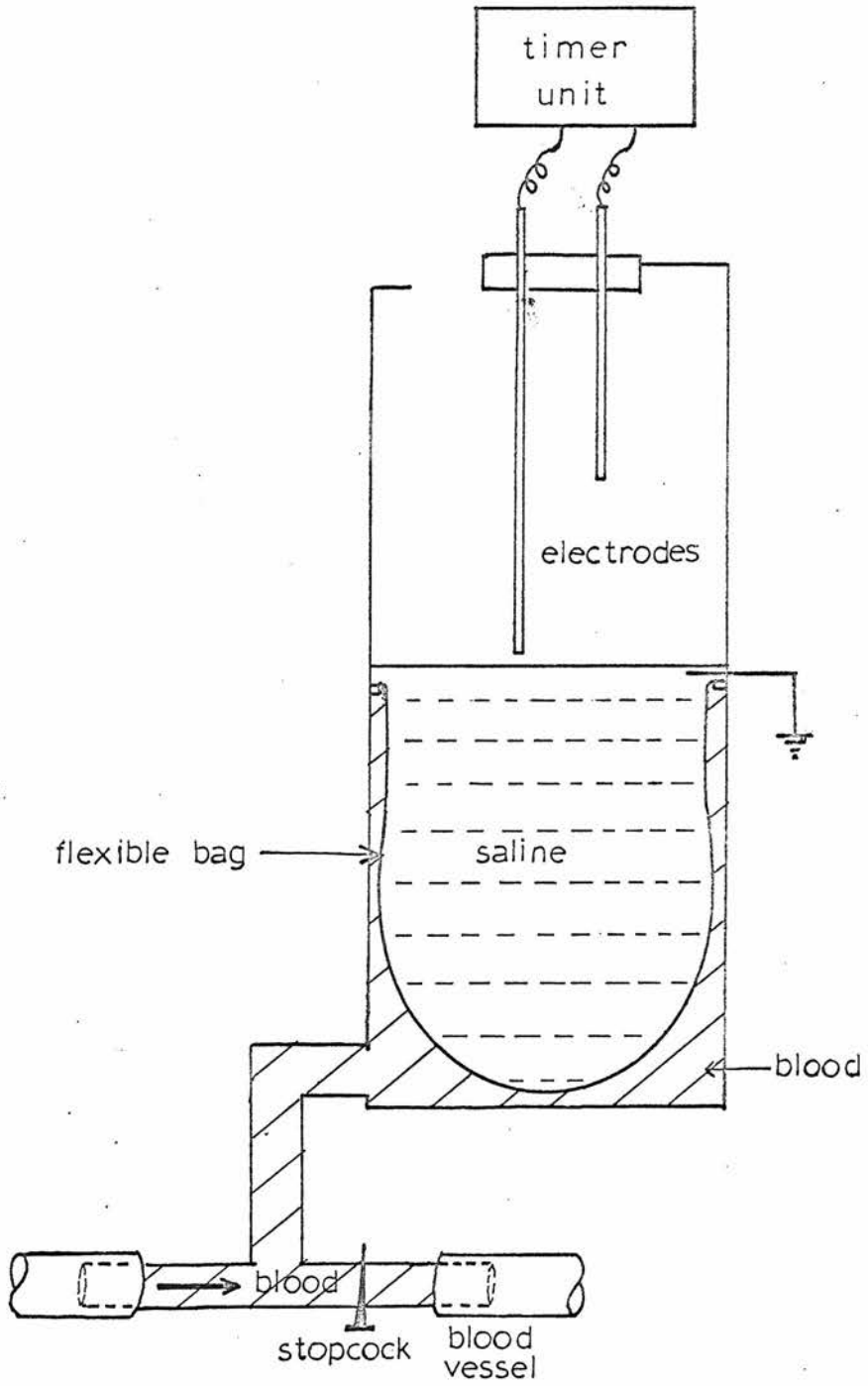

Figure A.1.2. A diagram of the chamber of the flowmeter designed by Dawes et al.[91]

and those exploiting the force experienced by an obstacle in the flow stream.

The pressure difference between two points along a tube through which fluid is flowing is caused by friction and, when the fluid is accelerated, by its inertia. The contribution caused by friction is proportional to the fluid velocity. Two types of acceleration, convective and local, produce the inertia contribution. The convective acceleration, that is the change in velocity along the axial direction between two points, results in a pressure difference which is approximately related to the difference between the squares of the respective velocities at the two points. Velocity may therefore be estimated from the pressure difference measurement. The local acceleration, that is the rate of change of velocity with respect to time, results in a pressure change which is approximately proportional to the local acceleration. Hence, the velocity may be obtained by integrating the pressure with respect to time. Examples of flowmeters operating on these principles are shown in figure A.1.3. Pressure differences are recorded by a differential manometer connected to the meter. The calibration of these meters in terms of velocity is to various degrees dependent on the velocity profile.[80] Further, volumetric flow measurements are restricted to those systems whose tube diameters are time independent. Table 1.2, which has in part been reproduced from reference 92, outlines the advantages and disadvantages of the different meters.

The second type of hydromechanical flowmeter, in which the force experienced by an obstacle in the flow stream is measured, is

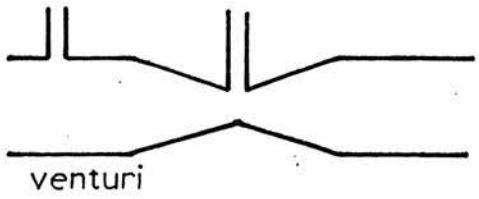

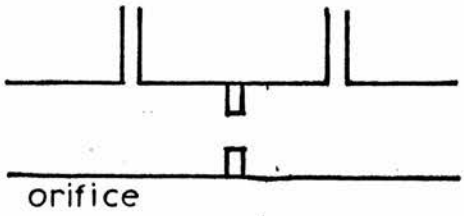

Venturi and orifice meters are based on the generation of convective acceleration by variation of the cross-sectional area of the tube.

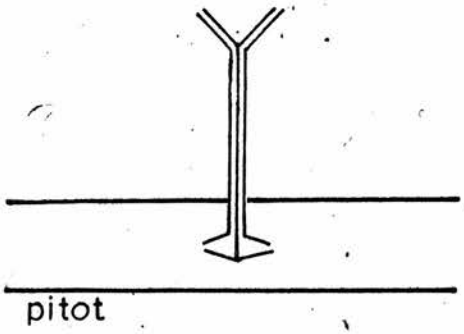

Pitot meters register the same effect over a small bundle of streamlines. The pressure difference is generated by creating local stagnation.

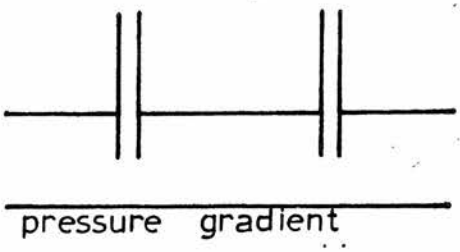

The pressure gradient type is concerned with the registration of local acceleration and the frictional term.

Figure A.1.3. Diagrams of flowmeter transducers which operate by registering pressure differences.

now primarily of historical interest. Three main types have been used, the rotameter, the electroturbinometer and the pendulum and bristle flowmeter. The rotameter[80] shown in figure A.1.4 operates by displaying the displacement of a metal float which partially fills a vertical tube. The blood, flowing up the tube, accelerates on passing the float. The velocity difference above and below the float causes a pressure difference to develop. The resulting force lifts the float such that its displacement is proportional to the mean rate of flow of the blood. The calibration is linear if the rotameter is properly designed and the volumetric flow rate is measured directly.

The electroturbinometer[93] is a stainless steel turbine driven by the blood stream. The rotor placed in the blood stream contains a permanent magnet which induces, by its rotation, an a.c. voltage in the stator located around the vessel. The frequency of the voltage induced is proportional to the rotational speed of the rotor which is in turn proportional to the volumetric flow rate.

The bristle and pendulum flowmeters[94] shown in figure A.1.5 operate by measuring the displacement of a rod or needle placed in the flow stream perpendicular to the direction of flow. The method of measuring the displacement may be mechanical, electrical or optical. The body experiences a force F, which is made up of two contributions

$$F = c_1 v + c_2 \Delta v^2$$

Frictional Term — Convective acceleration term

v is the velocity of the fluid acting on the body and c_1 and c_2 are coefficients which depend on the viscosity and density, respectively,

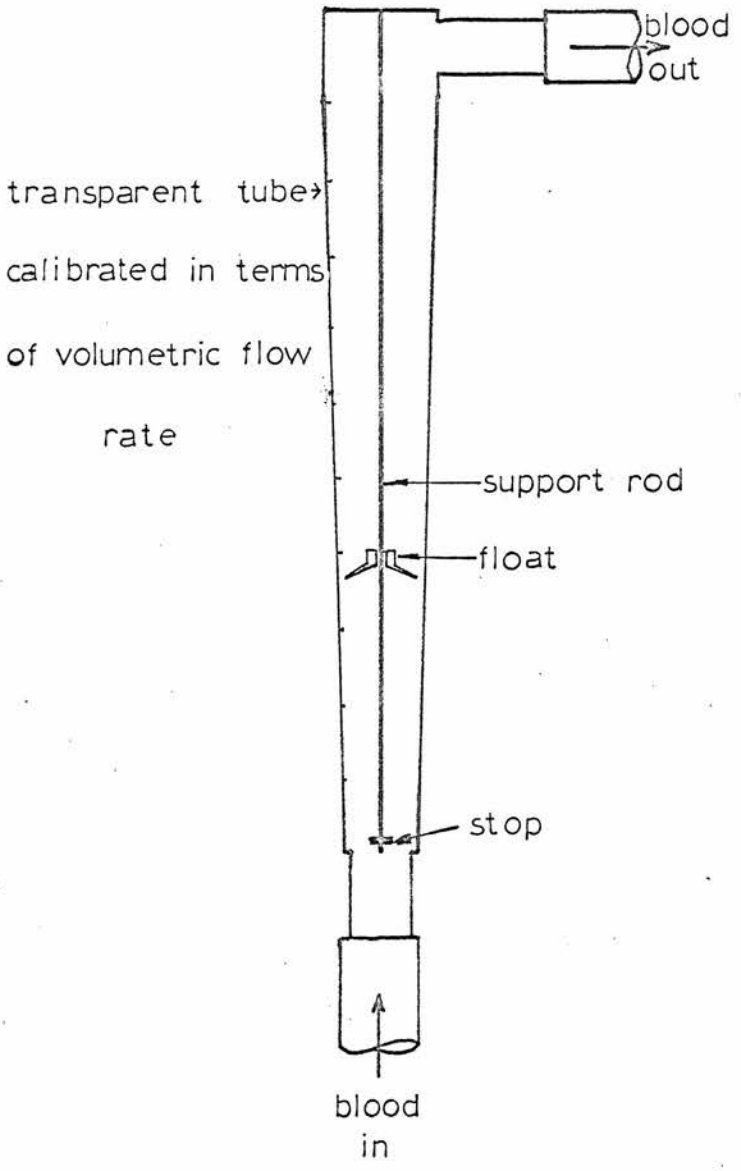

Figure A.1.4. A diagram of a simple rotameter.

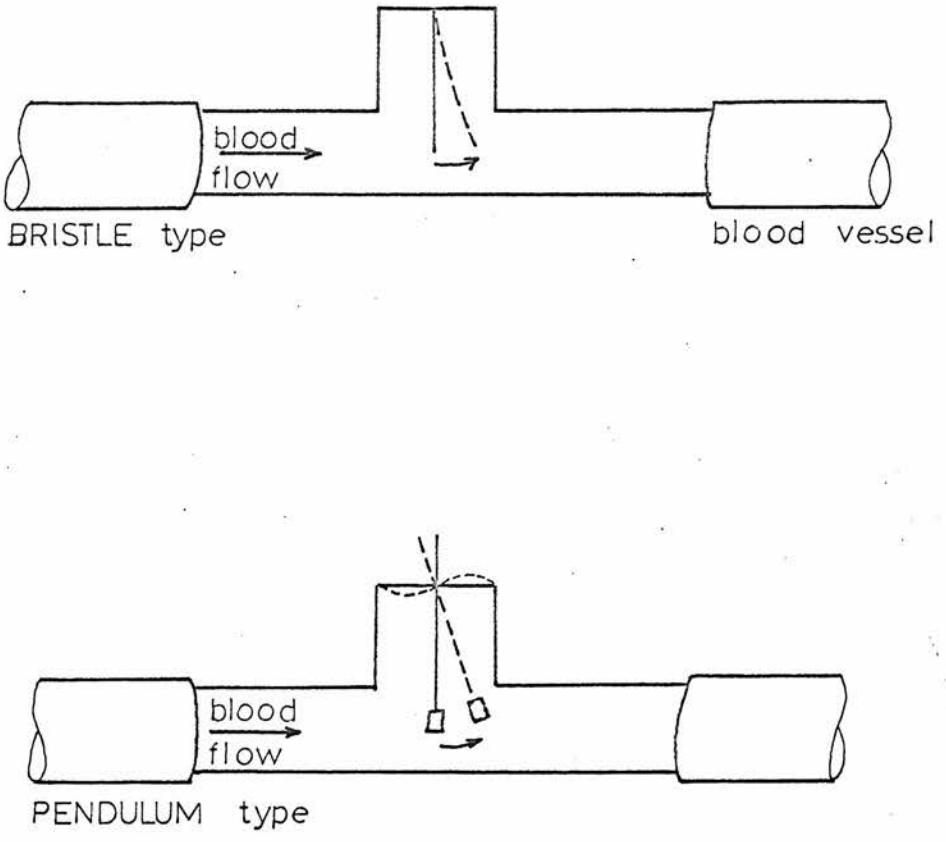

Figure A.1.5. Diagram of the transducers of bristle and pendulum types of flowmeter.

of the fluid, the size and shape of the body and on the local distribution of velocities. The calibration of the flowmeter is in general non-linear and is a function of the velocity profile and fluid properties.

All three of these flowmeters require that the blood is heparinized. Even under these conditions fibrin deposits[30] are liable to collect on the parts in the flowstream and hemolysis is probable. Table 1.2 outlines their relevant advantages and disadvantages.

A.1.8 Thermal methods

Some thermal methods have already been described in the sections dealing with travelling markers and marker dilution. There are several other flowmeters based on the measurement of heat transfer.

Historically the first flowmeter of this type,[95] shown in figure A.1.6, consisted of a tube surrounded by a concentric water jacket which was flushed by a constant flow of water at room temperature. When the tube is located in a cannulated vessel with blood flowing through it, the temperature increase in the outflowing water is found to be proportional to the volumetric flow rate of the blood, providing the density of blood is constant. The slow response time of the system to flow changes, of the order of one minute, is the principal disadvantage.

Later flowmeters[96,97,98,99,100] exploit a system whereby heat is transferred to the blood from a heated section of the vessel wall. Figure A.1.7 shows one such arrangement. Two thermocouples register the blood temperature at points upstream and downstream from the

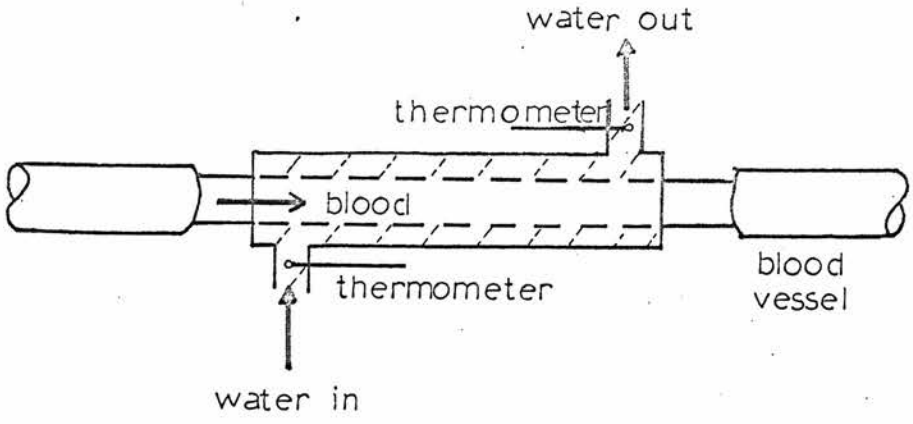

Figure A.1.6. The heat exchange probe.

⊗ marks the location of thermocouples in the blood vessel.

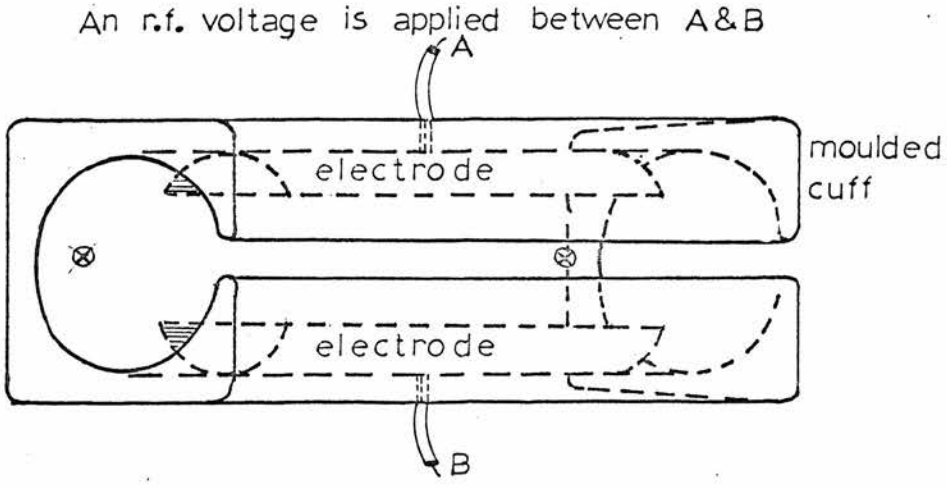

Figure A.1.7. A diagram of Rein's Thermostrohmuhr.

heated section. If the system is operated with a constant heat input, the temperature difference is a decreasing function of the fluid velocity providing the shape velocity profile does not change and the blood properties are constant. Catheter probe versions[101, 102] of this system have been developed in which the temperature sensors and heater are mounted on a needle which is inserted into the blood stream. The main disadvantages of these flowmeters are that at zero and low flow rates the blood and vessel wall may be overheated, and at high velocities there is a loss of sensitivity. Further, for quantitative measurements of volumetric flow rate the diameter of the blood vessel must be constant. This is a particular problem with catheter probe flowmeters together with the difficulty of insuring that the probe location is fixed. The instruments are capable of detecting reverse flow; however, the forward calibration curve may not be applicable since the sensor arrangement is not necessarily symmetrical.

The overheating problem at low flow rates has been overcome by employing a constant temperature difference mode of operation rather than the constant heat input mode. This also improves the instrument's sensitivity at high velocities[8]. The isothermal flowmeter shown in figure A.1.8 illustrates a typical example of this type[104]. Two thermistors, which are part of a bridge circuit, are placed in a fixed location in the blood stream. One thermistor monitors the undisturbed blood temperature, the other is maintained, by direct or indirect heating, at a constant temperature difference above the blood temperature. The magnitude of the heating current required is a measure of the flow velocity. Again, the calibration

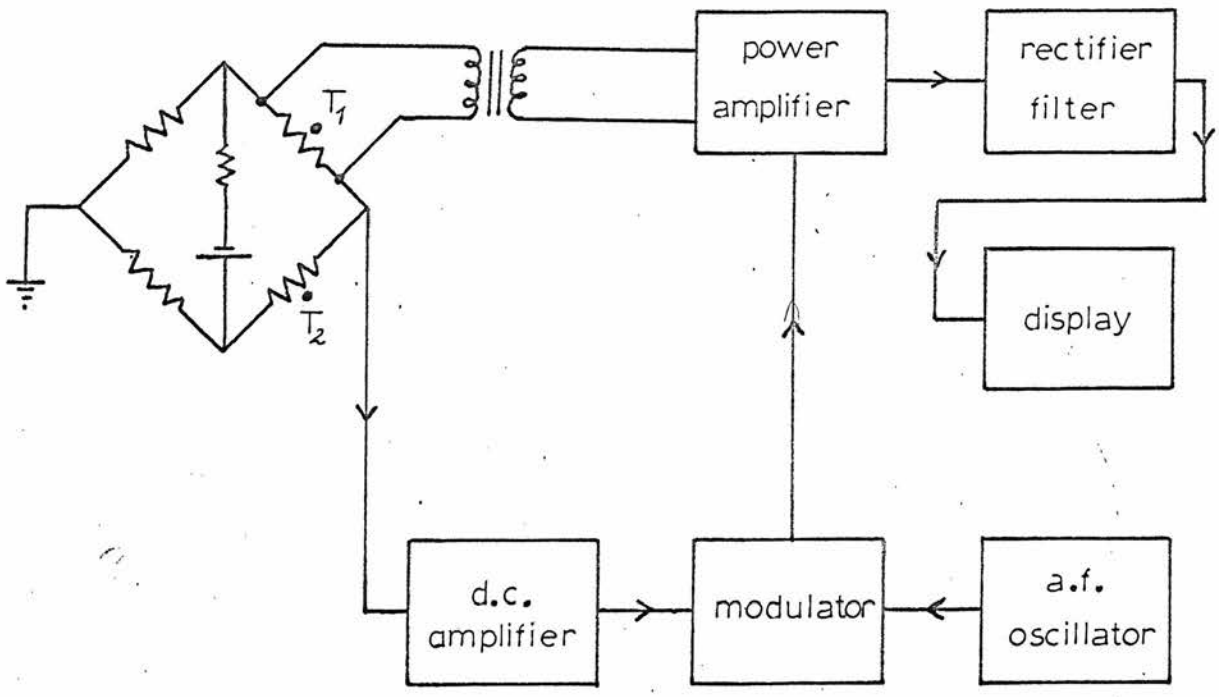

T_1 – flowmeter transducer

T_2 – reference thermistor

Figure A.1.8. A block diagram of an isothermal flowmeter.

is dependent on the fluid properties and the velocity profile, and for volumetric measurements, the tube diameter must be constant. In general these flowmeters do not detect the direction of flow. Mellander and Rushmore[103] developed such a system with a frequency response of 5Hz and an error of $\pm$ 5% in the flow range 100 to 1300 ml/minute in a tube with a 1 cm bore. Katsura et al.[104] measured flow rates in the range 0 to 600 ml/minute with an error of $\pm$ 10% in a 6 mm diameter vessel. The temperature differences employed are not stated. Other similar systems use a 5°C[105,106,107] and 10°C[108,109] temperature difference.

Local capillary flow may also be measured using a steady state heat transfer system. The Hensel needle,[110] shown in figure A.1.9, is an example of one such system. It operates in the constant heat input mode. Since the thermal conductivities of the individual body tissues are approximately constant, the variations in temperature in the heated region can be interpreted as reflecting the mass flow through the sphere of influence of the heater. This is essentially a method of determining relative flow rates.

Thermal methods of regional flow measurement in tissue may, however, disturb the physiological conditions.[85] The temperature rise may cause local vascodilation so that the flow rates may be altered by the measurement technique.

A.1.9 The electromagnetic flowmeter

The electromagnetic flowmeter is the most popular type for the continuous recording of pulsatile flow. The system operates by monitoring the e.m.f. induced in a conductor, the blood, when moving in a magnetic field. For the physical arrangement shown

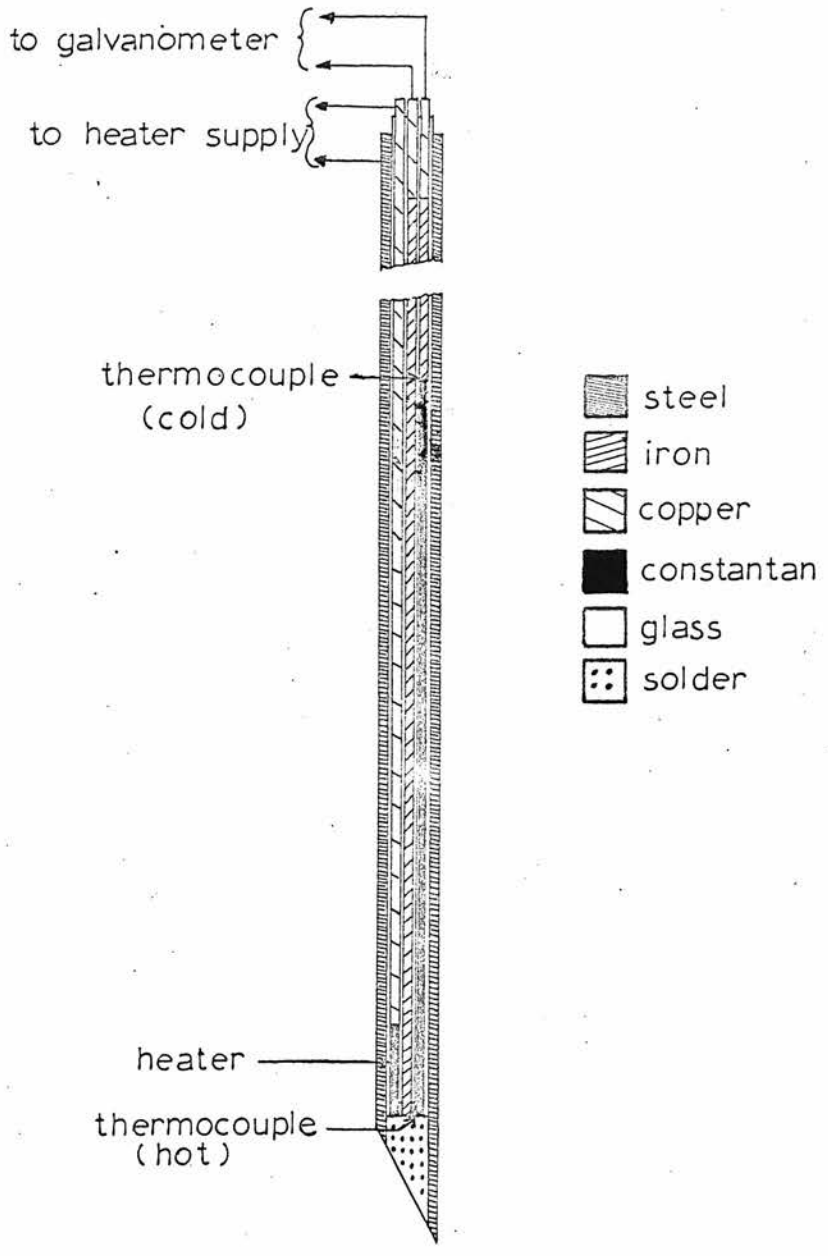

Figure A.1.9. A schematic drawing of Hensel's needle.

in figure A.1.10, the expression for the voltage induced in the blood, V_i, is

$$V_i = B\int_{-R}^{+R} v(r)\, dr$$

where B is the magnetic flux density and v(r) is the instantaneous velocity, v(r) is a function of the tube radius when the velocity profile is axially symmetrical. Now, the induced voltage distribution across the diameter will have a similar form to the velocity profile so that circulating currents may occur in the blood and modify the induced voltage distribution. Thurlemann[111] found that the resulting voltage monitored by the electrodes is given by

$$V_i = 2BR\bar{v}_A$$

where $\bar{v}_A$ is the instantaneous velocity average over the cross-sectional area. The monitored voltage is linearly related to the instantaneous velocity, $\bar{v}_A$, and hence the instantaneous volumetric flow rate. The required conditions are that the magnetic field is uniform, the conductivity of the blood is uniform and the velocity profile is axially symmetrical. The principal advantages of this system are that the blood vessel need not be cut, and the calibration is linear and, in general, independent of the velocity profile. Further, it is capable of a high frequency response, is equally sensitive to flow in both directions and detects such changes, and operates independently of the density, viscosity and temperature of the blood. E.m.f.s of the order of microvolts are picked up by the electrodes and amplified.

It was first exploited by Kolin[112,113], who used large electromagnets to supply a constant magnetic field, and non-polarizable

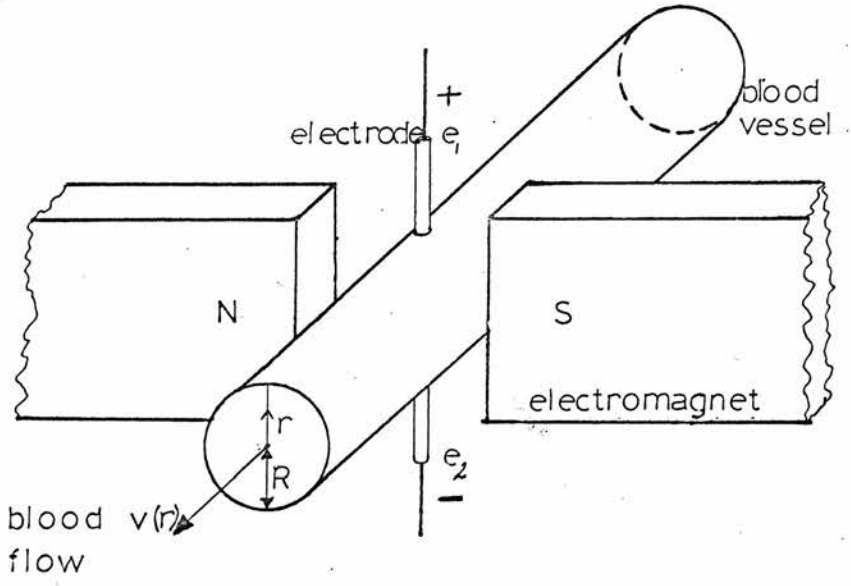

Figure A.1.10. A diagram of the basic arrangement for electromagnetic flow measurement.

electrodes in contact with the artery. The main problem with the arrangement was that the electrodes were bulky and only relatively free from polarization effects. He later suggested[114] using an alternating sinusoidal magnet drive current to overcome this. However, while eliminating the electrode problem, this arrangement causes unwanted voltages to be induced by the time-varying magnetic field in the loop formed by the conductor, electrodes and electrode wire. The electrode voltage V_i now contains two components, the flow-induced voltage V_f and the "transformer" voltage V_t.

Hence $$V_i = 2B_0R\bar{v}_A \sin\omega t + KB_0\omega\cos\omega t$$

when the magnetic flux density equals Bo sinωt. K is a coefficient related to the coupling of the transformer induced voltage.

Considerable research effort has been expended in this field in order to solve the problems defined by Kolin. Various techniques have been evolved[115] to minimise the transformer component. The geometry of wires within the magnetic field have been suitably designed to minimise the induced voltage and compensating coils have been added to balance it out. Three important approaches, shown in figures A.1.11, A.1.12, A.1.13 taken from reference 116 are currently used to reduce it further. Two exploit the 90° phase difference between the flow-induced signal and the transformer-induced voltage. In 1959 Kolin and Kado[117] and, independently, Westersten et al,[118] described a flowmeter which sampled the electrode voltage when the quadrature voltage equals zero, that is, when the rate of change of the magnet drive current is zero.

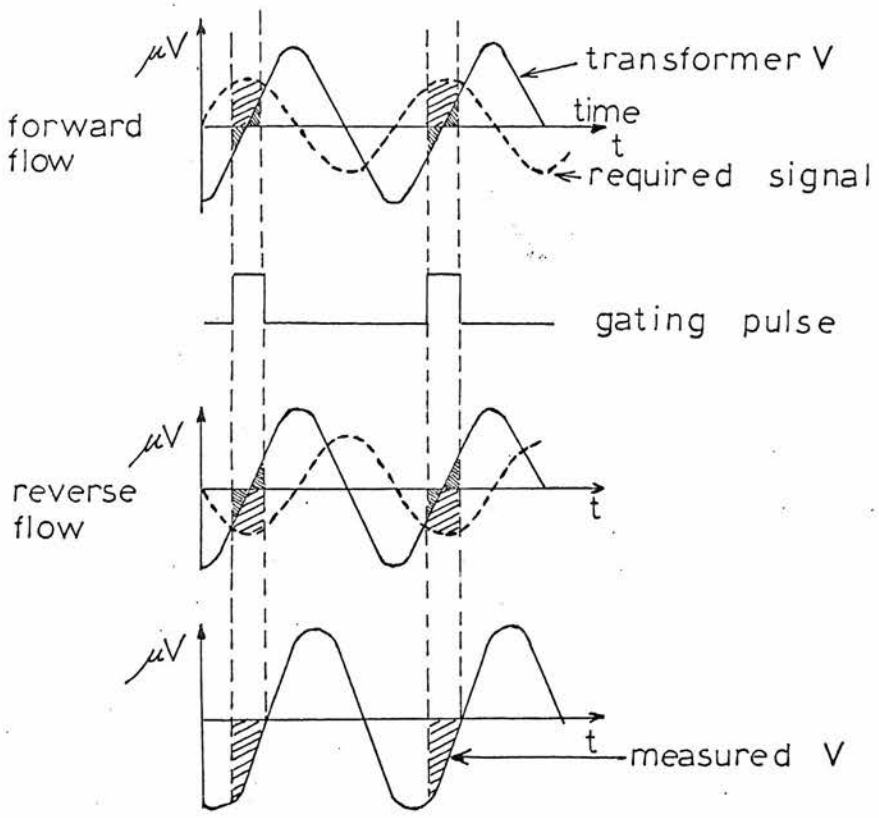

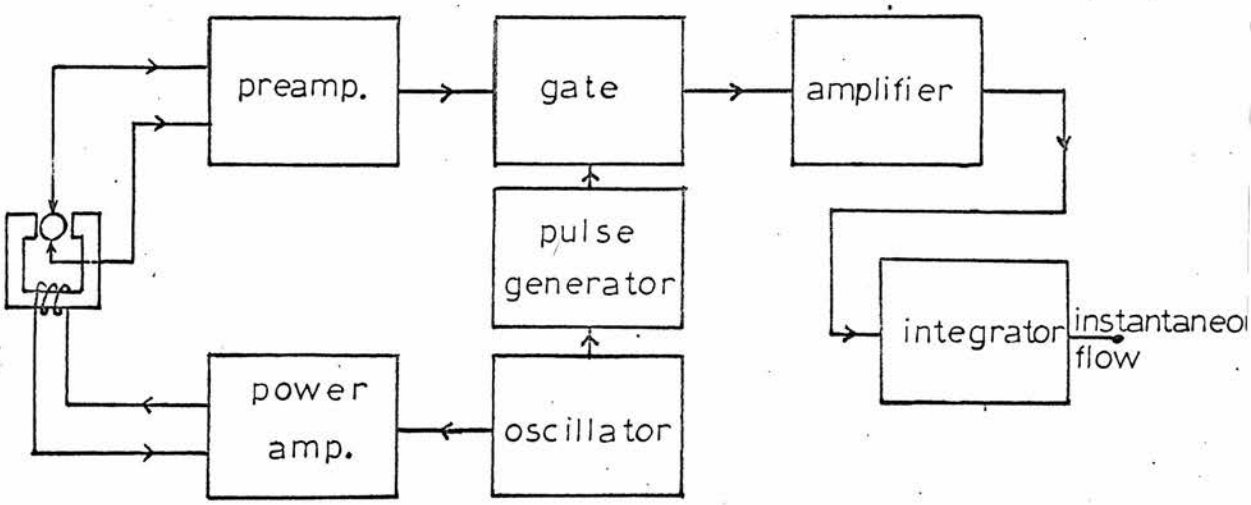

Figure A.1.11. The waveforms and block diagram of the gated sine-wave electromagnetic flowmeter.

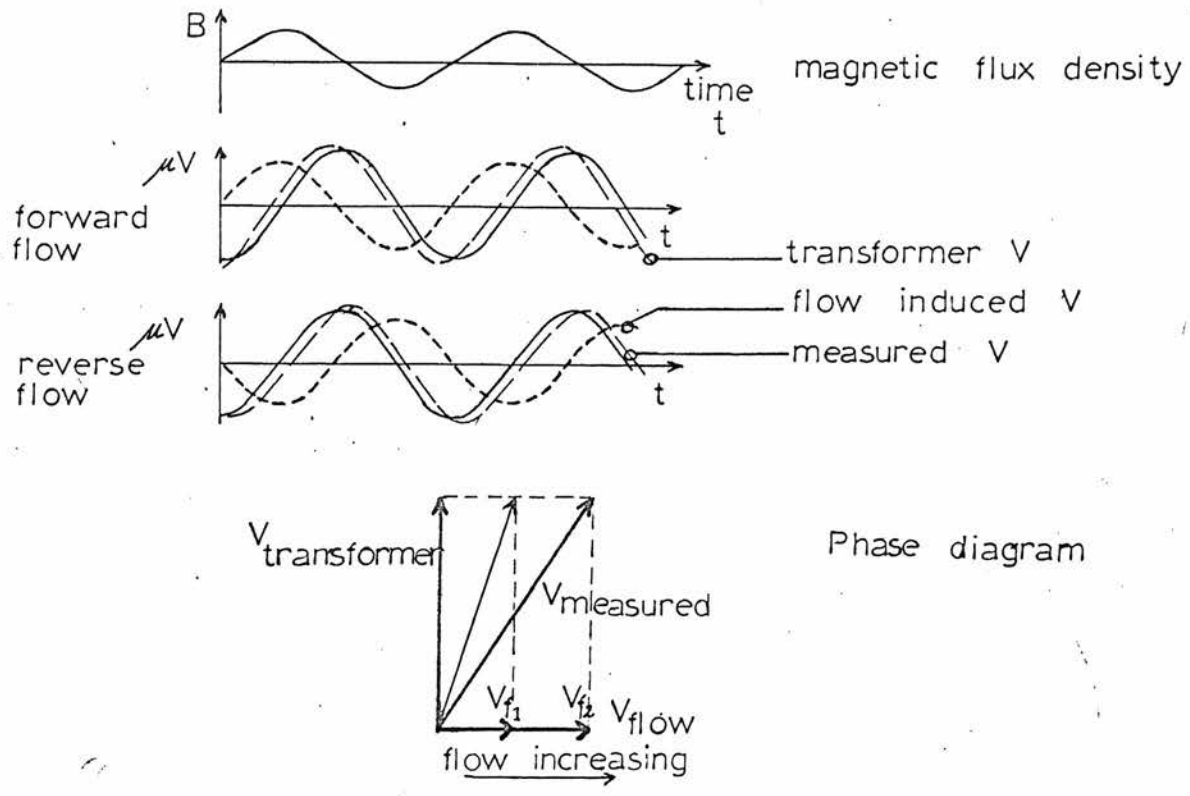

Figure A.1.12. The waveforms and block diagram of the phase shift electromagnetic flowmeter.

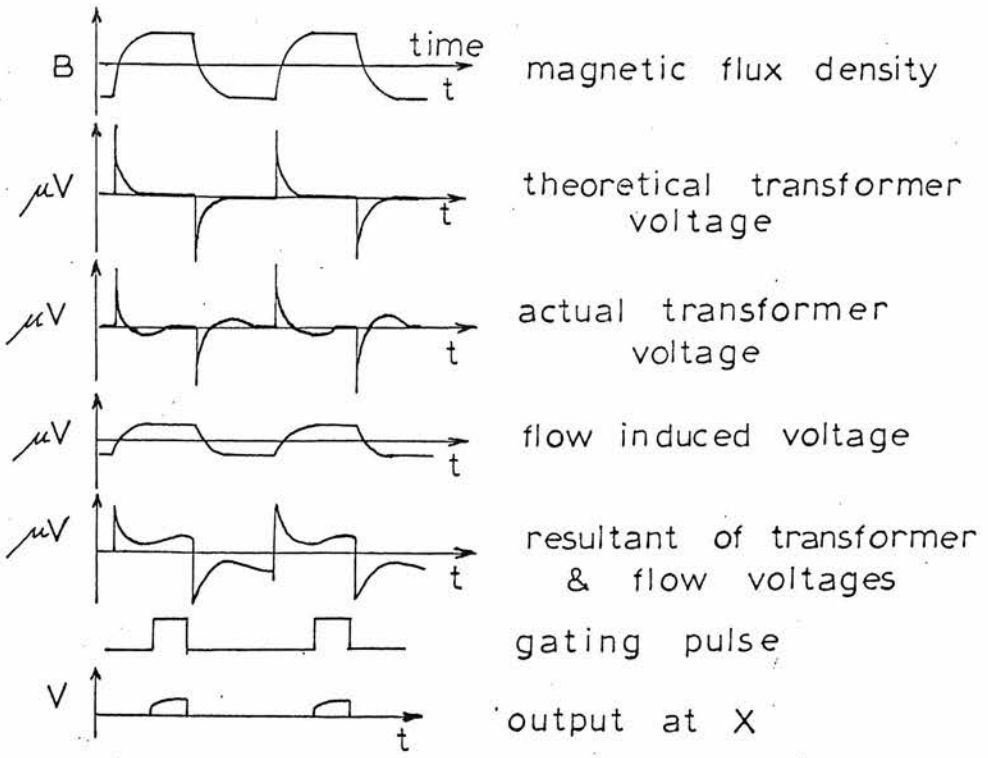

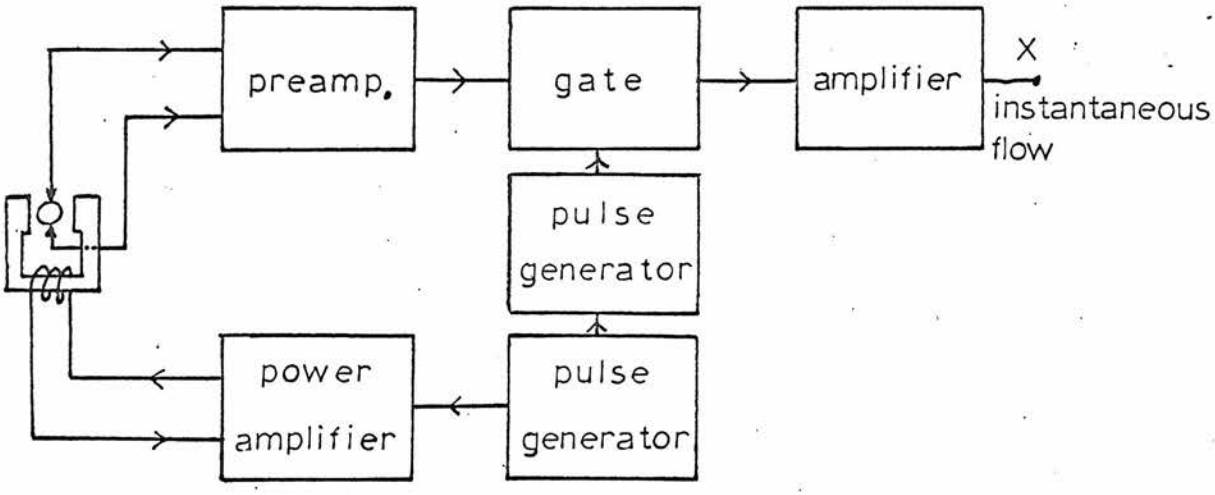

Figure A.1.13. The waveforms and block diagram of the square wave electromagnetic flowmeter.

Figure A.1.11 ilustrates their solution. In 1962 Olmstead described[119] a second system shown in block diagram form in figure A.1.12 in which the phase difference between the electrode voltage and the magnet drive current is measured. This is based on the fact that the measured voltage is shifted in phase by an amount proportional to the magnitude of the flow-induced voltage.

The third approach, which is a compromise between the D.C. and sine wave A.C. flowmeter, was described by Spencer and Denison [120,121] in 1959. (Figure A.1.13.) They used a square wave a.c. magnet drive current, thereby providing a steady magnetic field which switches from one polarity to the other. During the portion of the cycle when the magnetic field is steady there is no quadrature voltage at the electrodes. This only occurs at the switching point, and by using an amplifier which is gated off during the transients, the quadrature voltage will not appear at the output.

Other sources of interfering voltage have been described in detail by Wyatt,[122,123,124] and a large number of modifications have been described to overcome these. However, in general, the errors can be minimised, though not eliminated, by careful design and construction of the transducer. Manufacturers quote[125,126] transudcer sensitivities from 20 to 200 ml/minute/μV with stabilities in the range 0.25 to 1 μV/hour. In normal use of the instrument the reproducability of the flow measurements[88] is approximately $\pm$ 10%. The frequency response[115] is in the range 20 to 100 Hz. An accuracy [115] of $\pm$ 5% in the flow measurement is achievable when the transducer-blood vessel orientation and the vessel diameter is constant, and when the instrument is calibrated in situ.

The a.c. transducers are commercially available for use on vessels with a minimum diameter of 1 mm. For implant applications the sine wave transducer is used in preference to the square wave type because the ampere-turn value required to obtain fields of equal effectiveness is smaller in the sine wave case. Hence the transducer is smaller in size and cooler. Typical heat dissipation[127] for a transducer designed to operate on a 4 cm diameter vessel is 5 watts. These relatively high power levels obtain because the magnetic flux density is directly related to the electrode voltage. For example,[128] with a flux density of 300 gauss, a vessel diameter of 1.5 cm and a peak flow velocity of 100 cm/s, the maximum voltage generated at the electrodes is 450 μV. Problems arising from the magnitude of the electrode voltage have been found[128] in determining the zero flow base line. The principle problem in implant work lies in insuring that the transducer-vessel orientation is fixed. Catheter probe transducers,[129] in which the flow passes around the probe, are currently being developed.

A.1.10 Ultrasonic flowmeters

This type of flowmeter is also capable of continuous measurement of pulsatile flow. The design is based on one of two physical phenomena exhibited when sound waves travel in blood. One type exploits the fact that the effective velocity of sound propogated through a moving medium is equal to the sum of the velocity of the medium and the velocity of sound in the stationary medium. The second exploits the doppler shift in frequency of reflected sound energy caused by the relative motion between the source and

a reflector which, in this case, in the red corpuscles.

Considering the arrangement shown in figure A.1.14 the time difference, Δt, between the upstream and downstream transit times of sound waves travelling a distance, D, in the moving fluid is given[130] by

$$\Delta t = \frac{D\cos\theta}{c+v} - \frac{D\cos\theta}{c-v}$$

$$= \frac{2vD\cos\theta}{c^2 - v^2} \doteq \frac{2vD}{c^2}\cos\theta \quad , \text{ since } c^2 \gg v^2.$$

C is the velocity of sound in the stationary fluid and v is the mean velocity of the fluid. Hence the velocity of the medium averaged over the signal path can be determined by measuring the difference in transit times upstream and downstream. Another possibility is to compare the phase difference of the received and transmitted signals for the upstream and downstream cases. If f is the frequency of the sound wave then

$$\Delta\phi = \phi_D - \phi_u = 2\pi f \Delta t$$

where ϕ_D is the phase difference between the received and transmitted signals when sound travels downstream and ϕ_u is the phase difference for the upstream case. Typical values[130] of Δt and $\Delta\phi$ are included in figures A.1.14 and A.1.16 respectively. It is obvious that the requirements for sensitivity and stability of the electronic equipment are severe.

Franklin et al.[131,132] designed a pulsed flowmeter shown as a simplified block diagram in figure A.1.14 to measure the difference in transit times. The system transmits bursts of sound alternately upstream and downstream. The transit times are measured and the upstream-downstream difference recorded. A single transmitter and

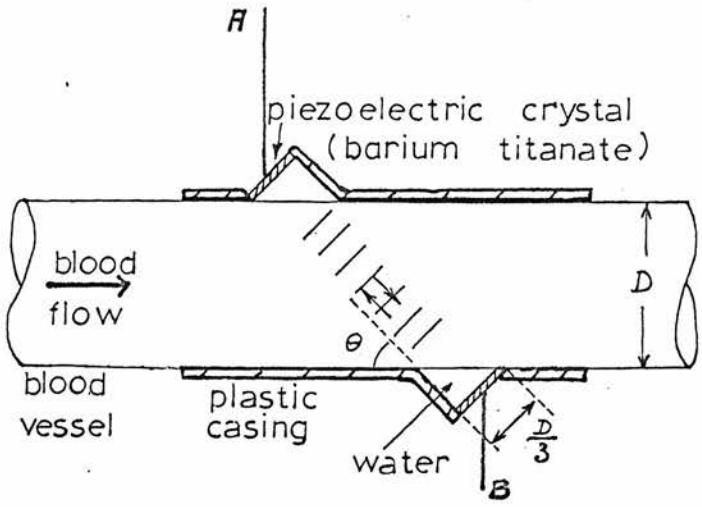

$$\Delta t = \frac{2Dv\cos\theta}{c^2}$$

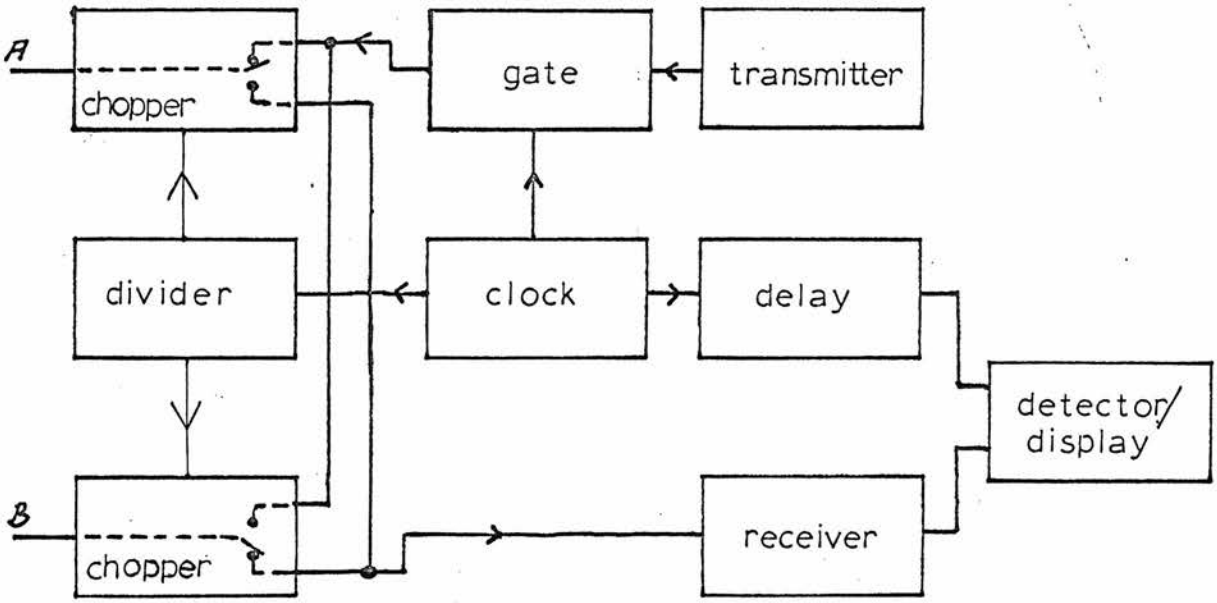

typical values:

$c = 1{\cdot}5 \times 10^5$ cm/s : $v = 1 \rightarrow 100$ cm/s

$D = 2{\cdot}54$ cm. : $\Delta t = 2\times10^{-10} \rightarrow 2\times10^{-8}$ s

Figure A.1.14. The pulsed transit time flowmeter

receiver are used with a switching arrangement. They claim[131] a minimum error in the forward and reverse flow measurements of ± 5% with an upper limit on frequency response of at least 15 Hz. Under optimal conditions the minimum velocity that can be measured is 0.5 cm/s. This limit is imposed by instrument stability and noise. Further, they claim that the calibration is independent of the velocity profile. However, this type of flowmeter measures the velocity averaged over the vessel diameter and not averaged over the cross-sectional area so that the calibration ought to be dependent on the velocity profile. This argument is illustrated[133] in figure A.1.15. The problem of the calibration dependence on velocity profile has not yet been fully investigated.

Zarnstoff et al.[134] described a similar system, shown in figure A.1.16 in which they measured the upstream and downstream phase differences of a continuous sinusoidal acoustic wave. The wave is alternately transmitted upstream and downstream as in the previous case. They claim a linear calibration of better than 2%. Nobel et al.[135] designed a system which eliminates the need for switching by transmitting in both directions at the same time using two different frequencies. Each crystal transmits and receives simultaneously. The frequency response of this system is claimed to be approximately 500 Hz. A simplified block diagram of the arrangement is shown in figure A.1.17. The disadvantage of the system is that the electronic equipment must have excellent phase stability since two transmitters and receivers are employed. They quote a sensitivity of 0.7 degrees phase shift/cm/s with a linear steady flow calibration for a crystal separation of 1.5 cm.

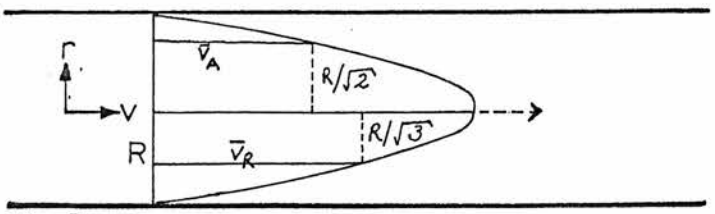

$v = K(R^2 - r^2)$ where K = constant.

$\bar{v}_R = \frac{2}{3} K R^2$

$\bar{v}_A = \frac{1}{2} K R^2$

$\bar{v}_R : \bar{v}_A = 4 : 3$

flow rate $= \bar{v}_A \pi R^2$

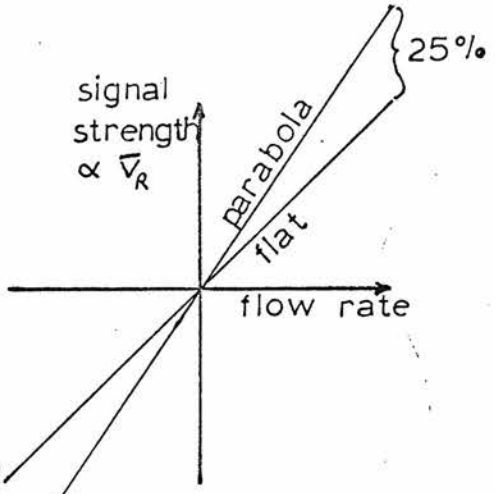

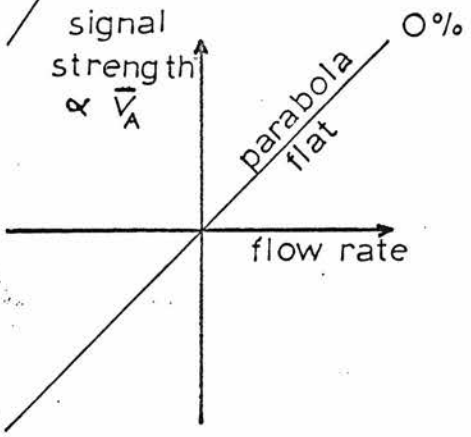

Signal strength versus flow rate for flowmeters which monitor (A) velocity averaged over the radius, $\bar{v}_R$, (B) velocity averaged over the cross-sectional area, $\bar{v}_A$, for the two extremes of velocity profile (namely parabolic and flat).

Figure A.1.15. A diagram illustrating the dependence of the calibration of particular flowmeters on velocity profile.

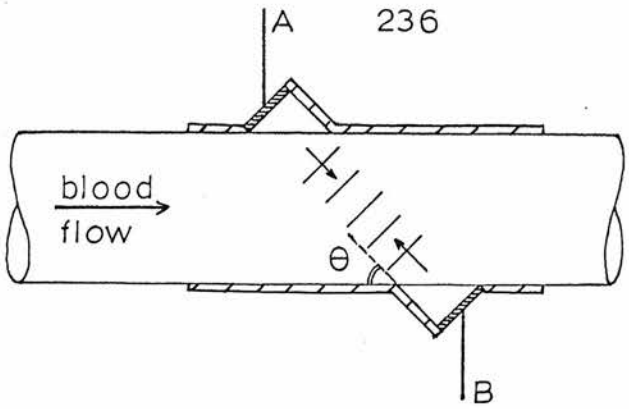

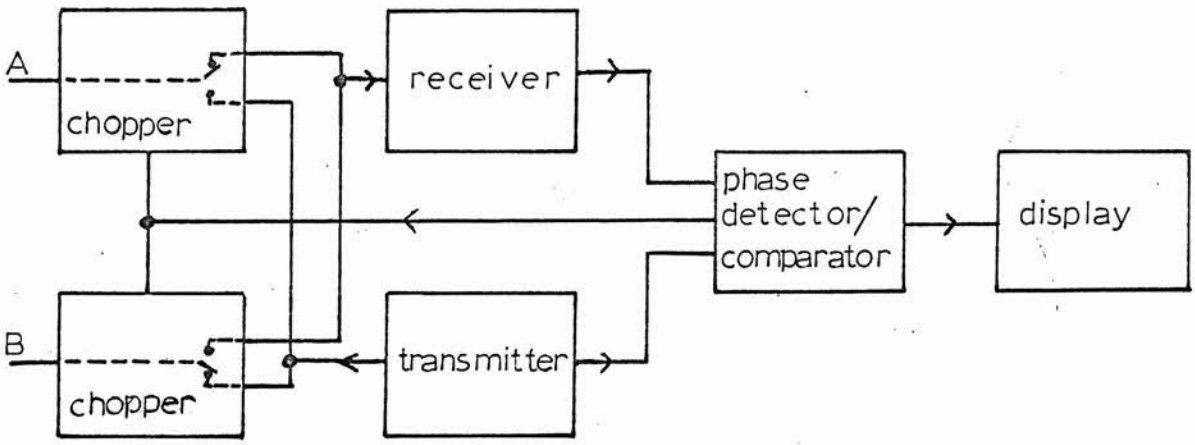

$$\Delta\phi = 2\pi f \Delta t$$
$$= 4\pi f \frac{Dv\cos\theta}{c^2}$$

$c = 1{\cdot}5\times10^{5}$ cm/s

$D = 2{\cdot}54$ cm.

$f = 380$ kHz

$v = 1 \rightarrow 100$ cm/s

$\Delta t = 2\times10^{-10} \rightarrow 2\times10^{-8}$ s

$\Delta\phi = 0{\cdot}03^\circ - 2{\cdot}74^\circ$

Figure A.1.16. A diagram of the time multiplexed phase shift flowmeter.

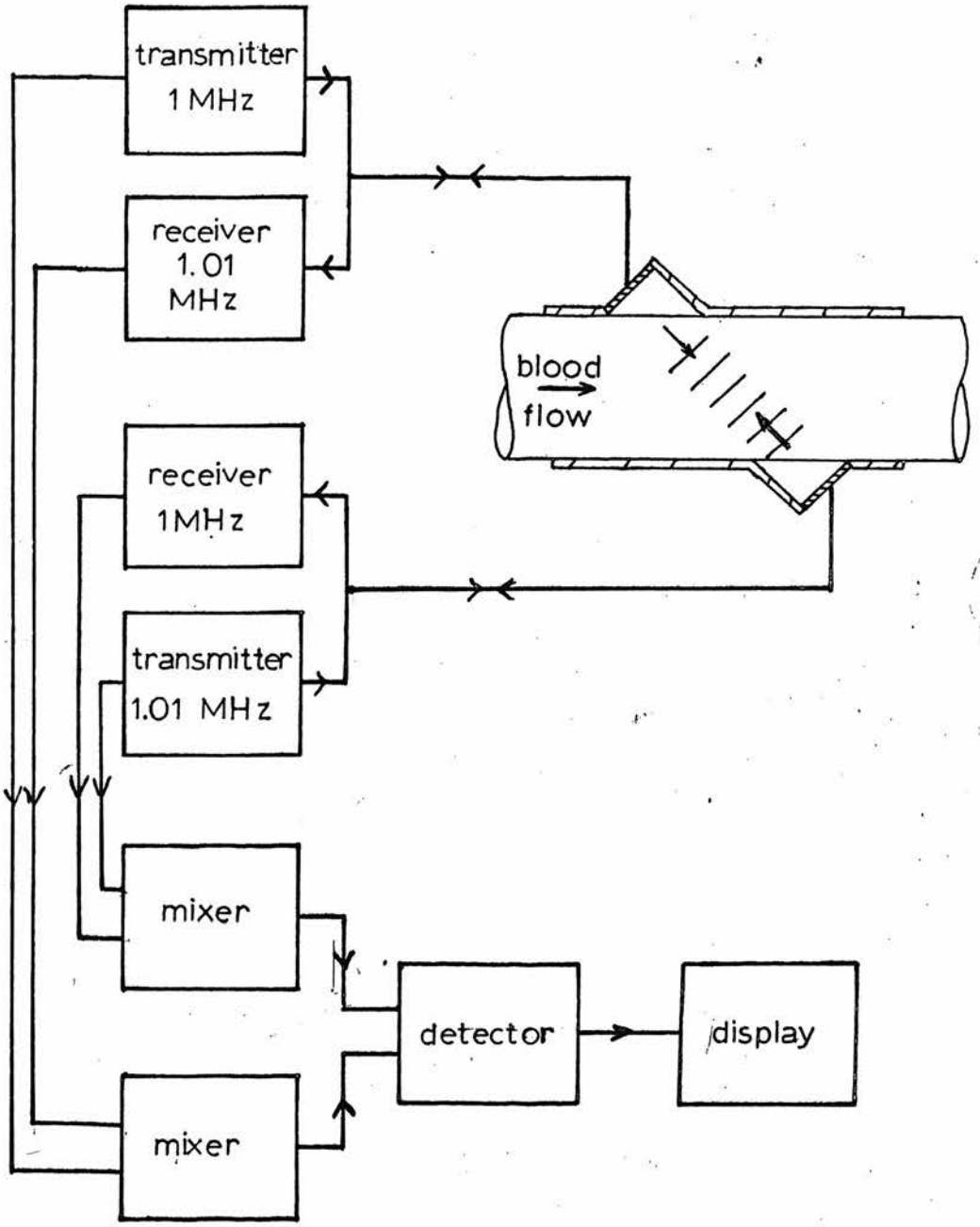

Figure A1.17 A diagram of the frequency multiplexed phase shift oscillator

The second type of ultrasonic flowmeter, the doppler shift flowmeter,[136,137] is shown as a simplified block diagram in figure A.1.18. This is the only ultrasonic flowmeter to be produced commercially. Sound waves are coupled diagonally through the vessel wall into the blood stream. The transmitted and back-scattered signals are mixed at the receiver crystal and the beat frequency formed is linearly related to the instantaneous velocity of the reflector particles. The difference between the emitted and received signal frequencies, Δf, is given[137] by

$$\Delta f = f_e - f_r = \frac{2 f_e v \cos\theta}{c}$$

where f_e is the emitted frequency, v the velocity of the scattering medium, c the velocity of sound in blood and θ the angle between the flow direction and the acoustical axis. The sensitivity of the instrument when used in large arteries in dogs with a transmitted power density of 2 watts/cm^2 into the blood is claimed[136] to be 3.5 Hz/mm/s in the range 3 mm/s to 100 cm/s. The lower limit is imposed by the circuitry. The instrument output is linearly related to the flow velocity within 5% at 100 cm/s.

The disadvantages of this system are that it does not sense flow direction and the calibration is dependent, to some extent, on the velocity profile of the flow since back scattering occurs from a poorly defined central area of the blood vessel cross-section. For volumetric flow measurements, the diameter of the vessel must be constant. Modifications[138] have been suggested to make the system sensitive to flow direction.

The dimensions of the piezoelectric crystals used in the flowmeter transducer are limited[132,139] by difficulties in fabrication

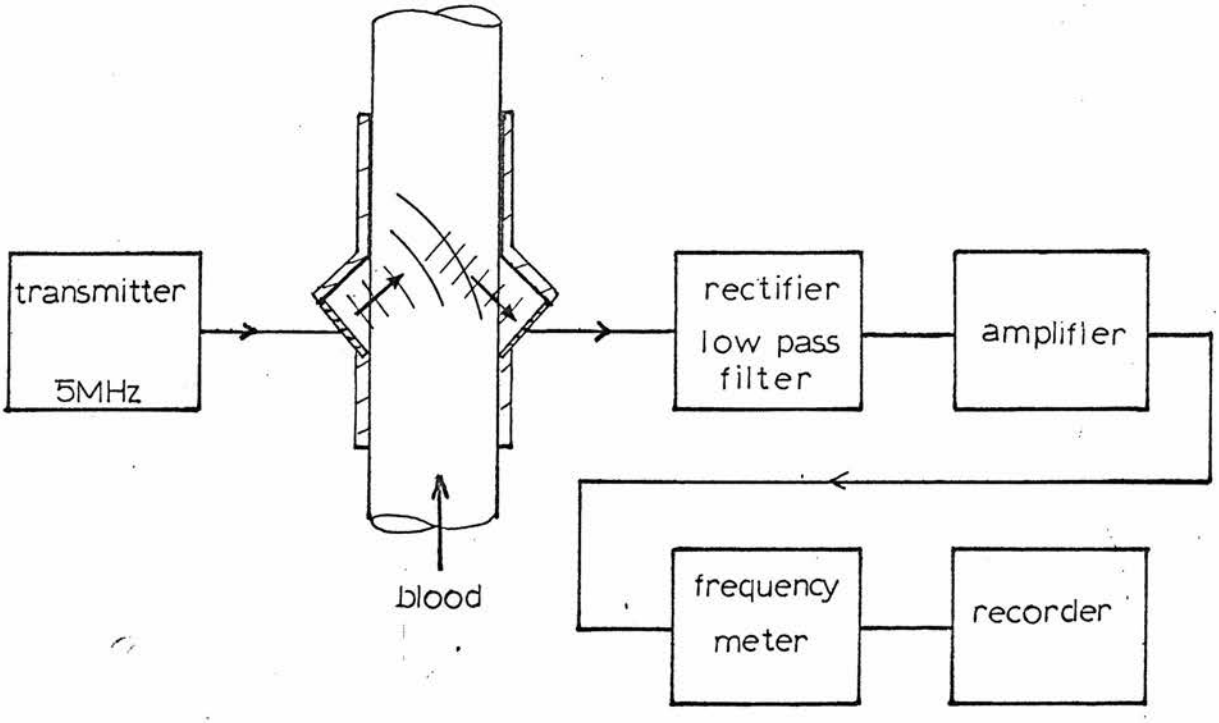

Figure A.1.18. A diagram of the doppler back-scattered flowmeter

to a minimum lumen diameter of 3 mm.

A.1.11 Nuclear magnetic resonance

Attempts to exploit the phenomenon of nuclear magnetic resonance are still in the research stage[140]. The theory of the phenomenon is readily available.[141,142,143] Essentially it is concerned with the behaviour of a nucleus in a magnetic field which has a steady and time-varying component. In the case of biological systems the reaction of the hydrogen nucleus is exploited because it results in an especially strong signal so that proton magnetic resonance (P.M.R.) is, in fact, utilised. The proton can be considered as a magnet spinning about its polar magnetic axis and experiencing a force which tends to tilt the axis, thereby causing it to precess about its initial axis. A steady magnetic field will tend to align the individual nucleii with the field and a time varying field which is oscillating at the same frequency as the nucleii are precessing will produce a condition of resonance. This resonance condition may be detected by monitoring the absorption of energy from the oscillating field, or by using a coil isolated from the exciting field to extract the energy absorbed by the nucleii as shown in figure A.1.19. If the time taken by a nucleus to flow through the field is of the same order of magnitude as the time required to generate the resonance in it, then the degree of resonance is limited by the flow so that the P.M.R. signal diminishes with increasing volumetric flow. Alternatively if the times are such that the degree of resonance reaches an upper limit and a saturation effect occurs then increasing the flow rate will increase the P.M.R. signal. The calibration of the system is non-linear. Initial experiments

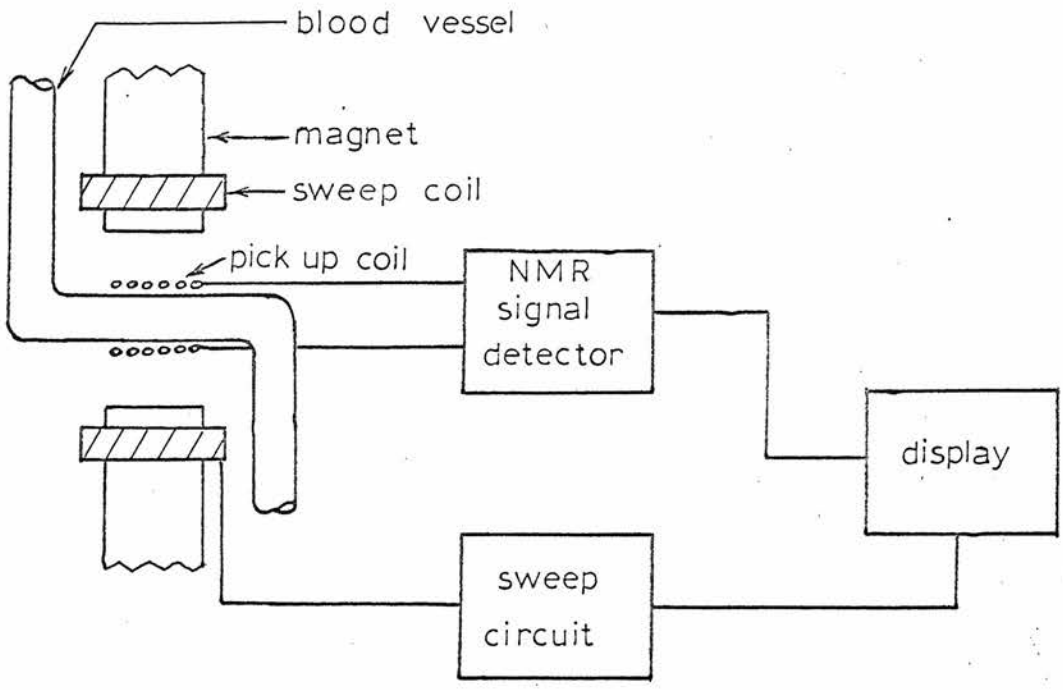

Figure.A1.19. A diagram of an N.M.R. flowmeter.

indicate that in the flow range 1 to 500 ml/minute the response of the system is reproducable without appreciable error. Another possibility, in this case for measuring flow velocity, is to use P.M.R. transients as a method of marking protons and then detect them at a known distance downstream.

APPENDIX 2

The Glow Discharge Mechanism

Considering the V-I characteristic of a discharge between parallel plates shown in figure A.2.1, at the breakdown voltage, V_b, the current increases at constant voltage until the space charge caused by the relatively slow moving ions becomes sufficient to raise the potential close to the cathode. This causes an increase in the field strength/pressure ratio at the cathode surface and an increase in the emission coefficient, γ, so that the voltage required to maintain the discharge falls. Further increase in current produces the glow discharge. In the glow discharge region the potential, V, and electric field strength $\bar{E}$, at any point between the electrodes are severely modified by the space charge effects of the charged particles at that point, as shown in figure A.2.2. The factors α, the first Townsend coefficient, and γ which act to maintain the discharge are determined by the field strength in the region between the cathode and d^1 of figure A.2.2. α is described here by the equation

$$\alpha = pf\left(\frac{V_c}{pd^1}\right) \qquad \text{A.2.1}$$

where V_c is the potential shown in figure A.2.2. The length of the positive column is largely irrelevant to the maintenance of the discharge. The current density and voltage remain constant over the normal glow region of figure 4.2.2 so that the cross sectional area of the negative glow varies in direct proportion to the current. The equation for current density, [144] J, is

$$J = J_0^+(1+\gamma) \qquad \text{A.2.2}$$

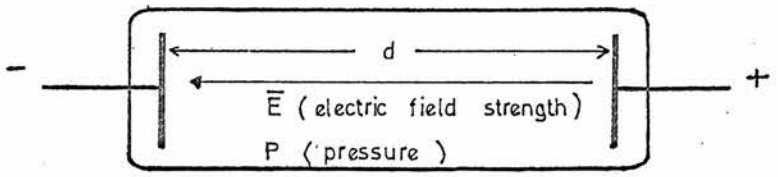

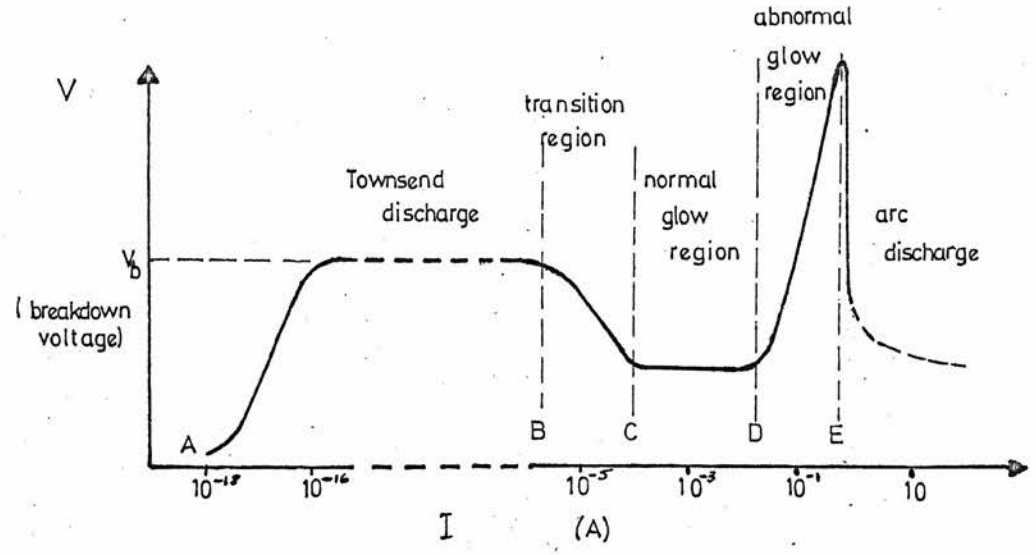

Figure A.2.1. A diagram of parallel plane electrodes and the V-I characteristic of the discharge between them.[144]

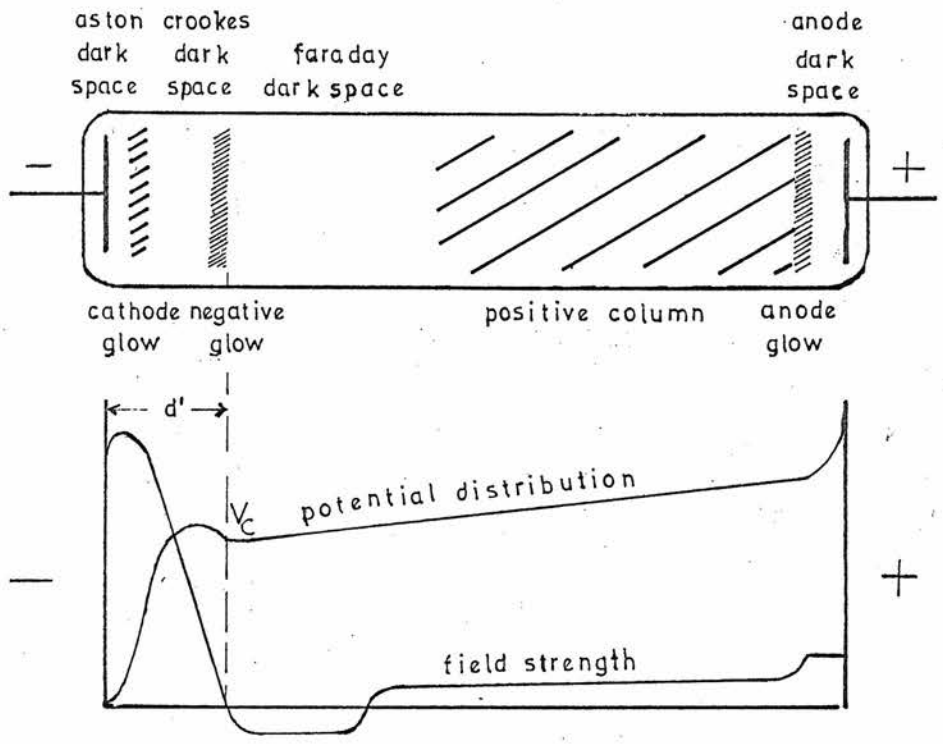

Figure A.2.2. A diagram of the physical appearance of a glow discharge, together with the voltage and electric field distribution.[144]

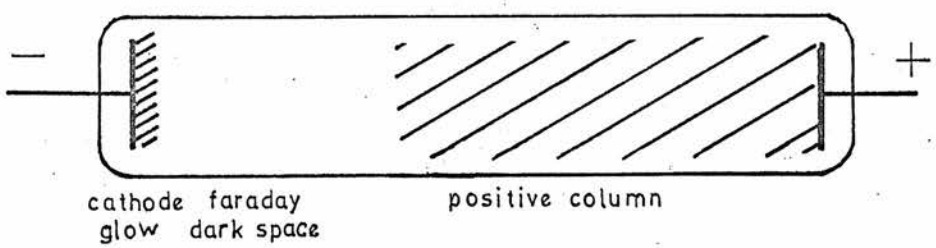

Figure A.2.3. A diagram of the physical appearance of an abnormal glow discharge.[144]

where J_o^+ is the ion current density striking the cathode. This can be shown[144] to equal

$$\frac{V_c^2 \mu^+}{\pi (d')^3}$$

where μ^+ is the positive ion mobility. Hence

$$J = \frac{V_c^2 \mu^+}{\pi (d')^3} (1 + \gamma) \qquad \text{A.2.3}$$

and the condition for stability is

$$\frac{1}{\gamma} = e^{\alpha d'} \qquad \text{A.2.4}$$

If the current is increased beyond the point where the whole cathode is covered by the negative glow, the discharge enters the "abnormal glow" section of its characteristic. From equation A.2.3 it can be seen that, in order to increase the current density, it is necessary to increase the voltage, V_c. This results in an increase in the space charge due to the positive ions, and a decrease in the distance d^1. The appearance of the discharge also changes, as shown in figure A.2.3. The three regions which are discernible are the cathode glow, the dark space where the electrons have not yet acquired sufficient energy to cause ionising collisions with the gas atoms, and the "positive column" plasma. Further increase in current leads to an unstable condition where an arc discharge may occur.

It is generally necessary to shield those parts of the cathode from which no sputtering is required. This is achieved by placing an earthed shield close to these parts at a critical distance, D, from them so that no discharge occurs in the intervening space. The required separation, D, can be found from the equation[145]

$$\alpha_b = P f\left(\frac{V_b}{PD}\right)$$

where α_b = Townsend coefficient for breakdown. The breakdown potential, V_b, is a function of the product of pressure and distance D. Figure A.2.4 illustrates this relationship (Paschen's Law) for air, under uniform field conditions.

In the region where the product P x D is less than 2.5, V_b increases rapidly with decreasing P x D, indicating that the mean free path of the electrons is of the same order of magnitude as the screen-cathode spacing, D. Consequently, if D is small so that the product PD is small at maximum operating pressure, the voltage required for breakdown will be greater than the maximum applied voltage and no discharge will occur in the shield-cathode spacing.

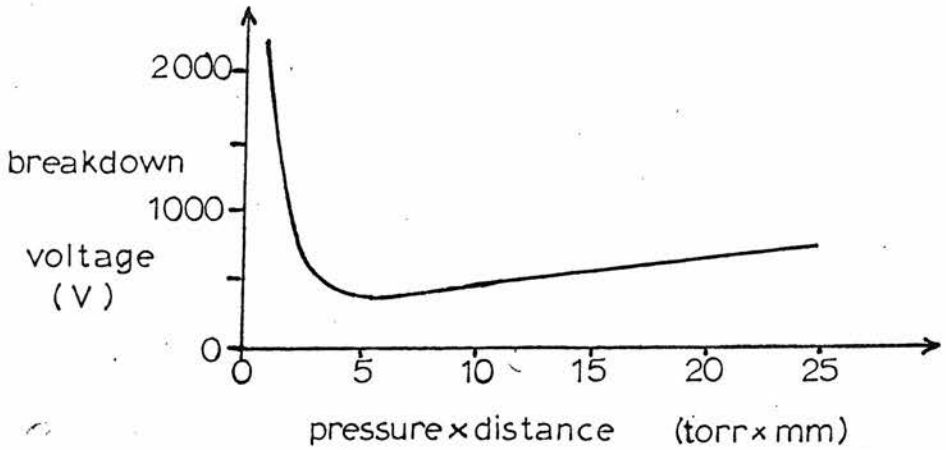

Figure A.2.4. The breakdown potential for air as a function of the product of the pressure and the spacing between parallel plate electrodes.[145]

APPENDIX 3

The Effect of a Magnetic Field on Sputtering Rate

A magnetic field acting in parallel with the discharge field $\bar{E}$ is found to increase the deposition rate when the other parameters are held constant. The explanation of this effect is contained in the following calculation. Consider the force, $\bar{F}$, exerted on an electron moving with a velocity, $\bar{v}$, in a magnetic field of $\bar{B}$ Wb/m^2 which acts parallel to the discharge field, $\bar{E}$.

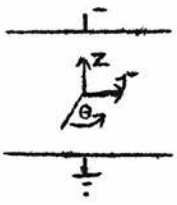

$$\bar{F} = -e\left(\bar{E} + (\bar{v} \times \bar{B})\right)$$

$$\bar{E} = E_z \;;\; \bar{B} = B_z$$

$$\Rightarrow F = -e\left(-\frac{dv}{dz} i_z + \begin{vmatrix} \bar{i}_r & \bar{i}_\theta & \bar{i}_z \\ \frac{dr}{dt} & r\frac{d\theta}{dt} & \frac{dz}{dt} \\ 0 & 0 & B_z \end{vmatrix}\right)$$

$$= -e\left(-\frac{dv}{dz} i_z + \left(B_z \frac{dr}{dt}\right) i_\theta - \left(B_z r \frac{d\theta}{dt}\right) i_r\right) .$$

$$F_r = -e r B_z \frac{d\theta}{dt} .$$

$$F_\theta = e B_z \frac{dr}{dt} .$$

$$F_z = e\frac{dv}{dz} .$$

The presence of the centrifugal component, F_r, reduces the number of electrons lost to the chamber walls. The component, F_θ causes the electrons to travel in a spiral path, thereby increasing their mean free path, so that the energy acquired between collisions increases, and the collisions are more likely to produce ionisation of the gas atoms. Hence a larger number of positive ions are available to bombard the target and the deposition rate increases.

REFERENCES

1. Martindale L., personal communication.

2. Draper M.H. & Lake P.E., Environmental Control in Poultry Production, Carter T.C. ed., Oliver & Boyd, 1968, 87-99.

3. Draper M.H., personal communication.

4. Sturkie P.D., Avian Physiology, Cornell Univ. Press, 1965, 447-498.

5. Bellhouse B.J. & Schultz D.L., J. Fluid Mech., 24, 1966, 379-400.

6. Scarr R.W.A. & Setterington R.A. Proc. IEE, 107B, 1960, 395-409.

7. Becker J.A. et al., Trans. AIEE, 65, 1946, 711-724.

8. Rasmussen R.A., Rev. Sci. Instrum., 33, 1962, 38-42.

9. Filshie J.H., The in Vivo Measurement of the Phases of Egg Formation in the Oviduct of Sallus Domesticus and their Correlation with Blood Electrolyte Concentrations, Ph.D. Thesis, University of Edinburgh, 1971.

10. Froemel J.G. & Sapoff M., 1st Symp. on Deposition of Thin Films by Sputtering, Rochester N.Y., 1966, 62-74.

11. Nelson R.S., Phil. Mag., 11, 1965, 291-302.

12. von Hippel A., Ann, Physik, 80, 1926, 672-706.
Ann. Physik, 81, 1926, 1043-1075.

13. Townes C.H., Phys. Rev., 65, 1944, 319-326.

14. Wehner G.K., Phys. Rev., 102, 1956, 690-704.

15. Laegreid N. & Wehner G.K., J. Appl. Phys., 32, 1961, 365-369.

16. Bradley R.C., Phys. Rev., 93, 1954, 719-728.

17. Wehner G.K., Trans. 8th Nat. Vac. Symp., 1, 1961, 239-244.

18. von Stark J., Z. Elektrochem., 14, 1908, 752-756.

19. Kingdon K.H. & Langmuir I., Phys. Rev., 22, 1923, 148-160.

20. Pease R.S., Rc. Scu. int.Fis. 'Enrico Fermi', 13, 1959, 158-165.

21. Silsbee R.H., J. Appl. Phys., 28, 1957, 1246-1250.

22. Onderdelinden D., Sputtering of F.C.C. Metals, Ph.D. Thesis, University of Leiden, 1968.

23. von Jan R. & Nelson R.S., Phil.Mag., 17, 1968, 1017-1032.

24. Kay E., Adv. Electronics Electron Phys., 17, 1962, 245-317.

25. Lounsbury J.B., J. Vac. Sci. & Technol., 6, 1969, 838-842.

26. Harvey J. & Corkhill J., Thin Solid Films, 6, 1970, 277-287.

27. Jones R.E. et al. J. Vac, Sci, & Technol., 5, 1968, 84-87.

28. Bulter H.S. & Kino G.S., Phys. Fluids, 6, 1963, 1346-1355.

29. Winters H.F., Ramondi D.L. & Horne E.D., A Proposed Model for the Composition of Sputtered Multicomponent Thin Films, ~~1968 Unpublished work~~. J. Appl. Phys., 40, 1969, 2996-3006.

30. Hayward D.O. & Trapnell B.M.W., Chemisorption, Butterworth, 1964.

31. Lanyon M.A.H. & Trapnell B.M.W., Proc. Roy. Soc., 227A, 1954-1955 387-399.

32. Winters H.F. & Kay E., J. Appl. Phys., 38, 1967, 3928-3934.

33. King H.A., Properties of Reactively Sputtered Silicon Nitride and Equipment Design, Honours Project (HSP/75), Dept. of Elect. Engng., University of Edinburgh, 1969.

34. Valdes L.B., Proc. IRE, 42, 1954, 420-427.

35. Klugg H.P. & Alexander L.E., X-ray Diffraction Procedures, Wiley, 1954.

36. Jenkins R. & De Vries J.L. Practical X-ray Spectrometry, Philips Technical Library, 1967.

37. Van Houten S., J. Phys. Chem. Solids, 17, 1960, 7-17.

38. Honig J.M., J. Chem. Educ., 43, 1966, 76-82.

39. Jones R.E. et al., J. Appl. Phys., 38, 1967, 4656-4662.

40. Schlichting H., Boundary Layer Theory, Pergamon, 1955, 38-47.

41. Schlichting H., ibid., 63.

42. Schlichting H., ibid., 219.

43. Schlichting H., ibid., 198.

44. Schlichting H., ibid., 245-255.

45. Whitmore R.L., Rheology of the Circulation, Pergamon, 1968, 1-15.

46. Whitmore R.L., ibid., 109-113.

47. Whitmore R.L., ibid., 62-87.

48. Whitmore R.L., ibid., 97.

49. Whitmore R.L., ibid., 145.

50. Hershey D. & Gupta B.P., Biorheol., 5, 1968, 313-321.

51. Maude A.D. & Whitmore A.L., J. Appl. Physiol., 12, 105-113.

52. Furukawa T., Med. Biol. Engng., 4, 1966, 467-472.

53. Vand D., J. Phys. Colloid. Chem. 52, 1948, 277-299.

54. Maude A.D. & Whitmore A.L., Brit. J. Appl. Phys., 7, 1956, 98-102.

55. Sturkie P.D., Avian Physiology, Cornell Univ. Press, 1965, 20

56. von Graetz L., Ann. Phys. u. Chem., 25, 1885, 337-357.

57. Knudsen J.G. & Katz D.L., Fluid Dynamics and Heat Transfer, McGraw-Hill, 1958, 361-377.

58. Sellars J.R. et al., Trans. ASME, 78, 1956, 441-448.

59. Jacob M., Heat transfer, 1, Wiley, 1949, 454-456.

60. Jacob M., ibid., 254.

61. Bellhouse B.J., Blood Flow through Organs and Tissues, Bain W.H. & Harper A.M., ed., Livingstone, 1968, 53.

62. Disa Information, 10, 1970, 30.

63. Merrill E.W. et al., Biophys. J., 3, 1963, 199-213.

64. Ham T.H. et al., Blood, 3, 1948, 373-403.

65. Bronwell A., Advanced Mathematics in Physics & Engineering McGraw-Hill, 1953, 266-267.

66. Baier R.E. & Dutton R.C., J. Biomed, Material Res., 1969, 191-202.

67. Baier R.E. et al., Surface Chemistry of Biological Systems, Blank M. ed., Plenum, 1970, 235-260.

68. Weast R.C., Handbook of Chemistry and Physics, The Chemical Rubber Co., Cleveland, 49th ed., 1968.

69. Mendlowitz M., Science, 107, 1948, 97-98.

70. Singh A. & Blackshear P.L. Digest of 7th Intemat. Conf. Med. Biol. Engng., Stockholm, 1967, 400.

71. Rand P.W. et al., J. Appl. Physiol., 19, 1964, 117-122.

72. Corning Data sheet, No. CEP2/5M/9-62, Corning Glass Works N.Y. 1962.

73. Gray D.E., American Institute of Physics Handbook, McGraw-Hill, 1957.

74. P.T.F.E. Data Handbook, No. 10M/7/68, G.H. Bloore Ltd., Stanmore, Middlesex, 1968.

75. Warner M.W. & Fordemwalt J. N. ed., Integrated Circuits, McGraw-Hill, 1965, 150-153.

76. Harrison J.A., Am. J. Surgery, 95, 1958, 3-15.

77. Williams P., Wireless World, 72, 1966, 456.

78. Digital Logic Handbook, Digital Equipment Corp., 1971, 98-99.

79. Filshie J.H., Unpublished Work.

80. Hamilton W.P. & Dow P. ed., Handbook of Physiology, section II, 2, American Physiological Society, 1963, 1277-1324.

81. Lindgren P., Acta Physiol. Scand., 42, 1958, 5-11.

82. Volkman H.W., Die Haemodynamik, Breitkopf and Hartel, Leipzig, 1850.

83. Rockemann W., Pflugers Arch. ges. Physiol., 272, 1960-61, 293-296.

84. Nash C.W. & Milligan J.V., Trans. IRE, ME-6, 1959, 274-276.

85. Stow R.W., Trans. N.Y. Acad. Sci., ser. II, 27, 1965, 748-757.

86. Hosie K.H., Circ. Res., 10, 1962, 491-504.

87. Richards J.B., Bio. Med. Engng. 5, 2, 1970, 65-70.

88. Schenk W.G. & Race D., New Findings in Blood Flowmetry, Cappelen C. ed., Universitsforlaget, Oslo, 1968, 146-153.

89. Lewis D.H. & Gelin L.E., ibid., 27-31.

90. Green H.D. et al., Trans. IRE, ME-6, 1959, 277-282.

91. Dawes G.S. et al., J. Physiol., 121, 1953, 72-79.

92. Fry D.L., Trans. IRE, ME-6, 1959, 264-266.

93. Sarnoff S.J. & Berglund E., Ibid., 270-274.

94. Brecher G.A., Ibid., 294-304.

95. Gesell R. & Bronk D.W., Am. J. Physiol., 79, 1926-7, 61-71.

96. Rein H., Z. Biol., 87, 1928, 394-418.

97. Rein H., Ergebn. Physiol., 45, 1944, 514-572.

98. Schmidt C.H. & Walker A.M., Proc. Soc. Exptl. Biol. Med., 33, 1935, 346-349.

99. Baldes E.J. & Herrick J.F., Am. J. Physiol., 129, 1940, 304.

100 Felix W. & Groll H., Z. Biol., 106, 1953, 208-218.

101. Gibbs F.A., Proc. Soc. Exptl. Biol. Med., 31, 1933, 141-146.

102. Mowbray J.F., J. Appl. Physiol., 14, 1959, 647-648.

103. Mellander S. & Rushmere R.F., Acta Physiol. Scand., 48, 1960, 13-19.

104. Katsura I. et al., Trans. IRE, ME-6, 1959, 283-285.

105. Sneed W.A. & Wood N.B., Cardiovasc. Res., 4, 1970, 253-263.

106. Ling S.C. & Atabek H.B., Proc. 19th Annual Conf. Engng. in Med. & Biol., San Fransisco, 8, 1966, 113.

107. Bellhouse B.J. et al., Blood Flow through Organs and Tissues, Bain W.H. & Harper A.M. ed, Livingstone, 1968, 43-41.

108. Grahn A.R. & Wessel H.M., Proc. 19th Annual Conf. Engng. in Med. & Biol., San Fransisco, 8, 1966, 167.

109. Lawn L. et al., Phys. Med. Biol., 9 (3), 1964, 407-411.

110. Hensel H. & Ruef J., Pflugers Arch. ges. Physiol., 259, 1954, 267-280.

111. Thurlemann B., Helv. Phys. Acta, 14, 1941, 383-419.

112. Kolin A., Proc. Soc. Exper. Biol. & Med., 35, 1936, 53-56.

113. Kolin A., Am. J. Physiol., 119, 1937, 355-356.

114. Kolin A., Proc. Soc. Exper. Biol. & Med., 46. 1941, 235-239.

115. Jochim K.E., Trans. IRE, B.M.E. - 9, 1962, 228-235.

116. Peronneau P. & Hinglais J., Onde Elect., 46, 1966, 224-237.

117. Kolin A. & Kado R., Proc. Nat. Acad. Sci. (Wash.), 45, 1959, 1312-1361.

118. Westeren A. et al., Trans. IRE, ME-6, 1959, 213-215.

119. Olmstead F., Trans. IRE, BME-9, 1962, 88-92.

120. Spenser M.P. et al., Circ. Res., 3, 1955, 39-46.

121. Spenser M.P. & Denison A.B., Trans. IRE., ME-6, 1959, 220-228.

122. Wyatt D.G., Phys. Med. Biol., 5, 1961, 289-320.

123. Wyatt D.G., ibid., 369-399.

124. Wyatt D.G., Med. Biol. Engng., 4(4), 1966, 333-348.

125. Philips C.M. & Davila J.C., Am.J.Med.Electron., 4, 1965, 166-169.

126. Kayser K.L., ibid., 113-116.

127. Spencer M.P. & Barefoot C.A., New Findings in Blood Flowmetry, Cappelen C. ed., Universitetsforlaget, Oslo, 1968, 75-87.

128. Bergel D.H. & Gessner U., Methods in medical research, Rushmer R.F. ed., 2, Year Book Medical publishers INC, Chicago, 1966, 70-82.

129. Mills C.J., New Findings in Blood Flowmetry, Cappelen C. ed., Universitetsforlaget, Oslo, 1968, 114-118.

130. Herrick J.F. & Anderson J.A., Trans. IRE, ME-6, 1959, 195-196.

131. Franklin D.L. et al., ibid., 204-206.

132. Franklin D.L. et al., Trans. IRE, BME-9, 1962, 44-49..

133. Wetterer E., ibid., 165-173.

134. Zarnstorff C.W., et al., ibid., 199-203.

135. Noble F.W. et al., Digest 15th Internat. Conf. Engng. Med. Biol., Chicago, 1962, 15.

136. Franklin D.L. et al., Science, 134, 1961, 546-565.

137. Franklin D.L. et al., Proc. I.S.A. Biomed. Sciences, I, 1963, 309-315.

138. Stegall H.F. et al., Proc 19th Annual Conf. Engng. Med. Biol., San Fransisco, 8, 1966, 109.

139. Hirschberg H., New Finding in Blood Flowmetry, Cappelen C. ed., Universitetsforlaget, Oslo, 1968, 23-26.

140. Singer J.R., Trans. IRE, ME-7(1) 1960, 23-28.

141. Soto P.B. & Tolbert B.M., Advances in Biol. & Med. Phys. 5, 1957, 1-35.

142. Suryan G., Proc. Indian Acad. Sci., 33(2) 1951, 107-111.

143. Andrews E.R., Nuclear Magnetic Resonance, Cambridge Univ. Press, 1955.

144. Leob L.B., Fundamental Processes of Electrical Discharge in Gases, Wiley, 1947.

145. Ramey R.L. Physical Electronics, Prentice-Hall, 1961, 228-243.